Oliver Zimmer

Contributions to the Fundamental Understanding of Nanoparticle Cell Interactions and Target-Specific Biodistribution

---

The presented work was carried out from July 2018 until November 2023 at the Department of Pharmaceutical Technology at the University of Regensburg.

The thesis was prepared under the supervision of Prof. Dr. Achim Göpferich.

Doctoral application submitted on: November 13th, 2023
Date of examination: January 22nd, 2024

Examination board:

Chair:	Prof. Dr. Ursula Storch
1st Expert:	Prof. Dr. Achim Göpferich
2nd Expert:	Prof. Dr. Miriam Breunig
3rd Expert:	Prof. Dr. Antje Bäumner

Contributions to the Fundamental Understanding of Nanoparticle Cell interactions and Target-Specific Biodistribution

Dissertation to obtain the Degree of Doctor of Natural Sciences

(Dr. rer. nat.)

From the Faculty of Chemistry and Pharmacy

University of Regensburg

Presented by

Oliver Zimmer

from Hamburg (Germany)

November 2023

Dedicated to my family.

What we know is a drop, what we don't know is an ocean.

Isaac Newton (1643 – 1727)

Table of Contents

Chapter snippets

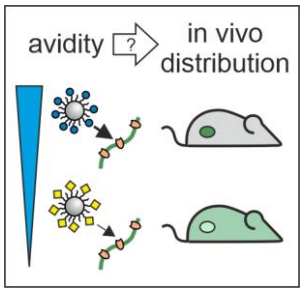

Chapter 1:

Goal: Investigate Correlation of Avidity and Nanoparticle Biodistribution in vivo.

Method: Review of available literature.

Outcome: A need for fundamental research on nanoparticle-cell interactions was identified.

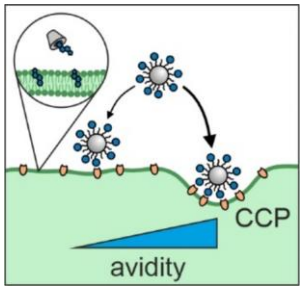

Chapter 3 (*SI: Chapter 4*):

Goal: Study the impact of nano-scale membrane morphology (i.e., CCPs) on nanoparticle avidity.

Method: Nanoparticle-cell binding assay & small-molecular CCP formation inhibitors.

Outcome: CCPs resemble high-avidity binding sites for nanoparticles.

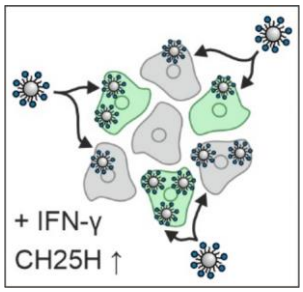

Chapter 5 (*SI: Chapter 6*):

Goal: Determine the impact of IFN-γ on nanoparticle distribution.

Method: Nanoparticle distribution studies in target/off-target cell co-culture models.

Outcome: IFN-γ reverses ligand-induced target cell specificity due to CH25H upregulation.

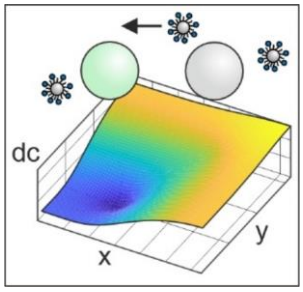

Chapter 7:

Goal: Understand the underpinning mechanism of the observed change in nanoparticle distribution.

Method: Spatiotemporal simulation of target/off-target particle distribution.

Outcome: Depletion of nano-scale high-avidity binding sites can indeed affect micro-scale particle distribution.

Chapter 1

Nature of the Correlation between Nanoparticle Avidity and Biodistribution

To be submitted for publication to the
European Journal of Pharmaceutics and Biopharmaceutics

Abstract

The specific delivery of a drug to its site of action also known as targeted drug delivery is a topic in the field of pharmaceutics studied for decades. One approach extensively studied in this context is the use ligand functionalized nanoparticles. These particles are modified to carry receptor specific ligands, enabling them to accumulate at a desired target site. However, while this concept initially appears straightforward to implement, in-depth research has revealed several challenges hindering target site specific particle accumulation - some of which remain unresolved to this day. One of these challenges is the still incomplete understanding of how nanoparticles interact with biological systems. This knowledge gap significantly compromises the predictability of particle distribution in biological systems, which is critical for therapeutic efficacy.

One of the most crucial steps is nanoparticle attachment to cell surfaces at the target site. This attachment occurs via the formation of multiple ligand receptor bonds. A process also referred to as multivalent interaction. While multivalency has been described extensively for individual molecules and macromolecules respectively, little is known on the multivalent binding of nanoparticles to cells. Here, we will specifically introduce the concept of avidity as a measure for favorable particle membrane interactions. Also, an overview about nanoparticle and membrane properties affecting avidity will be given. Thereafter, we provide a thorough review on literature investigating the correlation between nanoparticle avidity and success in targeted particle delivery.

Graphical Abstract

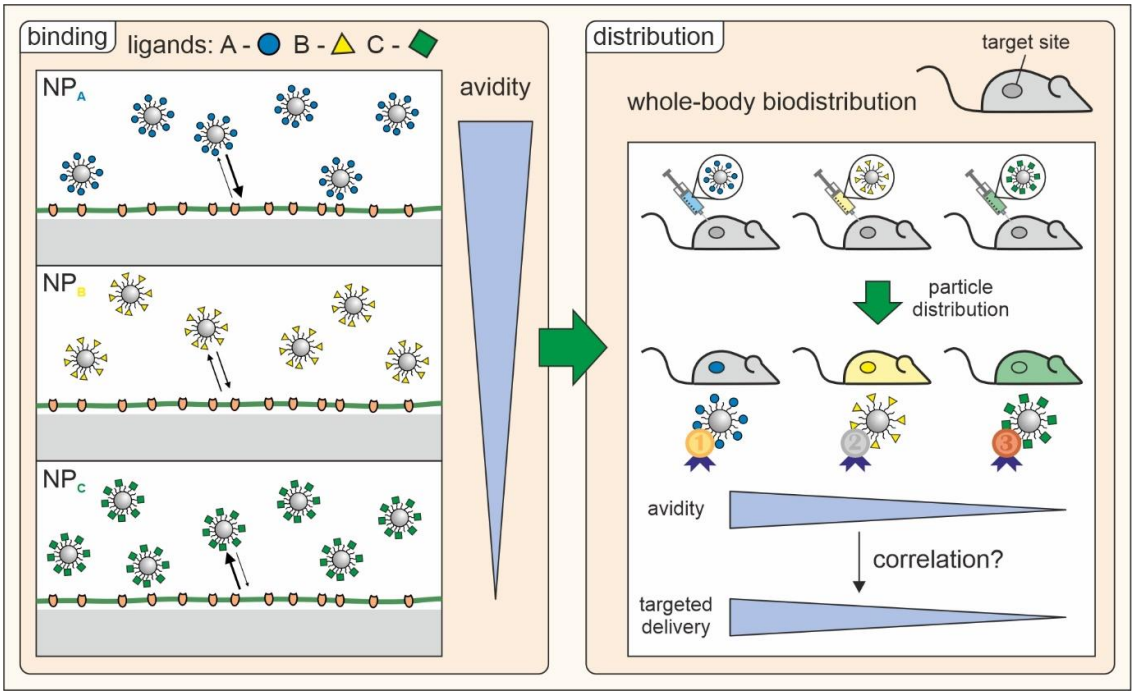

The hypothetical example of three particles exhibiting decreasing binding avidity due to their different ligands is used to illustrate the question addressed by the present work: To what extend does binding avidity correlate with targeted particle delivery? Data on the evidence and degree of correlation between nanoparticle avidity and successful targeted delivery published in literature are presented and discussed.

Introduction

Targeted drug delivery is an intensively studied topic in pharmaceutics [1]. The concept aims for an exclusive distribution of a drug at its intended site of action. This way, an administered dose can efficiently unfold the drugs therapeutic effect, while no other sites are at risk of potential side-effects. One approach employed to achieve targeted drug delivery is the use of nanoparticles [2–4]. Herein, we focus on ligand functionalized nanoparticles [5]. At the core of this concept, the particle surface is modified to carry ligand molecules [6,7] enabling recognition of target site specific cellular receptors [8] or ectoenzymes [9] via a key-lock mechanism. Once the particle encounters its site of action, multiple ligand receptor bonds are formed, attaching the particle to cell surfaces. Thus, the particle is retained at the target site or even induces active uptake into the cell via endocytosis [10,11]. Drug molecules can be incorporated into such particles to enable cell-specific delivery. Molecule-types incorporated into nanoparticles are small-molecular drugs [12], peptides [13,14], biopharmaceuticals [15,16], and nucleic acids of different nature [17–20]. A targeted delivery is very desirable for many applications especially in the case of highly potent agents, such as anti-cancer drugs, which can cause damage in healthy tissues and organs. Also, highly valuable agents such as biologics or vaccines would benefit greatly from targeted delivery [21].

The optimal method to investigate in vivo nanoparticle deposition is to track the whole-body biodistribution [22–25]. A measure for successful targeted delivery is the percentage of administered dose found in the intended cell-type tissue [26]. In pursuing optimized particle distribution, a number of factors have been identified hindering targeted delivery of nanoparticles. Some of the most studied problems, which are mutually dependent to some extent, are the formation of a protein corona on the particle surface [27–29], interaction with immune cells [30], and undesired particle accumulation in typical off-target organs (e.g., liver and spleen) [31–33]. All these phenomena were shown to decrease particle accumulation at the desired site of action while increasing loss of particles due to rapid elimination or unspecific deposition [34–37]. While almost all steps in the journey of a particle have been intensively studied [38], it is somewhat surprising that the particle-cell surface interaction has received little attention in studies on nanoparticle biodistribution. As nanoparticle-membrane interactions are often studied in isolated experiments based on artificial or isolated membranes [39–41] using techniques like surface plasmon resonance (SPR) [42] or microscale thermophoresis

(MST) [43,44], we know very little about how distinct morphological entities at the nano-scale affect particle avidity. Concluding, we have a good understanding of how particle properties affect quantitative binding parameters like avidity. However, the relationship between avidity and biodistribution has hardly been studied and therefore remains elusive.

In the first part of this work, we will give a brief introduction to the theoretical background on nanoparticle binding to cell surfaces. As nanoparticles are usually multivalently functionalized, we will discuss the fundamental thermodynamics governing the formation of multivalent ligand receptor complexes. Specifically, we will illustrate the term of avidity as a commonly used quantity to describe multivalent interactions of particles binding to receptor carrying cell surfaces. Furthermore, we will shed a light on the impact of membrane properties on particle-membrane interactions. Here, we will specifically discuss the often-neglected role of membrane curvature. Overall, this section is intended to provide the reader with a fundamental understanding about particle and membrane properties dictating avidity of nanoparticle membrane binding. We also intend to discuss dose-dependence of nanoparticle biodistribution as an under-researched topic in the context of targeted nanoparticle delivery, which we believe should receive more attention.

In the second part of this work, we intend to provide an overview about studies investigating the impact of particle binding avidity or ligand density on particle biodistribution. We included studies specifically addressing this matter as well as publications providing relevant insights while pursuing a different research goal. Most interesting studies for our purpose to describe effect of nanoparticle avidity on biodistribution were whole-body biodistribution studies. However, we also included studies investigating the impact of avidity on particle distribution on the tissue or cell level. Based on the concepts introduced in the first section, we will elaborate to what extent avidity correlates with nanoparticle biodistribution. In conclusion, we will determine whether the data available in literature indicate a transferability of the theory of avidity to the case of nanoparticle distribution in a complex biological system.

Fundamentals of Nanoparticle Avidity Concept

A fundamental understanding of avidity is helpful to follow the work below. An excellent review on this matter is available in literature [45]. For this reason, here we will give a short, easily accessible overview. For more detailed insights, the interested reader is referred to the relevant original literature.

To begin, we want to look at thermodynamic models describing the Gibb's energy of a multivalent binding, since we can learn from these models what influencing variables determine avidity. Earliest works leading to thermodynamic models describing avidity of multivalent interactions were conducted by Jencks et al. [46,47]. To properly appreciate the models derived from this, one must consider the intentions of the respective authors. To this end, an initial model developed by Kitov and Bundle is excellently suited for computational simulation of Gibb's free energy of multivalent interactions ($\Delta G^0_{avidity}$) [48]. However, here the properties underlying and determining the avidity of the interacting structures remain somewhat elusive. Therefore, to gain a better insight into these properties, we will also consider the model developed by Krishnamurthy et al. [49] Here it is unraveled in more detail what is behind the possibly hard to grasp thermodynamic parameters. We will see that Krishnamurthy et al. derived their model on Gibb's free energy of multivalent interactions (here denoted as ΔG^0_N (i)), considering individual receptor-ligand interactions as additive and expanding the model by introducing enthalpy (ΔH) and entropy ($T\Delta S$) terms accounting for phenomena inherent of multivalent interactions. In this way, they derive a model from which we can derive properties of multivalent ligand complexes (e.g., ligand functionalized nanoparticles) can be derived, whose variation could affect particle avidity [49].

The model introduced by Kitov and Bundle is based on a simple expression for microscopic free binding energy Δg^0_i (Eq. 1) of a single interaction between a multivalent ligand L and a receptor R receptor-ligand complex denoted as rl(i). In clear words, rl(i) in our example of ligand functionalized nanoparticles binding to receptor carrying cell membrane would correspond to a single particle forming i ligand receptor bonds. ΔG^0_{mono} is a rather straightforward parameter as it represents the binding free energy of a monovalent interaction. $\Delta G^0_{interaction}$, however, might appear a bit more elusive. This is a parameter introduced to account for differences in the free energy of the first intermolecular bond and all 'intramolecular' bonds formed subsequently.

$$\Delta g_i^0 = i\Delta G_{mono}^0 + \Delta G_{interaction}^0 \qquad (1)$$

Again, transferred to our example of particle-membrane interactions, ΔG^0_{mono} would be the first ligand-receptor bond formed, while $\Delta G^0_{interaction}$ would describe the difference between the free energy of this initial bond and all other bonds formed subsequently.

The authors rearrange their model introducing the terms $\Delta G^0_{mono} = \Delta G^0_{inter}$ and $(i\text{-}1)\ \Delta G^0_{intra} = (i\text{-}1)\ \Delta G^0_{mono} + \Delta G^0_{interaction}$ which separates the free energy of the bonds formed after the-initial binding took place. Also, the authors extend the so far microscopic model (i.e., accounting for only a single rl(i) complex = a single particle bound to a membrane) to a macroscopic model (i.e., accounting for a large number of rl(i) complexes = particles) by introducing a degeneracy coefficient Ω_i. This is in simple words the number of microscopically distinguishable rl(i) complexes (i.e., in our example the number of particles in the i-th state) (Fig. 1A). The model ultimately has the following form where R is the gas constant and T is the absolute temperature:

$$\Delta G_i^0 = \Delta G_{inter}^0 + (i-1)\Delta G_{intra}^0 - RT\ln\Omega_i \qquad (2)$$

We learn from this first model of the free energy of multivalent interactions that avidity must not be understood as an ‘additive’ phenomenon. Instead, for must multivalent interactions, the bonds already formed influence the formation of further bonds. This property of multivalent interactions is called cooperativity. As cooperativity is a broad topic on its own, we will leave it here with a brief definition of the term. We consider a simple interaction of a monovalent ligand A and a bivalent receptor BB (Fig. 1C). This system can be described by the law of mass as following.

$$2K_1 = \frac{[A\cdot BB]}{[A][BB]} \qquad \text{and} \qquad \frac{1}{2}K_2 = \frac{[A_2\cdot BB]}{[A][A\cdot BB]} \qquad (3 \text{ and } 4)$$

The interaction is called cooperative if the condition

$$\frac{K_2}{K_1} \neq 1 \qquad (5)$$

is met. A ratio of the two reaction constants $K_2/K_1 > 1$ indicates a positive cooperative interaction (i.e., the first bond favors the second bond) while $K_2/K_1 < 1$ indicates a negative cooperative interaction (i.e., the first bond hinders the second bond) [45,50]. However, the model of Kitov and Bundle tells us little about particle properties that can affect avidity.

Next, we therefore consult the model developed by Krishnamurthy et al. to see if we can draw further insights from it on nanoparticle properties affecting avidity. The model ultimately has the following form:

$$\begin{aligned}\Delta G_N^0(i) = i\Delta H_{affinity}^0 - iT\Delta S_{affinity}^0 + (i-1)T\Delta S_{trans+rot}^0 \\ + (i-1)\Delta H_{linker}^0 \\ - (i-1)T\Delta S_{conf}^0 + (i-1)\Delta G_{coop}^0 - RT\ln(\Omega_i/\Omega_0)\end{aligned} \qquad (6)$$

As this model may seem a bit intimidating at first, let us take a step back. We first consider the general equation of Gibbs energy which is given as follows:

$$\Delta G = \Delta H - T\Delta S \qquad (7)$$

If we now take another look at the model, we will see that here only enthalpy (ΔH) and entropy (ΔS) amounts are added for different processes. For each term, there is an additional factor that determines whether the corresponding term is to be taken into account for all bonds (i) or for all bonds except the initial bond (i-1). And as we know that a negative free energy ΔG (ΔG < 0) indicates the volatility of a reaction (i.e., in our case, particle binding), we can deduce that to increase the avidity of our particle, the individual terms must be modified to overall achieve, at best, a negative binding enthalpy (-ΔH) and an increase in entropy (+ΔS). However, since we are studying the attachment of a particle to a membrane, an increase in entropy is not to be expected. Therefore, practically a minimum entropy loss is to be aimed for (Fig. 1B). In turn, this gives us indications as to which particle properties determine avidity.

As an example, let us consider the first two terms of the model:

$$\Delta G = \underbrace{\Delta H}_{i\Delta H^0_{affinity}} - \underbrace{T\Delta S}_{iT\Delta S^0_{affinity}} \quad (8)$$

These terms describe the independent formation of all i receptor ligand bonds. This part of the model therefore corresponds to the term ΔG^0_{mono} in the model of Kitov and Bundle. Note that for instance this expression does not yet account for cooperativity. In the model of Krishnamurthy et al. this is accounted for via a separate free energy term (i-1) ΔG^0_{coop} which is consequently considered for all bonds except the initial bond, as cooperativity can only occur after the formation of an initial bond. We learn from these first terms of the model that the nature of the ligand and its corresponding receptor will affect the avidity of the particle. An extended collection of free binding energy data has been published in this regard. In this context, there is literature as well as databases available for the selection of ligand-receptor pairs possessing a strongly negative free energy of binding ΔG [51–54].

Let us now go through some more terms to get a clearer understanding about further particle parameters affecting particle avidity. Krishnamurthy et al. stress the importance of the third term:

$$(i-1)T\Delta S^0_{trans+rot} \quad (9)$$

As this term accounts for another essential concept in multivalent interaction referred to as chelate or multivalency effect. To briefly introduce this concept, on the one hand, we envision a particle to which a certain number of ligands have been functionalized. On the other hand, we consider the same number of unbound ligands. Here, an entropy penalty must be ‘paid’ for each unbound ligand that attaches to a receptor. Each ligand almost completely loses its translational and rotational mobility upon binding. In the case of the particle, however, after the attachment of the initial ligand the translational and rotational mobility of all other ligands is already significantly reduced as they are all tethered to the same particle. The entropy penalty is therefore reduced for the formation of subsequent bonds (Fig. 1C) [46,47,55]. Since for the first ligand-receptor bond formed, the full entropic penalty has to be paid, this term is considered for all bonds but

the initial one (i-1). We can gain a clearer understanding of the influence of this term by considering at the separated fraction of translation entropy (ΔS_{trans}). Finkelstein and Janin derived an estimate for this parameter [56].

$$\Delta S_{trans} \approx 3R \ln\left(\frac{\delta x}{v^{1/3}}\right) \qquad (10)$$

Here, δx is the mean amplitude of the bound ligand in the three principal directions (i.e., after attachment), and v is the volume accessible to the ligand in solution (i.e., ahead of attachment). As a simple rule of thumb, we can deduce that the more the ligand is restricted in its freedom of movement due to the binding, the higher the entropic penalty. One way to optimize avidity could be to constrain the mobility of the ligand prior to binding on the particle (e.g., by tightly packing the ligands on the particle surface or rigid linkers). However, ligand mobility has been described as an essential prerequisite for the interaction of particles with membranes [57]. For this reason, we consider it unlikely that the (i-1) $\Delta S^0_{trans+rot}$ term is suitable as a starting point for optimizing avidity.

A promising approach to improve the avidity of a multivalent nanoparticle may lie in the use of cooperative membrane receptors. This would target (i-1) ΔG^0_{coop} term in the model of Krishnamurthy et al. Beneficial effects would be expected here, however, only in the case of positive cooperativity, in which the formation of the first bond favors that of the second ($-\Delta G^0_{coop}$, Eq. 5). Concretely, hetero-multivalent functionalized particles could be used, whose first ligand, upon binding to the receptor exposes the high-affinity binding site for the second ligand via a conformational shift. In this way, one could take advantage of receptor allostery. The strategy of allosteric binding cooperativity was already introduced by de Amici et al. with a mainly pharmacological focus [58]. A transfer of this strategy to the targeted delivery of nanoparticles, however, could be promising, considering the introduced models.

Finally, one of the most important factors influencing the avidity of multivalent ligands has to be discussed. This is the number of formed bonds i. If we take it as given that the enthalpy and entropy terms in the model introduced by Krishnamurthy et al. (Eq. 6) result in a negative Gibbs free energy (i.e., the binding of the particle will proceed voluntarily), then i alone determines the magnitude of the Gibbs free energy.

To deduce a hypothesis on nanoparticle distribution, let us consider the nanoparticle as a multivalent ligand (L) encountering two cell membrane surfaces (M_1 and M_2) with two different receptor (R) densities (ρ^{M1}_R ρ^{M2}_R). Under the prerequisite outlined above:

$$L + R \rightarrow LR \quad \text{has} \quad \Delta G < 0 \tag{11}$$

if

$$\rho_R^{M1} > \rho_R^{M2} \tag{12}$$

than the number of bonds (i) will accordingly vary, resulting in distinct Gibbs free energies for attachment of L to M_1 or M_2:

$$i_{M1} > i_{M2} \quad \rightarrow \quad \Delta G_{L\rightarrow M1} < \Delta G_{L\rightarrow M2} \tag{13}$$

Therefore, making the attachment of L (i.e., multivalently functionalized nanoparticle) to M_1 (i.e., membrane expressing the higher receptor level) favorable over the attachment to M_2. With the equations Eq. 12 and Eq. 13, we formulated the hypothesis to be derived from the introduced model under the assumption of Eq. 11 for the distribution of nanoparticles faced with membranes possessing different receptor densities. Initial supporting evidence for this hypothesis can be found in the work of Martinez-Veracoechea and Frenkel who found in simulations that even the smallest changes in receptor density may have a massive impact on binding behavior [59]. Transferred to the case of nanoparticle biodistribution our hypothesis suggests accumulation in the tissue or organ showing the highest receptor expression. One goal of this work will be to compare the experimental data on biodistribution of ligand-functionalized nanoparticles available in the literature against this hypothesis.

For this purpose, we intend to review biodistribution studies investigating ligand-functionalized nanoparticle, ideally providing quantitative particle binding parameters. Here, dissociation constants (K_D) would be the ideal parameter as K_D relates to the Gibbs free energy by the simple term [60]:

$$\Delta G = RT \ \ln K_D \tag{14}$$

At last, we want to discuss limitations of the theoretical framework introduced. For all considerations above, it must be emphasized that the presented models were formulated to describe interactions of oligovalent macromolecules. Whether a simple transferability of these models to the case of a multivalent nanoparticle is given must therefore be critically evaluated. Thus, Krishnamurthy et al. [49] explicitly stress that their model does not account for aggregation of receptors via simultaneous binding of multiple receptors to one oligovalent ligand. The assumption is made that the receptor is strongly diluted. Yet, with respect to ligand-functionalized nanoparticles, the phenomenon of ligand-receptor interaction-induced receptor aggregation has been frequently described [61–63].

A fundamental work on the avidity of multivalent particles was presented by Hong et al. They synthesized 5 poly(amidoamine)-based dendrimers functionalized with controlled amounts of folic acid molecules. Interactions with immobilized folate binding proteins were characterized using surface plasmon resonance (SPR) technique. In this early work, the authors found that avidity expressed as the dissociation constant K_D of dendrimer conjugates decreased with increasing valency, resulting from a linear increase in k_{on} and an exponential decrease in k_{off} [64]. So far, the observations follow the expectations based on the theoretical framework introduced. However, as we will see with the exemplary systems presented below, this observation on the mechanistic origin of avidity seems not to be generally applicable.

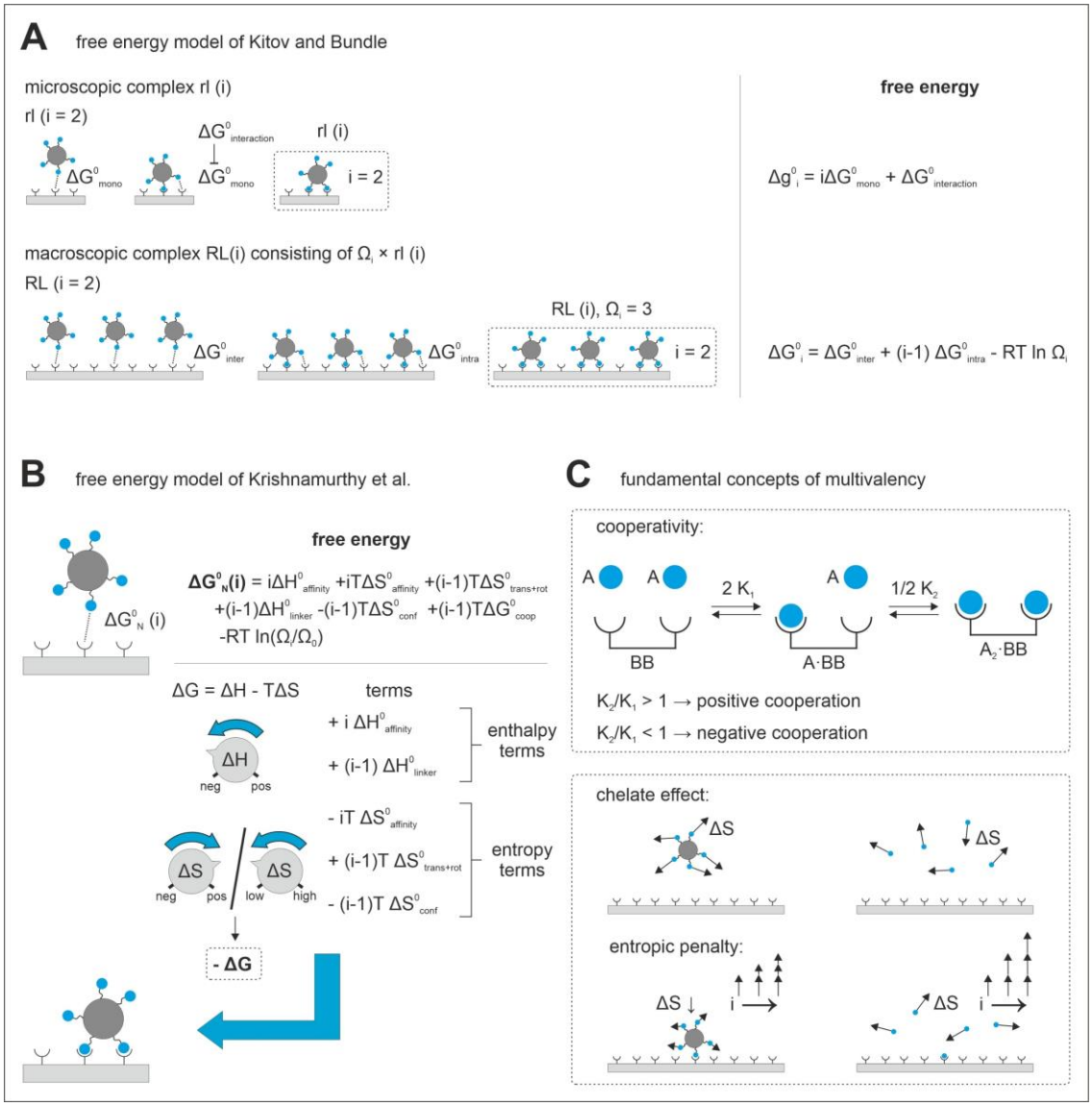
A
free energy model of Kitov and Bundle
microscopic complex rl (i)
rl (i = 2)
ΔG⁰ interaction
rl (i)
ΔG⁰ mono
ΔG⁰ mono
i = 2
free energy
Δg⁰ i = iΔG⁰ mono + ΔG⁰ interaction
macroscopic complex RL(i) consisting of Ωi × rl (i)
RL (i = 2)
RL (i), Ωi = 3
ΔG⁰ inter
ΔG⁰ intra
i = 2
ΔG⁰ i = ΔG⁰ inter + (i-1) ΔG⁰ intra - RT ln Ωi
B
free energy model of Krishnamurthy et al.
free energy
ΔG⁰N (i)
ΔG⁰N(i) = iΔH⁰affinity +iTΔS⁰affinity +(i-1)TΔS⁰trans+rot
+(i-1)ΔH⁰linker -(i-1)TΔS⁰conf +(i-1)TΔG⁰coop
-RT ln(Ωi/Ω0)
ΔG = ΔH - TΔS
terms
ΔH
neg
pos
+ i ΔH⁰affinity
+ (i-1) ΔH⁰linker
enthalpy terms
ΔS
neg
pos
ΔS
low
high
- iT ΔS⁰affinity
+ (i-1)T ΔS⁰trans+rot
- (i-1)T ΔS⁰conf
entropy terms
- ΔG
C
fundamental concepts of multivalency
cooperativity:
A
A
2 K1
A
1/2 K2
BB
A·BB
A2·BB
K2/K1 > 1 → positive cooperation
K2/K1 < 1 → negative cooperation
chelate effect:
ΔS
ΔS
entropic penalty:
ΔS ↓
i
ΔS
i

Figure 1: Fundamental theoretical framework governing the formation of multivalent interactions. (A) The model introduced by Kitov and Bundle initially describes the Gibbs free energy Δg^0_i of a microscopic receptor ligand complex rl(i). The terms in this model represent the formation of a monovalent intermolecular bond ΔG^0_{mono} while all subsequent intramolecular bonds are described by an interaction term $\Delta G^0_{interaction}$ correcting their free energy for all phenomena inherent to multivalency. This model is expended to (a) apply for the macroscopic scenario of several multivalent ligands L interacting with a multivalent receptor R by introducing a degeneracy factor Ω_i (forming a complex RL(i)), and (b) to consider the initial bond and the subsequent bonds separately (i.e., ΔG^0_{inter} and ΔG^0_{intra}). (B) The model of Krishnamurthy et al. has a slightly different form. Here, the enthalpy and entropy components of relevant properties of the multivalent receptor are summed to obtain the Gibbs free energy $\Delta G^0_N(i)$ of the interaction as a function of the number of formed bonds i. The cooperativity of the interaction is accounted for by a separate free energy term ΔG^0_{coop}. Again, a factor Ω_i/Ω_0 is introduced to obtain a macroscopic model. In this form, the model can be used to derive parameters that affect avidity. (C) Shows knowledge snippets on two key phenomena inherent to most multivalent interactions. Cooperativity describes the effect which the formation of an initial bond to a multivalent receptor exceeds on the formation of subsequent bonds. If the initial bond favors the formation of subsequent bonds a positive cooperativity is present ($K_1 < K_2$). In the opposite case when the initial bond hinders the formation of further bonds, the cooperativity is negative. The chelate effect describes how the attachment of a multivalent ligand via an initial bond reduces the entropy (represented by black arrows) of the not yet receptor-bound ligands tethered to the same backbone. This results in a reduced entropic penalty to be paid upon binding of these ligands compared to the attachment of an equal number of free ligands.

Impact of Membrane Curvature on Nanoparticle-Cell Interaction

Several papers have systematically investigated the impact of physicochemical nanoparticle properties like size [65–74], surface charge [75–77], and shape [78–81] on biodistribution. However, in this section we would like to shift our focus and shed a light on the counterpart of the particle in multivalent attachment, the cell membrane. Which properties of the membrane affect the interaction? And could a change in the membrane alone alter the avidity of a given particle? We consider these questions highly relevant because in biological systems the composition of cell membranes is constantly changing. Since the properties of membranes are highly sensitive to changes in their composition [82,83], a particle thus continuously encounters membranes with changing properties. Therefore, studying particle interactions with membranes of varying compositions and in different states could improve the predictability of biodistribution.

In our work, we want to focus on one particular membrane property, the membrane curvature. First, we want to give a brief introduction to this property. How should we picture the curvature of a membrane? To get a good idea, let us first consider a planar membrane. If we now press a spherical shape with the radius r_S onto this membrane, an invagination will form which corresponds to the negative shape of the sphere. The curvature K_m of the membrane section that is in contact with the sphere is then equal to the reciprocal of the square of r_S (Fig. 2A) [84]. This curvature is commonly referred to as gaussian curvature.

$$K_m = \frac{1}{{r_S}^2} \tag{15}$$

However, while the gaussian curvature is a suitable measure to characterize the shape of a membrane, what factor does indeed determine this shape? This factor is called spontaneous curvature and it can be thought of as an intended membrane shape that is continuously strived for by the actual membrane shape. One force contributing to this is the spontaneous curvature of the membrane's lipid components. This spontaneous curvature describes the tendency of individual lipid molecules to induce positively or negatively curved membranes (e.g., O/W- or W/O micelles, Fig. 2B) [85,86]. Next to the lipid components, also proteins attached to or intercalating the membrane also contribute to the overall spontaneous curvature [87].

This parameter is relevant for the interaction of nanoparticles with membranes, as any change in the membrane shape contrary to the direction dictated by the spontaneous curvature requires an energy input, referred to as bending energy. Since changes in membrane curvature occur during initial binding and further invagination of a particle at the membrane, the bending energy is a barrier to be overcome for these processes. In this context, fundamental scientific efforts have led to the realization that the height of this energetic barrier depends on the initial curvature of the membrane. It was found that a membrane curvature towards the particles reduces the bending energy to be supplied (Fig. 2C) [88–92]. Since the bending energy must be provided by the binding energy released during attachment, it follows that with a membrane curvature approaching the curvature of the binding particle, the binding energy to be applied approaches a minimum. Analogously, it can be concluded that for a given binding energy (e.g., for a given ligand attached to a particle), the bending energy to be overcome is lowest at the membrane whose curvature most closely matches that of the particle.

Finally, we want to propose a linkage between membrane curvature and the theoretical framework underlying the avidity of multivalent interactions. In doing so, we want to shed a light on the binding of ligand-functionalized particles, as these have been largely neglected in the previous investigation on the impact of membrane curvature. Let us consider a particle approaching a completely flat membrane (Fig. 2C (A)) and a membrane corresponding to its surface curvature (Fig. 2C (B)). What would the laws of avidity introduced in the previous section suggest in this case? It is reasonable to assume that the larger contact area will result in a higher number of ligands being located in close proximity to their receptors. Assuming the condition formulated in Eq. 11, it follows that a higher number i of bonds will form in this case, which is why process (B) can be assumed to be thermodynamically favorable (Eq. 12 and 13). Consider a third case (Fig. 2C (C)), in which a particle encounters two membrane structures concurrently, one of which contains many membrane segments like the one in (B). The considerations presented above lead to the conclusion that there will be a preferential binding of the particle to the membrane with the curved segments.

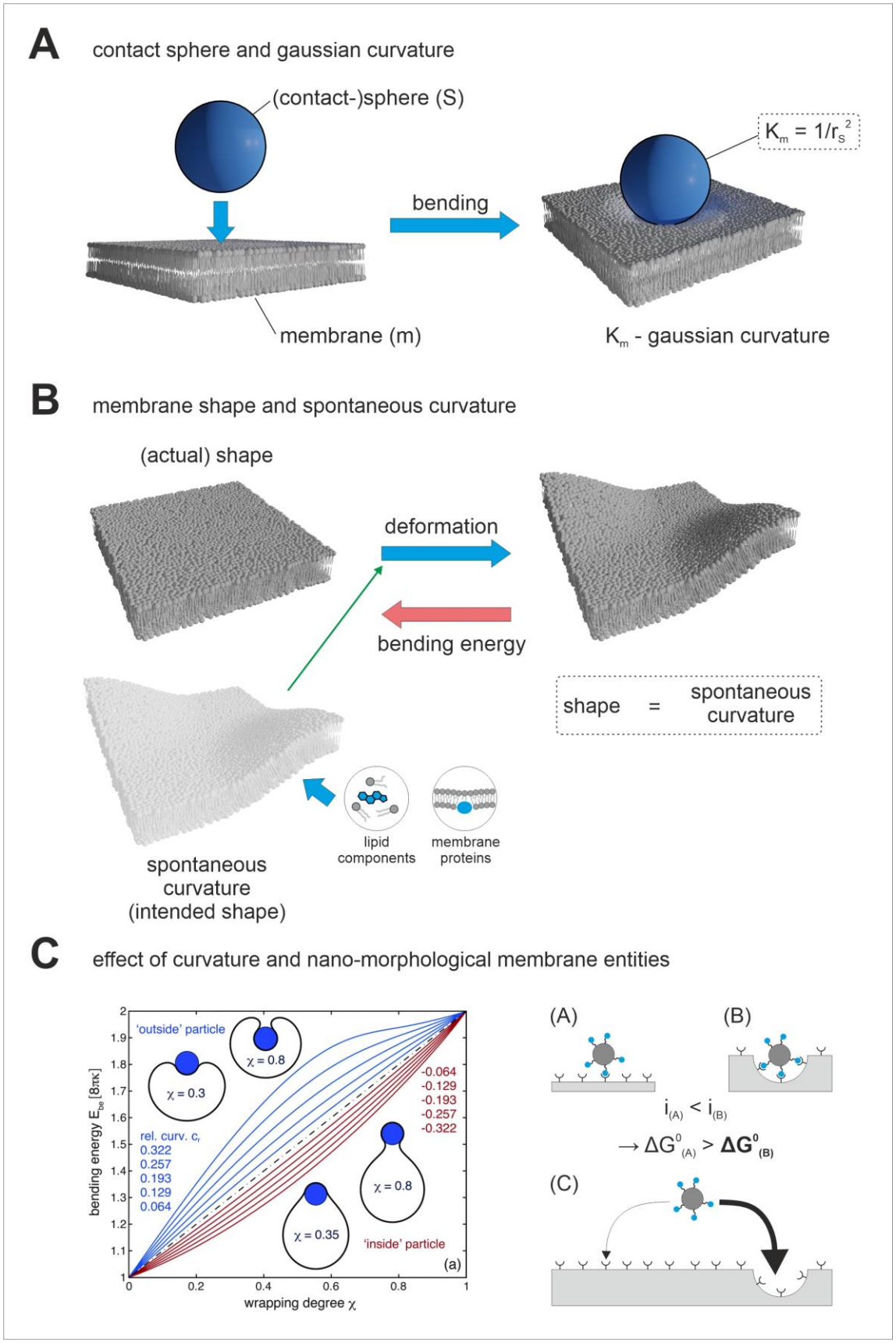
A
contact sphere and gaussian curvature
(contact-)sphere (S)
bending
$K_m = 1/r_S^2$
membrane (m)
K_m - gaussian curvature
B
membrane shape and spontaneous curvature
(actual) shape
deformation
bending energy
shape = spontaneous curvature
lipid components
membrane proteins
spontaneous curvature (intended shape)
C
effect of curvature and nano-morphological membrane entities
'outside' particle
χ = 0.8
χ = 0.3
rel. curv. c_r
0.322
0.257
0.193
0.129
0.064
-0.064
-0.129
-0.193
-0.257
-0.322
χ = 0.8
χ = 0.35
'inside' particle
(a)
bending energy E_{be} [8πκ]
wrapping degree χ
(A)
(B)
$i_{(A)} < i_{(B)}$
$\rightarrow \Delta G^0_{(A)} > \Delta G^0_{(B)}$
(C)

Figure 2: Introduction to the concept of membrane curvature and how it affects particle-membrane interactions. (A) As a measure to characterize the curvature of a membrane, we introduce the gaussian curvature K_m. This parameter can best be understood by imagining a sphere lowering onto the membrane and forming an invagination. The gaussian curvature of the membrane in contact with the sphere (i.e., contact sphere) then is given by $K_m = 1/r_S{}^2$, where r_S is the radius of the contact sphere. (B) The driving force determining the shape of a membrane is the spontaneous, which can be understood as an intended shape of the membrane which the membrane aims to adopt. The spontaneous curvature itself is determined by the composition of the membrane as wells as by membrane attached and intercalating proteins. Most importantly, we note that any deformation contrary to the spontaneous curvature requires energy to be supplied to the system. This energy is referred to as bending energy. (C) This bending energy is key to understand the impact of membrane curvature on particle-membrane interactions, as it resembles a barrier to be overcome to allow particle attachment and further ingestion. It was found that a membrane curvature facing towards a particle (i.e., 'inside' particle) reduces the required bending energy. Data presented plots the bending energy barrier against the wrapped membrane fraction (χ, i.e., the proportion of particle surface in contact with membrane). Red curves represent 'inside' particles (i.e., membrane curved toward the particle), blue curves represent 'outside' particles (i.e., membrane curved away from the particle) (Reproduced from Ref. [92] with permission from the Royal Society of Chemistry) [92]. Combining the presented theoretical framework on avidity with the curvature dependence of particle binding, we conclude that membrane sections matching particle curvature could represent binding hotspots. This appears evident, due to lower Gibbs free energies suggesting preferential attachment.

Interestingly, such curved membrane segments are not just a purely theoretical construct. They have a biological pendant. For instance, clathrin-coated pits (CCPs) are spontaneously formed [93] morphological membrane entities in good correspondence with nanoparticles of a diameter of 50-150 nm [94]. Given the introduced theoretical framework of avidity and the effects of membrane curvature on particle attachment, we consider it conceivable that CCPs might act as binding hot-spots in the interaction of ligand-functionalized nanoparticles with cell membranes. First investigations of our group point in that direction [95].

Effects Ligand Functionalization and Avidity on Particle Biodistribution

In the second main section of our work, we aim to review the literature available on the relationship between avidity and bio-distribution. To this end, we have consulted studies that investigate the in vivo distribution of ligand-functionalized nanoparticles, optimally still providing information on the avidity of the particle under investigation. Following, we present these studies and discuss their main findings relevant to our matter.

Choi et al. have prepared PEGylated gold nanoparticles (AuNP) functionalized with varying amounts of transferrin (Tf-PEG-AuNPs). These particles showed Tf functionalization level-dependent avidity to transferrin receptor (TfR)-bearing Neuro2A cells. Avidity was found in the low nM to pM range (17.5 Tf/AuNP: 1.06 nM; 144.3 Tf/AuNP: 0.13 nM).
In vivo tumor distribution was investigated in s.c. Neuro2A tumor bearing mice. Despite TfR overexpression confirmed via antiTfR-AF555 staining of Neuro2A cells, only very small amounts of administered Tf-PEG-AuNP doses accumulated in tumors (2-3%). Moreover, the extend of this accumulation was independent of Tf-functionalization degree (Fig. 3A). In contrast, at the tissue level an increasing accumulation of Tf-PEG-AuNP in the Neuro2A target cells depending on the Tf content could be observed in the tumor. While unfunctionalized particles and particles with low Tf content were found mainly in leukocytes, higher Tf content resulted in targeted accumulation in Neuro2A cells (Fig. 3B).
The authors conclude from these observations that ligand functionalization is not suitable to positively influence whole-body biodistribution. They see the beneficial effect of targeted nanoparticles at the tissue level, where ligand functionalization can lead to accumulation in target cells [96].

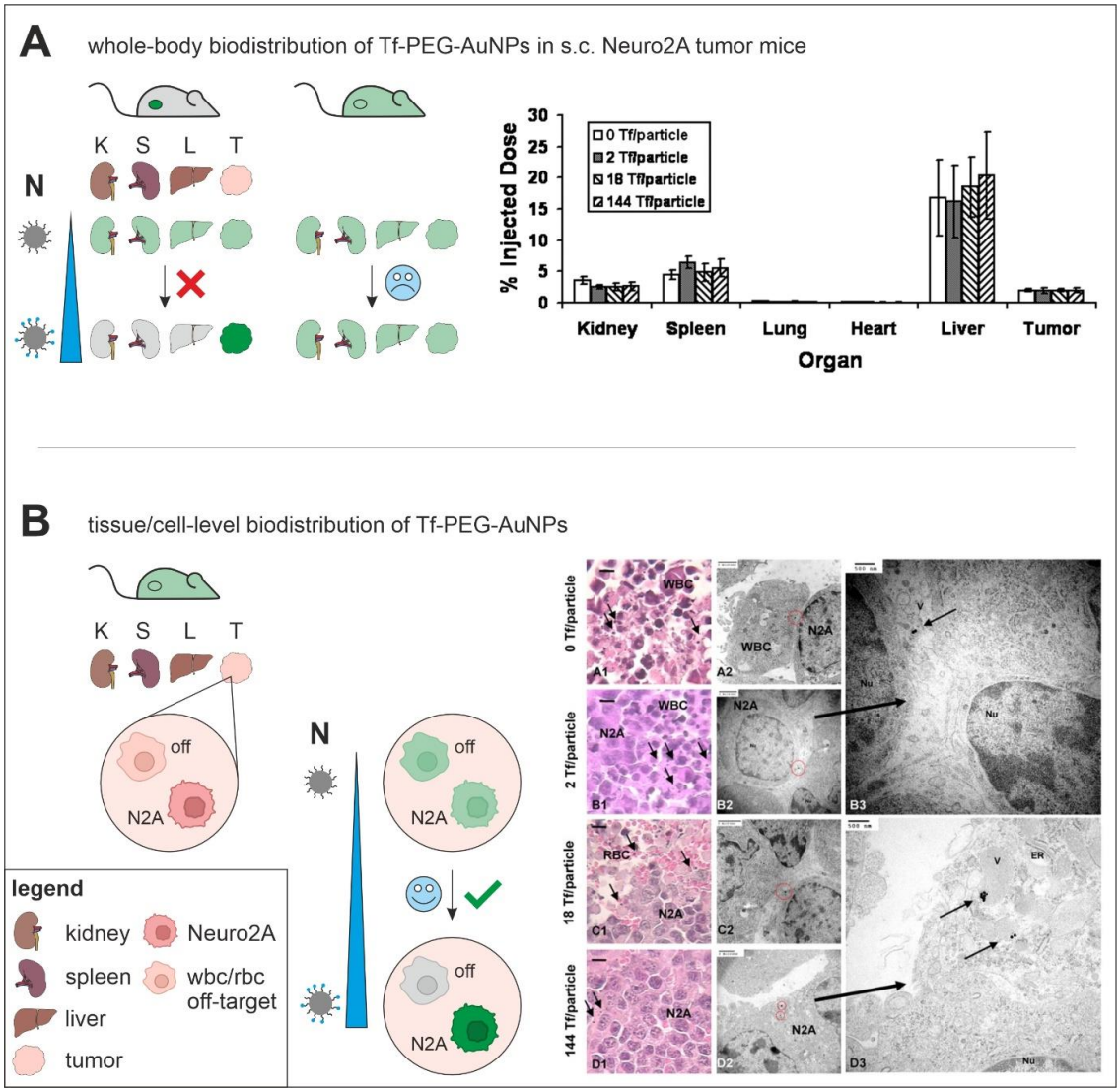

Figure 3: In vivo biodistribution of transferring functionalized PEGylated Au-nanoparticles targeting transferrin receptor in Neuro2A tumor-bearing mice. (A) The study found no significant effect of ligand functionalization on whole-body biodistribution. Also, with increasing degree of particle functionalization, no increased uptake in tumor or reduced accumulation in off-target organs was observed. (B) However, it was observed that at the tissue level, at the highest level of functionalization studied, there occurred a directional accumulation of particles in tumor cells. At the same time, no particles were found in the non-cancer cells within the tumor. It can be concluded that the observations at the tissue level are largely in line with expectations based on the theoretical framework of avidity (Copyright (2019) National Academy of Sciences).

A further study by Gu et al. investigated a nanoparticle based on poly(D,L-lactide-co-glycolide) (PLGA)-b-polyethylene glycol (PEG)-b di-block copolymers. Ligand decorated particles targeting prostate-specific membrane antigen (PSMA) were prepared by incorporating PLGA-b-PEG-b di-block-co-polymers additionally functionalized with A10 2'-fluoropyrimidine RNA aptamer (PLGA-b-PEG-b-Apt). Also in this study, the influence of ligand density was investigated by using different ratios of PLGA-b-PEG-b-Apt and PLGA-b-PEG-b to prepare nanoparticles. To allow quantification of nanoparticles in in vivo studies, particles were prepared using tritium-labeled PLGA. In vivo biodistribution was investigated in s.c. LNCaP xenograft mouse models (Fig. 4).

While the proportion of the administered dose reaching the tumor was also very low in this case, increased accumulation in the tumor was observed with increasing ligand density over a certain range. Interestingly, however, the accumulation decreased after a certain ligand density was exceeded. Additionally, ligand density was directly proportional to liver accumulation of the particles. Here, a degree of functionalization could be found at which the undesired liver accumulation liver had already decreased significantly, while tumor accumulation reached its maximum.
The authors concluded that there is a narrow window for the degree of functionalization at which an optimal targeting effect is achieved and that this window must be determined individually for each particle system [97].

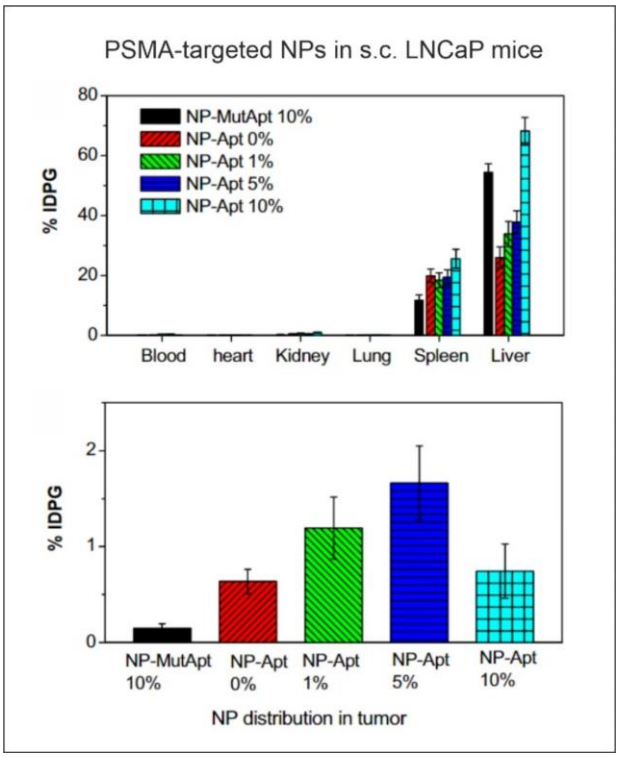

Figure 4: In vivo biodistribution of RNA-aptamer functionalize PLGA-b-PEG nanoparticles targeting prostate-specific membrane antigen (PSMA) in LNCaP tumor-bearing mice. The whole-body biodistribution study showed that most particles accumulate in the liver and in the spleen. The amounts increase in both organs with increasing degree of functionalization. It is specifically noteworthy that there are only minor differences between ligand functionalized particles and particles carrying a non-functional surrogate of the ligand. This implies that the accumulation in these organs did not occur due to a specific ligand-receptor interaction, but rather was the result of an unspecific mode of transport. The cascade leading on this accumulation has been described in detail in the literature [98–100]. Regarding tumor accumulation, however, the non-functional ligand particle is inferior to all other particles. Interestingly, also to the unfunctionalized nanoparticle. This leads to the conclusion, that unspecific RNA-functionalization appears to hinder the accumulation, which strongly indicates a specific ligand-receptor interaction to be causative for this observation. It is, however, further noteworthy that this effect inverts above a certain level of functionalization. The authors attribute this to a reduction of the PEG-related stealth effect [101–103] at higher levels of RNA aptamer functionalization. This explanation would also be coherent with the likewise increasing accumulation in liver and spleen at this degree of functionalization (Copyright (2008) National Academy of Sciences).

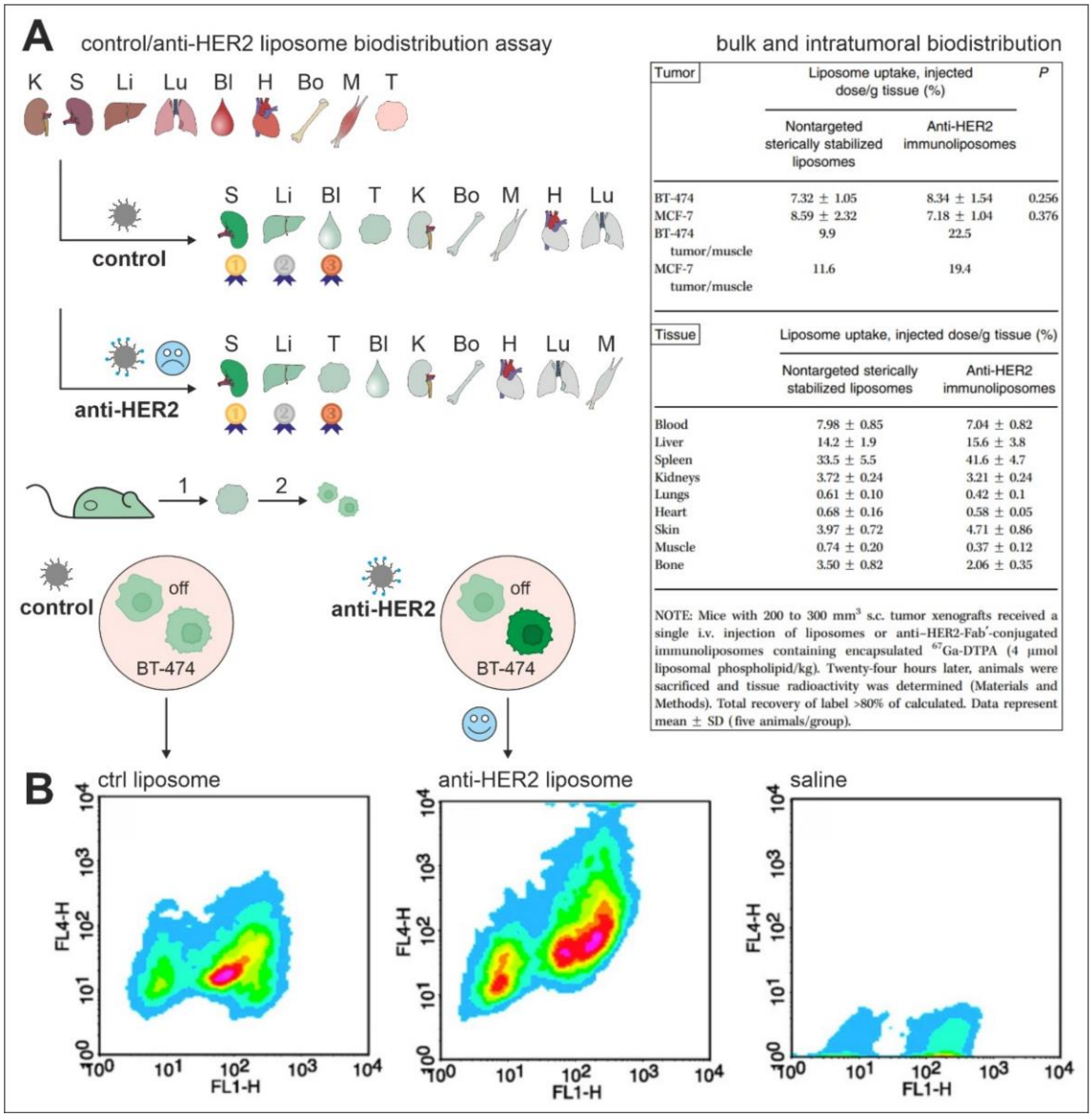

bulk and intratumoral biodistribution

Tumor	Liposome uptake, injected dose/g tissue (%)		P
	Nontargeted sterically stabilized liposomes	Anti-HER2 immunoliposomes	
BT-474	7.32 ± 1.05	8.34 ± 1.54	0.256
MCF-7	8.59 ± 2.32	7.18 ± 1.04	0.376
BT-474 tumor/muscle	9.9	22.5	
MCF-7 tumor/muscle	11.6	19.4	

Tissue	Liposome uptake, injected dose/g tissue (%)	
	Nontargeted sterically stabilized liposomes	Anti-HER2 immunoliposomes
Blood	7.98 ± 0.85	7.04 ± 0.82
Liver	14.2 ± 1.9	15.6 ± 3.8
Spleen	33.5 ± 5.5	41.6 ± 4.7
Kidneys	3.72 ± 0.24	3.21 ± 0.24
Lungs	0.61 ± 0.10	0.42 ± 0.1
Heart	0.68 ± 0.16	0.58 ± 0.05
Skin	3.97 ± 0.72	4.71 ± 0.86
Muscle	0.74 ± 0.20	0.37 ± 0.12
Bone	3.50 ± 0.82	2.06 ± 0.35

NOTE: Mice with 200 to 300 mm^3 s.c. tumor xenografts received a single i.v. injection of liposomes or anti–HER2-Fab′-conjugated immunoliposomes containing encapsulated ^{67}Ga-DTPA (4 μmol liposomal phospholipid/kg). Twenty-four hours later, animals were sacrificed and tissue radioactivity was determined (Materials and Methods). Total recovery of label >80% of calculated. Data represent mean ± SD (five animals/group).

Figure 5: In vivo biodistribution of anti-HER2-Mab functionalized PEGylated liposomes targeting human epidermal growth factor receptor 2 (HER2) in BT-474 and MCF-7 tumor-bearing mice. (A) The findings of Kirpotin et al. are essentially consistent with the observations made by Choi et al. This study, however, included a larger number of off-target organs. Yet still no substantial effect of ligand functionalization was found, regarding whole-body biodistribution. (B) To work of Kirpotin et al. further adds value, as a quantitative method was used to measure particle distribution at the tumor levels. For this, (1) tumors were extracted and (2) disaggregated to allow single cell analysis via flow cytometry. While a base-level of particle uptake was found in cancer as well as non-cancer cells for non-targeted particles considerably above the level of the particle free control, anti-HER2 liposomes showed a significantly higher uptake in cancer cells. Again, providing evidence for the fundamental laws of avidity to be applicable on the tissue-level (Adapted from Cancer Research, 2006, 66/13, 6732–6740, Kirpotin et al., Antibody Targeting of Long-Circulating Lipidic Nanoparticles Does Not Increase Tumor Localization but Does Increase Internalization in Animal Models, with permission from AACR).

Kirpotin et al. made similar observations with a distinct nanoparticle platform. Designing a PEG-chain functionalized liposome decorated with anti-HER2 monoclonal antibody fragments they aimed for solid tumor targeting. Biodistribution was investigated in s.c. BT-474 or MCF-7 tumor bearing mice.

For investigation of biodistribution, unfunctionalized and HER2-targeted liposomes were radio-labeled via encapsulation of ^{67}GA-DTPA chelate. A method that the group has thoroughly validated in terms of a possible influence of the labeling on pharmacokinetics and a possible leakage of the chelate [104].

However, also in their case, only a low proportion of administered liposome dose reached the desired tumor tissue in s.c. BT-474 tumor bearing mice (7-8%). Again, no significant effect of ligand functionalization on whole-body biodistribution was detected in this study. Specifically, no increased accumulation in tumors of HER2-targeted liposomes was found compared with unfunctionalized controls (Fig. 5A). It must be emphasized here that the authors had investigated the in vitro uptake of HER2-targeted and control liposomes in HER2 overexpressing SK-Br-3 cells and found a superior uptake of the anti-HER2 particles. Regrettably, only the functionalized liposome was compared with an unfunctionalized control. An investigation of the influence of increasing avidity with increasing valence of the particle was therefore unfortunately not possible.

One merit of the Kirpotin et al. study over Choi et al. is that the former examines bio-distribution at the tissue level in more detail by employing a quantitative method. This was done using flow cytometry analysis of extracted disaggregated tumor after i.v. treatment of tumor bearing mice with HER2-targeted or control liposomes. For detection ADS645WS was encapsulated in liposomes. To distinguish tumor and of target cells, EpCAM on tumor cells was stained using anti-EpCAM Mab-FITC. Additionally, gold-tagged liposomes were visualized in fixed tumor tissue samples via silver enhancement and imaged using bright-field and dark-field microscopy. In summary, intra-tumor biodistribution analysis showed a clear preferential uptake of anti-HER2 liposomes compared to control liposomes in tumor cells (Fig. 5B).

The authors conclude that the mechanism behind the improved efficacy of ligand-functionalized particle therapy differs from the classical understanding of targeted nanoparticles for their system. In their view, instead of an organ/tumor-specific accumulation, a cell-specific accumulation at the tissue level is in the foreground [105].

Another very informative study on this subject was conducted by Bartlett et al. Here, positron emission tomography (PET) and bioluminescent imaging were used to investigate the in vivo biodistribution. As Choi et al. they aimed for TfR targeting in Neuro2A tumors.

In this study, a nanoparticle system based on complexes formed from cyclodextrin-containing polycations and siRNA molecules was investigated. Addition of adamantane-PEG polymers functionalized with Tf yielded the ligand functionalized TfR-targeted nanoparticle. To enable PET-based biodistribution studies, a 1,4,7,10-tetraazacyclododecane-1,4,7,10-tetraacetic acid (DOTA) 5'-modified siRNA labeled with ^{64}Cu was employed [106]. Studies were conducted on mice bearing s.c. Neuro 2A tumors modified to express luciferase.

Although the authors observed similar bulk biodistribution and tumor localization of untargeted and Tf functionalized particles in micro-PET/CT imaging, therapeutic efficacy of targeted nanoparticles was found to be superior compared to control particles. This was demonstrated by a significantly higher reduction in luciferase activity after treatment with Tf functionalized particles compared with unfunctionalized particles. The proportion of the dose reaching the tumor was again low and was not significantly affected by Tf functionalization of the particles.

Unfortunately, the study did not experimentally investigate the intra-tumoral particle distribution. However, a very insightful compartment-based model is presented that demonstrates at which point ligand-functionalized particles can play to their strengths. The authors see this possibility primarily in the case of particles that can rapidly diffuse from interstitium back into the plasma. Here, ligand functionalization enables a significant improvement in cellular uptake [107].

The study of Bu et al. investigated immune-checkpoint inhibitor carrying dendrimers (G7-aPD-L1) targeting PD-L1 for their efficacy in cancer immunotherapy. It must be emphasized that in this study nanoparticle binding kinetics were characterized very thoroughly. For this, three distinct methods were applied. Biolayer interferometry (BLI), surface plasmon resonance (SPR), and atomic force microscopy (AFM) were conducted to determine dissociation constants (K_D) as well as association and dissociation rate constants (k_{on} an k_{off}). In summary, K_D for G7-aPD-L1 conjugate was found in a fM range (BLI: $K_D = 8.5\times10^{-11}$ M; SPR: $K_D = 6.6\times10^{-11}$ M). This corresponds to an avidity gain of about one order of magnitude compared to aPD-L1 (BLI: $K_D = 9.6\times10^{-10}$ M; SPR: $K_D = 3.8\times10^{-10}$), which was mainly caused by an increase in k_{on} (BLI: $2.38\times10^{5} \rightarrow 1.10\times10^{6}$

$M^{-1}s^{-1}$; SPR: 5.54×10^{4} → 3.61×10^{5} $M^{-1}s^{-1}$) with less prominent changes in k_{off} (BLI: 2.75×10^{-4} → 6.79×10^{-5} s^{-1}; SPR: 2.18×10^{-5} → 2.88×10^{-5} s^{-1}) (Fig. 6 A and B).

Interestingly, this observation is in direct contradiction with the results of Wang et al. who found for EC1-functionalized ErbB2-targeting micelles that superior avidity of the multivalent entity over free EC1 was due to a reduction of k_{off} (SPR: 6.21×10^{-2} → 3.1×10^{-3} s^{-1}), whereas k_{on} showed no clear trend and underwent only minor changes (SPR: 4.84×10^{3} → 8.42×10^{3} $M^{-1}s^{-1}$) [108]. Unfortunately, this particle system was not tested in vivo for the influence of its avidity on biodistribution. For this reason, no conclusive statement on the influence of the mechanism underlying nanoparticle avidity gain on biodistribution is possible.

Regarding biodistribution studies conducted by Bu et al., little to no differences can be made out comparing G7-aPD-L1 and the free binding entity aPD-L1. Tumor accumulation however is significantly enhanced. As a control for passive tumor targeting, the authors included an IgG dendrimer conjugate (G7-IgG). Also compared to this control, there is no significant difference in whole-body biodistribution. In terms of tumor accumulation, G7-aPD-L1 appears superior, but the difference is not statistically significant [109] (Fig. 6C).

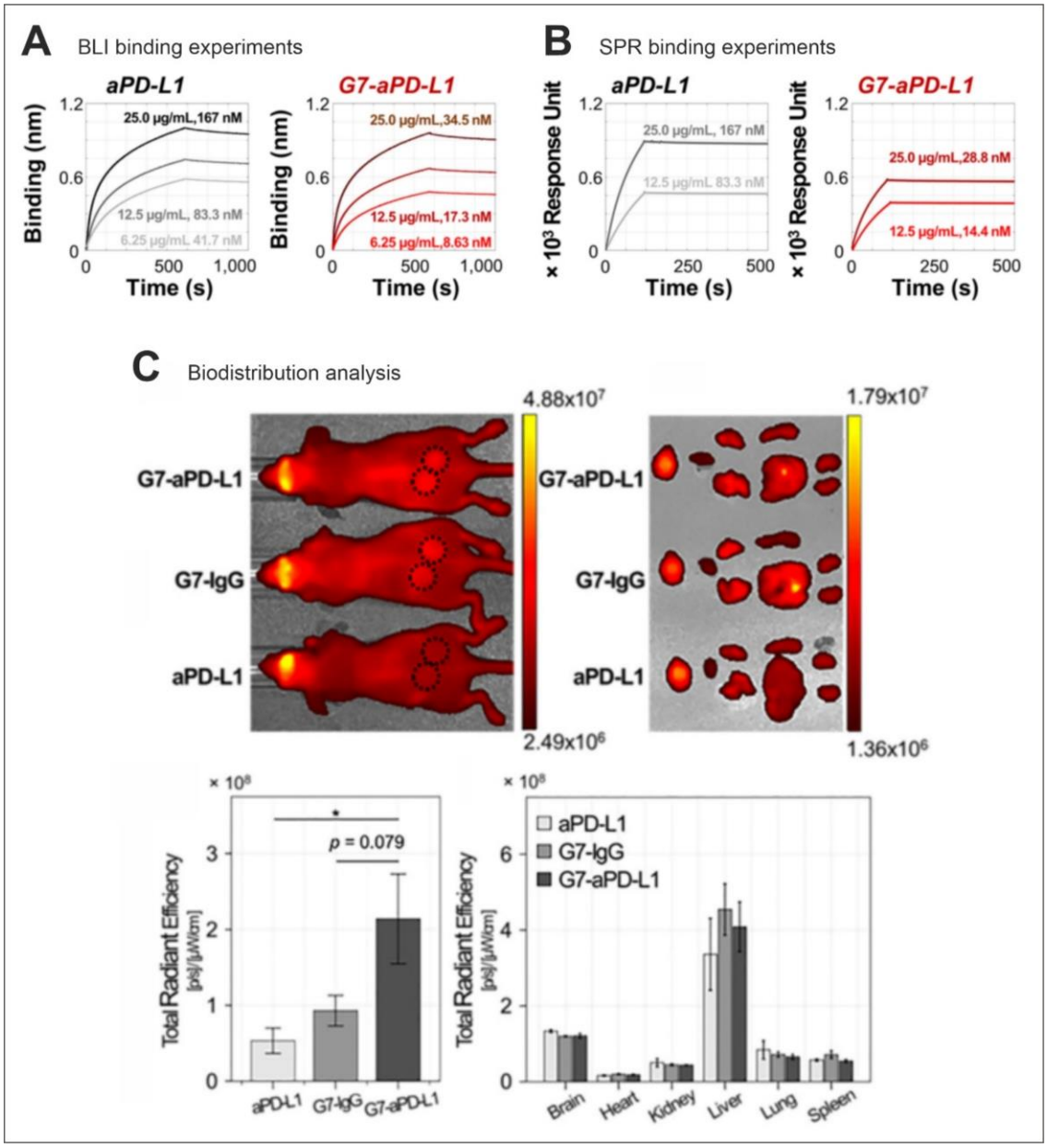

Figure 6: In vivo biodistribution of aPD-L1 functionalized PAMAM dendrimers targeting programmed death ligand 1 (PD-L1) in MOC1 tumor bearing mice. The study presented by Bu et al. is one of the few cases where particle avidity data is presented alongside a whole-body biodistribution experiment. The authors conducted (A) biolayer interferometry (BLI) as well as (B) surface plasmon resonance (SPR) binding experiments, yielding dissociation constants K_D in the fM range with an avidity-gain of the multivalently functionalized dendrimer over the free ligand of one order of magnitude. (C) However, the observations the observed biodistribution of the free ligand and the multivalent entity possessing a demonstrated avidity-gain over the free ligand did not differ significantly. A higher accumulation of the ligand functionalized particle was observed compared to the free ligand. The differences observed compared to the non-targeted particle were not found significant (Reprinted with permission from Nano Letters, Bu et al., An Avidity-Based PD-L1 Antagonist Using Nanoparticle-Antibody

Conjugates for Enhanced Immunotherapy, Nano letters 20 (2020) 4901–4909, (2020), American Chemical Society).

An outstanding fundamental work in this context was presented by Schmidt et al. Based on a mechanistic compartmental model [110], the authors derive predictions on affinity-dependence of tumor targeting in excellent overlay with experimental observations. In agreement with the experimental data [111], the model finds a plateau-like dependence in which the desired uptake into the tumor decreases in a step-like manner once the affinity falls below a critical value. The authors go further and provide another analysis highly relevant for the question of the influence of avidity of ligand-functionalized nanoparticles on their biodistribution.
In a simulation, they parallelly investigate the influence of (a) molecular weight and (b) the affinity of a binding entity on the percentage of dose per gram delivered to the tumor tissue. Using the rule of thumb to estimate the hydrodynamic diameter R_{mol} based on the molecular weight M_W - $M_W = 1.32\ {R_{mol}}^3$, it can be concluded from this analysis that the avidity of nanoparticles > 50 nm has hardly any influence on this parameter and that the accumulation in the tumor only decreases at very low avidities K_d > 100 nM.
In their conclusions, the authors highlight this observation, that for molecules exceeding a certain size, antigen targeting has little or no effect on tumor uptake, as one of the most intriguing findings of their study [112].

Another contribution to fundamental understanding of the interplay between the avidity of a ligand-functionalized nanoparticle and its biodistribution was provided by Zern et al. In their work, they make the argument that the ratio of specific to nonspecific accumulation (i.e., ratio of particle amount in target to off-target tissue) should be considered as a parameter of success for targeted nanoparticles. This target/off-target ratio should take precedence over absolute exposure of target tissues to the administered nanoparticle. With this shift in focus, the authors highlight the often-overlooked problem of lower-level expression of addressed target structures (e.g., receptors) in non-target tissues.

They investigated an intercellular adhesion molecule-1 (ICAM-1)-antibody decorated poly(4-vinylphenol) (PVPh) nanoparticle (anti-ICAM-1/NP) additionally radiolabeled with ^{124}I to allow PET/CT imaging. This particle was administered to untreated C57BL/6 mice to determine biodistribution of anti-ICAM-1/NP at basal ICAM-1 expression levels. To investigate the effect of ICAM-1 overexpression in lung vasculature on anti-ICAM-1/NP biodistribution, mice were challenged via intratracheal installation of lipopolysaccharide (LPS). Ligand density on PVPh nanoparticles was tuned by replacing a portion of ICAM-1 antibodies with IgG as control (Fig. 7A and C).

They find that already in untreated mice, uptake of anti-ICAM-1/NP in the lungs increases with increasing ligand density. An anti-ICAM-1/NP with 50 antibodies per particle was found to not differ significantly from IgG control nanoparticle regarding lung uptake. Upon LPS challenge, uptake increases as expected. However, while only a 2.4-fold increase is observed for the high-avidity anti-ICAM-1/NP (200 antibodies per particle), the low-avidity anti-ICAM-1/NP (50 antibodies per particle) shows a 5.3-fold increase in uptake. Since free anti-ICAM-1 antibody also shows a 2.4-fold higher uptake upon LBS treatment, one cannot conclude a beneficial influence of multivalent functionalization in the case of high-avidity anti-ICAM-1/NP in this regard (Fig. 7B).

With their focus on a diagnostic application to detect pulmonary inflammation, the authors conclude that the reduction in avidity achieved via decreasing ligand density, was beneficial regarding functionality of their particle [113]. It should be noted, however, that the avidity of anti-ICAM-1/NP was not quantified (e.g., via SPR or BLI). Furthermore, regarding a conceivable transfer of the findings to therapeutic applications, it should be noted that with low-avidity anti-ICAM-1/NP, a recognizable accumulation in the spleen persists even after LPS treatment. This was prevented when increasing ligand density to 200 antibodies per particle.

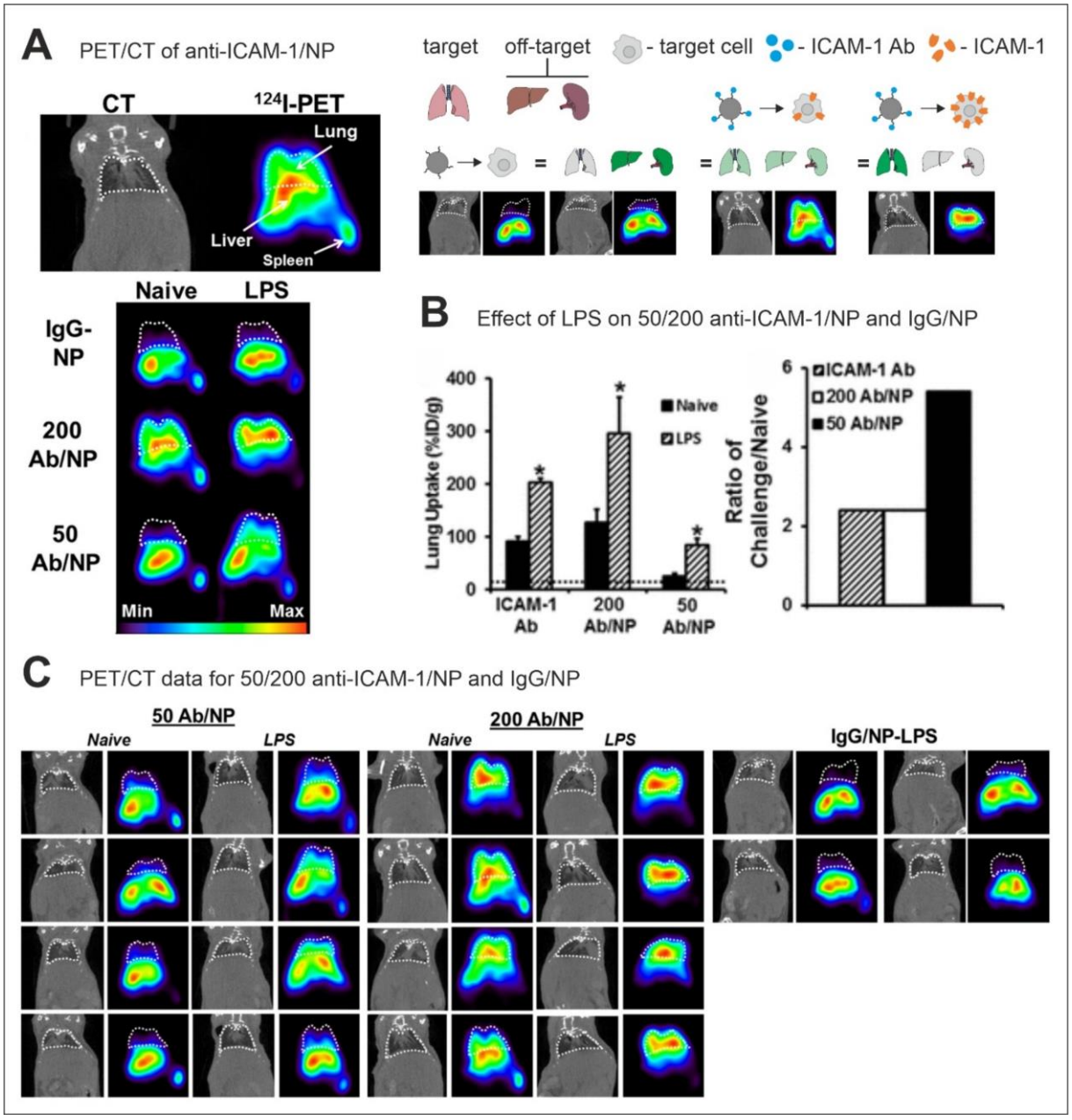
A
PET/CT of anti-ICAM-1/NP
CT
124I-PET
Lung
Liver
Spleen
Naive
LPS
IgG-NP
200 Ab/NP
50 Ab/NP
Min
Max
target
off-target
- target cell
- ICAM-1 Ab
- ICAM-1
B
Effect of LPS on 50/200 anti-ICAM-1/NP and IgG/NP
Lung Uptake (%ID/g)
400
300
200
100
0
Naive
LPS
ICAM-1 Ab
200 Ab/NP
50 Ab/NP
Ratio of Challenge/Naive
6
4
2
0
ICAM-1 Ab
200 Ab/NP
50 Ab/NP
C
PET/CT data for 50/200 anti-ICAM-1/NP and IgG/NP
50 Ab/NP
Naive
LPS
200 Ab/NP
Naive
LPS
IgG/NP-LPS

Figure 7: In vivo biodistribution of ICAM-1-Ab functionalized PVPh nanoparticles targeting intercellular adhesion molecule 1 (ICAM-1) in pulmonary vasculature of endotoxin-challenged mice. (A) Using a combined PET/CT imaging approach, Zern et al. followed the whole-body biodistribution of their particle system. It was found that ligand-functionalization induced accumulation in the lung as the intended target organ. While a lower degree of functionalization induced a partial shift of particle distribution, increasing the valency of the particles resulted in a near complete restriction of particles in the lung. The study of Zern et al. is particularly valuable to our matter, as via a lipopolysaccharide (LPS) challenge the author varied the receptor density in the target organ. In this way a significant impact of the receptor density could be shown. (B) The authors found that the uptake of the free ligand was increased upon LPS challenge to the same degree as the high-valency particle. A significantly higher effect of the LPS-induced increase of receptor density was found for the low valency particle. (C) Distribution data of all animals studied. The study of Zern et al. provides evidence for the transferability of the basic laws of avidity to the biodistribution of ligand-functionalized particles (Reprinted with permission from ACS nano, Zern et al., Reduction of nanoparticle avidity enhances the selectivity of vascular targeting and PET detection of pulmonary inflammation, ACS nano 7 (3), S. 2461-2469, (2013), American Chemical Society).

In an earlier study the same group investigated PVPh-based nanoparticles addressing a variety of target structures, all endothelial markers in pulmonary vasculature. These were platelet-endothelial cell adhesion molecule-1 (PECAM-1), thrombomodulin, and PV1. In this work the authors did not vary the ligand density on their particles. No significant effect of ligand functionalization on bulk biodistribution was found, but a massively increased uptake in the lung was detected [114]. This observation shows that even without a change in bulk biodistribution, ligand functionalization can lead to greatly enhanced uptake in the target tissue. This finding suggests that bulk biodistribution and distribution at the cellular level should be considered separately. The advantage of ligand functionalization could already lie in an improved cellular uptake in the target tissue. This would not necessarily be apparent if only bulk biodistribution were considered.

Frigell et al. investigated the suitability of multivalently ligand functionalized nanoparticles for targeted delivery to the central nervous system. For this purpose, glucose-coated gold nanoparticles (GNPs) were designed to carry opioid peptides as targeting ligands. Two peptides were tested with the intention to improve blood-brain

barrier passage. Particles were administered to male Sprague–Dawley rats via lateral tail veins. To allow analysis of whole-body biodistribution, a chelator for the positron emitter ^{68}Ga was additionally attached to the GNPs. Particle distribution was assessed using whole-body PET imaging (Fig. 8A) as well as gamma counter analysis of extracted organs.

Regarding the impact of the targeting ligand on particle biodistribution, the authors report ligand functionalization to increase accumulation in the kidney (Fig. 8B). Regarding the desired accumulation in the brain, for both ligand-functionalized and unfunctionalized particles only minor proportions of the initial doses were found here. However, one of the two tested peptides induced a 2.5-fold increase of particle accumulation in the brain Fig. 8C). It is surprising that only one of the two peptides tested showed an effect. This could be because the peptide that shows no effect lacks the Tyr-Gly-Gly-Phe amino acid sequence which is considered essential for opioid receptor binding and activation [115,116].

Wang et al. synthesized an RNA-oligonucleotide based nanoparticle platform (three-way junction RNA, 3WJ) which was labeled via hydrogen-tritium-exchange conducted on the oligonucleotides themselves. The authors furthermore prepared fluorescently labeled nanoparticles by introducing the AFDye 647 fluorophore. Two targeting ligands were evaluated, the first being folic acid (3WJ-FA) and the second being the CL4 RNA aptamer (3WJ-CL4), both of which are targeting the EGFR receptor. In vivo pharmacokinetic and biodistribution studies were carried out by administering 100 µL of a 20 µM nanoparticle dispersion to mice bearing KB or MDA-MB-231 tumors via tail vein injection. While KB tumors strongly express the folate receptor [117], MDA-MB-231 tumors are used as a model for cancers strongly overexpressing EGFR [118,119]. Next to targeted particles (3WJ-FA and 3WJ-CL4), unfunctionalized 3WJ particles and PBS were applied as controls.

Firstly, the authors employed fluorescently labeled nanoparticles to evaluate the binding avidity of 3WJ-FA and 3WJ-CL4 to their respective target cells. Particle concentration-dependent increase of fluorescent was recorded in flow cytometry experiments. For the avidity of 3WJ-FA to KB cells a K_D of 322.8 nM was found. For the interaction of 3WJ-CL4 with MDA-MB-231 cells the K_D was found to be 72.1 nM.

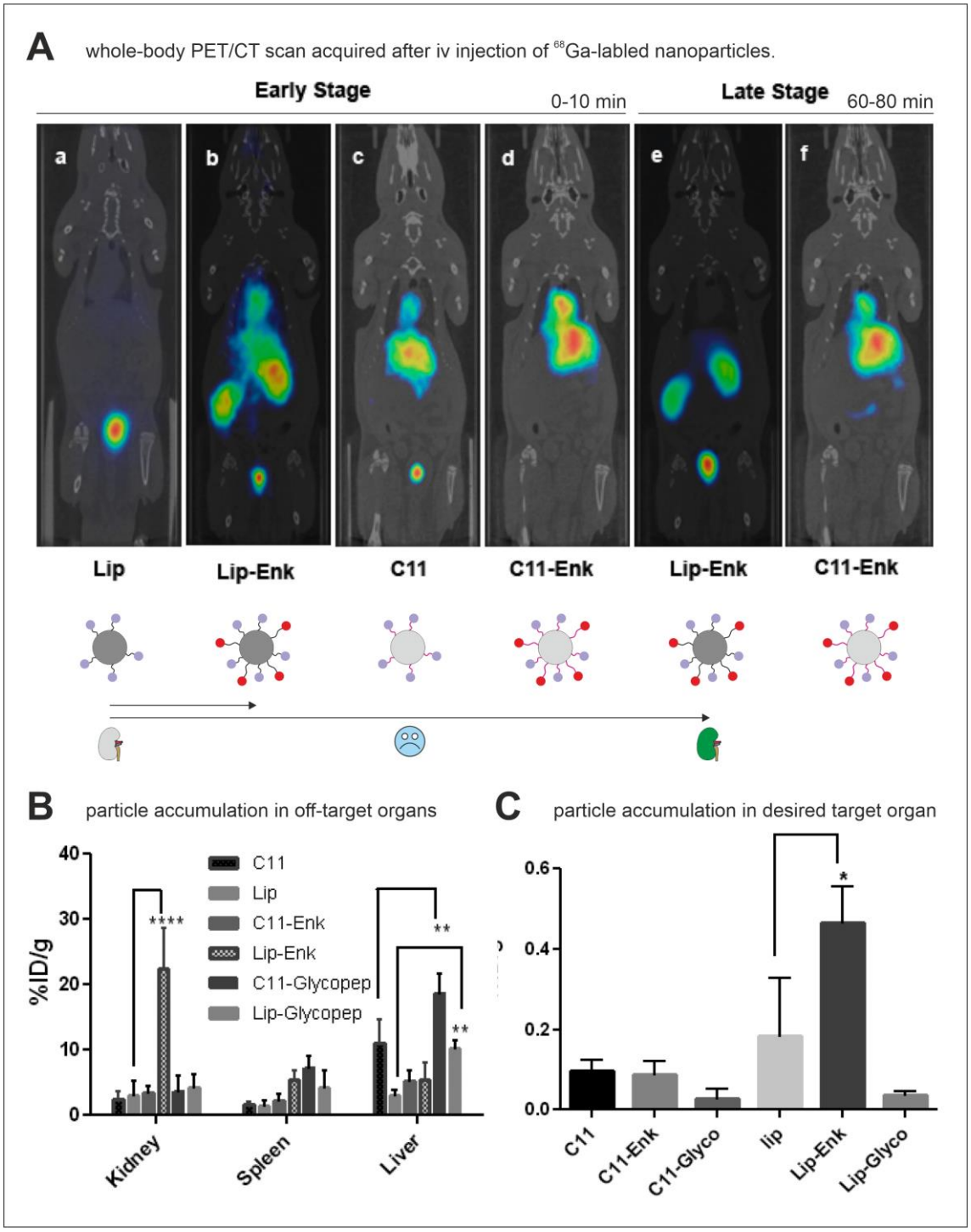
A
whole-body PET/CT scan acquired after iv injection of 68Ga-labled nanoparticles.
Early Stage
0-10 min
Late Stage
60-80 min
a
b
c
d
e
f
Lip
Lip-Enk
C11
C11-Enk
Lip-Enk
C11-Enk
B
particle accumulation in off-target organs
%ID/g
40
30
20
10
0
C11
Lip
C11-Enk
Lip-Enk
C11-Glycopep
Lip-Glycopep
****
**
**
Kidney
Spleen
Liver
C
particle accumulation in desired target organ
0.6
0.4
0.2
0.0
*
C11
C11-Enk
C11-Glyco
lip
Lip-Enk
Lip-Glyco

Figure 8: In vivo biodistribution of neuropeptide functionalized glucose-coated Au-nanoparticles targeting opioid receptors to achieve blood-brain barrier passage in Sprague–Dawley rats. (A) The study investigated biodistribution for particles carrying one of two ligands (Enk/Gylcopep) attached via one of two linkers (Lip/C11) using PET/CT scans acquired shortly after particle administration (0-10 min) and after an extended time (60-80 min). Regarding the ligand Enk attached via Lip, the authors found a strong undesired particle accumulation in the kidney. (B) Overall, accumulation in the off-target organs was highly variable, with ligand functionalization tending to increase this accumulation. (C) The accumulation in the intended target organ was low. Only for one ligand- linker combination, a beneficial effect of ligand functionalization was found (Reprinted with permission from Journal of the American Chemical Society, Frigell et al., 68Ga-labeled gold glyconanoparticles for exploring blood-brain barrier permeability: preparation, biodistribution studies, and improved brain uptake via neuropeptide conjugation, Journal of the American Chemical Society 136 (1), 449–457., (2013), American Chemical Society).

In mice sacrificed 4 or 8 h after nanoparticle administration, the authors found 5% of 3WJ-FA and 3% of 3WJ-CL4 accumulated in the tumor. For 3WJ-FA tumor accumulation was superior to that of unfunctionalized control particles at both time points (5% 3WJ-FA vs. 3% 3WJ at 4 and 8 h), while for 3WJ-CL4 this was only the case after 8 h (3% 3WJ-CL4 vs. 2% 3WJ at 4 h: ns.; and 1% at 8 h). For both investigated particle species, ligand functionalization had only minor effects on particle accumulation in off-target organs. The authors also performed in vivo fluorescence biodistribution studies, which yielded results similar to the radio-label based experiments. [120]

Putting the observations of Wang et al. into perspective with the general concept of multivalency-determined avidity of ligand functionalized nanoparticles, it is surprising that the particle with inferior avidity appears to outperform the one with a higher avidity to its target cell. 3WJ-FA shows an overall higher tumor accumulation which is consistently superior to unfunctionalized control particles. Also, 3WJ-FA shows a more favorable tumor to off-target ratio in the case of tumor/heart-tissue distribution compared to 3WJ-CL4. Regrettably, the authors did not vary the degree of ligand functionalization for either of their particles.

In their study Ganesh et al. investigate the biodistribution previously prepared and characterized by the group. The particle design is based on polyethylene glycol (PEG)

and polyethyleneimine (PEI) polymers linked to a hyaluronic acid (HA-PEG and HA-PEI) backbone. These polymers were found to poeses a self-assembling ability inducing the formation of 50-80 nm nanoparticles [121].
For the study on biodistribution, additionally to cisplatin and a siRNA duplex intended to exploit a beneficial effect on cisplatin-resistant tumors the authors encapsulated the near infrared (NIR) dye indocyanine green to measure whole-body distribution. Due to its HA functionalization, a CD44 directed targeting effect was expected. The biodistribution was examined in human non-small cell lung cancer A549 and $A549^{DDP}$ bearing mice after three injections via the tail vein administered over three days. Next to this experiment, the authors performed further biodistribution studies comparing tumors showing a high CD44 (i.e., A549 and $A549^{DDP}$) [122] expression with tumors known to express lower levels of CD44 (i.e., H69 and H69AR) [123]. NIR signal was recorded in living mice 10 min, 4, 10, and 24 h after administration. While distribution initially occurred throughout the entire body in all tumor models, accumulation in tumor tissue was evident after 4 h in A549 and after 10 h in $A549^{DDP}$. In H69 and H69AR, no accumulation in tumor tissue was seen during the entire observation period.
As another study of interest for distribution, the authors also quantified siRNA in off-target organs and in tumor tissue using a PCR technique. A strong decrease of siRNA in the liver tissue was found over the cause of 24 h. The proportion of the initial dose administered fell from 33.4% (1 h) to 13.4% (24 h). A similar pattern was observed for the spleen tissue, which contained 22.8% of the initial dose after 1 h and 17.4% after 24 h. At the same time, the proportion of initial dose found in tumor tissue increased from 0.5% to 0.9%. All changes were found to be statistically significant. While these observations are indicative of directional accumulation, it must be kept in mind, however, that they could also have resulted in part from degradation of siRNA by nucleases. [124].

Interestingly, the particle studied here accumulated in tumor tissue over time, during which the amount of particle present in off-target organs decreased significantly. Unfortunately, due to the particle design in which the avidity dictating moiety HA was also a part of self-assembling polymer backbone, it was not possible to vary ligand density or to investigate unfunctionalized particles in control experiments.

Akers et al. investigated perfluorocarbon-based nanoparticles which where functionalized with cRGD to enable $\alpha_v\beta_3$-integrin targeting. The particle surface was further functionalized with cypate-C18 (cypate–PFC-tNPs) to allow NIR-based detection

of in vivo distribution in living mice tumor models. Whole-body biodistribution was assessed in male nude NCr mice bearing luciferase-transfected 4T1 mouse mammary carcinoma cell (4T1luc) derived tumors. Regarding the improvement of tumor specific particle accumulation due to ligand functionalization the authors report a superior tumor-to-muscle distribution ratio for targeted nanoparticles compared to unfunctionalized control (6.9 to 3.0) in ex-vivo measurements. Unfortunately, in the whole-body imaging in this study's case, the targeted nanoparticle was compared only with a small-molecule cypate-cRGD compound and not with the unfunctionalized particle. Also, because the authors did not quantify the fraction of nanoparticle dose arriving in the tumor and have done hardly any detailed investigation of the distribution of particles into off-target organs (e.g., over time, comparison of targeted/non-targeted particles), it is difficult to assess the influence of ligand functionalization overall. The authors, however, found superiority of the small-molecule compound compared to the particle (8.1 to 6.9 tumor-to-muscle distribution ratio). [125]

This observation makes a simple transferability of the basic laws governing avidity to the case of biodistribution of ligand-functionalized nanoparticles questionable. Since these laws would suggest that the avidity of a multivalent entity is far superior to the single ligand affinity, this study thus suggests that factors act on the distribution of the particle which counteract the positive effect of multivalent functionalization.

Table 1: Investigated model systems and effect of ligand functionalization on particle biodistribution. The table provides an overview of the tissues or tumor models addressed with targeted particles in the studies consulted for this review. As a key parameter for describing the performance of the particle systems studied, we provide an overview of the dose fractions that reached the desired target tissue for both targeted (t) and non-targeted particles (nt). Also presented is whether a significant effect by ligand functionalization on whole-body biodistribution or tissue-level distribution was observed. In addition, for studies in which active compounds were encapsulated, we considered an improvement in therapeutic efficacy that may have been present (↑ - improvement, → - no significant change, ↓ - deterioration; arrows in brackets indicate conclusions subject to certain limitations). Abbreviations and cell classifications: A549 - adenocarcinoma human alveolar basal epithelial cells, $A549^{DDP}$ - cisplatin-resistant A549, BT-474 - invasive ductal mamma-carcinoma cells, H69 - epithelial lung carcinoma cells, H69AR - doxorubicin-resistant H69, ID - initial dose, ID/cm^3 - initial dose per cm^3 tissue, ID/g - initial dose per g tissue, KB - adenocarcinoma endocervix cells, LNCaP - epithelial prostate carcinoma cells, MCF-7 - adenocarcinoma mamma cells, MDA-MB-231 - adenocarcinoma mamma cells, MOC1 - mouse oral squamous cell carcinoma, n.d. - no data available, Neuro2A - Neuroblastoma neuroblast cells, NSCLC - non-small-cell lung cancer, TRE - total radiant efficiency, 4T1luc - Luciferase-transfected 4T1 mouse mamma-carcinoma cells.

Study	Target	Dose delivered	Biodistribution		Efficacy
			whole-body	tissue-level	
Choi et al.	Neuro2A	2 to 3% ID	→	↑	n.d.
Bartlett et al.		nt: 1.1% ID/cm^3 t: 1.4% ID/cm^3	→	n.d.	↑
Gu et al.	LNCaP	~ 0.2 to 1.8%	↓	↑	n.d.
Kirpotin et al.	BT-474 or MCF-7	BT-474: nt: 7.3% ID/g tissue t: 8.3% ID/g tissue MCF-7: nt: 8.6% ID/g tissue t: 7.2% ID/g tissue	→	↑	n.d.
Bu et al.	MOC1	nt: ~0.51x10^8 TRE t: ~2.1x10^8 TRE	→	↑	n.d.
Zern et al.	Pulmonary vessels	n.d.	(↑)	↑	n.d.
Frigell et al.	Brain	nt: 0.0073 ID/g tissue t: 0.020 ID/g tissue	↓	(↑)	n.d.
Wang et al.	KB and MDA-MB-231 tumor	KB: nt: 3% (4 h), 3% (8 h) ID t: 5% ID MDA-MB-231: nt: 2% (4 h), 1% (8 h) ID t: 3% ID	(↑)	n.d.	n.d.
Ganesh et al.	A549/A549^{DDP} (CD44 ↑) H69/H69AR (CD44 ↓) all NSCLC	t: 0.5-0.9% ID nt: n.d.	(↑)	n.d.	↑ [126]
Akers et al.	4T1luc tumor	t: n.d. nt: n.d.	→	n.d.	n.d.

Table 2: Technology of particle platforms and ligand-receptor pairs employed for targeting. This table provides an overview about the type of particle systems investigated. We present the material of the particle technology used. In addition, we list the ligands used for functionalization with the according receptors addressed by them. We have compiled available data on these ligand-receptor pairs regarding their respective binding affinities, taking into account the method used for their determination. All relevant references are listed in the table. Abbreviations: ^{125}I - radioisotope of iodine, A10 RNA - 2′-fluoropyrimidine RNA aptamer, (a)PD-L1 - programmed cell death 1 ligand 1 (human antibodies), BLI - biolayer interferometry, CL4 - EGFR-binding nuclease-resistant RNA aptamer, cRGD(yK) - cyclic Arg-Gly-Asp peptide (D-Tyr-Lys-pentapeptide), [^{3}H]DAMGO - μ-opioid receptor ligand (structure: ^{3}H-Tyr-D-Ala-Gly-N-MePhe-Gly), DHM-^{3}H - ^{3}H-dihydromorphine, [^{3}H]DPDPE - δ-opioid ligand (structure: ^{3}H-D-Pen^2-D-Pen^5-enkephalin), EGFR - epidermal growth factor receptor, FP - fluorescence polarization, Glc - glucose, HER2 - human epidermal growth factor receptor 2, IC_{50} - half maximal inhibitory concentration, ICAM-1 - intercellular adhesion molecule 1, K_D - dissociation constant, K_i - inhibition constant, Leu-Enk - Leu-enkephalin, (rhu)(M)Ab - (recombinant human) (monoclonal) antibody, MOR/DOR - μ/δ-opioid receptor, n.d. - no data available, NAALADase - N-acetylated alpha-linked acidic dipeptidase, PAMAM - poly(amidoamine), PEG - polyethylene glycol, PEI - polyethylenimine, PFC - perfluorocarbon, PLGA-b-PEG - poly(ethylene glycol)-block-poly(D,L-lactic acid), PSMA - prostate-specific membrane antigen, PVPh - poly (4-vinylphen-ol), (si)RNA - (small interfering) ribonucleic acid, SPR - surface plasmon resonance, $\alpha_v\beta_3$ - integrin alpha V/integrin beta 3 receptor.

Study	Particle	Ligand	Receptor	affinity (technique)	Ref.
Choi et al.	PEGylated Au	transferrin	transferrin receptor	K_{D1} = 1.1 nM, K_{D2} = 29 nM (SPR)	[127–129]
Bartlett et al.	Gu complex			K_{D1} < 0.1 nM* K_{D2} = 3.8 nM (SPR) K_D = 48 nM (^{125}I-lable)	
Gu et al.	PLGA-b-PEG polymer	A10 RNA aptamer	PSMA	K_i = 11.9 nM (NAALADase activity)	[130]
Kirpotin et al.	PEGylated liposome	anti-HER2 MAb	HER2	rhuMAbHER2-Fab: K_D = 1.8 nM (SPR) anti-HER2 scFv F5: K_D = 160 nM (SPR)	[131–133]
Bu et al.	PAMAM dendrimers	aPD-L1	PD-L1	K_D = 0.96 nM (BLI), K_D = 0.38 nM (SPR)	[109]
Zern et al.	PVPh polymer	ICAM-1 Ab	ICAM-1	n.d.	-
Frigell et al.	Glc-coated Au	Leu-Enk Glycopep	MOR/DOR	K_D = ~0.6 nM (DHM-^{3}H) IC_{50} μ = 1.8 nM ([^{3}H]DAMGO) IC_{50} δ = 0.6 nM ([^{3}H]DPDPE) n.d.	[134,135]
Wang et al.	RNA	Folic acid CL4 RNA aptamer	Folate receptor EGFR	K_D = 0.19 nM ([^{3}H]-folic acid) K_D = 10 nM (filter binding analysis)	[136,137]
Ganesh et al.	PEI/PEG/siRNA	hyaluronic acid*	CD44	K_D = 21 μM (flow cytometry) K_D = 36.6 μM (SPR)	[138,139]
Akers et al.	PFC	cRGD	$\alpha_v\beta_3$	IC_{50} = 0.11 μM (FP) IC_{50} = 414/422/358 nM (^{125}I-echistatin) IC_{50} = 37 nM (^{125}I-c(RGDyK))	[140–144]

Table 3: Ligand-related nanoparticle properties and avidity-biodistribution correlation. This table gives an overview about the nanoparticle properties size, valency, and ligand density. We have also included data on nanoparticle avidity where it was investigated. Finally, we list our conclusions on presence and nature of correlation between nanoparticle valency (N) and avidity (K) as well as between valency and whole-body (w-b) and tissue-level (t-l) biodistribution. Abbreviations: ? - no conclusion possible based on present data, E - enkephalin-functionalization, G - glycopep-functionalization, (Mut)Apt - (mutated i.e., non-functional) aptamer, N.A. - not applicable, n.d. - no data available.

Study	**size [nm]**	***N***	**ligand density**	**particle avidity**	**valency *N* dependence?**	
					K	**biodistribution**
Choi et al.	74.9 77.7 81.3 87.5	control 2.1 17.5 144.3	0 nm^{-3} 1.1 $x10^{-4}$ nm^{-3} 8.4 $x10^{-4}$ nm^{-3} 6.0 $x10^{-3}$ nm^{-3}	n.d. n.d. 1.06 nM 0.13 nM	yes	w-b.: no t-l.: threshold for particle uptake in target cells
Bartlett et al.	~80 to 125	n.d.	n.d	n.d.	?	?
Gu et al.	160	n.d.	10% MutApt 0% Apt 1% Apt 5% Apt 10% Apt	n.d.	?	w-b.: no t-l.: accumulation increases with % Apt up to 5% Apt then decreases.
Kirpotin et al.	~90 to 110	> 20	~5.3 $x10^{-4}$ nm^{-3} to 7.9 $x10^{-4}$ nm^{-3}	n.d.	?	?
Bu et al.	~25 to 35	3.7	~9.6 $x10^{-4}$ nm^{-3} to 1.9 $x10^{-3}$ nm^{-3}	targeted: 85/66 fM blank: 0.96/0.38 nM	?	w-b.: no t-l.: ligand induces significant increase in dose delivered to tumor.
Zern et al.	187 183 186 192 198	blank 5 50 100 200	0 nm^{-3} 1.1 $x10^{-4}$ nm^{-3} 8.4 $x10^{-4}$ nm^{-3} 6.0 $x10^{-3}$ nm^{-3} 6.0 $x10^{-3}$ nm^{-3}	n.d. n.d. 1.0 $x10^{10}$ nm^3 n.d. 1.2 $x10^{11}$ nm^3	yes	w-b.: particle dose in liver appears to decrease with increasing *N*. t-l.: Dose accumulated in lungs increases with increasing *N*.
Frigell et al.	2.4 2.1 2.7 2.2 3.2	blank 13 E 10 E 6 G 15 G	0 nm^{-3} 0.94 nm^{-3} 0.44 nm^{-3} 0.39 nm^{-3} 0.47 nm^{-3}	n.d.	?	w-b.: Partially, ligands increase accumulation in off-target organs. t-l.: One ligand-linker pairing induced higher dose in target organ.
Wang et al.	6.0[1]/ 14.8[2]	n.d.	n.d.	n.d.	?	?
Ganesh et al.	200/ 90	N.A.	N.A.	N.A.	?	?
Akers et al.	250	n.d.	n.d.	n.d.	?	?

Discussion

In the first part of this work, we introduce the concept of avidity and review literature providing evidence on what factors affect this property and how this concept translates to the case of nanoparticle-cell membrane interactions. In doing so, we were able to derive a general hypothesis about the distribution of ligand-functionalized nanoparticles in an environment with varying receptor densities, suggesting accumulation at high-receptor densities. Ultimately, the aim of this work was to investigate whether the experimentally found bio-distribution follows this hypothesis. Thus, whether there is a correlation between avidity and bio-distribution. We also introduce the impact of membrane curvature on particle-membrane interactions, deducing the question about the transferability of the described relations on the case of a ligand-functionalized nanoparticle. Already from these reflection on fundamental principles, approaches for further investigations can be derived. The available literature, for instance, provides evidence that different particle systems may differ in the mechanism underlying their avidity. Thus, it appears that the avidity can result from both accelerated association (↑ k_{on}) and slowed dissociation (↓ k_{off}) [64,108,109]. As to the question of what influence the presence of one or the other mechanism has on the biodistribution of a nanoparticle, there is, to the best of our knowledge, no evidence available.

Summarizing the findings of the studies presented in the second part of the paper, it must be concluded that a clear assessment of the correlation of avidity and biodistribution is hardly possible based on presently available data. This is due in no small part to the fact that studies are lacking that have systematically investigated the biodistribution of a constant particle system with an avidity that varies over a quantified range. One reason for this is the all too understandable fact that in application-oriented research projects, it is primarily the most promising particle systems that are further investigated in in vivo experiments. Particles with poorer in vitro binding properties are not pursued further. However, this focus has led to a relevant knowledge gap regarding our understanding of nanoparticle interactions with biological systems that may inhibit the rational development of nanotherapeutics. In this context, our review points out an existing need for basic research on avidity-biodistribution correlation.

From the authors' perspective, only three of the relevant papers consulted for this review demonstrated directional accumulation of nanoparticles. Whereby, by directed

accumulation we imply an accumulation of particles over time in the desired target tissue with simultaneous depletion in off-target tissues or organs. Only the works of Zern et al., Wang et al., and Ganesh et al. satisfy this strict interpretation of the term. To evaluate the question about decisive influencing factors for a directed biodistribution, it is worthwhile to consider in which properties the particles investigated in these studies differ from others. Thus, it is particularly noteworthy that with the work of Ganesh et al. the particle system associated with the ligand possessing the lowest receptor affinity is among the most successful systems. While this fact may be surprising at first, considering the basic principles of multivalency-induced avidity, it is consistent with previous theoretical considerations [145–147] and experimental observations [148–151]. Here, it has been reported that a lower affinity of the ligand used for functionalization leads to a higher target organ specificity of the resulting particle. A factor possibly causative of this circumstance can be deduced when taking a closer look at the “real-world” situation of nanoparticle-membrane interactions. Here, the initial binding of the particle already brings many ligands into close proximity to receptors. Once several ligand-receptor bonds have been formed, it is very likely, especially with high-affinity ligands, that even if individual ligands dissociate, they will quickly bind a receptor again due to the spatial proximity. It has been described that this phenomenon can lead to a practically irreversible binding of multivalent entities [45,152,153].

Furthermore, we find it remarkable that the study of Zern et al. is the only one in which an increasing avidity with particle valency could be demonstrated, which in turn led to a positive influence on the whole-body biodistribution. It should be emphasized that the targeted structure in this case was not a tumor tissue. This allows the hypothesis that factors typical of tumor environments counteract the targeted accumulation of ligand-functionalized nanoparticles. Cancer specific challenges in targeted nanoparticle delivery have very recently been reviewed by Chan [154] Drozdov et al. [155]. In brief summary the key factors known to date are opsonization of particle surface with biomolecules [156,157], undesired accumulation in the reticuloendothelial system (i.e., liver, spleen, lymph nodes) [99], access to tumor microenvironment (i.e., vessel evasion, endothelial crossing) [158], and navigating through complex tumor microenvironment (i.e., immune-cell interactions, extracellular matrix interactions, interstitial pressure) [159–163]. In this context, it is a pity that the studies of Wang et al. and Ganesh et al. do not contain any data on particle avidity and that also the degree of ligand functionalization was not varied. Thus, although these studies show that successful targeting is possible in tumor models, they do not allow a conclusion as to whether there

is a correlation between avidity and biodistribution. A steep valency-dependent increase in avidity, however, has previously been demonstrated for folic acid-functionalized dendrimers (~4 nm) [64].

We would further like to point out a finding by Choi et al. that is important for the question about correlation between particle avidity and biodistribution. Besides the study by Zern et al. this is the only work in which a correlation between valency and avidity has been demonstrated. Although the authors find no influence of ligand functionalization in this case, an influence at the tissue level was noted. Concretely, the authors describe a threshold value for particle valence, above which a more favorable bio-distribution of the particle occurs. In our view, this observation raises the question about the 'reach' of avidity in biological systems. It must be discussed whether the attempt to directly transfer the avidity concept to the use case of particle distribution in a biological system may not be an oversimplification. Very valuable in this context is the study by Akers et al. which showed that a free ligand can even outperform a multivalently functionalized particle in terms of targeted delivery. Considering this the following points come to mind:
(1) The unmodified transfer of the concept presupposes the assumption that the distribution of a particle between two tissues is determined exclusively or at least primarily by the process of binding per se. In other words, that there are no or only neglectable factors influencing distribution of the unbound particles other than undirected diffusion. As many studies on the troublesome road of nanoparticles to their target tissue already cited in this work have shown, this assumption must at least be considered bold.
(2) An uncritical transfer further comes with a strong focus on ligand- and receptor-densities when attempting prediction of nanoparticle distribution. While this approach might be appropriate to derive meaningful binding parameters in experiments based on artificial or extracted membranes, it potentially oversimplifies the complexity of the surrounding encountered by the particle in an actual biological system. For instance, the cell membrane curvature is neglected, which we believe could be a crucial factor determining the availability of receptors for interaction with nanoparticles.
Previous work by our group indicates such importance of membrane nanomorphology. A significant decrease in avidity was observed for a model particle system after inhibition of clathrin-coated pits (CCPs) as typical nanostructures in the membrane [95]. We also observed that biomolecules more abundant in tumors, which might have a comparable

effect on CCPs, unfavorably influence the distribution of particles between target and off-target cells [164].

Overall, the present review identifies an urgent need for systematic fundamental research. We have outlined two possible approaches for a systematic proceeding to stimulate research that could lead to a better understanding of nano-bio-interactions (Fig. 9A) and the correlation of avidity and biodistribution (Fig. 9B).

Conclusion

The overview of data available on the correlation of nanoparticle avidity and biodistribution provided in this work revealed that the matter is strongly under-researched. After a thorough review of the available literature, we cannot draw a definitive conclusion whether an increasing particle avidity will lead to increased particle accumulation at the desired target site. Since this observation stands in contradiction with the theoretical fundamentals of avidity, this in turn allows for four conclusions: (A) The particle avidity is influenced by to date unknown factors that counteract its expected positive effect on biodistribution, (B) all systems studied so far in literature exhibit extremely high entropic penalties that prevent the formation of ligand-receptor interactions, (C) The concept of avidity is in fact not applicable to the case of particle distribution in a biological system, and (D) the data collected so far are not sufficient to recognize any correlation that may exist.

With these approaches, our work has the potential to stimulate further research that may lead to a better understanding of the interaction of avidity and biodistribution. Further insights in this field could in turn contribute to the development of improved targeted delivery systems. Basis of the present work was the research need arising from point (A) to identify factors influencing the avidity of particles when interacting with their target cells.

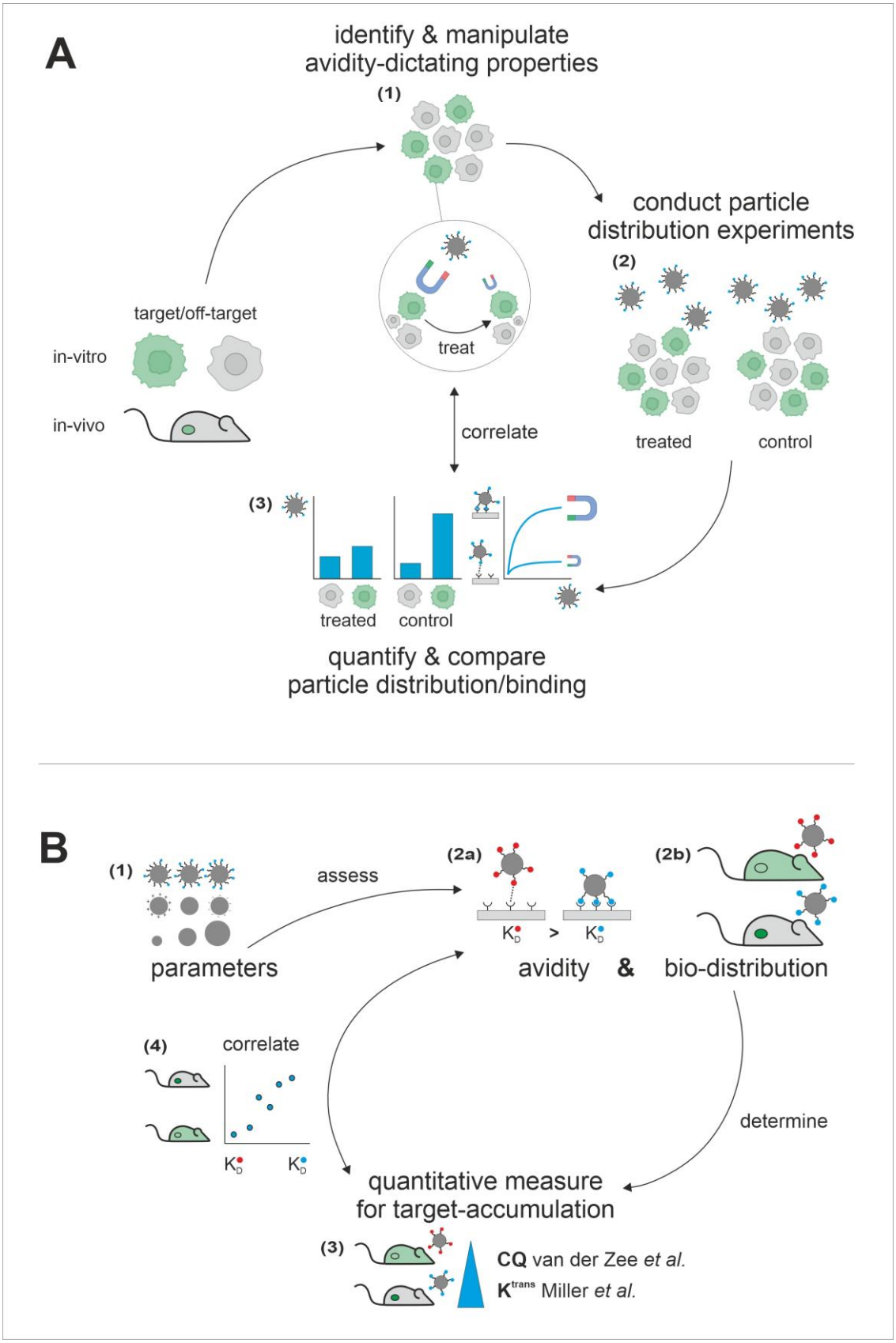
A
identify & manipulate
avidity-dictating properties
(1)
conduct particle
distribution experiments
(2)
target/off-target
in-vitro
in-vivo
treat
correlate
treated
control
(3)
treated
control
quantify & compare
particle distribution/binding
B
(1)
parameters
assess
(2a)
(2b)
avidity & bio-distribution
(4)
correlate
determine
quantitative measure
for target-accumulation
(3)
CQ van der Zee et al.
K trans Miller et al.

Figure 9: Approaches for systematic investigation of nano-bio-interactions and avidity-biodistribution studies. In these schemes we outline principal study proceedings suitable to (A) identify and characterize biological properties affecting nanoparticle avidity and (B) to systematically investigate the correlation of nanoparticle avidity and biodistribution. (A) A more complete understanding of biological parameters affecting nanoparticle-cell interactions is key to increase predictability of particle biodistribution. For this, a systematic proceeding is outlined above, which in brief suggests to (1) hypothesize parameters to investigate and to identify tools enabling controlled manipulation of these properties, (2) to conduct particle binding or distribution assays, where possible in a cellular or even in an in vivo setting, and (3) to quantify and compare binding or distribution data for a series of parameter states. Optimally, the correlation of parameter state and binding/distribution data should be studied to identify a model describing their interaction. This could allow not only to identify the presence of a correlation but also to understand its precise nature. (B) One circumstance that complicates the assessment of avidity-biodistribution correlation is that there have been only few studies with a dedicated focus on the matter. Most of the knowledge available today on this subject must be gathered from individual publications, each of which often contains only incomplete sets of information on the relationship in question. We outline here a blueprint for an approach to systematically investigate the relationship between avidity and biodistribution. In brief, (1) the particle parameters to be studied should be varied individually and in a controlled manner. In this way, a design space for the studied particle can be covered. (2) Both avidity and bio-distribution should be determined for each individual particle. Finally, (3) a correlation analysis should be performed to investigate the relationship between avidity and bio-distribution. In this step, it is preferable to use quantitative measures for the degree of accumulation, to in turn allow for a subsequent quantitative assessment of correlation. Applicable parameters were presented in the literature by van der Zee et al. [165] and Miller et al. [166].

References

[1] J.K. Mills, D. Needham, Targeted drug delivery, Expert Opinion on Therapeutic Patents 9 (1999) 1499–1513.

[2] P. Kumari, B. Ghosh, S. Biswas, Nanocarriers for cancer-targeted drug delivery, Journal of drug targeting 24 (2016) 179–191.

[3] A.I. Freeman, E. Mayhew, Targeted drug delivery, Cancer 58 (1986) 573–583.

[4] S. Sur, A. Rathore, V. Dave, K.R. Reddy, R.S. Chouhan, V. Sadhu, Recent developments in functionalized polymer nanoparticles for efficient drug delivery system, Nano-Structures & Nano-Objects 20 (2019) 100397.

[5] M. Srinivasarao, P.S. Low, Ligand-Targeted Drug Delivery, Chemical reviews 117 (2017) 12133–12164.

[6] S.-W. Choi, W.-S. Kim, J.-H. Kim, Surface Modification of Functional Nanoparticles for Controlled Drug Delivery, Journal of Dispersion Science and Technology 24 (2003) 475–487.

[7] N.H. Abd Ellah, S.A. Abouelmagd, Surface functionalization of polymeric nanoparticles for tumor drug delivery: approaches and challenges, Expert opinion on drug delivery 14 (2017) 201–214.

[8] M.J. Akhtar, M. Ahamed, H.A. Alhadlaq, S.A. Alrokayan, S. Kumar, Targeted anticancer therapy: overexpressed receptors and nanotechnology, Clinica chimica acta; international journal of clinical chemistry 436 (2014) 78–92.

[9] M. Walter, F. Baumann, K. Schorr, A. Goepferich, Ectoenzymes as Promising Cell Identification Structures for the High Avidity Targeting of Polymeric Nanoparticles, International journal of pharmaceutics (2023) 123453.

[10] S. Xu, B.Z. Olenyuk, C.T. Okamoto, S.F. Hamm-Alvarez, Targeting receptor-mediated endocytotic pathways with nanoparticles: rationale and advances, Advanced drug delivery reviews 65 (2013) 121–138.

[11] G.T. Tietjen, L.G. Bracaglia, W.M. Saltzman, J.S. Pober, Focus on Fundamentals: Achieving Effective Nanoparticle Targeting, Trends in molecular medicine 24 (2018) 598–606.

[12] Z.G. Chen, Small-molecule delivery by nanoparticles for anticancer therapy, Trends in molecular medicine 16 (2010) 594–602.

[13] A. Lalatsa, A.G. Schatzlein, I.F. Uchegbu, Strategies to deliver peptide drugs to the brain, Molecular pharmaceutics 11 (2014) 1081–1093.

[14] S.-J. Cao, S. Xu, H.-M. Wang, Y. Ling, J. Dong, R.-D. Xia, X.-H. Sun, Nanoparticles: Oral Delivery for Protein and Peptide Drugs, AAPS PharmSciTech 20 (2019) 190.

[15] A. Zeb, I. Rana, H.-I. Choi, C.-H. Lee, S.-W. Baek, C.-W. Lim, N. Khan, S.T. Arif, N.U. Sahar, A.M. Alvi, F.A. Shah, F.U. Din, O.-N. Bae, J.-S. Park, J.-K. Kim, Potential and Applications of Nanocarriers for Efficient Delivery of Biopharmaceuticals, Pharmaceutics 12 (2020).

[16] S. Mitragotri, P.A. Burke, R. Langer, Overcoming the challenges in administering biopharmaceuticals: formulation and delivery strategies, Nature reviews. Drug discovery 13 (2014) 655–672.

[17] Y. Xiao, K. Shi, Y. Qu, B. Chu, Z. Qian, Engineering Nanoparticles for Targeted Delivery of Nucleic Acid Therapeutics in Tumor, Molecular therapy. Methods & clinical development 12 (2019) 1–18.

[18] A. Amani, M.R. Alizadeh, H. Yaghoubi, M. Nohtani, Novel multi-targeted nanoparticles for targeted co-delivery of nucleic acid and chemotherapeutic agents to breast cancer tissues, Materials science & engineering. C, Materials for biological applications 118 (2021) 111494.

[19] J. Karlsson, K.M. Luly, S.Y. Tzeng, J.J. Green, Nanoparticle designs for delivery of nucleic acid therapeutics as brain cancer therapies, Advanced drug delivery reviews 179 (2021) 113999.

[20] H.J. Vaughan, J.J. Green, S.Y. Tzeng, Cancer-Targeting Nanoparticles for Combinatorial Nucleic Acid Delivery, Advanced materials (Deerfield Beach, Fla.) 32 (2020) e1901081.

[21] H.I. Labouta, R. Langer, P.R. Cullis, O.M. Merkel, M.R. Prausnitz, Y. Gomaa, S.S. Nogueira, T. Kumeria, Role of drug delivery technologies in the success of COVID-19 vaccines: a perspective, Drug delivery and translational research 12 (2022) 2581–2588.

[22] F. Meng, J. Wang, Q. Ping, Y. Yeo, Quantitative Assessment of Nanoparticle Biodistribution by Fluorescence Imaging, Revisited, ACS nano 12 (2018) 6458–6468.

[23] I.H.C. Miedema, G.J.C. Zwezerijnen, M.C. Huisman, E. Doeleman, R.H.J. Mathijssen, T. Lammers, Q. Hu, G.A.M.S. van Dongen, C.J.F. Rijcken, D.J. Vugts, C.W. van Menke-van der Houven Oordt, PET-CT Imaging of Polymeric Nanoparticle Tumor Accumulation in Patients, Advanced materials (Deerfield Beach, Fla.) 34 (2022) e2201043.

[24] S.J. Blocker, A.F. Shields, Imaging of Nanoparticle Distribution to Assess Treatments That Alter Delivery, Molecular imaging and biology 20 (2018) 340–351.

[25] O. Kochebina, A. Halty, J. Taleb, D. Kryza, M. Janier, A.B. Sadr, T. Baudier, S. Rit, D. Sarrut, In vivo gadolinium nanoparticle quantification with SPECT/CT, EJNMMI physics 6 (2019) 9.

[26] M. Torrice, Does Nanomedicine Have a Delivery Problem?, ACS central science 2 (2016) 434–437.

[27] R. Cai, C. Chen, The Crown and the Scepter: Roles of the Protein Corona in Nanomedicine, Advanced materials (Deerfield Beach, Fla.) 31 (2019) e1805740.

[28] C. Corbo, R. Molinaro, A. Parodi, N.E. Toledano Furman, F. Salvatore, E. Tasciotti, The impact of nanoparticle protein corona on cytotoxicity, immunotoxicity and target drug delivery, Nanomedicine (London, England) 11 (2016) 81–100.

[29] W. Xiao, H. Gao, The impact of protein corona on the behavior and targeting capability of nanoparticle-based delivery system, International journal of pharmaceutics 552 (2018) 328–339.

[30] M.A. Dobrovolskaia, P. Aggarwal, J.B. Hall, S.E. McNeil, Preclinical studies to understand nanoparticle interaction with the immune system and its potential effects on nanoparticle biodistribution, Molecular pharmaceutics 5 (2008) 487–495.

[31] S.M. Moghimi, Chemical camouflage of nanospheres with a poorly reactive surface: towards development of stealth and target-specific nanocarriers, Biochimica et biophysica acta 1590 (2002) 131–139.

[32] D. van Haute, J.M. Berlin, Challenges in realizing selectivity for nanoparticle biodistribution and clearance: lessons from gold nanoparticles, Therapeutic delivery 8 (2017) 763–774.

[33] M. Cataldi, C. Vigliotti, T. Mosca, M. Cammarota, D. Capone, Emerging Role of the Spleen in the Pharmacokinetics of Monoclonal Antibodies, Nanoparticles and Exosomes, International journal of molecular sciences 18 (2017).

[34] W. Xu, M. Xu, Y. Xiao, L. Yu, H. Xie, X. Jiang, M. Chen, H. Gao, L. Wang, Changes in target ability of nanoparticles due to protein corona composition and disease state, Asian journal of pharmaceutical sciences 17 (2022) 401–411.

[35] A. Salvati, A.S. Pitek, M.P. Monopoli, K. Prapainop, F.B. Bombelli, D.R. Hristov, P.M. Kelly, C. Åberg, E. Mahon, K.A. Dawson, Transferrin-functionalized nanoparticles lose their targeting capabilities when a biomolecule corona adsorbs on the surface, Nature nanotechnology 8 (2013) 137–143.

[36] T. Malachowski, A. Hassel, Engineering nanoparticles to overcome immunological barriers for enhanced drug delivery, Engineered Regeneration 1 (2020) 35–50.

[37] B.S. Zolnik, A. González-Fernández, N. Sadrieh, M.A. Dobrovolskaia, Nanoparticles and the immune system, Endocrinology 151 (2010) 458–465.

[38] J.J. Milligan, S. Saha, A Nanoparticle's Journey to the Tumor: Strategies to Overcome First-Pass Metabolism and Their Limitations, Cancers 14 (2022).

[39] J.L. Cuellar-Camacho, S. Bhatia, V. Reiter-Scherer, D. Lauster, S. Liese, J.P. Rabe, A. Herrmann, R. Haag, Quantification of Multivalent Interactions between Sialic Acid and Influenza A Virus Spike Proteins by Single-Molecule Force Spectroscopy, Journal of the American Chemical Society 142 (2020) 12181–12192.

[40] D. Di Iorio, M.L. Verheijden, E. van der Vries, P. Jonkheijm, J. Huskens, Weak Multivalent Binding of Influenza Hemagglutinin Nanoparticles at a Sialoglycan-Functionalized Supported Lipid Bilayer, ACS nano 13 (2019) 3413–3423.

[41] H. Jung, A.D. Robison, P.S. Cremer, Multivalent ligand-receptor binding on supported lipid bilayers, Journal of structural biology 168 (2009) 90–94.

[42] J.E. Silpe, M. Sumit, T.P. Thomas, B. Huang, A. Kotlyar, M.A. van Dongen, M.M. Banaszak Holl, B.G. Orr, S.K. Choi, Avidity modulation of folate-targeted multivalent dendrimers for evaluating biophysical models of cancer targeting nanoparticles, ACS chemical biology 8 (2013) 2063–2071.

[43] D. Lauster, M. Glanz, M. Bardua, K. Ludwig, M. Hellmund, U. Hoffmann, A. Hamann, C. Böttcher, R. Haag, C.P.R. Hackenberger, A. Herrmann, Multivalent Peptide-Nanoparticle Conjugates for Influenza-Virus Inhibition, Angewandte Chemie (International ed. in English) 56 (2017) 5931–5936.

[44] D. Peterhoff, S. Thalhauser, P. Neckermann, C. Barbey, K. Straub, J. Nazet, R. Merkl, G. Laengst, M. Breunig, R. Wagner, Multivalent display of engineered HIV-1 envelope trimers on silica nanoparticles for targeting and in vitro activation of germline VRC01 B cells, European journal of pharmaceutics and biopharmaceutics official journal of Arbeitsgemeinschaft fur Pharmazeutische Verfahrenstechnik e.V 181 (2022) 88–101.

[45] S. Erlendsson, K. Teilum, Binding Revisited-Avidity in Cellular Function and Signaling, Frontiers in molecular biosciences 7 (2020) 615565.

[46] M.I. Page, W.P. Jencks, Entropic contributions to rate accelerations in enzymic and intramolecular reactions and the chelate effect, Proceedings of the National Academy of Sciences of the United States of America 68 (1971) 1678–1683.

[47] W.P. Jencks, On the attribution and additivity of binding energies, Proceedings of the National Academy of Sciences of the United States of America 78 (1981) 4046–4050.

[48] P.I. Kitov, D.R. Bundle, On the nature of the multivalency effect: a thermodynamic model, Journal of the American Chemical Society 125 (2003) 16271–16284.

[49] V.M. Krishnamurthy, L.A. Estroff, G.M. Whitesides, Multivalency in Ligand Design, in: W. Jahnke, D.A. Erlanson (Eds.), Fragment-based Approaches in Drug Discovery, Wiley, 2006, pp. 11–53.

[50] C.A. Hunter, H.L. Anderson, What is cooperativity?, Angewandte Chemie International Edition 48 (2009) 7488–7499.

[51] C.H. Reynolds, M.K. Holloway, Thermodynamics of ligand binding and efficiency, ACS medicinal chemistry letters 2 (2011) 433–437.

[52] M.K. Gilson, T. Liu, M. Baitaluk, G. Nicola, L. Hwang, J. Chong, BindingDB in 2015: A public database for medicinal chemistry, computational chemistry and systems pharmacology, Nucleic acids research 44 (2016) D1045-53.

[53] T. Liu, Y. Lin, X. Wen, R.N. Jorissen, M.K. Gilson, BindingDB: a web-accessible database of experimentally determined protein-ligand binding affinities, Nucleic acids research 35 (2007) D198-201.

[54] T.S.G. Olsson, M.A. Williams, W.R. Pitt, J.E. Ladbury, The thermodynamics of protein-ligand interaction and solvation: insights for ligand design, Journal of molecular biology 384 (2008) 1002–1017.

[55] G. Schwarzenbach, Der Chelateffekt, Helv. Chim. Acta 35 (1952) 2344–2359.

[56] A.V. Finkelstein, J. Janin, The price of lost freedom: entropy of bimolecular complex formation, Protein engineering 3 (1989) 1–3.

[57] S. Maslanka Figueroa, D. Fleischmann, S. Beck, A. Goepferich, The Effect of Ligand Mobility on the Cellular Interaction of Multivalent Nanoparticles, Macromolecular bioscience (2020) e1900427.

[58] M. de Amici, C. Dallanoce, U. Holzgrabe, C. Tränkle, K. Mohr, Allosteric ligands for G protein-coupled receptors: a novel strategy with attractive therapeutic opportunities, Medicinal research reviews 30 (2010) 463–549.

[59] F.J. Martinez-Veracoechea, D. Frenkel, Designing super selectivity in multivalent nano-particle binding, Proceedings of the National Academy of Sciences 108 (2011) 10963–10968.

[60] P.A. Borea, K. Varani, S. Gessi, P. Gilli, A. Dalpiaz, Receptor binding thermodynamics as a tool for linking drug efficacy and affinity, Farmaco (Societa chimica italiana 1989) 53 (1998) 249–254.

[61] I. Nakase, N. Ueno, M. Katayama, K. Noguchi, T. Takatani-Nakase, N.B. Kobayashi, T. Yoshida, I. Fujii, S. Futaki, Receptor clustering and activation by multivalent interaction through recognition peptides presented on exosomes, Chemical communications (Cambridge, England) 53 (2016) 317–320.

[62] Y.-F. Huang, H. Liu, X. Xiong, Y. Chen, W. Tan, Nanoparticle-mediated IgE-receptor aggregation and signaling in RBL mast cells, Journal of the American Chemical Society 131 (2009) 17328–17334.

[63] M.B. Deci, M. Liu, Q.T. Dinh, J. Nguyen, Precision engineering of targeted nanocarriers, Wiley interdisciplinary reviews. Nanomedicine and nanobiotechnology 10 (2018) e1511.

[64] S. Hong, P.R. Leroueil, I.J. Majoros, B.G. Orr, J.R. Baker, M.M. Banaszak Holl, The binding avidity of a nanoparticle-based multivalent targeted drug delivery platform, Chemistry & biology 14 (2007) 107–115.

[65] C. He, Y. Hu, L. Yin, C. Tang, C. Yin, Effects of particle size and surface charge on cellular uptake and biodistribution of polymeric nanoparticles, Biomaterials 31 (2010) 3657–3666.

[66] S. Hirn, M. Semmler-Behnke, C. Schleh, A. Wenk, J. Lipka, M. Schäffler, S. Takenaka, W. Möller, G. Schmid, U. Simon, W.G. Kreyling, Particle size-dependent and surface charge-dependent biodistribution of gold nanoparticles after intravenous administration, European journal of pharmaceutics and biopharmaceutics official journal of Arbeitsgemeinschaft fur Pharmazeutische Verfahrenstechnik e.V 77 (2011) 407–416.

[67] D.L. Jasinski, H. Li, P. Guo, The Effect of Size and Shape of RNA Nanoparticles on Biodistribution, Molecular therapy the journal of the American Society of Gene Therapy 26 (2018) 784–792.

[68] G. Sonavane, K. Tomoda, K. Makino, Biodistribution of colloidal gold nanoparticles after intravenous administration: effect of particle size, Colloids and surfaces. B, Biointerfaces 66 (2008) 274–280.

[69] P. Decuzzi, B. Godin, T. Tanaka, S.-Y. Lee, C. Chiappini, X. Liu, M. Ferrari, Size and shape effects in the biodistribution of intravascularly injected particles, Journal of controlled release official journal of the Controlled Release Society 141 (2010) 320–327.

[70] G. Zhang, Z. Yang, W. Lu, R. Zhang, Q. Huang, M. Tian, L. Li, D. Liang, C. Li, Influence of anchoring ligands and particle size on the colloidal stability and in vivo biodistribution of polyethylene glycol-coated gold nanoparticles in tumor-xenografted mice, Biomaterials 30 (2009) 1928–1936.

[71] S.A. Kulkarni, S.-S. Feng, Effects of particle size and surface modification on cellular uptake and biodistribution of polymeric nanoparticles for drug delivery, Pharmaceutical research 30 (2013) 2512–2522.

[72] F. Alexis, E. Pridgen, L.K. Molnar, O.C. Farokhzad, Factors affecting the clearance and biodistribution of polymeric nanoparticles, Molecular pharmaceutics 5 (2008) 505–515.

[73] J.M. Caster, S.K. Yu, A.N. Patel, N.J. Newman, Z.J. Lee, S.B. Warner, K.T. Wagner, K.C. Roche, X. Tian, Y. Min, A.Z. Wang, Effect of particle size on the biodistribution, toxicity, and efficacy of drug-loaded polymeric nanoparticles in chemoradiotherapy, Nanomedicine nanotechnology, biology, and medicine 13 (2017) 1673–1683.

[74] S. Kaga, N.P. Truong, L. Esser, D. Senyschyn, A. Sanyal, R. Sanyal, J.F. Quinn, T.P. Davis, L.M. Kaminskas, M.R. Whittaker, Influence of Size and Shape on the Biodistribution of Nanoparticles Prepared by Polymerization-Induced Self-Assembly, Biomacromolecules 18 (2017) 3963–3970.

[75] K. Xiao, Y. Li, J. Luo, J.S. Lee, W. Xiao, A.M. Gonik, R.G. Agarwal, K.S. Lam, The effect of surface charge on in vivo biodistribution of PEG-oligocholic acid based micellar nanoparticles, Biomaterials 32 (2011) 3435–3446.

[76] L. Maurizi, A.-L. Papa, L. Dumont, F. Bouyer, P. Walker, D. Vandroux, N. Millot, Influence of Surface Charge and Polymer Coating on Internalization and Biodistribution of Polyethylene Glycol-Modified Iron Oxide Nanoparticles, Journal of biomedical nanotechnology 11 (2015) 126–136.

[77] S.G. Elci, Y. Jiang, B. Yan, S.T. Kim, K. Saha, D.F. Moyano, G. Yesilbag Tonga, L.C. Jackson, V.M. Rotello, R.W. Vachet, Surface Charge Controls the Suborgan Biodistributions of Gold Nanoparticles, ACS nano 10 (2016) 5536–5542.

[78] X. Huang, L. Li, T. Liu, N. Hao, H. Liu, D. Chen, F. Tang, The shape effect of mesoporous silica nanoparticles on biodistribution, clearance, and biocompatibility in vivo, ACS nano 5 (2011) 5390–5399.

[79] L. Li, T. Liu, C. Fu, L. Tan, X. Meng, H. Liu, Biodistribution, excretion, and toxicity of mesoporous silica nanoparticles after oral administration depend on their shape, Nanomedicine nanotechnology, biology, and medicine 11 (2015) 1915–1924.

[80] D. Shao, M.-M. Lu, Y.-W. Zhao, F. Zhang, Y.-F. Tan, X. Zheng, Y. Pan, X.-A. Xiao, Z. Wang, W.-F. Dong, J. Li, L. Chen, The shape effect of magnetic mesoporous silica nanoparticles on endocytosis, biocompatibility and biodistribution, Acta biomaterialia 49 (2017) 531–540.

[81] S. Shukla, F.J. Eber, A.S. Nagarajan, N.A. DiFranco, N. Schmidt, A.M. Wen, S. Eiben, R.M. Twyman, C. Wege, N.F. Steinmetz, The Impact of Aspect Ratio on the Biodistribution and Tumor Homing of Rigid Soft-Matter Nanorods, Advanced healthcare materials 4 (2015) 874–882.

[82] T. Harayama, H. Riezman, Understanding the diversity of membrane lipid composition, Nature reviews. Molecular cell biology 19 (2018) 281–296.

[83] E. Sezgin, I. Levental, S. Mayor, C. Eggeling, The mystery of membrane organization: composition, regulation and roles of lipid rafts, Nature reviews. Molecular cell biology 18 (2017) 361–374.

[84] A. Gray, E. Abbena, S. Salamon, Modern differential geometry curves and surfaces with Mathematica by Alfred Gray, Elsa Abbena and Simon Salamon, 3rd ed. ed., Chapman & Hall/CRC, Boca Raton, 2006.

[85] E.E. Kooijman, V. Chupin, N.L. Fuller, M.M. Kozlov, B. de Kruijff, K.N.J. Burger, P.R. Rand, Spontaneous curvature of phosphatidic acid and lysophosphatidic acid, Biochemistry 44 (2005) 2097–2102.

[86] M.K. Dymond, Lipid monolayer spontaneous curvatures: A collection of published values, Chemistry and physics of lipids 239 (2021) 105117.

[87] J. Zimmerberg, M.M. Kozlov, How proteins produce cellular membrane curvature, Nature reviews. Molecular cell biology 7 (2006) 9–19.

[88] J. Agudo-Canalejo, R. Lipowsky, Adhesive Nanoparticles as Local Probes of Membrane Curvature, Nano letters 15 (2015) 7168–7173.

[89] J. Agudo-Canalejo, R. Lipowsky, Uniform and Janus-like nanoparticles in contact with vesicles: energy landscapes and curvature-induced forces, Soft matter 13 (2017) 2155–2173.

[90] Q. Yu, S. Othman, S. Dasgupta, T. Auth, G. Gompper, Nanoparticle wrapping at small non-spherical vesicles: curvatures at play, Nanoscale 10 (2018) 6445–6458.

[91] M Deserno, T Bickel, Wrapping of a spherical colloid by a fluid membrane, Europhysics Letters (EPL) 62 (2003) 767–774.

[92] A.H. Bahrami, R. Lipowsky, T.R. Weikl, The role of membrane curvature for the wrapping of nanoparticles, Soft matter 12 (2016) 581–587.

[93] K.A. Sochacki, B.L. Heine, G.J. Haber, J.R. Jimah, B. Prasai, M.A. Alfonzo-Méndez, A.D. Roberts, A. Somasundaram, J.E. Hinshaw, J.W. Taraska, The structure and spontaneous curvature of clathrin lattices at the plasma membrane, Developmental cell 56 (2021) 1131-1146.e3.

[94] A.A. Yetisgin, S. Cetinel, M. Zuvin, A. Kosar, O. Kutlu, Therapeutic Nanoparticles and Their Targeted Delivery Applications, Molecules (Basel, Switzerland) 25 (2020) 2193.

[95] O. Zimmer, A. Goepferich, How clathrin-coated pits control nanoparticle avidity for cells, Nanoscale horizons 8 (2023) 256–269.

[96] C.H.J. Choi, C.A. Alabi, P. Webster, M.E. Davis, Mechanism of active targeting in solid tumors with transferrin-containing gold nanoparticles, Proceedings of the National Academy of Sciences of the United States of America 107 (2010) 1235–1240.

[97] F. Gu, L. Zhang, B.A. Teply, N. Mann, A. Wang, A.F. Radovic-Moreno, R. Langer, O.C. Farokhzad, Precise engineering of targeted nanoparticles by using self-assembled biointegrated block copolymers, Proceedings of the National Academy of Sciences of the United States of America 105 (2008) 2586–2591.

[98] N. Hoshyar, S. Gray, H. Han, G. Bao, The effect of nanoparticle size on in vivo pharmacokinetics and cellular interaction, Nanomedicine (London, England) 11 (2016) 673–692.

[99] Y.-N. Zhang, W. Poon, A.J. Tavares, I.D. McGilvray, W.C.W. Chan, Nanoparticle-liver interactions: Cellular uptake and hepatobiliary elimination, Journal of controlled release official journal of the Controlled Release Society 240 (2016) 332–348.

[100] W. Ngo, S. Ahmed, C. Blackadar, B. Bussin, Q. Ji, S.M. Mladjenovic, Z. Sepahi, W.C.W. Chan, Why nanoparticles prefer liver macrophage cell uptake in vivo, Advanced drug delivery reviews 185 (2022) 114238.

[101] N.J. Butcher, G.M. Mortimer, R.F. Minchin, Drug delivery: Unravelling the stealth effect, Nature nanotechnology 11 (2016) 310–311.

[102] S.-D. Li, L. Huang, Stealth nanoparticles: high density but sheddable PEG is a key for tumor targeting, Journal of controlled release official journal of the Controlled Release Society 145 (2010) 178–181.

[103] S. Zalba, T.L.M. ten Hagen, C. Burgui, M.J. Garrido, Stealth nanoparticles in oncology: Facing the PEG dilemma, Journal of controlled release official journal of the Controlled Release Society 351 (2022) 22–36.

[104] J.W. Park, K. Hong, D.B. Kirpotin, G. Colbern, R. Shalaby, J. Baselga, Y. Shao, U.B. Nielsen, J.D. Marks, D. Moore, D. Papahadjopoulos, C.C. Benz, Anti-HER2 immunoliposomes: enhanced efficacy attributable to targeted delivery, Clinical cancer research an official journal of the American Association for Cancer Research 8 (2002) 1172–1181.

[105] D.B. Kirpotin, D.C. Drummond, Y. Shao, M.R. Shalaby, K. Hong, U.B. Nielsen, J.D. Marks, C.C. Benz, J.W. Park, Antibody targeting of long-circulating lipidic nanoparticles does not increase tumor localization but does increase internalization in animal models, Cancer research 66 (2006) 6732–6740.

[106] D.W. Bartlett, M.E. Davis, Physicochemical and biological characterization of targeted, nucleic acid-containing nanoparticles, Bioconjugate chemistry 18 (2007) 456–468.

[107] D.W. Bartlett, H. Su, I.J. Hildebrandt, W.A. Weber, M.E. Davis, Impact of tumor-specific targeting on the biodistribution and efficacy of siRNA nanoparticles measured by multimodality in vivo imaging, Proceedings of the National Academy of Sciences of the United States of America 104 (2007) 15549–15554.

[108] J. Wang, J. Min, S.A. Eghtesadi, R.S. Kane, A. Chilkoti, Quantitative Study of the Interaction of Multivalent Ligand-Modified Nanoparticles with Breast Cancer Cells with Tunable Receptor Density, ACS nano 14 (2020) 372–383.

[109] J. Bu, A. Nair, M. Iida, W.-J. Jeong, M.J. Poellmann, K. Mudd, L.J. Kubiatowicz, E.W. Liu, D.L. Wheeler, S. Hong, An Avidity-Based PD-L1 Antagonist Using Nanoparticle-Antibody Conjugates for Enhanced Immunotherapy, Nano letters 20 (2020) 4901–4909.

[110] G.M. Thurber, K. Dane Wittrup, A mechanistic compartmental model for total antibody uptake in tumors, Journal of theoretical biology 314 (2012) 57–68.

[111] G.P. Adams, R. Schier, A.M. McCall, H.H. Simmons, E.M. Horak, R.K. Alpaugh, J.D. Marks, L.M. Weiner, High affinity restricts the localization and tumor

penetration of single-chain fv antibody molecules, Cancer research 61 (2001) 4750–4755.

[112] M.M. Schmidt, K.D. Wittrup, A modeling analysis of the effects of molecular size and binding affinity on tumor targeting, Molecular cancer therapeutics 8 (2009) 2861–2871.

[113] B.J. Zern, A.-M. Chacko, J. Liu, C.F. Greineder, E.R. Blankemeyer, R. Radhakrishnan, V. Muzykantov, Reduction of nanoparticle avidity enhances the selectivity of vascular targeting and PET detection of pulmonary inflammation, ACS nano 7 (2013) 2461–2469.

[114] E.A. Simone, B.J. Zern, A.-M. Chacko, J.L. Mikitsh, E.R. Blankemeyer, S. Muro, R.V. Stan, V.R. Muzykantov, Endothelial targeting of polymeric nanoparticles stably labeled with the PET imaging radioisotope iodine-124, Biomaterials 33 (2012) 5406–5413.

[115] A. Abrimian, T. Kraft, Y.-X. Pan, Endogenous Opioid Peptides and Alternatively Spliced Mu Opioid Receptor Seven Transmembrane Carboxyl-Terminal Variants, International journal of molecular sciences 22 (2021).

[116] J. Frigell, I. García, V. Gómez-Vallejo, J. Llop, S. Penadés, 68Ga-labeled gold glyconanoparticles for exploring blood-brain barrier permeability: preparation, biodistribution studies, and improved brain uptake via neuropeptide conjugation, Journal of the American Chemical Society 136 (2014) 449–457.

[117] K. Siwowska, R.M. Schmid, S. Cohrs, R. Schibli, C. Müller, Folate Receptor-Positive Gynecological Cancer Cells: In Vitro and In Vivo Characterization, Pharmaceuticals (Basel, Switzerland) 10 (2017).

[118] J.T. Price, T. Tiganis, A. Agarwal, D. Djakiew, E.W. Thompson, Epidermal growth factor promotes MDA-MB-231 breast cancer cell migration through a phosphatidylinositol 3'-kinase and phospholipase C-dependent mechanism, Cancer research 59 (1999) 5475–5478.

[119] D. Takabatake, T. Fujita, T. Shien, K. Kawasaki, N. Taira, S. Yoshitomi, H. Takahashi, Y. Ishibe, Y. Ogasawara, H. Doihara, Tumor inhibitory effect of gefitinib (ZD1839, Iressa) and taxane combination therapy in EGFR-overexpressing breast cancer cell lines (MCF7/ADR, MDA-MB-231), International journal of cancer 120 (2007) 181–188.

[120] H. Wang, P. Guo, Radiolabeled RNA Nanoparticles for Highly Specific Targeting and Efficient Tumor Accumulation with Favorable In Vivo Biodistribution, Molecular pharmaceutics 18 (2021) 2924–2934.

[121] S. Ganesh, A.K. Iyer, D.V. Morrissey, M.M. Amiji, Hyaluronic acid based self-assembling nanosystems for CD44 target mediated siRNA delivery to solid tumors, Biomaterials 34 (2013) 3489–3502.

[122] B. Hu, Y. Ma, Y. Yang, L. Zhang, H. Han, J. Chen, CD44 promotes cell proliferation in non-small cell lung cancer, Oncology letters 15 (2018) 5627–5633.

[123] M.B. Penno, J.T. August, S.B. Baylin, M. Mabry, R.I. Linnoila, V.S. Lee, D. Croteau, X.L. Yang, C. Rosada, Expression of CD44 in Human Lung Tumors, Cancer research 54 (1994) 1381–1387.

[124] S. Ganesh, A.K. Iyer, F. Gattacceca, D.V. Morrissey, M.M. Amiji, In vivo biodistribution of siRNA and cisplatin administered using CD44-targeted hyaluronic acid nanoparticles, Journal of controlled release official journal of the Controlled Release Society 172 (2013) 699–706.

[125] W.J. Akers, Z. Zhang, M. Berezin, Y. Ye, A. Agee, K. Guo, R.W. Fuhrhop, S.A. Wickline, G.M. Lanza, S. Achilefu, Targeting of alpha(nu)beta(3)-integrins expressed on tumor tissue and neovasculature using fluorescent small molecules and nanoparticles, Nanomedicine (London, England) 5 (2010) 715–726.

[126] S. Ganesh, A.K. Iyer, J. Weiler, D.V. Morrissey, M.M. Amiji, Combination of siRNA-directed Gene Silencing With Cisplatin Reverses Drug Resistance in Human Non-small Cell Lung Cancer, Molecular therapy. Nucleic acids 2 (2013) e110.

[127] R.D. Klausner, G. Ashwell, J. van Renswoude, J.B. Harford, K.R. Bridges, Binding of apotransferrin to K562 cells: explanation of the transferrin cycle, Proceedings of the National Academy of Sciences of the United States of America 80 (1983) 2263–2266.

[128] M.D. Kleven, S. Jue, C.A. Enns, Transferrin Receptors TfR1 and TfR2 Bind Transferrin through Differing Mechanisms, Biochemistry 57 (2018) 1552–1559.

[129] A.P. West, M.J. Bennett, V.M. Sellers, N.C. Andrews, C.A. Enns, P.J. Bjorkman, Comparison of the interactions of transferrin receptor and transferrin receptor 2 with transferrin and the hereditary hemochromatosis protein HFE, The Journal of biological chemistry 275 (2000) 38135–38138.

[130] S.E. Lupold, B.J. Hicke, Y. Lin, D.S. Coffey, Identification and characterization of nuclease-stabilized RNA molecules that bind human prostate cancer cells via the prostate-specific membrane antigen, Cancer research 62 (2002) 4029–4033.

[131] B.S. Hendriks, S.G. Klinz, J.G. Reynolds, C.W. Espelin, D.F. Gaddy, T.J. Wickham, Impact of tumor HER2/ERBB2 expression level on HER2-targeted

liposomal doxorubicin-mediated drug delivery: multiple low-affinity interactions lead to a threshold effect, Molecular cancer therapeutics 12 (2013) 1816–1828.

[132] D. Lakayan, R. Haselberg, R. Gahoual, G.W. Somsen, J. Kool, Affinity profiling of monoclonal antibody and antibody-drug-conjugate preparations by coupled liquid chromatography-surface plasmon resonance biosensing, Anal Bioanal Chem 410 (2018) 7837–7848.

[133] U.B. Nielsen, D.B. Kirpotin, E.M. Pickering, K. Hong, J.W. Park, M. Refaat Shalaby, Y. Shao, C.C. Benz, J.D. Marks, Therapeutic efficacy of anti-ErbB2 immunoliposomes targeted by a phage antibody selected for cellular endocytosis, Biochimica et biophysica acta 1591 (2002) 109–118.

[134] M. Horikawa, Y. Shigeri, N. Yumoto, S. Yoshikawa, T. Nakajima, Y. Ohfune, Syntheses of potent Leu-enkephalin analogs possessing beta-hydroxy-alpha,alpha-disubstituted-alpha-amino acid and their characterization to opioid receptors, Bioorganic & medicinal chemistry letters 8 (1998) 2027–2032.

[135] L. Terenius, A. Wahlström, G. Lindeberg, S. Karlsson, U. Ragnarsson, Opiate receptor affinity of peptides related to Leu-enkephalin, Biochemical and biophysical research communications 71 (1976) 175–179.

[136] C.L. Esposito, D. Passaro, I. Longobardo, G. Condorelli, P. Marotta, A. Affuso, V. de Franciscis, L. Cerchia, A neutralizing RNA aptamer against EGFR causes selective apoptotic cell death, PloS one 6 (2011) e24071.

[137] C. Chen, J. Ke, X.E. Zhou, W. Yi, J.S. Brunzelle, J. Li, E.-L. Yong, H.E. Xu, K. Melcher, Structural basis for molecular recognition of folic acid by folate receptors, Nature 500 (2013) 486–489.

[138] D. Bhattacharya, D. Svechkarev, J.J. Souchek, T.K. Hill, M.A. Taylor, A. Natarajan, A.M. Mohs, Impact of structurally modifying hyaluronic acid on CD44 interaction, Journal of materials chemistry. B 5 (2017) 8183–8192.

[139] L.-K. Liu, B.C. Finzel, Fragment-based identification of an inducible binding site on cell surface receptor CD44 for the design of protein-carbohydrate interaction inhibitors, Journal of medicinal chemistry 57 (2014) 2714–2725.

[140] W. Wang, Q. Wu, M. Pasuelo, J.S. McMurray, C. Li, Probing for integrin alpha v beta3 binding of RGD peptides using fluorescence polarization, Bioconjugate chemistry 16 (2005) 729–734.

[141] Y. Zheng, S. Ji, A. Czerwinski, F. Valenzuela, M. Pennington, S. Liu, FITC-conjugated cyclic RGD peptides as fluorescent probes for staining integrin αvβ3/αvβ5 in tumor tissues, Bioconjugate chemistry 25 (2014) 1925–1941.

[142] S. Ji, A. Czerwinski, Y. Zhou, G. Shao, F. Valenzuela, P. Sowiński, S. Chauhan, M. Pennington, S. Liu, (99m)Tc-Galacto-RGD2: a novel 99mTc-labeled cyclic RGD peptide dimer useful for tumor imaging, Molecular pharmaceutics 10 (2013) 3304–3314.

[143] L. Wang, J. Shi, Y.-S. Kim, S. Zhai, B. Jia, H. Zhao, Z. Liu, F. Wang, X. Chen, S. Liu, Improving tumor-targeting capability and pharmacokinetics of (99m)Tc-labeled cyclic RGD dimers with PEG(4) linkers, Molecular pharmaceutics 6 (2009) 231–245.

[144] J. Shi, L. Wang, Y.-S. Kim, S. Zhai, Z. Liu, X. Chen, S. Liu, Improving tumor uptake and excretion kinetics of 99mTc-labeled cyclic arginine-glycine-aspartic (RGD) dimers with triglycine linkers, Journal of medicinal chemistry 51 (2008) 7980–7990.

[145] S. Wang, E.E. Dormidontova, Nanoparticle design optimization for enhanced targeting: Monte Carlo simulations, Biomacromolecules 11 (2010) 1785–1795.

[146] M.R. Caplan, E.V. Rosca, Targeting drugs to combinations of receptors: a modeling analysis of potential specificity, Annals of biomedical engineering 33 (2005) 1113–1124.

[147] N.A. Licata, A.V. Tkachenko, Kinetic limitations of cooperativity-based drug delivery systems, Physical review letters 100 (2008) 158102.

[148] A. Quintana, E. Raczka, L. Piehler, I. Lee, A. Myc, I. Majoros, A.K. Patri, T. Thomas, J. Mulé, J.R. Baker, Design and function of a dendrimer-based therapeutic nanodevice targeted to tumor cells through the folate receptor, Pharmaceutical research 19 (2002) 1310–1316.

[149] F. Danhier, B. Vroman, N. Lecouturier, N. Crokart, V. Pourcelle, H. Freichels, C. Jérôme, J. Marchand-Brynaert, O. Feron, V. Préat, Targeting of tumor endothelium by RGD-grafted PLGA-nanoparticles loaded with paclitaxel, Journal of controlled release official journal of the Controlled Release Society 140 (2009) 166–173.

[150] C.B. Carlson, P. Mowery, R.M. Owen, E.C. Dykhuizen, L.L. Kiessling, Selective tumor cell targeting using low-affinity, multivalent interactions, ACS chemical biology 2 (2007) 119–127.

[151] A. Myc, A.K. Patri, J.R. Baker, Dendrimer-based BH3 conjugate that targets human carcinoma cells, Biomacromolecules 8 (2007) 2986–2989.

[152] J. Huskens, Models and Methods in Multivalent Systems, in: J. Huskens, L.J. Prins, R. Haag, B.J. Ravoo (Eds.), Multivalency, Wiley, 2018, pp. 23–74.

[153] G. Vauquelin, S.J. Charlton, Exploring avidity: understanding the potential gains in functional affinity and target residence time of bivalent and heterobivalent ligands, British journal of pharmacology 168 (2013) 1771–1785.

[154] W.C.W. Chan, Principles of Nanoparticle Delivery to Solid Tumors, BME Front 4 (2023).

[155] A.S. Drozdov, P.I. Nikitin, J.M. Rozenberg, Systematic Review of Cancer Targeting by Nanoparticles Revealed a Global Association between Accumulation in Tumors and Spleen, International journal of molecular sciences 22 (2021).

[156] M.P. Monopoli, D. Walczyk, A. Campbell, G. Elia, I. Lynch, F.B. Bombelli, K.A. Dawson, Physical-chemical aspects of protein corona: relevance to in vitro and in vivo biological impacts of nanoparticles, Journal of the American Chemical Society 133 (2011) 2525–2534.

[157] C.D. Walkey, J.B. Olsen, H. Guo, A. Emili, W.C.W. Chan, Nanoparticle size and surface chemistry determine serum protein adsorption and macrophage uptake, Journal of the American Chemical Society 134 (2012) 2139–2147.

[158] Y. Huai, M.N. Hossen, S. Wilhelm, R. Bhattacharya, P. Mukherjee, Nanoparticle Interactions with the Tumor Microenvironment, Bioconjugate chemistry 30 (2019) 2247–2263.

[159] Z.P. Lin, L.N.M. Nguyen, B. Ouyang, P. MacMillan, J. Ngai, B.R. Kingston, S.M. Mladjenovic, W.C.W. Chan, Macrophages Actively Transport Nanoparticles in Tumors After Extravasation, ACS nano 16 (2022) 6080–6092.

[160] M.A. Miller, R. Chandra, M.F. Cuccarese, C. Pfirschke, C. Engblom, S. Stapleton, U. Adhikary, R.H. Kohler, J.F. Mohan, M.J. Pittet, R. Weissleder, Radiation therapy primes tumors for nanotherapeutic delivery via macrophage-mediated vascular bursts, Science translational medicine 9 (2017).

[161] M.A. Miller, Y.-R. Zheng, S. Gadde, C. Pfirschke, H. Zope, C. Engblom, R.H. Kohler, Y. Iwamoto, K.S. Yang, B. Askevold, N. Kolishetti, M. Pittet, S.J. Lippard, O.C. Farokhzad, R. Weissleder, Tumour-associated macrophages act as a slow-release reservoir of nano-therapeutic Pt(IV) pro-drug, Nature communications 6 (2015) 8692.

[162] Q. Dai, S. Wilhelm, D. Ding, A.M. Syed, S. Sindhwani, Y. Zhang, Y.Y. Chen, P. MacMillan, W.C.W. Chan, Quantifying the Ligand-Coated Nanoparticle Delivery to Cancer Cells in Solid Tumors, ACS nano 12 (2018) 8423–8435.

[163] D. Kovács, N. Igaz, A. Marton, A. Rónavári, P. Bélteky, L. Bodai, G. Spengler, L. Tiszlavicz, Z. Rázga, P. Hegyi, C. Vizler, I.M. Boros, Z. Kónya, M. Kiricsi, Core-

shell nanoparticles suppress metastasis and modify the tumour-supportive activity of cancer-associated fibroblasts, Journal of nanobiotechnology 18 (2020) 18.

[164] O. Zimmer, M. Walter, M. Remmert, O. Maier, R. Witzgall, A. Goepferich, Impact of interferon-γ on the target cell tropism of nanoparticles, Journal of controlled release official journal of the Controlled Release Society 362 (2023) 325–341.

[165] L. van der Zee, A. Corzo Remigio, L.W. Casey, I. Purwadi, J. Yamjabok, A. van der Ent, G. Kootstra, M.G.M. Aarts, Quantification of spatial metal accumulation patterns in Noccaea caerulescens by X-ray fluorescence image processing for genetic studies, Plant methods 17 (2021) 86.

[166] H.A. Miller, A.W. Magsam, A.W. Tarudji, S. Romanova, L. Weber, C.C. Gee, G.L. Madsen, T.K. Bronich, F.M. Kievit, Evaluating differential nanoparticle accumulation and retention kinetics in a mouse model of traumatic brain injury via Ktrans mapping with MRI, Scientific reports 9 (2019) 16099.

Chapter 2

Goals of the Thesis

Targeted delivery of active compounds to an intended site of action is a most desirable goal pursued in the field of pharmaceutics. One approach employed to achieve this goal is the use of targeted nanoparticles. These particles are typically decorated with ligand molecules on their surface. Thereby, the particles are enabled to interact with target site specific cell surface receptors In this way, one aims to achieve target site specific particle accumulation, while avoiding particle deposition at off-target sites. This concept may appear straightforward and easily implementable. However, thorough research on the use of targeted nanoparticles revealed manyfold challenges in their design. Also, a vast number of particle properties as well as physiological factors affecting particle distribution in biological systems were previously identified. Despite these efforts, our understanding of nanoparticle behavior in biological environments remains incomplete. Advances to fill this knowledge gap would be highly relevant as it undermines the predictability of nanoparticle biodistribution.

Via a thorough review of the available literature on the interplay of nanoparticle avidity and in vivo biodistribution, we intended to investigate how these two parameters correlate with each other. In summary, this study has shown that the effect that avidity exerts on nanoparticle biodistribution must be considered unclear. Increasing particle avidity was not found to consistently result in a more desirable particle distribution (i.e., increased accumulation at target sites and/or decreased occurrence at off-target sites). As this observation is, in our view, in contrast to the theories underlying avidity, it gave rise to an urgent research need **(Chapter 1)**. We felt that basic research was essential to improve our understanding of the interactions between nanoparticles and cells to help resolve this apparent contradiction. Concretely, we decided that research into membrane properties affecting the attachment of ligand-functionalized nanoparticles was necessary, as this area must be acknowledged as under-researched. To foster the practical relevance of our work, we further aimed to identify and characterize biological factors determining relevant membrane properties in vivo.

Pursuing the first formulated goal of our work, we hypothesized curvature alignment of particle and membrane surface as beneficial for the formation of ligand-receptor bond. Hence, such an alignment could boost particle avidity. In our studies, we investigated a particle model system capable of binding to rat mesangial cells via the AT_1 receptor. This receptor is particularly associated with clathrin-coated pits (CCPs). We therefore

specified our hypothesis for the model system under investigation in the sense that CCPs should be a major determinant of avidity. We further considered this hypothesis plausible as the dimensions of CCPs closely match our particles geometry. Thus, a relevant degree of curvature alignment could be expected. To investigate this hypothesis, we identified a small-molecular tool kit enabling us to alter membrane curvature in a controlled manner. Using a functional binding assay measuring the receptor specific cell response to AT_1R activation, allowed us to study particle attachment on living cells **(Chapter 3, *SI: Chapter 4*)**.

The studies on the first goal of this thesis were intended to improve our understanding of particle-membrane interactions. However, as “artificial” tools were employed to alter membrane properties, we aimed to conduct further research underpinning the biological relevance of the findings made. The question arose as to whether conditions similar to those in our experiments could actually occur in biological systems. Inspiration for further research came from the field of virology. Here, it had long been known that cytokines like Interferon-γ (IFN-γ) to affect viral tropism (i.e., viral ability to accumulate in compartments allowing their replication). Given the similarity of viral pathogens and targeted nanoparticles regarding the strategy of ligand-receptor mediated target cell recognition as well as size and geometry, we hypothesized IFN-γ to exert comparable effects on nanoparticles. To investigate this hypothesis, we designed a target/off-target cell culture model system, allowing us to quantitatively investigate particle distribution via flow cytometry. To allow transferability of our findings, we employed the same model particle system as in our investigations on the role of CCPs in particle membrane attachment. For the same reason, we chose rat mesangial cells as the target cell population in our co-cultures. We investigated particle distribution at varying target cell densities. This way we aimed to mimic the situation of a particle far from its target site (low target cell density) and in close proximity or within its target site (high target cell density). To study the effect of IFN-γ we conducted particle distribution assays in presence and absence of IFN-γ concentrations typical for tumor tissues **(Chapter 5, *SI: Chapter 6*)**.

Finally, we were keen to further elaborate on the mechanism underlying the observations made in our experimental studies. Specifically, the question we faced was whether depletion binding sites at the nanoscale could indeed trigger relevant changes in particle behavior at a micrometer scale. This would be in fact the relevant scale for

particle distribution in a cellular system. As we had no experimental method at hand to investigate this matter, we decided to turn towards computational simulation. We used the VCell software package to design a simple geometrical model consisting of one target cell and one off-target cell within a closed simulation box. Also, a particle entity was defined as well as a high-avidity binding site resembling the CCPs. We next assigned reactions to the individual elements of the model (e.g., attachment of a particle to a CCP). Using a deterministic spatial solver, it was possible to derive extracellular particle concentrations, target- and off-target cell-uptake over time. Based on partial derivatives of the polynomial functions fitted to the extracellular concentration gradients, it was possible to calculate vector fields. These vector fields allowed us to study the effects of CCP depletion on particle movement on the micrometer-scale in detail **(Chapter 7)**.

Chapter 3

How Clathrin-Coated Pits Control Nanoparticle Avidity for Cells

Published in *Nanoscale Horizons*

2023, **8**, 256-269

This chapter was published as: O. Zimmer, A. Goepferich, How clathrin-coated pits control nanoparticle avidity for cells. *Nanoscale horizons* 8, 256–269 (2023).

Abstract

The paramount relevance of clathrin-coated pits (CCPs) to receptor-mediated endocytosis of nanoparticles, extracellular vesicles, and viruses has made them the focus of many studies; however, the role of CCP geometry in the ligand–receptor interactions between multivalent nanoparticles and cells has not been investigated. We hypothesized the general dependence of nanoparticle binding energy on local membrane curvature to be expandable to the specific case of ligand-functionalized nanoparticles binding cell membranes, in the sense that membrane structures whose curvature matches that of the particle (e.g., CCPs) significantly contribute to binding avidity. We investigated this hypothesis with nanoparticles that bind multivalently to angiotensin II receptor type 1, which is subject to clathrin-mediated endocytosis. When we used cholesterol extraction to prevent the action of CCPs, we found a 67 to 100-fold loss in avidity. We created a theoretical model that predicts this decrease based on the loss of ligand–receptor interactions when CCPs, which perfectly match nanoparticle geometry, are absent. Our findings shed new light on how cells “see” nanoparticles. The presence or absence of CPPs is so influential on how cells interact with nanoparticles that the number of particles required to be visible to cells changes by two orders of magnitude depending on CCP presence.

Graphical Abstract

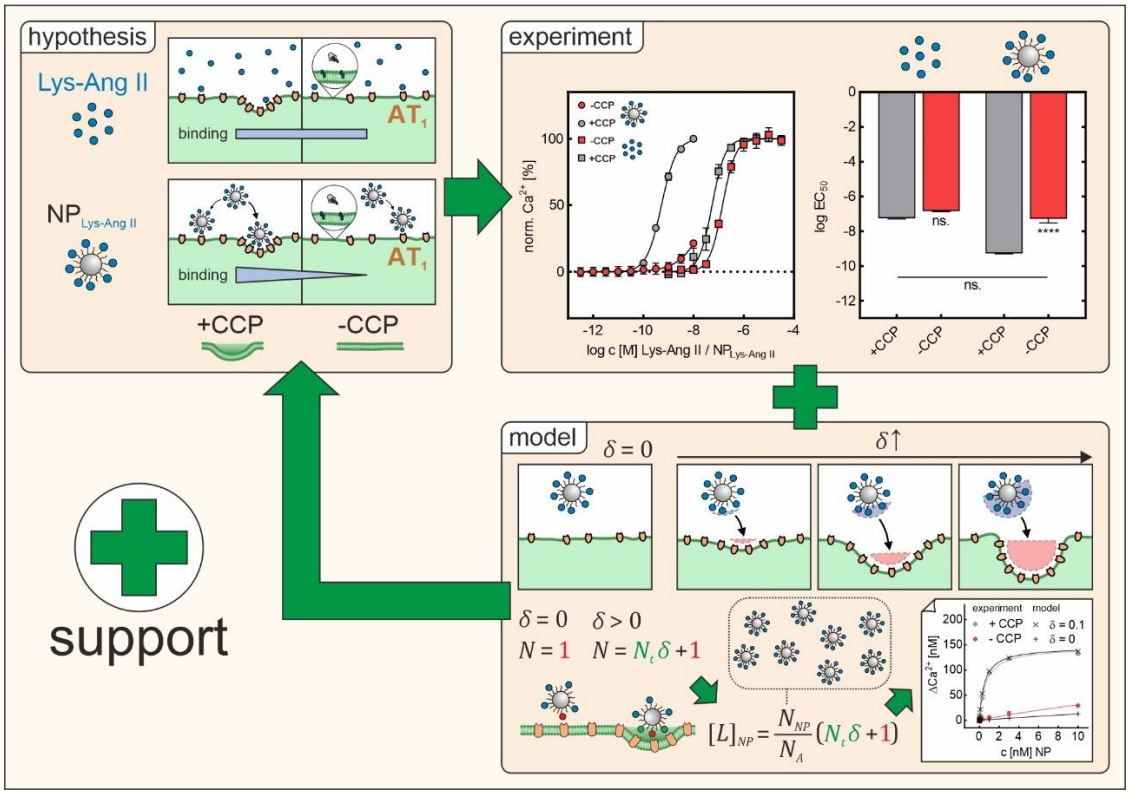

The graphical abstract illustrates how in the studies presented in this chapter, derived from the initial hypothesis, experimental investigations and theoretical modelling were conducted to test and to provide supportive evidence for the hypothesis. This approach revealed clathrin-coated pits as binding hotspots for nanoparticles, as they predominantly dictate particle avidity.

Introduction

Cell–nanoparticle interactions have been extensively investigated. This is because these interactions, as a crucial step of ligand–receptor-mediated target cell recognition by nanoparticles, are of outstanding importance for the development of targeted nanotherapeutics and the understanding of phenomena such as extracellular vesicle signaling and viral infections. Numerous investigations of size [1–5], shape [1,2,4], surface charge [2,4,6], receptor–ligand density and mobility [2,7–9], linker characteristics [7,9], and hetero-multivalency [10,11] have yielded a detailed picture of the avidity that nanoparticles have for cells, but surprisingly little attention has been given to the cell membrane structures that participate in particle identification and binding. A better understanding of these processes would be very beneficial to the development of novel nanotherapeutics because high binding avidity is key when designing targeted nanoparticles that are highly selective and specific [12]. To date, we have only a vague understanding of the impact of clathrin-coated pit (CCP) geometry on cell-nanoparticle interactions. Studies that have attempted to close this gap using supported lipid bilayers (SLBs) as model systems [13–15] were unsuccessful because the nanoscale invaginations are not maintained during SLB preparation.

The problem intensifies when nanoparticles carry ligands for cell surface receptors, making it possible that they will bind multivalently through several simultaneous ligand–receptor interactions [16]. When the receptor in question is subject to clathrin-mediated endocytosis it may be located on flat membrane sections or in CCPs, which are highly dynamic structures that undergo constant morphological changes [17]. Bucher *et al*. describe three morphological states during early- and late CCP maturation [18]. The flat, dome, and pit morphologies (Fig. 1) differ in surface area, membrane curvature, and clathrin lattice composition. CCP geometry has been described according to the constant area [19] and the constant curvature [20–22] approach. It was found that, on average, 20% CCPs have dome morphology [23]. We hypothesized that these dome-shaped CCPs should have a tremendous impact on nanoparticle binding to cells because dome morphology corresponds perfectly to the size and shape of most studied nanoparticles (spherical geometry, $d < 100$ nm) [24]. Receptors located in CCPs [25] with shapes complementary to nanoparticles should maximize the contact area between cell membrane and nanoparticle corona, yielding the highest possible number of receptor–ligand-interactions and significantly increasing nanoparticle avidity [26–28].

In the general context of nanoparticle membrane interactions Agudo-Canalejo *et al*., Yu *et al*., Deserno and Bickel, and Bahrami *et al*. have provided excellent work on the process of particle membrane wrapping, including investigations of the initial attachment of nanoparticles to membranes. Considering this initial attachment, the aforementioned works found that a membrane curved towards a particle will require a lower bending energy to be overcome during binding. Consequently, a lower adhesion strength will be sufficient for a particle to bind, or assuming a constant adhesion strength, more particles will bind to a membrane curved towards them. With these findings the groups provide a main body of fundamental knowledge about particle membrane interactions acquired to date [29–33]. Barbul *et al*. conducted simulations suggesting that multivalent nanoparticle binding can induce partial membrane wrapping [34]. Our approach in the present work differs insofar as our focus is on the study of multivalent ligand-functionalized nanoparticles and thus adds a parameter not fully investigated so far. We want to point out that our focus further differs from the aforementioned works by investigating the effect of the presence or absence of CCPs as particular geometrical entities spontaneously occurring [35] in the membrane.

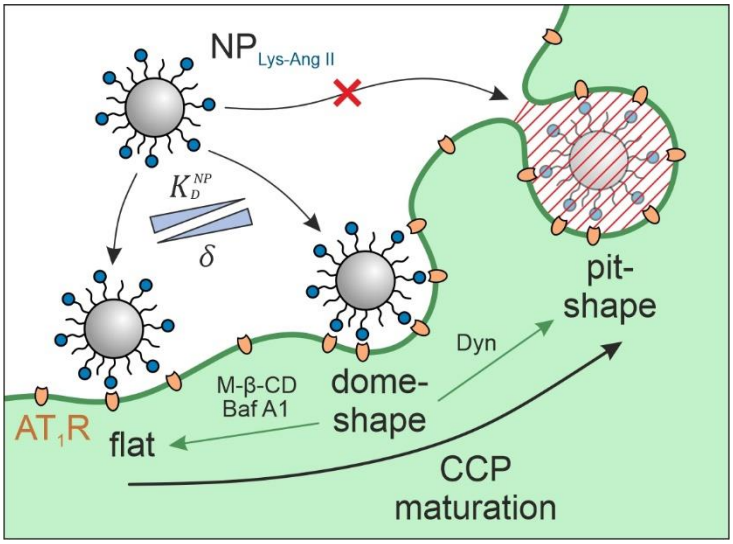

Figure 1: Interplay of membrane morphology and particle binding. The scheme illustrates the main maturation stages of clathrin-coated pits (CCPs). Flat structures initially undergo a transformation to dome-shaped CCPs. These, in turn, become more and more indented until a pit-shaped morphology is obtained. It is shown what effect the inhibitors used (M-β-CD, Baf A1, and Dyn; green arrows indicate the induced CCP morphology) have with respect to CCP maturation. The aim of the present study was to investigate the influence of the presence of membrane structures with high wrapping fraction δ for particles (e.g., dome-shaped CCPs) on the avidity K_D^{NP} of these particles. Abbveriations: $NP_{Lys\text{-}Ang\,II}$ – angiotensin II-functionalized nanoparticle, AT_1R – angiotensin II receptor subtype 1, M-β-CD – methyl-β-cyclodextrin, Baf A1 – bafilomycin A1, Dyn – dynasore.

To confirm our hypothesis, we investigated the avidity of receptor binding nanoparticles for their target cells in the presence and absence of CCPs invaginations. We depleted cell membranes of cholesterol, which increases membrane stiffness and enforces a flat CCP morphology [35,36]. To investigate the impact of CCP geometry on nanoparticle avidity, we used particles carrying angiotensin II ($NP_{Lys\text{-}Ang\,II}$) in their corona, which enables them to multivalently bind to the CCP-associated angiotensin II receptor type 1 (AT_1R) [37]. This receptor is present on rat mesangial cells, which were used for binding studies performed with and without several potent inhibitors of pit formation: methyl-β-cyclodextrin (M-β-CD), bafilomycin A1 (Baf A1), and dynasore (Dyn). M-β-CD extracts cholesterol from cell membranes [38,39]. M-β-CD induces a strong shift in the frequency distribution of the different maturation stages of CCPs. In untreated

cells, most CCPs in the membrane are present at intermediate or late maturation stages. Thus, the membrane is highly indented and dome-shaped and pit-shaped CCPs are present. Treatment with M-β-CD results in stopping almost all CCPs at early maturation stages, where the membrane has very shallow or no invaginations. The proportion of dome- and pit-shaped CCPs is significantly reduced [35,36,40]. Baf A1 is a specific inhibitor of vacuolar-type H^+ ATPase (VATPase) that inhibits pH-dependent lysosomal cholesterol transport, thus reducing intracellular cholesterol trafficking [41]. Similar to M-β-CD, inhibition of VATPase by Baf A1 was shown to almost completely eliminate the population of dome-shaped CCPs after treatment. The CCPs are predominantly present at earlier maturation stages, thus showing very little invagination and a significantly increased neck width [40,42,43]. Dyn is a potent inhibitor of dynamin GTPase that additionally hinders intracellular cholesterol trafficking and freezes CCPs late in their maturation phase. Thus, in terms of its effect on CCP morphology, Dyn has the opposite effect to M-β-CD and Baf A1. It accumulates late-stage CCPs that are about to undergo dynamin-induced pinching off from the membrane. The neck is already very narrow, and the membrane is deeply invaginated [44–46]. Along with this experimental data, we developed a theoretical model to predict the avidity change in the presence and absence of pits. It describes nanoparticle avidity (K_D^{NP}) as a function of ligand affinity (K_D^L) and the nanoparticle wrapping fraction (δ) between the nanoparticle corona and cell membrane structure. Overall, the intention of our experimental and theoretical work was to explore the impact of CCP geometry on nanoparticle avidity for target cells. Hereby, we aim to better understand the nano-bio interactions between ligand-functionalized nanoparticles and cell receptors, which is a crucial question in the rational development of nanotherapeutics [47–51].

Results

Cholesterol depletion of cell membranes decreases nanoparticle avidity for cells

For our binding experiments, we used a particle system well established in our group based on a core-shell design. A poly(ethylene glycol)-b-poly(D,L-lactide) (PEG-PLA)/poly(D,L-lactide-co-glycolide) (PLGA)-based particle was prepared. For this, a carboxy-terminated PEG-PLA polymer (carboxy-PEG-PLA) was synthesized via DBU catalyzed ring-opening polymerization of lactide on a carboxy-PEG starter. Ligand functionalization was performed by coupling Lys-Ang II to carboxy-PEG-PLA prior to particle preparation using EDC/NHS chemistry (Lys-Ang II-PEG-PLA). Coupling efficiency for Lys-Ang II-PEG-PLA and degree of ligand functionalization for $NP_{Lys\text{-}Ang\,II}$ was quantified using Pierce BCA and iodine assay. Synthesized carboxy-PEG-PLA was characterized via ^{1}H-NMR. $NP_{Lys\text{-}Ang\,II}$ size was determined via DLS (Fig. S2, also refer to experimental section for detailed specifications). The size of our particle $NP_{Lys\text{-}Ang\,II}$ was in good agreement with the dimensions of CCPs regarding depth and neck width [42] as wells as curvature [52] and found to be in range with dimensions of dome-shaped CCPs.

To investigate the role of CCPs in the binding of ligand-functionalized nanoparticles to cells, we incubated AT_1R-positive rat mesangial cells (rMCs) [53] with angiotensin II-decorated nanoparticles. The binding studies consisted of four sub-experiments, in which the binding of free ligand (Lys-Ang II) and ligand-functionalized nanoparticles $NP_{Lys\text{-}Ang\,II}$ was assessed in the absence and presence of CCP inhibitors [38,43,44].

We found the Fura-2 AM based Ca^{2+} mobilization assay to be best suited for our binding experiments as it enables us to directly compare the binding data found for the free ligand with the data for our ligand functionalized nanoparticle due to the identical readout. The interaction of Ang II with the AT_1 receptor induces the activation of phospholipase C, which in turn catalyzes the formation of diacylglycerol (DAG) and inositol trisphosphate (IP_3) [54]. The latter induces the intracellular release of Ca^{2+} from the endoplasmic reticulum (ER) [55].

Since we use $NP_{Lys\text{-}Ang\ II}$-AT_1R binding-induced Ca^{2+} response as a measure of the interaction of $NP_{Lys\text{-}Ang\,II}$ with rMCs in our binding assays, it is of paramount importance

to demonstrate that this response is solely due to the specific ligand-receptor interaction. This is particularly important as it has previously been shown that nanoparticles can also non-specifically induce Ca^{2+} influx into cells due to cytotoxic effects [56]. To investigate this, two control experiments were necessary: (1) We tested an unfunctionalized nanoparticle (NP_{COOH}) that was otherwise identical to $NP_{Lys\text{-}Ang\ II}$ using the Fura-2 AM-based Ca^{2+} assay. (2) We tested $NP_{Lys\text{-}Ang\ II}$ in a Fura-2 AM based Ca^{2+} assay but had incubated the rMCs with AT_1R antagonist Exp3174 in advance. There was no Ca^{2+} response in either of these experiments (Fig. 2A). Thus, in conjunction, these experiments demonstrate that no nonspecific Ca^{2+} influx is triggered by NP_{COOH} and that Ca^{2+} influx induced by $NP_{Lys\text{-}Ang\ II}$ results exclusively from the specific interaction of Lys-Ang II and AT_1R. For both experiments (Fig. 2B), control data demonstrate that Fura-2 AM loading was successful (Fig. 2A) and that an intracellular Ca^{2+} increase thus would have been detectable.

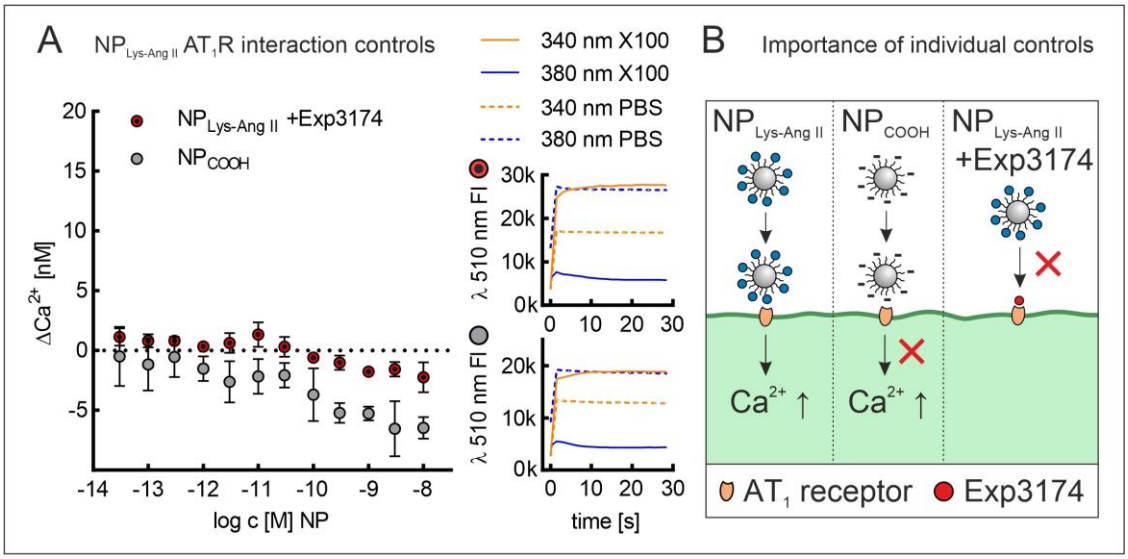

Figure 2: Control experiments demonstrate specificity of Ca^{2+} signal for $NP_{Lys\text{-}Ang\ II}$-AT_1R interaction. (A) Data obtained from Ca^{2+} mobilization assays conducted using non-functionalized nanoparticle NP_{COOH} (grey symbols) and $NP_{Lys\text{-}Ang\ II}$ (red symbols with black sphere) on Exp3174 pre-incubated rMCs. For both experiments investigating $NP_{Lys\text{-}Ang\ II}$ +Exp3175 and NP_{COOH}, controls of rMCs exposed to Triton X-100 demonstrated successful Fura-2 AM loading. (B) Scheme illustrates the concept of our control experiment setup intended to confirm specificity of Ca^{2+} signal for $NP_{Lys\text{-}Ang\ II}$-AT_1R interaction.

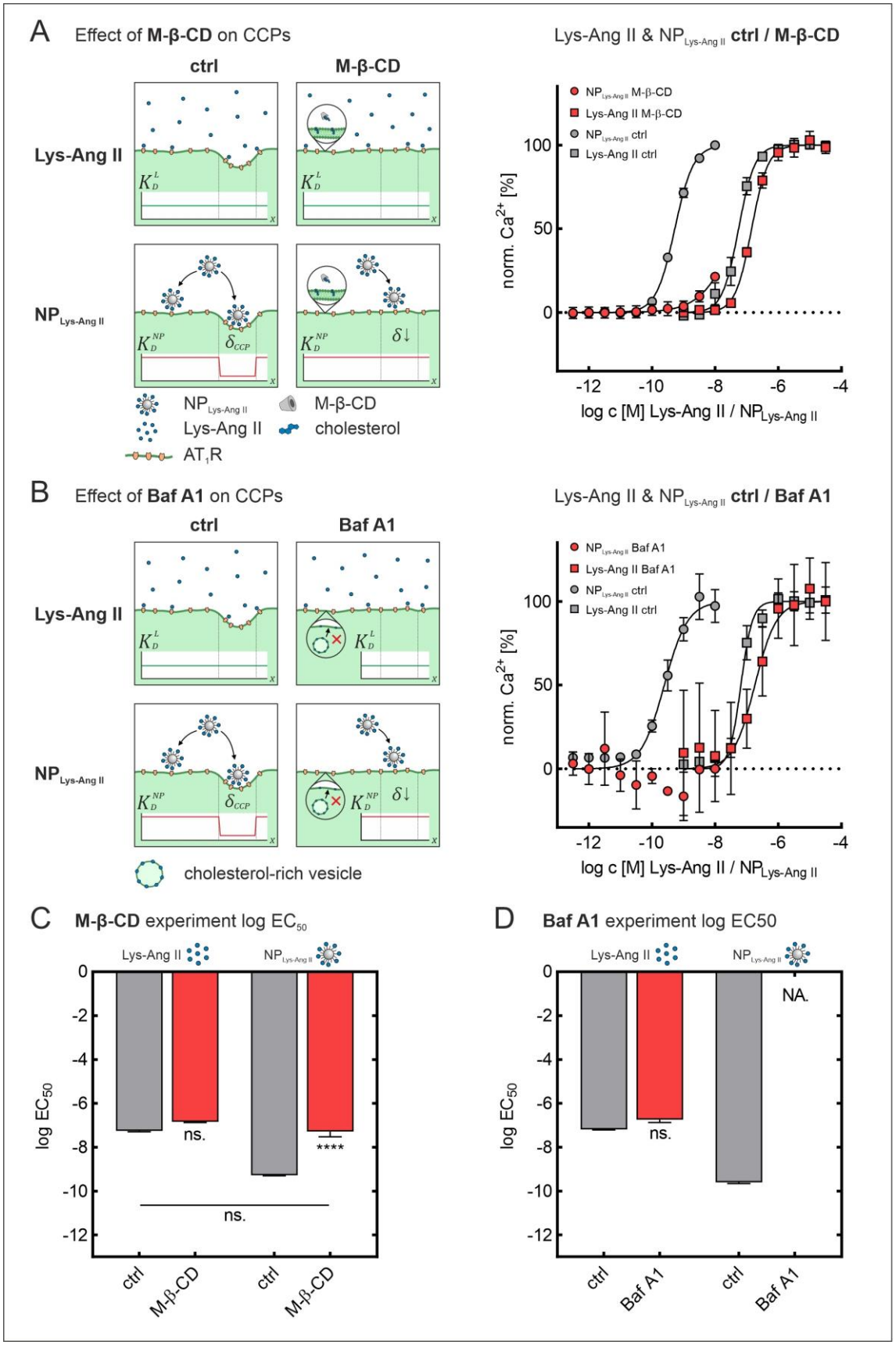
A
Effect of M-β-CD on CCPs
ctrl
M-β-CD
Lys-Ang II
NP Lys-Ang II
NP Lys-Ang II
Lys-Ang II
AT1R
M-β-CD
cholesterol
Lys-Ang II & NP Lys-Ang II ctrl / M-β-CD
NP Lys-Ang II M-β-CD
Lys-Ang II M-β-CD
NP Lys-Ang II ctrl
Lys-Ang II ctrl
norm. Ca2+ [%]
log c [M] Lys-Ang II / NP Lys-Ang II
B
Effect of Baf A1 on CCPs
ctrl
Baf A1
Lys-Ang II
NP Lys-Ang II
cholesterol-rich vesicle
Lys-Ang II & NP Lys-Ang II ctrl / Baf A1
NP Lys-Ang II Baf A1
Lys-Ang II Baf A1
NP Lys-Ang II ctrl
Lys-Ang II ctrl
norm. Ca2+ [%]
log c [M] Lys-Ang II / NP Lys-Ang II
C
M-β-CD experiment log EC50
Lys-Ang II
NP Lys-Ang II
log EC50
ns.
****
ns.
ctrl
M-β-CD
ctrl
M-β-CD
D
Baf A1 experiment log EC50
Lys-Ang II
NP Lys-Ang II
log EC50
NA.
ns.
ctrl
Baf A1
ctrl
Baf A1

Figure 3: Effect of M-β-CD and Baf A1 on $NP_{Lys\text{-}Ang\,II}$ cell binding. (A) Binding curves derived from Ca^{2+} mobilization assays showing the effect of M-β-CD-induced cholesterol depletion on ligand (Ang II) and $NP_{Lys\text{-}Ang\,II}$ (NP) binding. (B) Corresponding data derived from experiments investigating effects of Baf A1 on Ang II and NP binding. Serial dilutions of the free ligand Lys-Ang II (N = 3) and $NP_{Lys\text{-}Ang\,II}$ (N = 3) were prepared and measured on Fura-2 AM-loaded rMCs (error bars reflect standard deviation). Schemes show how the employed inhibitors (M-β-CD and Baf A1) effect the membrane morphology. While M-β-CD directly extracts cholesterol from the membrane (A), Baf A1 interferes with intracellular cholesterol trafficking (B), thereby depleting the membrane from cholesterol. It is further shown, how flat CCP shape results in loss of wrapping fraction δ and what effects on dissociation constants K_D must be expected. The parameters considered were free ligand affinity K_D^L and nanoparticle avidity K_D^{NP}. As K_D is inversely proportional to affinity and avidity, it is important to note in this context that the binding experiments with $NP_{Lys\text{-}Ang\,II}$ were performed considering the molar particle concentration. Thus, the particle as a whole is considered as a single binding entity and the binding parameters found reflect its avidity. δ_{CCP} is the expected wrapping fraction for binding in a clathrin-coated pit. In theory, δ ranges from 0 to 1 (no vs. full wrapping of the particle). (C) Derived log EC_{50} values for M-β-CD experiments. (D) Corresponding data derived for Baf A1 experiments. Statistical significance was assessed via one-way ANOVA analysis with subsequent Tukey's multiple comparison test (ns. – not significant, **** – P < 0.0001; error bars reflect standard error of mean; α = 0.01, $F_{M\text{-}β\text{-}CD}$ = 226.7, $F_{Baf\ A1}$ = 339.3, $df_{M\text{-}β\text{-}CD}$ = 11, $df_{Baf\ A1}$ = 8). For the Baf A1 treatment experiment, a log EC_{50} of $NP_{Lys\text{-}Ang\,II}$ binding could not be determined because a reliable fitting of the data was not possible (NA.).

First, we investigated the effect of M-β-CD-induced cholesterol depletion on the binding intensity of Lys-Ang II and $NP_{Lys\text{-}Ang\,II}$ to cells (Fig. 3A). The EC_{50} values revealed no significant effect of M-β-CD treatment on Lys-Ang II affinity (ctrl: log EC_{50} = −7.26 ± 0.02; M-β-CD: log EC_{50} = −6.84 ± 0.02; mean ± sem), while the avidity of $NP_{Lys\text{-}Ang\,II}$ decreased significantly compared to control (ctrl) (ctrl: log EC_{50} = −9.28 ± 0.01; M-β-CD: log EC_{50} = −7.28 ± 0.14; mean ± sem) (Fig. 3C). In the context of Ca^{2+} mobilization based binding assays, our control experiments consisted throughout of testing both free Lys-Ang II and $NP_{Lys\text{-}Ang\,II}$ on untreated rMCs that were otherwise handled identically.

One concern we had regarding the results of the M-β-CD experiments was the ability of M-β-CD to complex hydrophobic molecules. In the case of complexation of particle-bound ligands by M-β-CD, a significant effect on particle binding would have been expected. Thus, the observations could also have been due to such complexation.

On the one hand, the fact that hardly any effects on the interaction of the free ligand with the rMCs were observed speaks against this possibility. In addition, we wanted to test a CCP inhibitor that would affect CCP morphology in the same way as M-β-CD but would not be able to complex particle-bound ligands. To rule out this concern, we investigated the impact of Baf A1 on Lys-Ang II and $NP_{Lys\text{-}Ang\,II}$ binding parameter $\log EC_{50}$ in binding assays on rMCs (Fig. 3B). Baf A1 inhibits CCP formation via a different mechanism of V-ATPase inhibition inducing cytosolic acidification resulting in impairment of cholesterol transport to the plasma membrane [45]. The results confirmed the observations made with M-β-CD. While no significant effect was observed for the free ligand (ctrl: $\log EC_{50}$ = −7.18 ± 0.03; Baf A1: $\log EC_{50}$ = −6.74 ± 0.14; mean ± sem). $NP_{Lys\text{-}Ang\,II}$ binding was massively reduced. The avidity of particles in the presence of Baf A1 was poor. Not even with the highest possible nanoparticle concentration was it possible to elicit enough biological effect to obtain a binding curve that allowed for the calculation of an EC_{50} value (ctrl: $\log EC_{50}$: −9.61 ± 0.05; Baf A1: exceeds limit of quantification; mean ± sem) (Fig. 3D).

Because both inhibitors act by depleting cell membranes of cholesterol, we decided to repeat the experiments with Dyn, which operates via a different mechanism. Dyn freezes CCPs in late maturation stages. Most CCPs in the membrane exhibit a strong invagination as well as a narrow neck width after Dyn treatment. The Dyn experiments are of particular importance because of this primary mechanism of action. Since M-β-CD and Baf A1 exert their effects mainly via a change in membrane cholesterol content, a change in lateral receptor mobility [57] cannot be ruled out in these cases. Due to its different mechanism of action, at least a smaller effect on receptor mobility can be assumed for Dyn treatment. The Dyn experiments supported the previous results. Again, while Lys-Ang II binding (ctrl: $\log EC_{50}$ = −6.94 ± 0.04; Dyn: $\log EC_{50}$ = −6.64 ± 0.02; mean ± sem) was unaltered, nanoparticle avidity (ctrl: $\log EC_{50}$ = −9.22 ± 0.03; Dyn: $\log EC_{50}$ = −7.39 ± 0.12; mean ± sem) was massively reduced in the Dyn-mediated absence of CCPs (Fig. 4A and B). In summary, these studies confirmed that dome-shaped CCPs are crucial for nanoparticle avidity, as their absence decreased nanoparticle binding significantly, irrespective of the type of CCP inhibitor that was used (Fig. 4C).

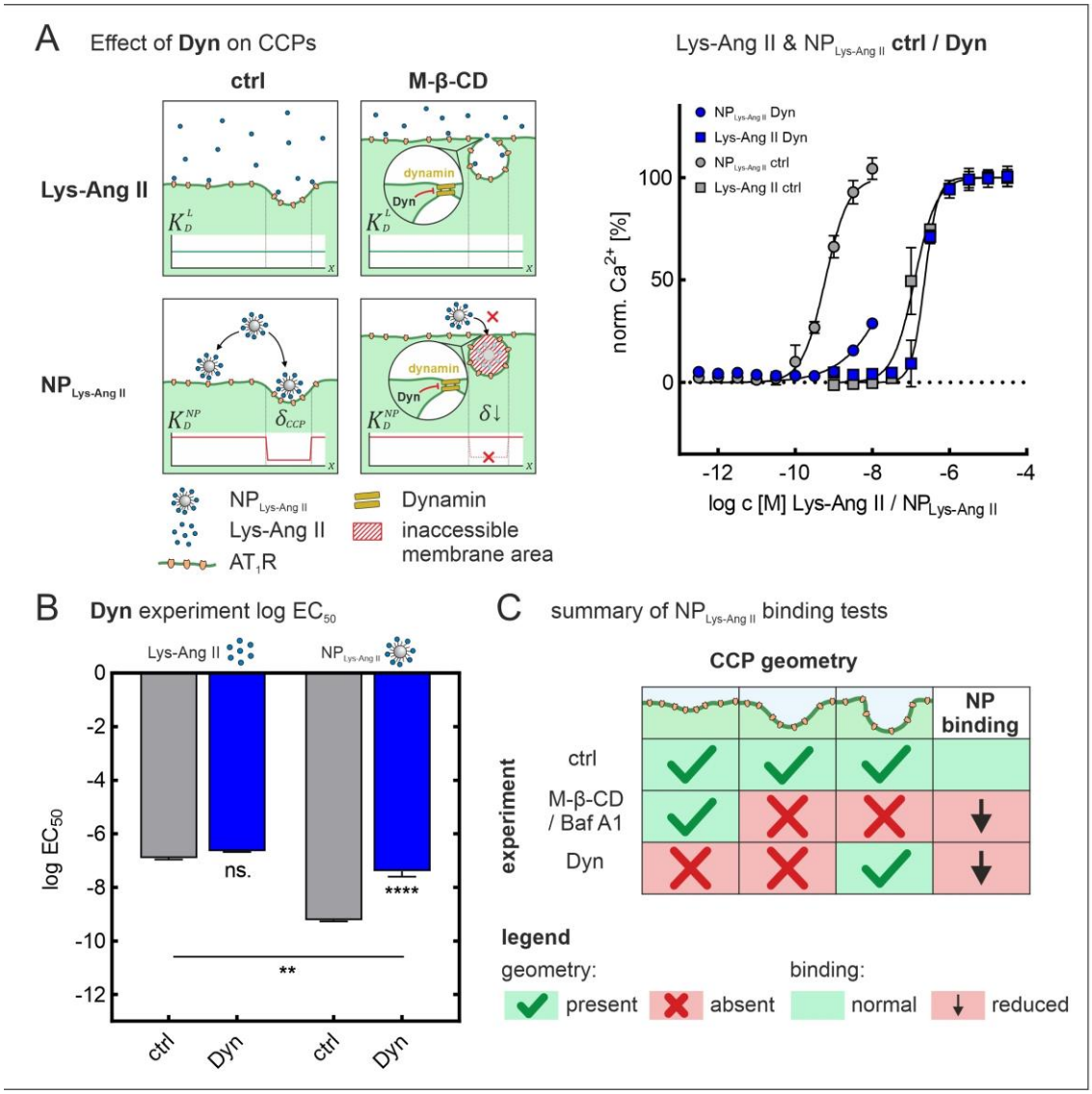

Figure 4: Effect of Dyn on $NP_{Lys\text{-}Ang\,II}$ cell binding. (A) Binding curves derived from Ca^{2+} mobilization assays showing the effect of Baf A1 on free ligand (Lys-Ang II) and $NP_{Lys\text{-}Ang\,II}$ binding to cells. Data was recorded for serial dilutions of the free ligand Lys-Ang II (N = 3) and $NP_{Lys\text{-}Ang\,II}$ (N = 3) using Fura-2 AM loaded rMCs (error-bars reflect standard deviation). Scheme gives an overview about the underlying mechanism of flattening CCP shape resulting in loss of wrapping fraction δ and expected effects dissociation constant K_D. The parameters considered were free ligand affinity K_D^L and nanoparticle avidity K_D^{NP}. As K_D is inversely proportional to affinity and avidity, it is important to note in this context that the binding experiments with $NP_{Lys\text{-}Ang\,II}$ were performed considering the molar particle concentration. Thus, the particle as a whole is considered as a single binding entity and the binding parameters found reflect its avidity. δ_{CCP} is the expected wrapping fraction for binding in a clathrin-coated pit. In theory, δ ranges from 0 to 1 (no vs. full wrapping of the particle). (B) Derived log EC_{50} values were compared via one-way ANOVA analysis with subsequent Tukey's multiple comparison test (ns. – not significant, ** – P < 0.01, **** – P < 0.0001; error-bars reflect standard-error of mean; α = 0.01, F_{Dyn} = 331.7,df_{Dyn} = 11). (C) In summary, our binding experiments allow to conclude that neither flat CCPs nor pit-shaped CCPs alone are

sufficient to recover normal binding behavior of $NP_{Lys\text{-}Ang\ II}$. Therefore, an essential role of the dome-shaped CCPs can be deduced for the attachment of our model particle system.

We demonstrated that it was possible to extract cholesterol from the membrane in a controlled manner using M-β-CD. With increasing concentration of M-β-CD, larger amounts of cholesterol were extracted (Fig. 5C). Also, based on the agreement of the results from the $NP_{Lys\text{-}Ang\ II}$ binding studies with Baf A1 and M-β-CD (Fig. 3A and B), we concluded that M-β-CD does not appear to complex the ligands on the particle surface. With these given prerequisites, we decided to further investigate the effects of cholesterol depletion on nanoparticle binding (Fig. 5A to C). To this end, we quantified the amount of cholesterol extracted from cell membranes as a function of M-β-CD concentrations (Fig. 5C and Fig. S4). We observed that M-β-CD only induced a change of EC_{50} values when its concentration was sufficiently high to reduce the cell cholesterol content (Fig. 5A and B). We noticed a strong correlation ($r^2 = 0.98$, $P = 0.011$) between the $\log EC_{50}$ value and the normalized cholesterol signal obtained (Fig. 5C and E). Our observation of decreasing nanoparticle binding with decreasing cholesterol content (Fig. 5D) is in line with findings that cholesterol depletion increases mechanical membrane stiffness [36,38,58], which, as Bucher *et al*. recently confirmed, suppresses the transition of flat clathrin-associated membrane structures to CCPs [23]. This is consistent with simulations conducted by Hassinger *et al*. Here, the effect of increased membrane tension on the formation of membrane curvature was investigated [59].

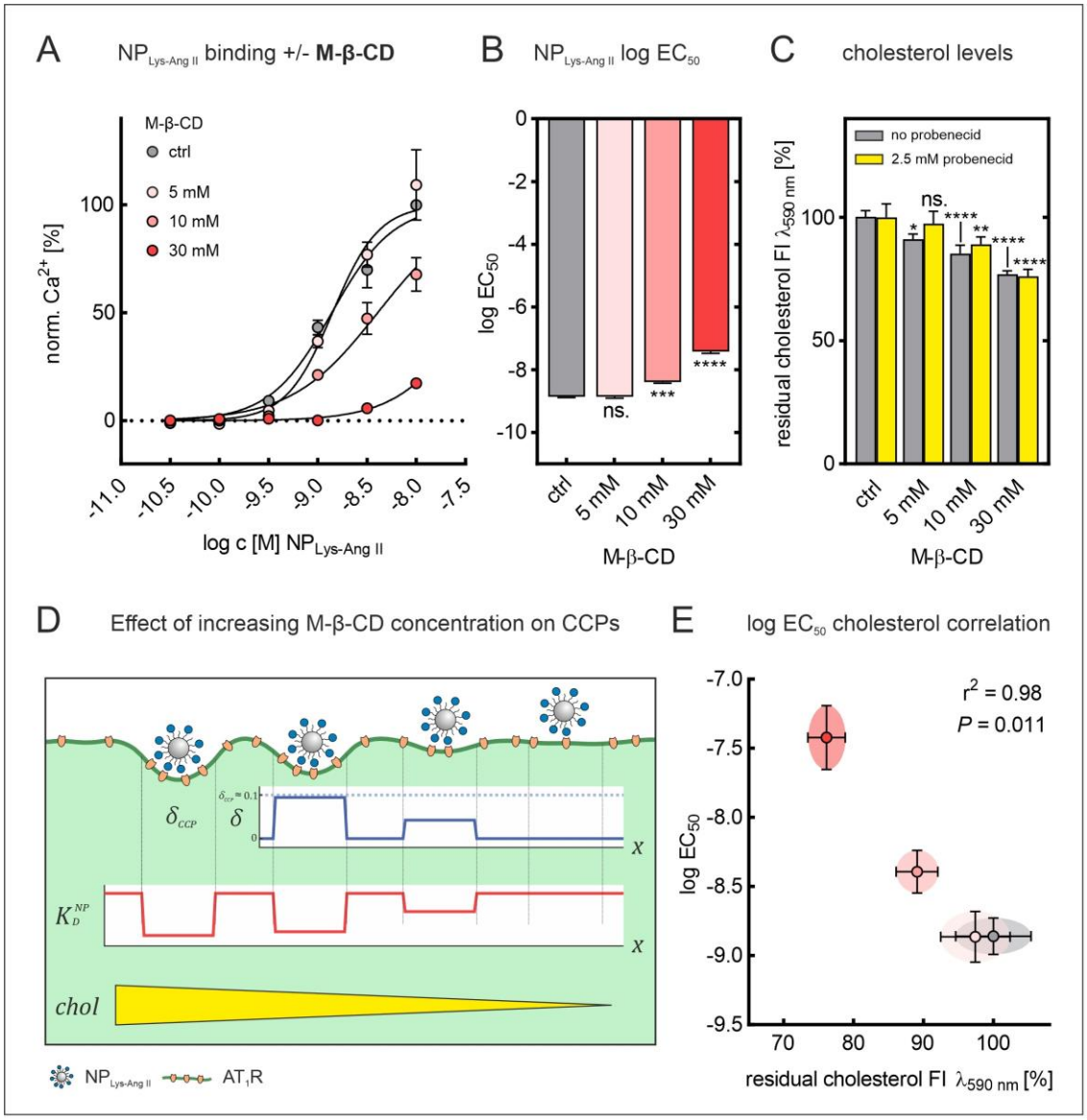

Figure 5: Cholesterol level dependence of log EC_{50} of $NP_{Lys\text{-}Ang\,II}$. (A) Binding curves derived from Ca^{2+} mobilization assay for each M-β-CD concentration (ctrl, 5, 10, and 30 mM). For each M-β-CD concentration, serial dilutions of $NP_{Lys\text{-}Ang\,II}$ (N = 3) were prepared and measured on Fura-2 AM-loaded rMCs (error bars reflect standard deviation). (B) log EC_{50} values determined for each M-β-CD concentration were compared via one-way ANOVA analysis with subsequent Tukey's multiple comparison test (ns. – not significant, *** P < 0.001, **** – P < 0.0001; error bars reflect standard error of mean; α = 0.01, F = 262.1, df = 11). (C) The graph represents the results of Amplex™ red-based cholesterol quantification experiments conducted with different concentrations of M-β-CD. As a measure for residual cholesterol, we plotted the normalized fluorescence intensity (FI) signals (λ_{em} 590 nm) determined via Amplex™ red cholesterol quantification assay conducted in presence and absence of 2.5 mM probenecid. All concentrations were investigated on sets of rMC samples (in presence and absence of 2.5 mM probenecid, each N = 4). Impact of M-β-CD on rMC cholesterol content and the effect of probenecid on M-β-CD mediated cholesterol extraction were analyzed via two-way ANOVA analysis with subsequent Tukey's multiple comparison test (* – P < 0.1, ** – P < 0.01 *** – P <

0.001, **** – P < 0.0001; error bars reflect the 95% CI; α = 0.01, F_{prob} = 3.26, $F_{M\text{-}\beta\text{-}CD}$ = 68.07, F_{int} = 1.86, df = 31). (D) Schematic illustration of the effect of different M-β-CD concentrations on wrapping fraction δ and nanoparticle avidity K_D^{NP}. δ_{max} is the highest wrapping fraction for a particular membrane section, where δ theoretically ranges from 0 to 1 (no vs. full wrapping of the particle). (E) log EC_{50} values plotted against the corresponding normalized cholesterol fluorescence signal intensities (error bars reflect the 95% CI). Pearson analysis revealed a strong inverse correlation (two-tailed, r^2 = 0.98, P = 0.011) of the two parameters.

Modelling nanoparticle binding to CCPs can predict nanoparticle avidity

To explore the impact of CCP presence on nanoparticle avidity, we developed a model that estimates the efficacy of nanoparticle binding to the cell membrane based on the nanoparticle wrapping fraction in CCPs. First, we defined the conditions for a perfect morphological alignment of nanoparticle and cell membrane. We assumed that this was the case when the nanoparticle curvature k_{NP} is equal to the membrane Gaussian curvature K_m (Fig. 6A, Supplementary Text). To account for the degree of geometrical match, we employed the nanoparticle wrapping fraction δ, which is defined as the ratio of the part of the membrane surface area that is in contact with the nanoparticle Am ($K_m \approx k_{NP}$) and the total nanoparticle surface area O_{NP} (Eq. 1, Fig. 6A).

$$\delta = \frac{A_m(K_m \approx k_{NP})}{O_{NP}} \quad (1)$$

Initially, considering the case where a single nanoparticle binds to a membrane, the number of ligand–receptor bonds formed N can be estimated by correcting the valence N_t of the particle (total number of ligands on the particle) by the wrapping factor δ (ranging from 0 to 1: no to full wrapping of the particle). We consider this step justified as Wang *et al*. and Silpe *et al*. showed a clear valency dependence for nanoparticle avidity [60,61]. The term +1 denotes a single ligand–receptor bond that can be formed regardless of whether a membrane structure is present (e.g., CCPs) that provides a wrapping fraction > 0 to the particle.

$$N = \delta N_t + 1 \quad (2)$$

In the next step, we extend this expression (Eq. 2) to describe the interaction of multiple particles with a membrane. For this purpose, we introduce the effective ligand concentration $[L]_{NP}$ which corresponds to the number of ligand–receptor bonds all nanoparticles will form taken together $N_{all\ NP}$ for a given wrapping fraction δ. Assuming that the same wrapping fraction occurs for all particles, this can be easily done by multiplying the number of particles considered N_{NP} by the number of ligands binding per particle determined according to Eq. (2) ($N_{all\ NP} = N_{NP}(\delta N_t + 1)$). The introduction of the Avogadro constant N_A (Fig. 6B, Supplementary Text, Eqs. 10 and 11) yields $[L]_{NP}$ as shown in Eq. (3).

$$[L]_{NP} = c_{NP}(\delta N_t + 1) \tag{3}$$

The expression for $[L]_{NP}$ in Eq. (3) can now be inserted into classical saturation binding models that relate ligand concentrations [X] (let X be any ligand) to an effect E as shown in Eq. (4) [62].

$$\frac{E}{E_{max}} = \frac{[X]}{[X]+K_D^X} \tag{4}$$

Substituting $[L]_{NP}$ for [X] (consider L the nanoparticle attached ligands) in Eq. (3) yields Eq. (5) in which K_D^L is the affinity of a single bond.

$$\frac{E}{E_{max}} = \frac{c_{NP}(\delta N_t+1)}{c_{NP}(\delta N_t+1)+K_D^L} \tag{5}$$

Here, E is the measured response (e.g., Ca^{2+} signal) and E_{max} is the maximum inducible response (e.g., maximum Ca^{2+} signal inducible by $NP_{Lys\text{-}Ang\ II}$). For our Ca^{2+} mobilization assay, E_{max} was calculated by fitting data of $NP_{Lys\text{-}Ang\ II}$ control experiment (Fig. 6B, grey symbols) using Eq. (12) (materials & method section). Now Eq. (5) can be used to model saturation binding curves for any given ligand-functionalized nanoparticle with a known number of ligands N_t and ligand affinity K_D^L for any given wrapping fraction δ (Fig. 6C). A nanoparticle's avidity K_D^{NP} can be calculated for $E = E_{max}/2$ where c_{NP} equals K_D^{NP}. If we modify Eq. (5) in this way, we obtain Eq. (6), the first step of a derivation of a general relation of K_D^{NP} and K_D^L in dependence of the wrapping fraction δ.

$$\frac{E_{max}}{2} = E_{max}\frac{K_D^{NP}(\delta N_t+1)}{K_D^{NP}(\delta N_t+1)+K_D^L} \quad (6)$$

In the cause of further solving Eq. (6) for K_D^{NP}, E_{max} drops out and we yield a general relation of K_D^{NP} and K_D^L as a function of δ in Eq. (7) which we refer to as the preferential binding model (Fig. 6D). This allows us to predict the shift of K_D^{NP} for any given shift in wrapping fraction δ (e.g., to be expected upon cholesterol depletion, Fig. 6E).

$$K_D^{NP} = \frac{K_D^L}{(\delta N_t+1)} \quad (7)$$

Based on literature data for Gaussian curvature and corresponding surface areas of CCPs [63], a wrapping fraction δ of 0.07 to 0.23 for $NP_{Lys\text{-}Ang\,II}$ can be considered realistic. For the presence of exclusively flat-shaped CCPs our model would predict an avidity loss of 2.1 to 2.7 orders of magnitude, which is perfectly in line with our experimentally observed K_D^{NP} shifts of $NP_{Lys\text{-}Ang\,II}$ (Fig. 7E and F).

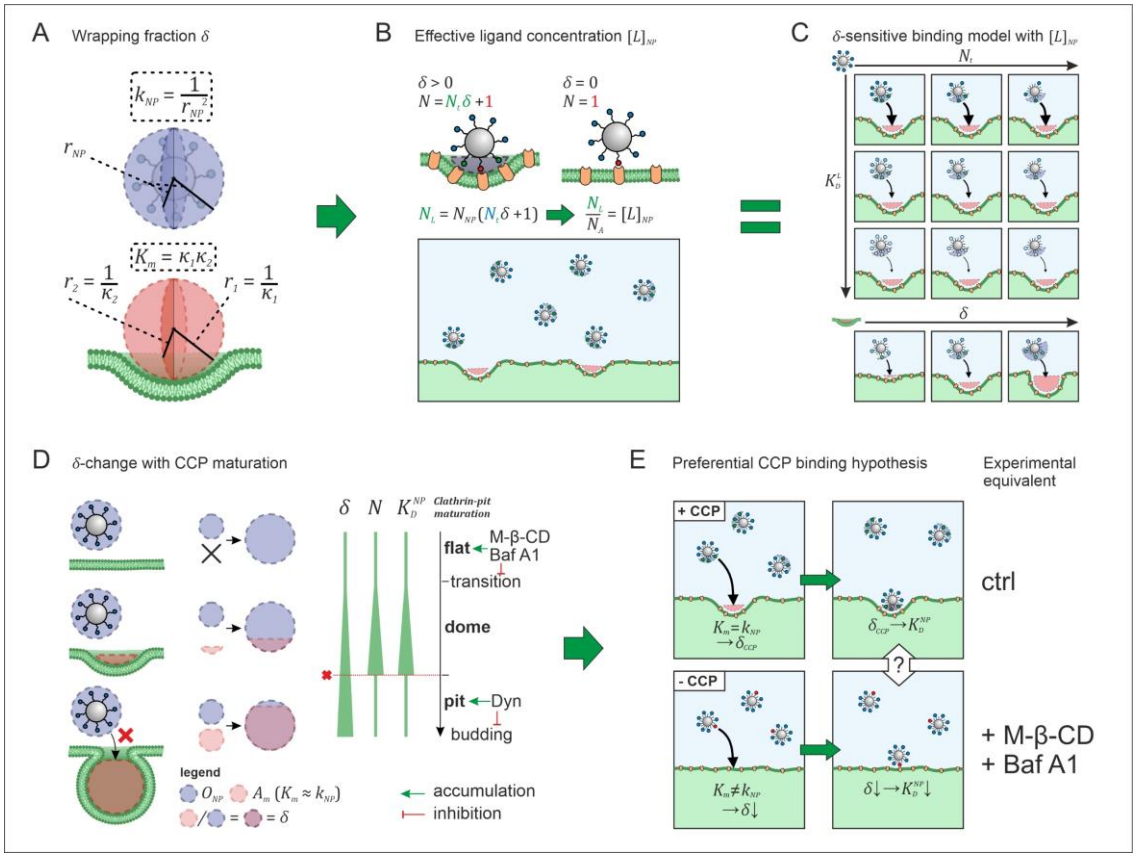

Figure 6: Model to predict K_D^{NP} shifts occurring upon cholesterol depletion. (A) Scheme illustrating the alignment of nanoparticle curvature k_{NP} and Gaussian membrane curvature K_m of a CCP. (B) Illustration how the effective ligand concentration $[L]_{NP}$ is calculated when a nanoparticle interacts with a cell membrane in the presence and absence of non-flat CCPs. (C) Illustration how the developed model (Eq. 5) can be used to derive binding curves for any combination of nanoparticle valency N_t, ligand affinity K_D^L and wrapping fraction δ. (D) Presentation of the preferential nanoparticle binding model assuming the constant curvature model [20–22] for CCP maturation. After the initiation of membrane curvature, wrapping fraction δ increases as the maturation proceeds. Number of involved ligands N and nanoparticle avidity K_D^{NP} increase until dome-pit-transition occurs. After this, accessibility to the CCP for the nanoparticle is no longer given (red dashed line). The preferential nanoparticle binding model was also applied to a novel maturation model most recently introduced by Bucher *et al*. [23] yielding the same conclusion of preferential binding of nanoparticles to dome-state CCPs (Fig. S1). (E) Scheme illustrates the goal of Eq. (7) to describe the effect of CCP invaginations on NP avidity K_D^{NP}. δ_{CCP} is the highest wrapping fraction for the considered membrane section. It occurs where Gaussian membrane curvature K_m and nanoparticle curvature k_{NP} align ($K_m = k_{NP}$). δ theoretically ranges from 0 to 1 (no vs. full wrapping of the particle).

To investigate the predictive power of our theoretical model, we analyzed the impact of cholesterol-depletion via M-β-CD on the dissociation constant K_D^{NP} of nanoparticle binding and on their avidity. For this, we plotted data derived from Ca^{2+} mobilization assays investigating effects of M-β-CD to obtain saturation curves (Fig. 7A and B). In untreated cells, the nanoparticle's K_D^{NP} of 0.67 nM exceeded the free ligand's K_D^L of 108 nM by approximately 160-fold. In contrast, when cells were treated with M-β-CD, nanoparticles were subject to a massive avidity loss. K_D^{NP} values increased to 37.7 nM, meaning that the nanoparticles had a mere 2.9-fold binding strength increase compared to the free ligand.

Based on K_D^L values found for the free ligand Lys-Ang II, we predicted binding curves to investigate the impact of the wrapping fraction δ (Eq. 5) and the corresponding Hill-slope n modified model (Eq. 9, Fig. 7C). This allowed us to find the best possible estimate of δ for our nanoparticle model system in the presence and absence of CCPs (Fig. 7D and Fig. S5).

$$\frac{E}{E_{max}} = \frac{c_{NP}(\delta N_t+1)^n}{c_{NP}(\delta N_t+1)^n+{K_D^L}^n} \quad (8)$$

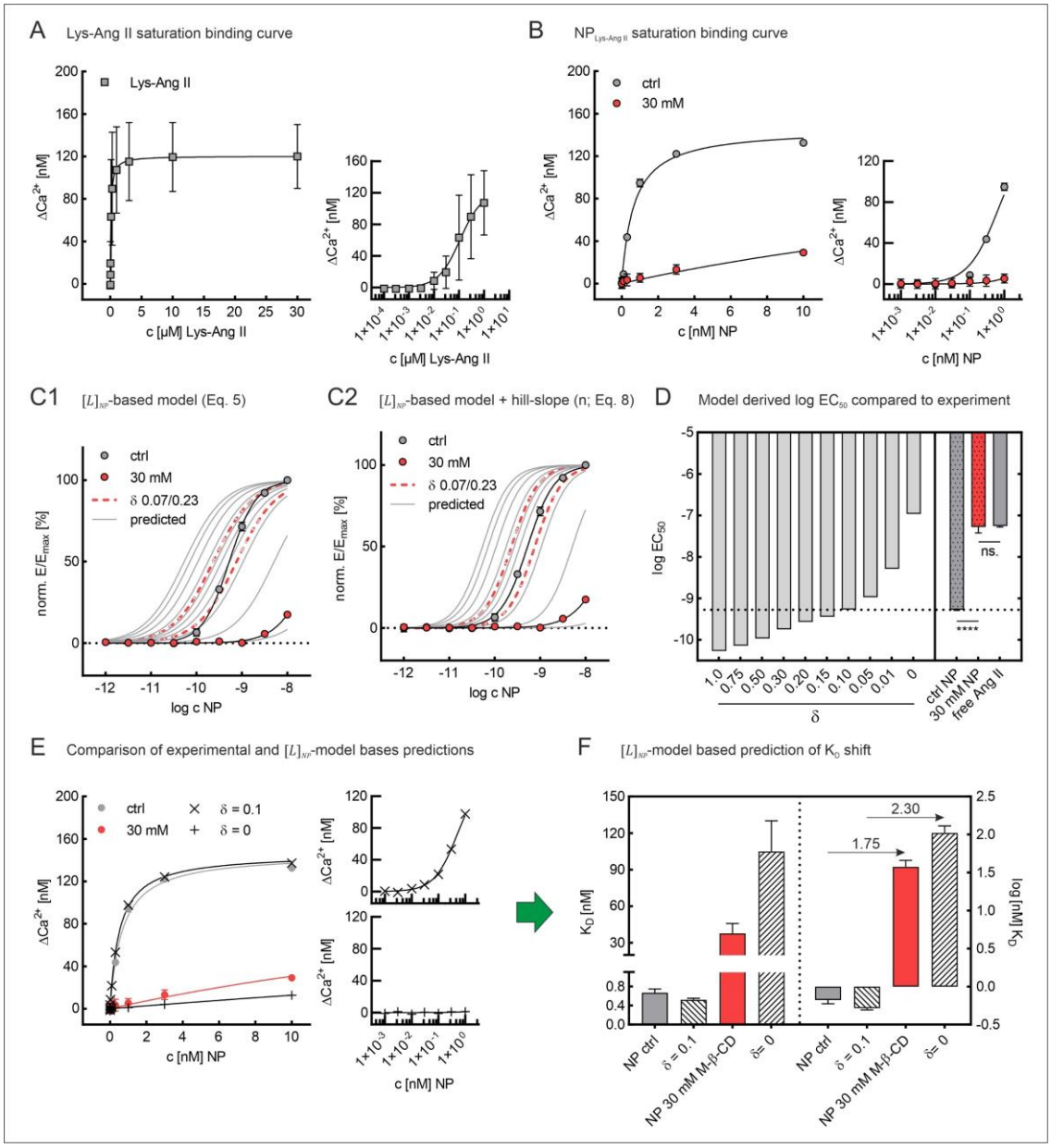

Figure 7: Comparison of model to predicted K_D^{NP} shift with experimental data. (A) Saturation curve derived from data acquired for free Lys-Ang II in Ca^{2+} mobilization assay (experiment + one repeat, each N = 3). (B) Saturation curves derived for binding of $NP_{Lys\text{-}Ang\,II}$ to untreated and 30 mM M-β-CD pretreated cells (N = 3). In (A) and (B), data acquired for lower concentrations (Lys-Ang II 0.1 nM–1 µM; $NP_{Lys\text{-}Ang\,II}$ 1 pM–1 nM) were also plotted against a log-scale for clarity. (C) Binding curves predicted for a series of δ-values were plotted and compared to binding curves based on data derived from Ca^{2+} mobilization assay. Binding curves were predicted using Eq. (5) (C1) and the model further modified via Hill-extension (Eq. 8) (C2). Red dashed lines are predicted binding curves for the lower and upper limits of δ (δ = 0.07 and δ = 0.23, see Supplementary Text) (error bars in (A), (B), and (C) reflect standard deviation). (D) Comparison of log EC_{50} values of predicted binding curves for a series of values of δ and log EC_{50} values determined for Ca^{2+} mobilization assays for $NP_{Lys\text{-}Ang\,II}$ in presence (ctrl NP) and absence (30 mM NP) of CCPs and for Lys-Ang II. Dashed line refers to the log EC_{50} value for the

binding of $NP_{Lys\text{-}Ang\ II}$ in control experiments (ctrl NP). Data were compared via one-way ANOVA analysis with subsequent Tukey's multiple comparison test (ns. – not significant, **** – P < 0.0001; error bars reflect standard error of mean; α = 0.001, F = 194.1, df = 8). (E) Comparison of experimental saturation curves and model-based predictions for best-fit value δ = 0.1 and δ = 0. (F) Corresponding K_D values (error-bars reflect the 95% CI). The values above the arrows indicate the decrease of K_D in log-steps.

Model-based data simulation employing the identified best-fit value for δ (Fig. 7C, D and Fig. S5) predicted an increase of K_D^{NP} by 2.30 log-steps. The experimental saturation curves, indeed, revealed an increase of the same order of magnitude. M-β-CD-induced CCP flattening resulted in a K_D^{NP} increase by 1.75 log-steps (Fig. 7E and F), confirming the high predictive power of our preferential binding model. For detailed theoretical derivation refer to Supplementary Text.

Discussion

Our studies have shown that CCPs, which provide a given wrapping fraction for nanoparticles due to their perfect geometric match, are essential for receptor-mediated nanoparticle membrane interactions. We found a 1–2 order of magnitude lower avidity of $NP_{Lys\text{-}Ang\,II}$ for receptor-positive mesangial cells in the absence of CCPs. We attribute this to decreases in multivalent receptor binding and the number of interactions between nanoparticle and cell when dome- and pit-shaped CCPs are absent. We conclude that the arrangement of receptors in invaginated CCPs allows for more ligand receptor interactions leading to the observed affinity increase. In this context, reference should be made to the work of Martinez-Veracoechea *et al*. who demonstrated that accumulation of nanoparticles occurs in a directional manner towards cells with higher receptor concentration [64]. Also, observations made by Barbul *et al*. indicated that smallest changes in receptor density can have significant effects on nanoparticle membrane binding [34]. By analogy, our results suggest that particle accumulation could also occur on a single cell depending on the wrapping fraction. The results of Martinez-Veracoechea *et al*. suggest that due to the higher proximity of ligands and receptors in a membrane section with a given wrapping fraction for particles (e.g., CCPs), there might be a preferential accumulation of nanoparticles towards such sections. M-β-CD treatment decreases the EC_{50} of $NP_{Lys\text{-}Ang\,II}$ to the value obtained for the free ligand Lys-Ang II on cells that were not cholesterol-depleted. From this we conclude that the avidity gain of multivalent nanoparticles is a combined effect of multivalency [65,66] and the presence of membrane structures (e.g., CCPs) offering nanoparticles a certain wrapping fraction for initial membrane attachment.

Comparison of the results presented in this work with findings of Bahrami *et al*. [33] indicates that fundamental laws governing the interaction of particles with membranes may be transferable to the case of a multivalent ligand-functionalized particle. In the mentioned work, total energies of particles interacting with the inside of a vesicle enclosing them are described. With the radius of particle and vesicle membrane approaching each other, a steepening decrease of the internal energy with increasing wrapping fraction is reported. Considering CCPs as structures offering a particle a membrane section that already displays an area $A_m(K_m \approx k_{NP}) > 0$ (consequently $\delta > 0$), it can be concluded from the results of Bahrami *et al*. that this interaction should be energetically favored.

This was confirmed by our simple theoretical model that accounts for the morphological match of nanoparticle and CCP geometry. An effective available ligand concentration $[L]_{NP}$ derived from the contact area between nanoparticle and pit allowed us to predict nanoparticle binding curves based on the free ligand's affinity. Our model suggests 10% alignment between CCPs and our model nanoparticle surfaces ($\delta = 0.10$), which corresponds very well with our initial expectations ($\delta = 0.07–0.23$) estimated from the geometrical fit of $NP_{Lys\text{-}Ang\,II}$ to unaltered CCPs (Fig. 7C and D) [52,63]. When we calculated the cholesterol depletion-induced avidity loss of $NP_{Lys\text{-}Ang\,II}$, it predicted a 2.3 order of magnitude decrease, which is close to the experimental value (Fig. 7E and F). This underlines the predictive power of our model and the relevance of our theoretical considerations.

The implications of our findings go far beyond a more precise understanding of the role of CCPs in nanoparticle binding to cells. The relationship between the relative curvatures of the nanoparticle and cell membrane suggest how nanoparticle size and geometry can be tailored to improve their interactions with target cells. It provides researchers designing targeted nanoparticles with a solid rational for the optimization of binding avidity. A second important consideration for nanoparticle design is the target receptor; for example, nanoparticles binding to caveolae-associated receptors may be subject to similar considerations as we had for CCPs. Ultimately, these two factors need to be reconciled to yield a nanoparticle in good morphological correspondence to the membrane structure most relevant for the targeted receptor. However, morphological dependence of nanoparticle binding could be a challenging aspect to consider for biomedical applications in which nanoparticle geometry cannot be altered. An approach could be to design systems that adapt their structure according to the membrane morphology they encounter, such as flexible nanofibers [67]. Moreover, our results could explain recent findings that the avidity of influenza as well as SARS-CoV-2 virions for target cells is cholesterol sensitive, but this conclusion awaits further exploration [68,69].

Finally, we want to point out and discuss limitations of the present work. Regarding our theoretical model it should be noted that the procedure of correcting the valency of the nanoparticle (N_t) for its wrapping fraction (δ) (Eq. 2) determines the maximum possible number of receptor–ligand pairs that could theoretically be formed based on the particle valency. For the case of low receptor–ligand binding energy, the number of receptor–

ligand pairs formed could be lower than Eq. (2) would suggest due to receptor entropy loss during binding.

Regarding the $NP_{Lys\text{-}Ang\,II}$ binding experiments, we think that based on our control experiments with the free ligand, a significant influence on the receptor activity due to cholesterol extraction (via M-β-CD and Baf A1 treatment) can be excluded as a primary cause for the presented observations. However, with respect to lateral receptor mobility, it should be noted that Dyn also influences cholesterol trafficking in addition to its primary mechanism of action (arrest of CCPs in late stages of maturation). Thus, a partial involvement of reduced lateral receptor mobility [57] or abrogation of cholesterol dependent liquid-ordered lipid phases [70] cannot be excluded with certainty. To estimate the involvement or the degree of involvement of this factor, methods would be required to inhibit the formation of CCPs without further side effects on the membrane. Currently, we do not see any method that perfectly fulfills this requirement.

Regarding the general applicability of the presented theoretical model, the present work provides a first insight into the role of CCPs for avidity of particle-membrane interactions. To draw clearer conclusions in this context, it would be helpful to study particles with varying size and geometry. This is difficult to do with the PEG-PLA/PLG-based particle used in this study. Other particle models that allow precise control of size and geometry (e.g. Au nanoparticles) [71] would be a promising platform for this purpose. Further studies investigating different nanoparticle platforms will also have to reveal how parameters like ligand density or linker lengths effect the model's predictive power.

Conclusion

The results of the conducted experimental studies, and in particular their excellent agreement with the predictions of the theoretical model established in this work, provide supportive evidence for the initial hypothesis suggesting a critical role of CCPs in the avidity of ligand-functionalized nanoparticle attachment to cell membranes. It was observed that inhibitors proven to freeze the maturation of CCPs at early or late stages shift the particle avidity to the range of affinity of the free ligand. From this, it can be concluded that the absence of dome-shaped CCPs leads to a near-complete loss in multivalency-induced avidity gain.

Materials and Methods

Materials

Fura-2 AM (Thermo Scientific, USA) was used as a ratio-metric Ca^{2+} indicator. Custom peptide Lysine-Angiotensin II (sequence: NH_2-KDRVYIHPF-COOH) was synthesized to order (GenScript, Netherlands). The inhibitors used in cell binding assays were methyl-β-cyclodextrin, dynasore (both Sigma-Aldrich, USA), bafilomycin A1 (Cayman Chemical, USA), and Exp3174 (Santa Cruz Biotechnology, USA). Polymers used for synthesis of block-copolymer were carboxy-PEG5k (JenKem Technology, USA, M_n = 5000 ± 500 g mol^{-1}, stated on certificate of analysis) and ester-terminated PLGA (Resomer® RG 502, ester-terminated, M_w 7000–17 000, Sigma-Aldrich, USA). Other chemicals used in the syntheses were 3,6-dimethyl-1,4-dioxane-2,5-dione and 1,8-diazabicyclo[5.4.0]undec-7-ene (both Sigma-Aldrich, USA). Cholesterol was quantified using components of the Amplex™ Red Cholesterol Assay Kit (Thermo Scientific, USA). Lys-Ang II was quantified using Pierce™ BCA Protein Assay Kit (Thermo Scientific, USA).

Syntheses and nanoparticle preparation

Carboxy-terminated poly(ethylene glycol)-b-poly(D,L-lactide) (carboxy-PEG-PLA) block-copolymer was synthesized as previously described by our group [11]. Briefly, 3.0 g of 3,6-dimethyl-1,4-dioxane-2,5-dione was recrystallized from ethyl acetate at 85 °C and dried under vacuum at 40 °C for 12 h. Carboxy-terminated poly(ethylene glycol) (carboxy-PEG) was dried under vacuum at 45 °C for 12 h before use. For polymerization, 677.9 mg (0.13 mmol) carboxy-PEG (Mn = 5085 g mol−1) was charged into a round-bottom flask and dissolved in 10 mL anhydrous DCM. Subsequently, 1.322 g (9.17 mmol) of 3,6-dimethyl-1,4-dioxane-2,5-dione and 437 µL (0.46 mmol) of 1 M 1,8-diazabicyclo[5.4.0]undec-7-ene in THF were added.50 The round-bottom flask was fitted with a CaCl2 drying tube. The reaction mixture was stirred at room temperature for 1 h, after which the polymerization was quenched by adding 280 mg (2.29 mmol) of benzoic acid. Finally, the solution was finally added dropwise to 200 mL vigorously stirred diethyl ether to precipitate the carboxy-PEG-PLA block-copolymer. Dried co-polymer was characterized via ^{1}H-NMR. Number-average molecular weight M_n = 14 459 g mol^{-1} was derived by calculating number-average PLA molecular weight from ^{1}H-NMR data using the following equation.

$$M_{PLA-p} = \frac{(A_{PLA\,CH_3} + A_{PLA\,CH}) M_{PLA-u}}{A_{PEG} M_{PEG-u}} M_{PEG-p} \qquad (9)$$

Here $M_{PLA\text{-}p}$ and $M_{PEG\text{-}p}$ are number-average molecular weights of the PLA- and PEG-polymer block. $M_{PLA\text{-}u}$ and $M_{PEG\text{-}u}$ are monomer molecular weights. $A_{PLA\,CH3}$ is the lactic acid (–CH_3) integral, $A_{PLA\,CH}$ is the lactic acid (–CH–) integral, and A_{PEG} is the PEG (–OCH_2CH_2–) integral (Fig. S3). Note that both monomer units possess the same number of protons (four each). ^{1}H-NMR data was also analyzed to estimate monomer conversion rate. Considering the employed quantities of carboxy-PEG (0.13 mmol) and 3,6-dimethyl-1,4-dioxane-2,5-dione (9.17 mmol equivalent to 2 × 9.17 mmol PLA monomer), based on $M_{PLA\text{-}u}$ = 72 g mol^{-1} we yield a maximum number-average molecular weight of $M_{PLA\text{-}p}$ = 10157 g mol^{-1}. Based on ^{1}H-NMR data, we calculated a number-average molecular weight of $M_{PLA\text{-}p}$ of 9374 g mol^{-1} yielding an estimated monomer conversion rate of 92.3%.

To conjugate the lysine-N-modified angiotensin II (Lys-Ang II) to the carboxy-PEG-PLA block copolymer, 200 mg (13.8 µmol) of carboxy-PEG-PLA, 66 mg (172.5 µmol) EDC, and 40 mg (172.5 µmol) NHS were dissolved in 1 mL of anhydrous DMF and reacted under stirring at 500 rpm for 3 h at room temperature. 120 µL (862.5 µmol) 2-mercaptoethanol was added to quench the reaction. 19.6 mg (16.7 µmol) of Lys-Ang II peptide was dissolved in 500 µL anhydrous DMF. Before adding the peptide solution, 23 µL (66.0 µmol) of N,N-diisopropylethylamine was added to the polymer solution. After adding Lys-Ang II peptide, the united solution was stirred at 500 rpm for an additional 48 h at room temperature. The mixture was diluted in 15 mL of milliQ H_2O to yield a DMF content below 10% (v : v). This solution was dialyzed for 24 h using a 6–8 kDa regenerated cellulose (RC) membrane. Medium was replaced after 30, 60 min, 2, 4, 6, 12, and 24 h. Finally, the solution was frozen at −80 °C and lyophilized for four days (0.005 mbar, −20 °C). Polymer micelles were prepared for characterization as follows. Lyophilized product was dissolved in acetonitrile (ACN) to yield a 40 mg mL^{-1} stock solution. 75 µL of this stock solution was mixed with 225 µL ACN to yield 10 mg mL^{-1} working solution for micelle preparation. This was added dropwise to 3 mL of milliQ H_2O under stirring at 700 rpm. ACN was allowed to evaporate for 3 h. Lys-Ang II-PEG-PLA micelles were characterized regarding Lys-Ang II and PEG molarity to determine the Lys-Ang II coupling efficiency (Fig. S2C). Lys-Ang II was quantified using a Pierce™

BCA assay kit. A standard serial dilution of free Lys-Ang II was prepared (1000, 750, 500, 250, 125, and 25 µg mL^{-1} + milliQ H_2O as blank) to yield a calibration curve (Fig. S2B). 25 µL of micelle sample and each standard were pipetted on a 96-well plate. 200 µL of BCA working reagent prepared according to manufactures instructions were added to each well. The plate was placed on a lab shaker for 30 s (50 rpm) and incubated for further 30 min (37 °C, 5% CO_2, protected from light). After cooling down to room temperature the absorbance was recorded at 562 nm on a FLUOstar Omega plate-reader (BMG Labtech, Germany). PEG was quantified via an iodine assay. A standard serial dilution was prepared using carboxy-PEG (40, 30, 20, 10, 5 µg mL^{-1} + milliQ H_2O as blank) to derive a calibration curve (Fig. S2A). 40 µL 5% (m/V) $BaCl_2$ solution in 1 M HCl and 20 µL 0.1 M iodine solution were mixed in each well of a 96-well-plate. 140 µL of a 1 : 60 diluted micelle sample and undiluted standards were added. The plate was incubated for 15 min at room temperature. Absorbance was measured at 535 nm on a FLUOstar Omega plate-reader. $NP_{Lys\text{-}Ang\,II}$ was analyzed as described above except that a 1 : 100 dilution was used for the iodine assay. The molar ratio of Lys-Ang II to PEG found for the Lys-Ang II-PEG-PLA micelles gave the coupling efficiency, while the ratio found for $NP_{Lys\text{-}Ang\,II}$ characterizes the degree of particle functionalization.

Nanoparticles were prepared using solvent evaporation technique. Lys-Ang II-modified PEG-PLA, carboxy-PEG-PLA, and poly(D,L-lactide-co-glycolide) (PLGA) were dissolved in ACN to obtain 40 mg mL^{-1} stock solutions. These were mixed to obtain a molar core (PLGA)/shell (Lys-Ang II-PEG-PLA and carboxy-PEG-PLA) ratio of 3 : 7 and a normalized ligand density for Lys-Ang II of 0.2. The mixed polymers were diluted with ACN to obtain a total polymer concentration of 10 mg mL^{-1}. This solution was added dropwise to 10 mL DPBS stirring at 500 rpm on a magnetic stirrer. ACN was allowed to evaporate for 3 h. Subsequently, nanoparticles were re-concentrated using Microsep® Advance 30k centrifugal filters (2.5 rcf, 20 min). Nanoparticles were characterized for ligand density using an iodine and BCA assay. Particle hydrodynamic diameters were determined by DLS on a Nano ZS Zetasizer (Malvern, UK) (Fig. S2D and E) using 633 nm He–Ne laser and 173° backscatter configuration. By measuring polymer dry weight mp after freeze drying, the number of nanoparticles per volume Vs was determined. Using a literature value of 1.25 g cm^{-3} for the density (ρ) of PEG-PLA [51], the hydrodynamic diameter dh as determined by DLS, and the reciprocal Avogadro's constant N_A, Eq. (10) yields the molar nanoparticle concentration c_{NP}.

$$c_{NP}[M] = \frac{m_p}{\rho \times \frac{4}{3}\pi \times \left(\frac{d_h}{2}\right)^3} \times \frac{1}{V_s} \times \frac{1}{N_A} \quad (10)$$

Cholesterol quantification

Cholesterol extracted by M-β-CD was quantified using an Amplex™ Red-based two-step enzymatic cholesterol quantification assay. rMCs were grown to confluency on 96-well plates and treated with 5, 10, 30, or 50 mM M-β-CD in Leibovitz's medium. M-β-CD-free medium was used as control to quantify the cholesterol content in untreated rMCs. After 45 min incubation at room temperature, the supernatant was discarded, and rMCs were washed twice using DPBS. rMCs were lysed by incubating with 0.25% trypsin for 24 h at 37 °C with 5% CO_2. Complete cell lysis was confirmed by light microscopy, and the lysate was used for the cholesterol quantification assay.

80 µL samples of the cell lysates were collected (N = 3), mixed with 160 µL assay reaction buffer (0.1 M potassium phosphate, 0.05 M NaCl, 5 mM cholic acid, and 0.1% Triton® X-100; pH 7.4), and pre-incubated for 2.5 h (37 °C, 5% CO_2) to ensure sufficient solubilization of cholesterol for the assay. From these pre-incubated samples, 10 µL samples were collected (N = 2) and mixed with 90 µL Amplex™ Red reagent buffer (300 µM Amplex™ Red reagent, 2 U mL^{-1} horseradish peroxidase, and 2 U mL^{-1} cholesterol oxidase in 1× assay reaction buffer). The reaction was incubated for 30 min (37 °C, 5% CO_2) protected from light. Fluorescence intensities were measured using a FLUOstar Omega plate-reader using top-optics (ex/em: 544/590 nm, double orbital shaking at 500 rpm) (Fig. S4A). The measured fluorescence signals were normalized against a control.

To confirm that the cholesterol quantification assay worked in our cell-based setting, we conducted preliminary experiments measuring cholesterol in 37.5, 75, 150, and 300 k cell rMC pellets. Lysates were prepared as described above. Fitting of the fluorescence signals confirmed good linearity of the signal and absence of significant background fluorescence. Assays performed on cell lysates yielded results comparable to the cholesterol standards (Fig. S4C and D). Possible stability issues due to the enzymes used in the assay being exposed to residual trypsin during the reaction were also

addressed by preliminary testing. For this, 2 U mL^{-1} horseradish peroxidase and 2 U mL^{-1} cholesterol oxidase were incubated for 45 min (37 °C, 5% CO_2, protected from light) in the presence of 300 µM Amplex™ Red reagent and 4 µg mL^{-1} cholesterol standard in the presence or absence of 0.016% trypsin. No significant loss in activity was found (Fig. S4B).

Fura-2 AM-based Ca^{2+} mobilization assay

For Fura-2 AM-based Ca^{2+} mobilization assays, rMCs were harvested by applying 0.25% Trypsin for 90 s (37 °C, 5% CO_2). Prior to use, 50 µL DMSO was added to 50 µg of Fura-2 AM. We incubated the vial for 3 h, desiccated and protected from light to ensure complete dissolution of Fura-2 AM. For Fura-2 AM loading, rMCs were centrifuged at 0.2 rcf for 5 min using slow acceleration and deceleration mode on a 5702 R centrifuge (Eppendorf, Germany). The supernatant was discarded, and the cell pellet was carefully resuspended in Leibovitz's-based Fura-2 AM loading medium, transferred to a small culture dish, and incubated with 8.3 µM Fura-2 AM, 2.5 mM OAT-inhibitor probenecid, and 0.017% (m:V) pluronic F127 on a lab shaker at 50 rpm for 2.5 h at room temperature protected from light.

The dye-loaded cells were centrifuged using the settings described above. The Fura-2 AM loading medium was discarded, and the cells were resuspended in Leibovitz's-based measurement buffer containing 2.5 mM OAT-inhibitor probenecid. Cell number was adjusted to 1 10^6 rMCs mL^{-1} using a Neubauer-improved counting chamber (Marienfeld, Germany). Cell suspensions were immediately used for measurements with M-β-CD (5, 10, 30 mM, 45 min) or Dyn (100 µM, 1 h) treatment. To investigate the effect of Baf A1, cells were pretreated with 100 nM Baf A1 for 24 h ahead of the assay. All buffers used during the assay were supplemented with 100 nM Baf A1. All treatments were carried out in the presence of 2.5 mM OAT-inhibitor probenecid. The effect of probenecid on cholesterol extraction efficiency of M-β-CD was investigated and found to be negligible for M-β-CD concentrations ≥10 mM (Fig. 4C). Baf A1 and Dyn were used at concentrations known to perturb CCP maturation [42–46]. To prove that the measured Ca^{2+} signals were exclusively triggered by the specific Lys-Ang II-AT_1R interaction, we performed a Ca^{2+} assay with an unfunctionalized nanoparticle (NP_{COOH}). In addition, another Ca^{2+} assay was performed with $NP_{Lys\text{-}Ang\ II}$. In this case, however, 10 µM

Exp3174 were added to the loading buffer. Also, 10 µM Exp3174 were added to the measurement buffer in which the Fura-2 loaded rMCs were resuspended.

Ratio-metric fluorescence intensity read-out was performed on a FLUOstar Omega plate-reader. Plates were prepared by adding 10 µL of ten-fold over-concentrated serial dilutions of Lys-Ang II and $NP_{Lys\text{-}Ang\,II}$ per well. The assay was started by adding 90 µL of Fura-2 AM-loaded cell suspension to each sample via the FLUOstar Omega pump system set to a speed of 100 µL s^{-1}. Each sample was alternately excited at λ 340 nm and 380 nm every 1.5 s, measuring emission at λ 510 nm. Data was collected for 30 s per sample. Three replicates were measured for each concentration of Lys-Ang II and $NP_{Lys\text{-}Ang\,II}$. The highest measured ratio of each sample was used for the calculation of intracellular Ca^{2+} levels using the Grynkiewicz-equation [72]. For calibration, the maximum ratio (R_{max}) was obtained by measuring Fura-2 AM-loaded cells lysed with 10 µL of 1% Triton® X-100 in PBS. The minimum ratio (R_{min}) was measured using 10 µL of 1% Triton® X-100 in PBS supplemented with 45 mM EGTA and 0.5 M NaOH.

Fitting models

The binding curves obtained from the Lys-Ang II and $NP_{Lys\text{-}Ang\,II}$ Ca^{2+} mobilization assays were fit using a four-parameter nonlinear regression model (Eq. 11).

$$Y = 100/\left(1 + 10^{(\log EC_{50} - X)\times n}\right) \qquad (11)$$

Data for saturation curves were fitted using one-site specific binding model (Eq. 12).

$$Y = E_{max} \times X/(K_D + X) \qquad (12)$$

All fittings were conducted using GraphPad Prism (v8.3.0, GraphPad Software, San Diego, USA).

References

[1] B.D. Chithrani, A.A. Ghazani, W.C.W. Chan, Determining the size and shape dependence of gold nanoparticle uptake into mammalian cells, Nano letters 6 (2006) 662–668.

[2] A. Albanese, P.S. Tang, W.C.W. Chan, The effect of nanoparticle size, shape, and surface chemistry on biological systems, Annual review of biomedical engineering 14 (2012) 1–16.

[3] W. Jiang, B.Y.S. Kim, J.T. Rutka, W.C.W. Chan, Nanoparticle-mediated cellular response is size-dependent, Nature nanotechnology 3 (2008) 145–150.

[4] A.E. Nel, L. Mädler, D. Velegol, T. Xia, E.M.V. Hoek, P. Somasundaran, F. Klaessig, V. Castranova, M. Thompson, Understanding biophysicochemical interactions at the nano-bio interface, Nature materials 8 (2009) 543–557.

[5] N. Hoshyar, S. Gray, H. Han, G. Bao, The effect of nanoparticle size on in vivo pharmacokinetics and cellular interaction, Nanomedicine (London, England) 11 (2016) 673–692.

[6] Z.-G. Yue, W. Wei, P.-P. Lv, H. Yue, L.-Y. Wang, Z.-G. Su, G.-H. Ma, Surface charge affects cellular uptake and intracellular trafficking of chitosan-based nanoparticles, Biomacromolecules 12 (2011) 2440–2446.

[7] K. Abstiens, M. Gregoritza, A.M. Goepferich, Ligand Density and Linker Length are Critical Factors for Multivalent Nanoparticle-Receptor Interactions, ACS applied materials & interfaces 11 (2019) 1311–1320.

[8] S. Maslanka Figueroa, D. Fleischmann, S. Beck, A. Goepferich, The Effect of Ligand Mobility on the Cellular Interaction of Multivalent Nanoparticles, Macromolecular bioscience (2020) e1900427.

[9] C.H. Kapadia, S. Tian, J.L. Perry, J.C. Luft, J.M. DeSimone, Role of Linker Length and Antigen Density in Nanoparticle Peptide Vaccine, ACS omega 4 (2019) 5547–5555.

[10] C.L. Modery-Pawlowski, A.S. Gupta, Heteromultivalent ligand-decoration for actively targeted nanomedicine, Biomaterials 35 (2014) 2568–2579.

[11] S. Maslanka Figueroa, A. Veser, K. Abstiens, D. Fleischmann, S. Beck, A. Goepferich, Influenza A virus mimetic nanoparticles trigger selective cell uptake, Proceedings of the National Academy of Sciences 116 (2019) 9831–9836.

[12] M.B. Deci, M. Liu, Q.T. Dinh, J. Nguyen, Precision engineering of targeted nanocarriers, Wiley interdisciplinary reviews. Nanomedicine and nanobiotechnology 10 (2018) e1511.

[13] S. Block, V.P. Zhdanov, F. Höök, Quantification of Multivalent Interactions by Tracking Single Biological Nanoparticle Mobility on a Lipid Membrane, Nano letters 16 (2016) 4382–4390.

[14] D. Di Iorio, M.L. Verheijden, E. van der Vries, P. Jonkheijm, J. Huskens, Weak Multivalent Binding of Influenza Hemagglutinin Nanoparticles at a Sialoglycan-Functionalized Supported Lipid Bilayer, ACS nano 13 (2019) 3413–3423.

[15] H. Jung, A.D. Robison, P.S. Cremer, Multivalent ligand-receptor binding on supported lipid bilayers, Journal of structural biology 168 (2009) 90–94.

[16] R.S. Kane, Thermodynamics of multivalent interactions: influence of the linker, Langmuir the ACS journal of surfaces and colloids 26 (2010) 8636–8640.

[17] M. Ehrlich, W. Boll, A. van Oijen, R. Hariharan, K. Chandran, M.L. Nibert, T. Kirchhausen, Endocytosis by random initiation and stabilization of clathrin-coated pits, Cell 118 (2004) 591–605.

[18] M. Kaksonen, A. Roux, Mechanisms of clathrin-mediated endocytosis, Nature reviews. Molecular cell biology 19 (2018) 313–326.

[19] O. Avinoam, M. Schorb, C.J. Beese, J.A.G. Briggs, M. Kaksonen, ENDOCYTOSIS. Endocytic sites mature by continuous bending and remodeling of the clathrin coat, Science (New York, N.Y.) 348 (2015) 1369–1372.

[20] T. Kirchhausen, Coated pits and coated vesicles — sorting it all out, Current Opinion in Structural Biology 3 (1993) 182–188.

[21] T. Kirchhausen, Imaging endocytic clathrin structures in living cells, Trends in cell biology 19 (2009) 596–605.

[22] M. Lampe, S. Vassilopoulos, C. Merrifield, Clathrin coated pits, plaques and adhesion, Journal of structural biology 196 (2016) 48–56.

[23] D. Bucher, F. Frey, K.A. Sochacki, S. Kummer, J.-P. Bergeest, W.J. Godinez, H.-G. Kräusslich, K. Rohr, J.W. Taraska, U.S. Schwarz, S. Boulant, Clathrin-adaptor ratio and membrane tension regulate the flat-to-curved transition of the clathrin coat during endocytosis, Nature communications 9 (2018) 1109.

[24] A.A. Yetisgin, S. Cetinel, M. Zuvin, A. Kosar, O. Kutlu, Therapeutic Nanoparticles and Their Targeted Delivery Applications, Molecules (Basel, Switzerland) 25 (2020) 2193.

[25] T. Kirchhausen, D. Owen, S.C. Harrison, Molecular structure, function, and dynamics of clathrin-mediated membrane traffic, Cold Spring Harbor perspectives in biology 6 (2014) a016725.

[26] A.J. Simnick, C.A. Valencia, R. Liu, A. Chilkoti, Morphing low-affinity ligands into high-avidity nanoparticles by thermally triggered self-assembly of a genetically encoded polymer, ACS nano 4 (2010) 2217–2227.

[27] M. Mammen, S.-K. Choi, G.M. Whitesides, Polyvalent Interactions in Biological Systems: Implications for Design and Use of Multivalent Ligands and Inhibitors, Angewandte Chemie International Edition 37 (1998) 2754–2794.

[28] M. Wang, S.R. Ravindranath, M.K. Rahim, E.L. Botvinick, J.B. Haun, Evolution of Multivalent Nanoparticle Adhesion via Specific Molecular Interactions, Langmuir the ACS journal of surfaces and colloids 32 (2016) 13124–13136.

[29] J. Agudo-Canalejo, R. Lipowsky, Adhesive Nanoparticles as Local Probes of Membrane Curvature, Nano letters 15 (2015) 7168–7173.

[30] J. Agudo-Canalejo, R. Lipowsky, Uniform and Janus-like nanoparticles in contact with vesicles: energy landscapes and curvature-induced forces, Soft matter 13 (2017) 2155–2173.

[31] Q. Yu, S. Othman, S. Dasgupta, T. Auth, G. Gompper, Nanoparticle wrapping at small non-spherical vesicles: curvatures at play, Nanoscale 10 (2018) 6445–6458.

[32] M Deserno, T Bickel, Wrapping of a spherical colloid by a fluid membrane, Europhysics Letters (EPL) 62 (2003) 767–774.

[33] A.H. Bahrami, R. Lipowsky, T.R. Weikl, The role of membrane curvature for the wrapping of nanoparticles, Soft matter 12 (2016) 581–587.

[34] A. Barbul, K. Singh, L. Horev−Azaria, S. Dasgupta, T. Auth, R. Korenstein, G. Gompper, Nanoparticle-Decorated Erythrocytes Reveal That Particle Size Controls the Extent of Adsorption, Cell Shape, and Cell Deformability, ACS Appl. Nano Mater. 1 (2018) 3785–3799.

[35] K.A. Sochacki, B.L. Heine, G.J. Haber, J.R. Jimah, B. Prasai, M.A. Alfonzo-Méndez, A.D. Roberts, A. Somasundaram, J.E. Hinshaw, J.W. Taraska, The structure and spontaneous curvature of clathrin lattices at the plasma membrane, Developmental cell 56 (2021) 1131-1146.e3.

[36] F.J. Byfield, H. Aranda-Espinoza, V.G. Romanenko, G.H. Rothblat, I. Levitan, Cholesterol depletion increases membrane stiffness of aortic endothelial cells, Biophysical journal 87 (2004) 3336–3343.

[37] W.G. Thomas, T.J. Thekkumkara, K.M. Baker, Molecular mechanisms of angiotensin II (AT1A) receptor endocytosis, Clinical and experimental pharmacology & physiology. Supplement 3 (1996) S74-80.

[38] S.K. Rodal, G. Skretting, O. Garred, F. Vilhardt, B. van Deurs, K. Sandvig, Extraction of cholesterol with methyl-beta-cyclodextrin perturbs formation of clathrin-coated endocytic vesicles, Mol. Biol. Cell. 10 (1999) 961–974.

[39] S. Mahammad, I. Parmryd, Cholesterol Depletion Using Methyl-β-cyclodextrin, in: D.M. Owen (Ed.), Methods in Membrane Lipids, Springer New York, New York, NY, 2015, pp. 91–102.

[40] A. Subtil, I. Gaidarov, K. Kobylarz, M.A. Lampson, J.H. Keen, T.E. McGraw, Acute cholesterol depletion inhibits clathrin-coated pit budding, PNAS 96 (1999) 6775–6780.

[41] R. Zidovetzki, I. Levitan, Use of cyclodextrins to manipulate plasma membrane cholesterol content: evidence, misconceptions and control strategies, Biochimica et biophysica acta 1768 (2007) 1311–1324.

[42] T. Furuchi, K. Aikawa, H. Arai, K. Inoue, Bafilomycin A1, a specific inhibitor of vacuolar-type H(+)-ATPase, blocks lysosomal cholesterol trafficking in maceophages, J. Biol. Chem. 268 (1993) 27345–27348.

[43] P. Kozik, N.A. Hodson, D.A. Sahlender, N. Simecek, C. Soromani, J. Wu, L.M. Collinson, M.S. Robinson, A human genome-wide screen for regulators of clathrin-coated vesicle formation reveals an unexpected role for the V-ATPase, Nature cell biology 15 (2013) 50–60.

[44] E. Macia, M. Ehrlich, R. Massol, E. Boucrot, C. Brunner, T. Kirchhausen, Dynasore, a cell-permeable inhibitor of dynamin, Developmental cell 10 (2006) 839–850.

[45] E. Girard, J.L. Paul, N. Fournier, P. Beaune, L. Johannes, C. Lamaze, B. Védie, The dynamin chemical inhibitor dynasore impairs cholesterol trafficking and sterol-sensitive genes transcription in human HeLa cells and macrophages, PloS one 6 (2011) e29042.

[46] G. Preta, J.G. Cronin, I.M. Sheldon, Dynasore - not just a dynamin inhibitor, Cell communication and signaling CCS 13 (2015) 24.

[47] S. Hua, M.B.C. de Matos, J.M. Metselaar, G. Storm, Current Trends and Challenges in the Clinical Translation of Nanoparticulate Nanomedicines: Pathways for Translational Development and Commercialization, Frontiers in pharmacology 9 (2018) 790.

[48] J.I. Hare, T. Lammers, M.B. Ashford, S. Puri, G. Storm, S.T. Barry, Challenges and strategies in anti-cancer nanomedicine development: An industry perspective, Advanced drug delivery reviews 108 (2017) 25–38.

[49] L. Sercombe, T. Veerati, F. Moheimani, S.Y. Wu, A.K. Sood, S. Hua, Advances and Challenges of Liposome Assisted Drug Delivery, Frontiers in pharmacology 6 (2015) 286.

[50] H. Nehoff, N.N. Parayath, L. Domanovitch, S. Taurin, K. Greish, Nanomedicine for drug targeting: strategies beyond the enhanced permeability and retention effect, International journal of nanomedicine 9 (2014) 2539–2555.

[51] J.-M. Rabanel, J. Faivre, S.F. Tehrani, A. Lalloz, P. Hildgen, X. Banquy, Effect of the Polymer Architecture on the Structural and Biophysical Properties of PEG-PLA Nanoparticles, ACS applied materials & interfaces 7 (2015) 10374–10385.

[52] V. Ramanan, N.J. Agrawal, J. Liu, S. Engles, R. Toy, R. Radhakrishnan, Systems biology and physical biology of clathrin-mediated endocytosis, Integrative biology quantitative biosciences from nano to macro 3 (2011) 803–815.

[53] R. Hennig, K. Pollinger, J. Tessmar, A. Goepferich, Multivalent targeting of AT1 receptors with angiotensin II-functionalized nanoparticles, Journal of drug targeting 23 (2015) 681–689.

[54] K.K. Griendling, S.E. Rittenhouse, T.A. Brock, L.S. Ekstein, M.A. Gimbrone, R.W. Alexander, Sustained diacylglycerol formation from inositol phospholipids in angiotensin II-stimulated vascular smooth muscle cells, Journal of Biological Chemistry 261 (1986) 5901–5906.

[55] S. Greco, M. Elia, A. Muscella, C. Storelli, S. Marsigliante, AT1 Angiotensin II receptor mediates intracellular calcium mobilization in normal and cancerous breast cells in primary culture, Cell Calcium 32 (2002) 1–10.

[56] C. Meindl, T. Kueznik, M. Bösch, E. Roblegg, E. Fröhlich, Intracellular calcium levels as screening tool for nanoparticle toxicity, Journal of applied toxicology JAT 35 (2015) 1150–1159.

[57] J. Brejchová, J. Sýkora, P. Ostašov, L. Merta, L. Roubalová, J. Janáček, M. Hof, P. Svoboda, TRH-receptor mobility and function in intact and cholesterol-depleted plasma membrane of HEK293 cells stably expressing TRH-R-eGFP, Biochimica et biophysica acta 1848 (2015) 781–796.

[58] A. Biswas, P. Kashyap, S. Datta, T. Sengupta, B. Sinha, Cholesterol Depletion by MβCD Enhances Cell Membrane Tension and Its Variations-Reducing Integrity, Biophysical journal 116 (2019) 1456–1468.

[59] J.E. Hassinger, G. Oster, D.G. Drubin, P. Rangamani, Design principles for robust vesiculation in clathrin-mediated endocytosis, Proceedings of the National Academy of Sciences 114 (2017) E1118-E1127.

[60] J. Wang, J. Min, S.A. Eghtesadi, R.S. Kane, A. Chilkoti, Quantitative Study of the Interaction of Multivalent Ligand-Modified Nanoparticles with Breast Cancer Cells with Tunable Receptor Density, ACS nano 14 (2020) 372–383.

[61] J.E. Silpe, M. Sumit, T.P. Thomas, B. Huang, A. Kotlyar, M.A. van Dongen, M.M. Banaszak Holl, B.G. Orr, S.K. Choi, Avidity modulation of folate-targeted multivalent dendrimers for evaluating biophysical models of cancer targeting nanoparticles, ACS chemical biology 8 (2013) 2063–2071.

[62] A.J. Clark, The reaction between acetyl choline and muscle cells, J Physiol 61 (1926) 530–546.

[63] N.J. Agrawal, J. Nukpezah, R. Radhakrishnan, Minimal mesoscale model for protein-mediated vesiculation in clathrin-dependent endocytosis, PLoS computational biology 6 (2010) e1000926.

[64] F.J. Martinez-Veracoechea, D. Frenkel, Designing super selectivity in multivalent nano-particle binding, Proceedings of the National Academy of Sciences 108 (2011) 10963–10968.

[65] L. Woythe, N.B. Tito, L. Albertazzi, A quantitative view on multivalent nanomedicine targeting, Advanced drug delivery reviews 169 (2021) 1–21.

[66] P. Varilly, S. Angioletti-Uberti, B.M. Mognetti, D. Frenkel, A general theory of DNA-mediated and other valence-limited colloidal interactions, The Journal of chemical physics 137 (2012) 94108.

[67] S. Kajdič, O. Planinšek, M. Gašperlin, P. Kocbek, Electrospun nanofibers for customized drug-delivery systems, Journal of Drug Delivery Science and Technology 51 (2019) 672–681.

[68] I.N. Goronzy, R.J. Rawle, S.G. Boxer, P.M. Kasson, Cholesterol enhances influenza binding avidity by controlling nanoscale receptor clustering, Chemical science 9 (2018) 2340–2347.

[69] D.W. Sanders, C.C. Jumper, P.J. Ackerman, D. Bracha, A. Donlic, H. Kim, D. Kenney, I. Castello-Serrano, S. Suzuki, T. Tamura, A.H. Tavares, M. Saeed, A.S. Holehouse, A. Ploss, I. Levental, F. Douam, R.F. Padera, B.D. Levy, C.P. Brangwynne, SARS-CoV-2 requires cholesterol for viral entry and pathological syncytia formation, eLife 10 (2021).

[70] D. Marsh, Liquid-ordered phases induced by cholesterol: a compendium of binary phase diagrams, Biochimica et biophysica acta 1798 (2010) 688–699.

[71] L. Freitas de Freitas, G.H.C. Varca, J.G. Dos Santos Batista, A. Benévolo Lugão, An Overview of the Synthesis of Gold Nanoparticles Using Radiation Technologies, Nanomaterials (Basel, Switzerland) 8 (2018).

[72] G. Grynkiewicz, M. Poenie, R.Y. Tsien, A New Generation of Ca2+ Indicators with Greatly Improved Fluorescence Properties, The Journal of biological chemistry 260 (1985) 3440–3450.

Chapter 4 – Supplementary Information

How Clathrin-Coated Pits Control Nanoparticle Avidity for Cells

Content:

Supplementary Text

Detailed Derivation on -sensitive Binding Model

The key conceptual approach of our theoretical considerations is the correction of the nanoparticle's valency for the particles wrapping fraction.

$$N = \delta N_t \quad (1)$$

In Eq. (1) N_t is the total amount of ligands attached to the respective nanoparticle and δ expressing the wrapping fraction ranging from 0 (no wrapping) to 1 (total wrapping of the particle). The term +1 is inserted to account for a single ligand-receptor bond that can be formed regardless of the wrapping fraction (i.e., on an entirely flat membrane; Eq. 2).

$$N = \delta N_t + 1 \quad (2)$$

With δ expressed as the ratio of membrane area where gaussian curvature Km of the membrane is in good correspondence to the curvature k_{NP} of the given spherical nanostructure A_m ($K_m \approx k_{NP}$) and the nanostructures surface area O_{NP} (Eq. 5 in the main text), we yield a factor describing the wrapping fraction. A first definition for the degree of wrapping of a particle at a membrane was introduced by Deserno et al. [1]. Later, Agudo-Canalejo et al. [2] introduced a degree of invagination that corresponds to the one we employed. The wrapping fraction is based on the surface area on the membrane where particle curvature k_{NP} and gaussian membrane curvature K_m align. k_{NP} is given as [3].

$$k_{NP} = \frac{1}{{r_{NP}}^2} \quad (3)$$

And the gaussian curvature K_m is given as the product of the principal curvatures κ_1 and κ_2 corresponding to the contact sphere radii r_1 and r_2 [4].

$$K_m = \kappa_1 \kappa_2 = \frac{1}{r_1} \times \frac{1}{r_2} \quad (4)$$

Ramanan et al. calculated gaussian curvature K_m profiles for clathrin-coated pits based on simulated membrane deformation profiles [5]. For early- and medium-stage clathrin-coated pits gaussian curvature K_m was found to range from 0.8 to $2.4 \cdot 10^{-3}$ nm^{-2}, which is in good correspondence with our nanoparticle's curvature k_{NP} of $0.8 \cdot 10^{-3}$ nm^{-2}, given by the hydrodynamic diameter d_h of our model system estimated via dynamic light scattering, in accordance with equation (3). Based on corresponding surface area values calculated by Agrawal et al. for clathrin-coated pits at early and medium stages of maturation (early: 1140 nm^2; medium: 3760 nm^2) [6], we estimated δ to range from 0.07 to 0.23 (with O_{NP} = 16326 nm^2) for our nanoparticle model system binding into a pit.

As we consider the limits for δ → 0 (Eq. 4) and δ → 1 (Eq. 5) it is apparent that our expression is suitable to describe the number of ligand receptor pairs formed in dependence of the wrapping fraction δ. However, the introduction of this expression is only permissible if N_t is significantly higher than 1, so the addition of 1 in equation (2) resembling a single ligand binding regardless of the presence of membrane structures providing nanoparticles with a given wrapping fraction δ (e.g., CCPs) becomes negligible as δ increases (Eq. 5). This requirement can be considered given for most ligand-carrying nanostructures. It should also be noted that this mathematical consideration of the limiting cases of N in dependence of δ neglects the possibility of dissociation of the particle at low values of δ (in this case: $\lim_{\delta \to 0} N = 0$).

$$\lim_{\delta \to 0} N = 1 \qquad (5)$$

$$\lim_{\delta \to 1} N = \delta N_t \qquad \text{if } N_t \gg 1 \qquad (6)$$

The absence of a given wrapping fraction corresponds to A_m ($K_m \approx k_{NP}$) = 0 within our model. Consequently, in this case δ = 0 (Eq. 1). Due to the correction of the particle valence N_t by δ the number of receptor-ligand bonds formed for a single particle results to be N = 1 (see equation 6 main text) and for a particle number > 1 would be equal to $[L]_{NP}$ = c_{NP} (this corresponds to the binding of one ligand per particle, see equation 7 in main text). In such a case nanoparticle binding is likely predominantly dictated by single ligand affinity and membrane bending energy as described by Bahrami et al. [7]. In the presence of membrane structures possessing a curvature equal to nanoparticles curvature (e.g., CCPs), however, this membrane In the presence of a membrane

structure with a curvature K_m corresponding to the curvature of the nanoparticles k_{NP} (e.g. CCPs), this membrane already has an area A_m ($K_m \approx k_{NP}$) > 0, which is available for the particles ahead of initial binding. This could also be referred to as a given wrapping fraction, in the sense that the particle already has a wrapping fraction δ > 0 at the time of initial binding.

Basic Model for Binding Curve Predictions

Considering the simplest case of linear receptor response [8], for the simple reaction equation given below, it can be assumed that the effect E triggered by ligand binding is proportional to the concentration [RL]. In addition, the maximum effect Emax is proportional to the total number of receptors [RT], since [RT] is equal to [RL] if all receptors are occupied.

$$L + R \rightleftarrows RL \rightarrow E$$

$$E \propto [RL] \quad \text{and} \quad E_{max} \propto [R_T]$$

Consequently, the degree of receptor occupation y can be expressed as follows.

$$y = \frac{[RL]}{[R_T]} = \frac{E}{E_{max}} \tag{7}$$

The concentration [RL] can be expressed according to the law of mass action.

$$[RL] = \frac{[R_T][L]}{K_D^L + [L]} \tag{8}$$

By transforming the law of mass action (Eq. 7) and inserting the derived expression for the degree of receptor occupation y (Eq. 6), we obtain an expression allowing us to predict binding curves for a ligand with a known dissociation constant K_D.

$$\frac{[RL]}{[R_T]} = \frac{E}{E_{max}} = \frac{[L]}{[L] + K_D^L} \tag{9}$$

A necessary condition for this approach is a linear relationship between receptor occupancy [RL]/[RT] and the fractional response E/E_{max}.

$$\frac{[RL]}{[R_T]} \propto \frac{E}{E_{max}} \tag{10}$$

The relation $[RL]/[RT] \propto E/E_{max}$ in equation (11) can be considered as given in case of the interaction of Ang II with the AT_1 receptor since the general prerequisites for the assumption of a linear response-receptor occupancy relation as pointed out by Buchwald [8] are met as (1) Ang II is known to act as a full agonist of AT_1R [9], (2) there occurs no Ca^{2+} signal amplification in the intracellular signal cascade of the AT_1R [10,11], and (3) wild-type AT_1R exceeds no significant constitutive activity [12] regarding the PLC-IP_3/Ca^{2+}-signal pathway [13].

Using the expression for the δ-corrected nanoparticle valency N (Eq. 1), we introduced a modified expression for [L] allowing us to estimate the effective ligand molar concentration $[L]_{NP}$ as a function of the particle's molar concentration c_{NP}, the number of ligands attached to the nanoparticle N_t, and the wrapping fraction δ.

$$N_{NP} = c_{NP} N_A \tag{11}$$

We begin the derivation of $[L]_{NP}$ by assuming a number of particles N_{NP} to attach to a membrane where δ is constant for every particle. In doing so, we can calculate the number of binding ligands on all particles L by multiplying N calculated according to Eq. (2) with the expression for N_{NP} in Eq. (11).

$$L = c_{NP} N_A (\delta N_t + 1)$$

$$L = c_{NP} N_A \delta N_t + c_{NP} N_A \quad \Big| \times \frac{1}{N_A} \qquad [L]_{NP} = \frac{L}{N_A}$$

$$[L]_{NP} = c_{NP} \delta N_t + c_{NP}$$

$$[L]_{NP} = c_{NP} (\delta N_t + 1) \tag{12}$$

The effective ligand concentration $[L]_{NP}$ combined with the free ligand's dissociation constant K_D determined based on data obtained in the Ca^{2+} mobilization assays were employed to predict binding curves for a series of values for δ. To test the significance of our theoretical considerations regarding preferential nanoparticle binding to CCPs, we specifically predicted binding curves for the threshold values of δ (δ = 0.07-0.23) derived from the structural data of the CCPs [14,15]. This allowed us to assess the overlay of experimental nanoparticle binding data and the derived expectation range for δ. The number of ligands attached to a single nanoparticle N_t was previously determined at ~2000 ligands per particle for the used nanoparticle model system [16].

$$\frac{E}{E_{max}} = \frac{c_{NP}(\delta N_t+1)}{c_{NP}(\delta N_t+1)+K_D^L} \qquad (13)$$

Finally, equation (13) - obtained by inserting $[L]_{NP}$ (Eq. 12) for [L] in equation (8) - can be further modified by introducing a Hill-type extension as previously suggested by Buchwald [8] (Eq. 14). Since the Hill coefficient n is a solid measure for the degree of cooperativity α [17], this extension enables our model to account for cooperativity, thereby, significantly increasing its relevance considering multivalent interactions. Consequently, the integration of Hill coefficient values derived from curve fittings of our experimental data into the binding curve predictions resulted in a better overlap of experimental and predicted data.

$$\frac{E}{E_{max}} = \frac{c_{NP}(\delta N_t+1)^n}{c_{NP}(\delta N_t+1)^n+K_D^{L^n}} \qquad (14)$$

For all predicted binding curves log EC_{50} was determined and compared with the values found for nanoparticle binding to untreated and 30 mM M-β-CD pretreated cells and for the free ligand

Lys-Ang II. The residual sum of square (RSS) analysis showed that the curve predicted for δ = 0.10 using the model given in equation (14) had the highest overlap with the experimental data acquired for nanoparticle binding to untreated cells. Also, the found log EC_{50} for δ = 0.10 values aligned best. For M-β-CD pretreated cells on the other hand, the binding curve derived from experimental data laid between the predicted curves for δ of 0.01 and 0 (Fig. 6C).

Finally, the obtained best-fit value for δ was re-integrated into the standard binding saturation model (Eq. 15) modified to account for morphological correspondence δ by substituting the term $[L]_{NP}$ given in equation (12) for [L]. For E and E_{max} we inserted the change of Ca^{2+} level ΔCa^{2+} and maximum change of Ca^{2+} level ΔCa^{2+}_{max} to make the model applicable for data derived from Ca^{2+} mobilization assays.

$$\Delta Ca^{2+} = \Delta Ca^{2+}_{max} \frac{[L]_{NP}}{[L]_{NP}+K_D^L} \qquad (15)$$

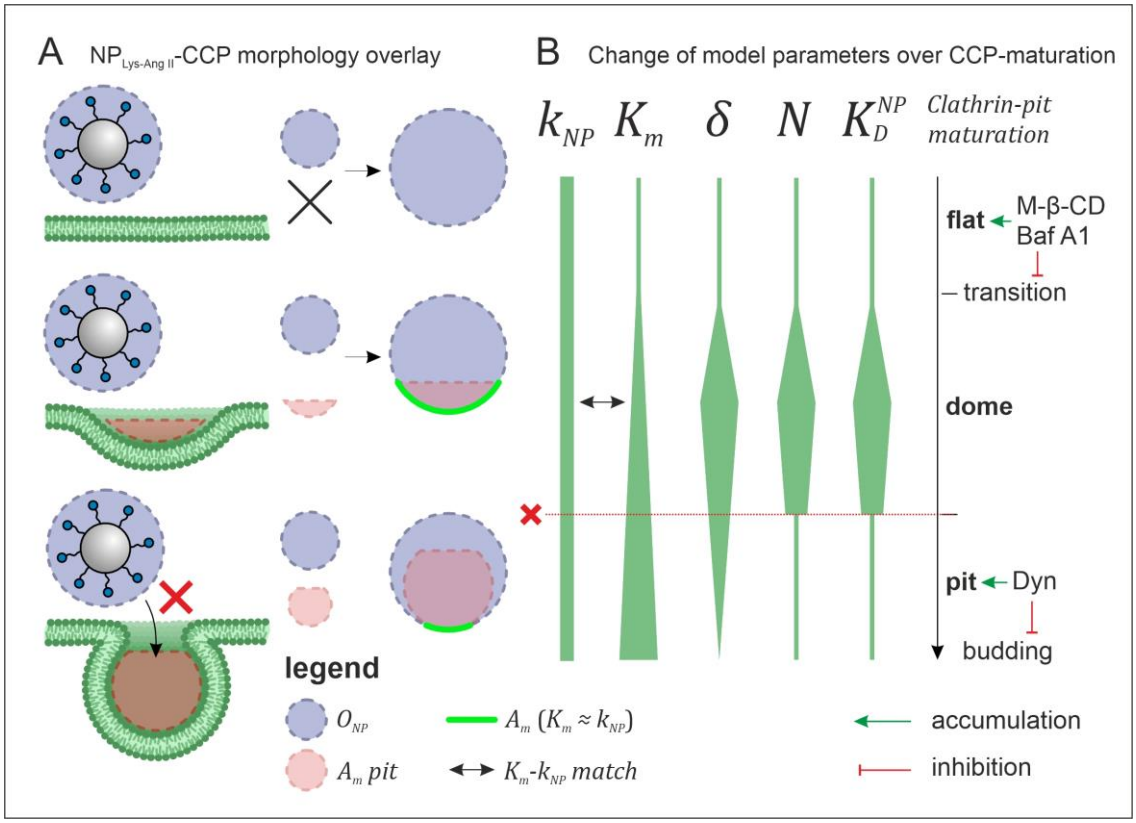

Supplementary Figure 1: Application of CCP binding hypothesis to theoretical to novel constant-area clathrin-coated pit maturation model introduced by Bucher et al. [18]. According to Bucher's model, after the flat-dome-state transition, membrane curvature K_m continuously increases with ongoing maturation of the clathrin-coated pit (A). Applying this model to our theoretical nanoparticle binding model, it turns out that at a certain point in maturation, K_m coincides with the curvature of the nanoparticle k_{NP}. Consequently, at this point in maturation the wrapping fraction δ, the number of binding ligands N, and ultimately the nanoparticles avidity K_D^{NP} will peak. Again, after dome-pit-transition, the accessibility of the clathrin-coated pit for the nanoparticle is expected to be no longer given. All in all, these considerations suggest a preferential binding of ligand-functionalized nanoparticles to clathrin-coated pits in dome-state (B). We conclude from this that the choice of CCP maturation model does not affect the predictions of our theoretical model.

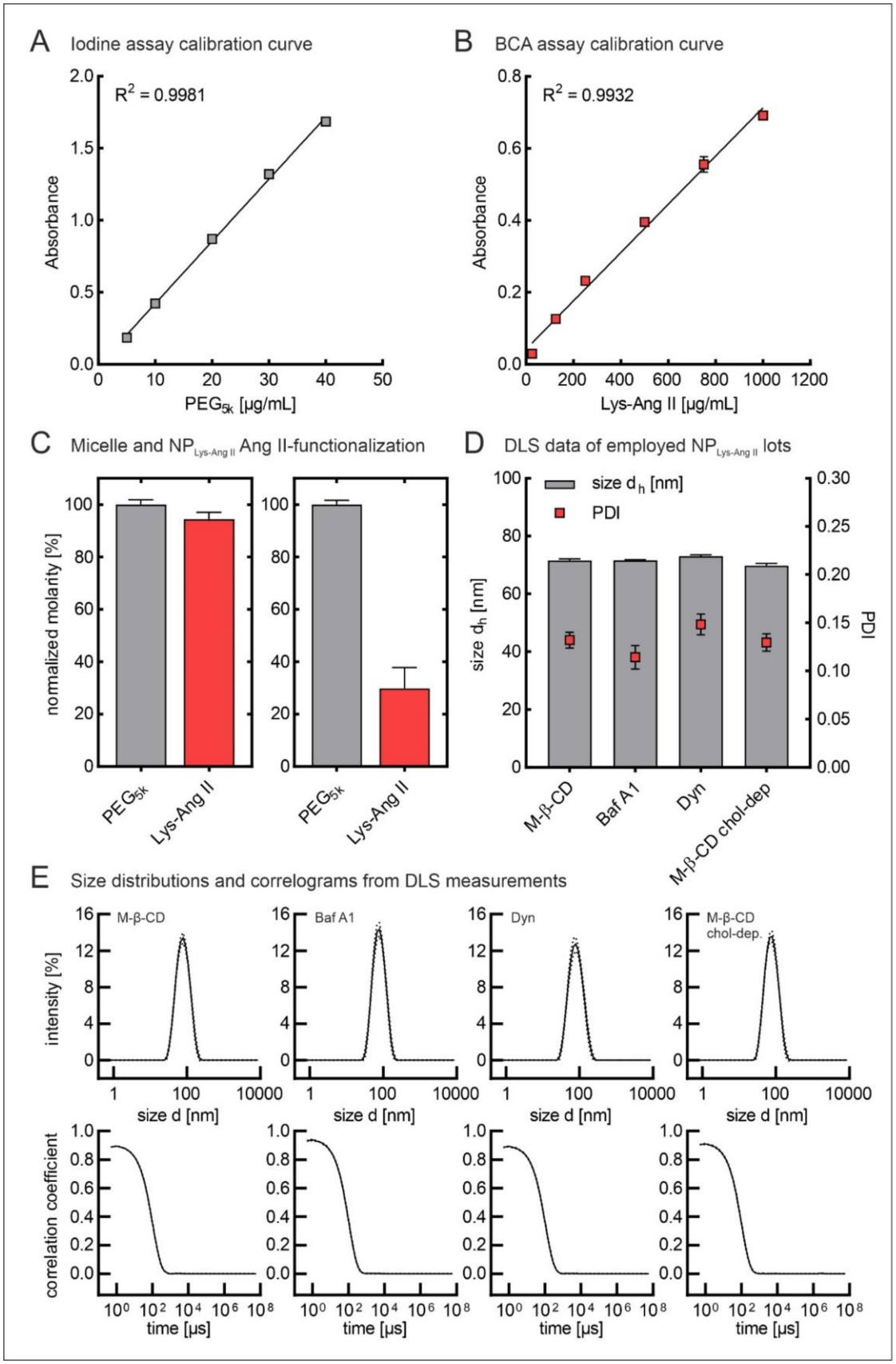

Supplementary Figure 2: Characterization of Lys-Ang II modified PEG_{5k}-PLA_{10k} and $NP_{Lys\text{-}Ang\ II}$ (A, B) Lys-Ang II coupled PEG_{5k}-PLA_{10k} polymer and functionalized

nanoparticles were characterized using Pierce BCA assay and $BaCl_2$ based iodine assay to quantify Lys-Ang II and PEG molarity. Quantification was done via linear regression analysis conducted with serial dilutions of PEG_{5k} (40, 30, 20, 10, and 5 µg/mL) and Lys-Ang II (1000, 750, 500, 250, 125, and 25 µg/mL). (C) Coupling efficiency was quantified as the molar ratio of Lys-Ang II to PEG in Lys-Ang II-PEG-PLA micelles. For EDC/NHS-catalyzed Lys-Ang II functionalization of carboxy-PEG_{5k}-PLA_{10k} it was found to be 94.4 ± 2.7% (mean ± std.). Prepared nanoparticles were determined to carry 29.9 ± 9.0% (mean ± std.) Lys-Ang II ligand. (D) DLS characterization was done for each particle lot prepared for investigation of the three employed inhibitors M-β-CD, Baf A1, and Dyn. Hydrodynamic diameter d_h (z-average) was determined as 71.5 ± 0.5 (M-β-CD), 71.6 ± 0.2 (Baf A1), 73.1 ± 0.5 (Dyn), and 69.8 ± 0.5 (M-β-CD chol-dep). Polydispersity indices (PDI) were 0.13, 0.11, 0.15, and 0.13 (all error-bars reflect standard deviation). All data was derived from intensity-based distributions (E) DLS distribution curves and raw correlation data for each particle lot (dashed lines indicate std., N = 3).

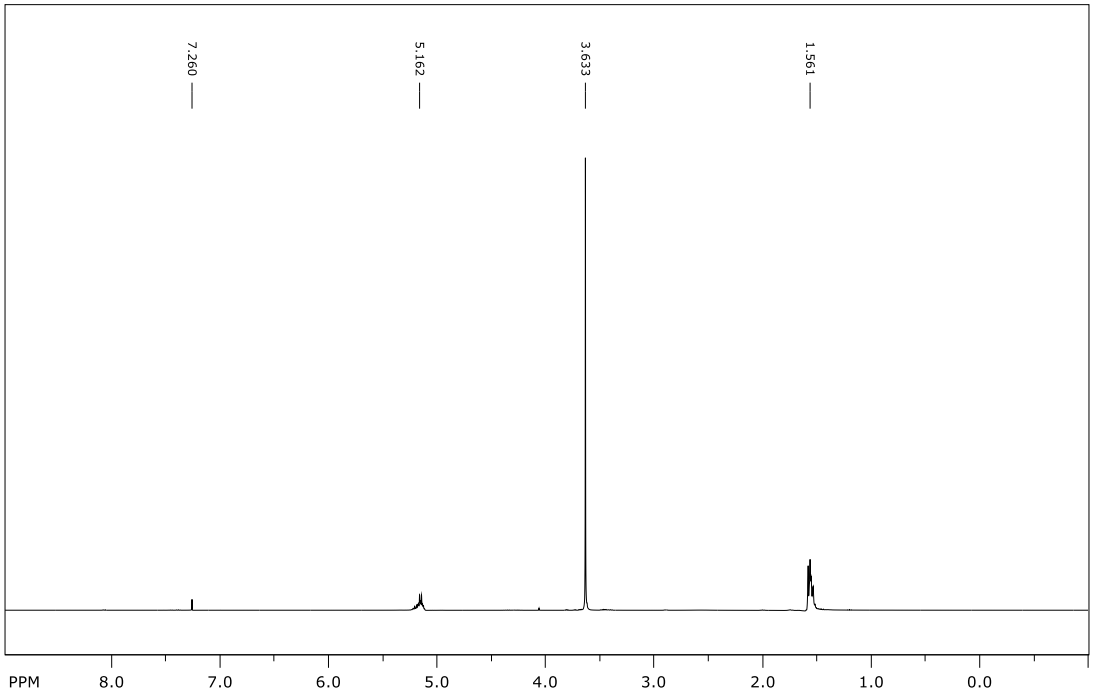

Supplementary Figure 3: ^{1}H-NMR ($CDCl_3$, 400 MHz) of carboxy-PEG_{5k}-PLA_{10k} block copolymer. δ (ppm): 1.561 (-C(CH_3)H-, A_{PLA} CH_3 = 0.8514), 3.633 (-OCH_2CH_2-, A_{PEG} set to 1), 5.162 (-C(CH_3)H-, A_{PLA} CH = 0.2752), 7.260 (solvent peak).

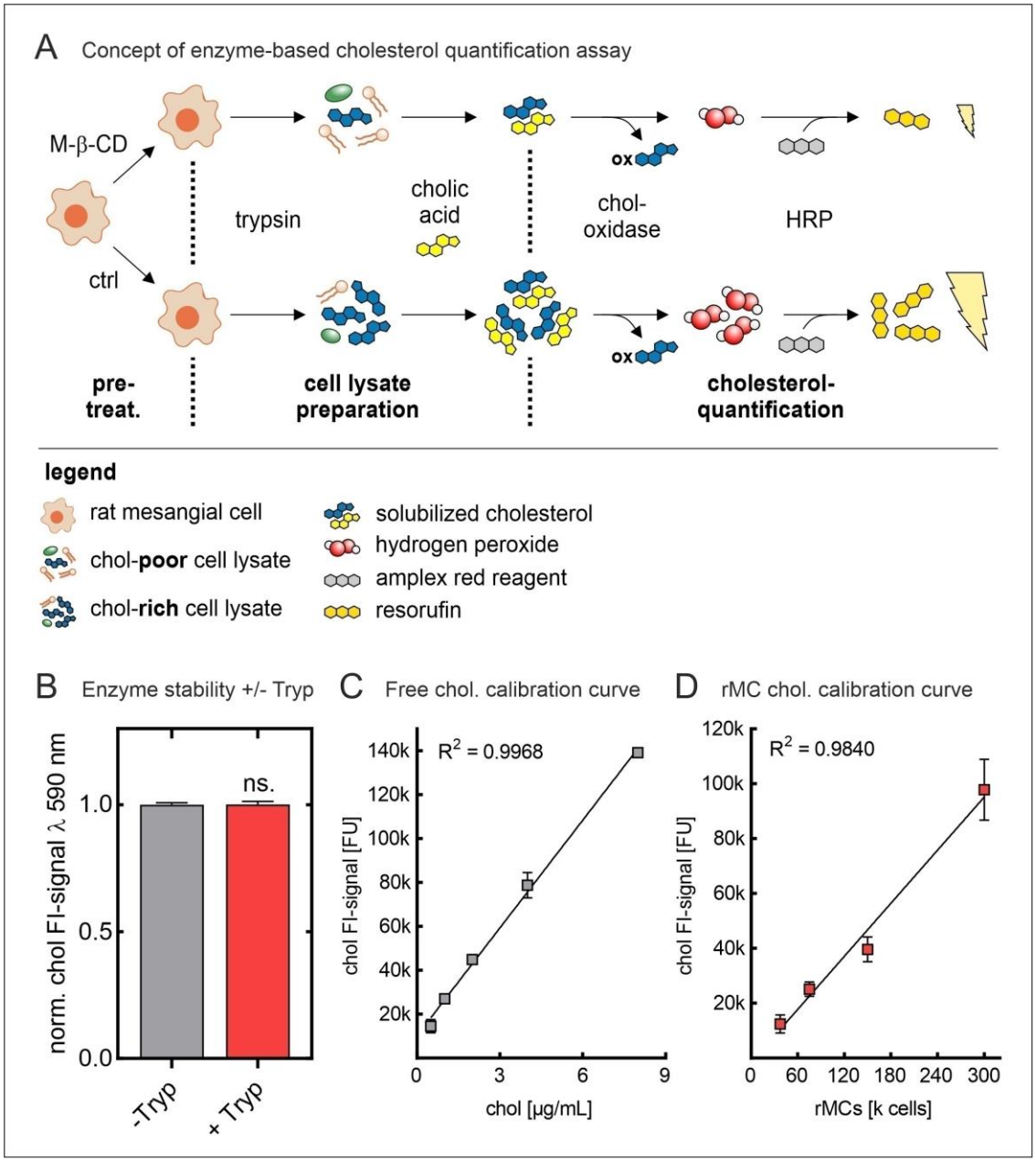

Supplementary Figure 4: Cholesterol Quantification Assay (A) Scheme gives an overview about the sample preparation for Amplex™ Red-based cholesterol quantification assay. (B) Effect of possible residues of endopeptidase trypsin on the enzyme-stability of cholesterol oxidase (chol-oxidase) and horseradish peroxidase (HRP) was tested by performing the assay in presence and absence of 0.016% trypsin measuring 4 µg/mL cholesterol standard. Normalized fluorescence intensity detected was compared via un-paired two-tailed t-test (P = 0.729, t = 0.356, df = 10; ns. - not significant). (C) A serial dilution of cholesterol standard (8, 4, 2, 1, and 0.5 µg/mL) was prepared and measured (ex/em: 544/590 nm) on plate-reader to confirm linearity of obtained results and absence of significant background fluorescence. (D) To confirm linearity and absence of background fluorescence for cholesterol measurements in cells, cell pellets (300, 150, 75, and 37.5 k rMCs) were prepared and treated as shown in the scheme (for details refer to materials and methods section; all error-bars reflect standard deviation).

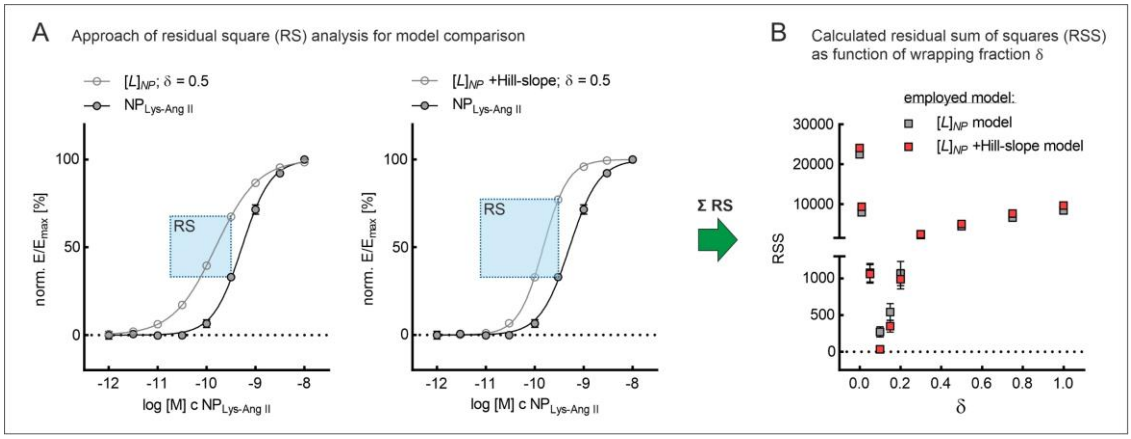

Supplementary Figure 5: Residual sum of square (RSS) analysis conducted for $[L]_{NP}$ based model and $[L]_{NP}$ +Hill-slope based model. (A) Residual squares (RS) were calculated to evaluate overlay of predicted binding curves with experimental data obtained in nanoparticle binding experiments. (B) Residual sum of square (RSS) values were plotted against δ. RSS values were determined for nanoparticle binding data against predicted data derived from basic binding curve model accounting for δ (Eq. 13) and binding curve model with Hill-extension (Eq. 14). Best overlay was found for δ = 0.10 employing binding curve model with Hill-extension (error-bars reflect standard deviation).

Supplementary Table 1: Predicted binding data derived from $[L]_{NP}$ based model (Eq. 13). Data yielded from binding curve predictions employing basic δ-sensitive model (Eq. 13). [a]Dissociation constant K_D for free ligand Lys-Ang II was derived from saturation curve analysis using one-site specific binding model (see Quantification and Statistical Analysis).

			δ									
			0	0.01	0.05	0.10	0.15	0.20	0.30	0.50	0.75	1.0
c_{NP} $[M]$	N_t (14)	K_D $[M]$ [a]	E/E_{max}									
1.00E-12			9.24E-6	1.94E-4	9.33E-4	1.85E-3	2.77E-3	3.69E-3	5.52E-3	9.17E-3	1.37E-2	1.82E-2
3.16E-12			2.92E-5	6.13E-4	2.94E-3	5.84E-3	8.72E-3	1.16E-2	1.73E-2	2.84E-2	4.20E-2	5.53E-2
1.00E-11			9.24E-5	1.94E-3	9.25E-3	1.82E-2	2.71E-2	3.57E-2	5.26E-2	8.47E-2	0.122	0.156
3.16E-11			2.92E-4	6.10E-3	2.87E-2	5.55E-2	8.09E-2	0.105	0.149	0.226	0.305	0.369
1.00E-10	~2000	1.08E-7	9.23E-4	1.90E-2	0.0854	0.157	0.218	0.270	0.357	0.481	0.581	0.649
3.16E-10			2.91E-3	5.78E-2	0.228	0.370	0.468	0.540	0.637	0.745	0.814	0.854
1.00E-9			9.16E-3	0.163	0.483	0.650	0.736	0.788	0.847	0.902	0.933	0.949
3.16E-9			2.84E-2	0.380	0.747	0.855	0.898	0.921	0.946	0.967	0.978	0.983
1.00E-8			8.46E-2	0.660	0.903	0.949	0.965	0.974	0.982	0.989	0.993	0.995

Supplementary Table 2: Predicted binding data derived from $[L]_{NP}$ +Hill-slope based model (Eq. 14). Data yielded from binding curve predictions employing δ-sensitive model modified via Hill-extension (Eq. 14). [a]Dissociation constant K_D for free ligand Lys-Ang II was derived from saturation curve analysis using one-site specific binding model. [b]Hill-coefficient was derived from binding curve analysis of Ca^{2+} mobilization data obtained for Lys-Ang II functionalized nanoparticles employing four-parameter nonlinear regression model (see Quantification and Statistical Analysis).

				δ									
				0	0.01	0.05	0.10	0.15	0.20	0.30	0.50	0.75	1.0
c_{NP} $[M]$	N_t (14)	K_D $[M]$ [a]	n [b]	E/E_{max}									
1.00E-12	~2000	1.08E-7	1.47	3.93 E-8	3.46 E-6	3.49 E-5	9.61 E-5	1.74 E-4	2.65 E-4	4.81 E-4	1.02 E-3	1.85 E-3	2.82 E-3
3.16E-12				2.14 E-7	1.88 E-5	1.90 E-4	5.22 E-4	9.46 E-4	1.44 E-3	2.61 E-3	5.51 E-3	9.96 E-3	1.51 E-2
1.00E-11				1.16 E-6	1.02 E-4	1.03 E-3	2.83 E-3	5.12 E-3	7.79 E-3	1.40 E-2	2.93 E-2	5.1 9E-2	7.71 E-2
3.16E-11				6.33E-6	5.57E-4	5.59E-3	1.52E-2	2.72E-2	4.09E-2	7.19E-2	0.141	0.229	0.312
1.00E-10				3.44E-5	3.02E-3	2.96E-2	7.76E-2	0.132	0.188	0.296	0.471	0.618	0.712
3.16E-10				1.87E-4	1.62E-2	0.142	0.314	0.453	0.558	0.696	0.829	0.898	0.931
1.00E-9				1.02E-3	8.23E-2	0.475	0.713	0.818	0.873	0.926	0.963	0.980	0.987
3.16E-9				5.50E-3	0.328	0.831	0.931	0.961	0.974	0.985	0.993	0.996	0.997
1.00E-8				2.92E-2	0.726	0.964	0.987	0.993	0.995	0.997	0.999	1.00	1.00

References

[1] M Deserno, T Bickel, Wrapping of a spherical colloid by a fluid membrane, Europhysics Letters (EPL) 62 (2003) 767–774.

[2] J. Agudo-Canalejo, R. Lipowsky, Uniform and Janus-like nanoparticles in contact with vesicles: energy landscapes and curvature-induced forces, Soft matter 13 (2017) 2155–2173.

[3] A. Gray, E. Abbena, S. Salamon, Modern differential geometry of curves and surfaces with Mathematica, 3. ed. ed., Chapman & Hall/CRC, Boca Raton, Fla., 2006.

[4] B. O'Neill, Elementary differential geometry, Revised 2. ed. ed., Elsevier Academic Press, Amsterdam, 2006.

[5] V. Ramanan, N.J. Agrawal, J. Liu, S. Engles, R. Toy, R. Radhakrishnan, Systems biology and physical biology of clathrin-mediated endocytosis, Integrative biology quantitative biosciences from nano to macro 3 (2011) 803–815.

[6] N.J. Agrawal, J. Nukpezah, R. Radhakrishnan, Minimal mesoscale model for protein-mediated vesiculation in clathrin-dependent endocytosis, PLoS computational biology 6 (2010) e1000926.

[7] A.H. Bahrami, R. Lipowsky, T.R. Weikl, The role of membrane curvature for the wrapping of nanoparticles, Soft matter 12 (2016) 581–587.

[8] P. Buchwald, A single unified model for fitting simple to complex receptor response data, Scientific reports 10 (2020) 13386.

[9] Y.H. Feng, K. Noda, Y. Saad, X.P. Liu, A. Husain, S.S. Karnik, The docking of Arg2 of angiotensin II with Asp281 of AT1 receptor is essential for full agonism, The Journal of biological chemistry 270 (1995) 12846–12850.

[10] S.J. Forrester, G.W. Booz, C.D. Sigmund, T.M. Coffman, T. Kawai, V. Rizzo, R. Scalia, S. Eguchi, Angiotensin II Signal Transduction: An Update on Mechanisms of Physiology and Pathophysiology, Physiological reviews 98 (2018) 1627–1738.

[11] M. de Gasparo, K.J. Catt, T. Inagami, J.W. Wright, T. Unger, International union of pharmacology. XXIII. The angiotensin II receptors, Pharmacological reviews 52 (2000) 415–472.

[12] D. Hoyer, E.P. Zorrilla, P. Cottone, S. Parylak, M. Morelli, N. Simola, J.D. Lane, M.M. Morgan, M.J. Christie, C.J. Hillard, A.J. Budney, R.G. Vandrey, T. Robbins, P. Nencini, M.S. Milella, N. Mirza, V.L. Harvey, T. Dickenson, S. Miyamoto, O. Almeida, N. Sousa, S. Yu, A. Absalom, D. Menon, P.L. Delgado, C. Höschl, T.L. White, R. Depue, C. Baltes, T. Mueggler, M. Rudin, P.J. Flor, I. Neumann, C.A.

Erickson, D.J. Posey, K. Blankenship, K.A. Stigler, C.J. McDougle, E. Sibille, N. Edgar, M. Lader, T. Duka, E. Childs, B. Hahn, J. Harro, P. Newhouse, H. Wilkins, Y. Alici, W. Breitbart, E. Nestler, A.R. Isles, L. Wilkinson, S. Pandey, S.G. Siris, P. Willner, M. Billiard, B. Lemmer, J.-M. Scherrmann, L.H. Price, T.J. Banasikowski, R.J. Beninger, J. Harvey, B.E. Leonard, K. Wolff, A. Padhi, N. Fineberg, W.H. Meck, C.V. Buhushi, L.R. McMahon, Y. Chudasama, M. Kuhar, J.D. Uys, P.W. Kalivas, M. Shoaib, D. Bertrand, H. Rollema, R.S. Hurst, M. Bloch, J.F. Leckman, B.J. Sahakian, S. Morein-Zamir, A. Jackson, B.J. Harrison, C. Pantelis, I. Hindmarch, A.J. Bond, J.M. Monti, D.R. Christensen, W.K. Bickel, M.J. Bubar, K.A. Cunningham, C.A. Franco, M. Potenza, M.-I. López-Ibor, J.J. López-Ibor, J.H. Friedman, A. Hofer, M.I. Palmatier, R.A. Bevins, T. Tzschentke, D. Roberts, S. Anagnostaras, J.R. Sage, S.A. Carmack, S.J. Kohut, A.L. Riley, R.F. Mucha, J. Prickaerts, O. Stiedl, S.O. Ögren, K. Nader, O. Hardt, P.V. Migues, A. Christopoulos, G.D. Stewart, P.M. Sexton, Y. Shaham, S.G. Nair, S.H. Heil, S.C. Sigmon, S.T. Higgins, M.N. Branch, M. Cain, M.T. Bardo, R.L. Balster, S. Walsh, R. de Rijk, R. de Kloet, C.H. Bourke, M.J. Owens, C. Viollet, J. Epelbaum, K. Mann, F. Kiefer, M. Owens, C. Bourke, H. McAllister-Williams, A. Marneros, R. Andrade, I. Izquierdo, L.R.M. Bevilaqua, M. Cammarota, C. Hiemke, M.I. Colado, R. Green, Constitutive Activity, in: I.P. Stolerman (Ed.), Encyclopedia of Psychopharmacology, Springer Berlin Heidelberg, Berlin, Heidelberg, 2010, p. 349.

[13] M. Auger-Messier, G. Arguin, B. Chaloux, R. Leduc, E. Escher, G. Guillemette, Down-regulation of inositol 1,4,5-trisphosphate receptor in cells stably expressing the constitutively active angiotensin II N111G-AT(1) receptor, Molecular endocrinology (Baltimore, Md.) 18 (2004) 2967–2980.

[14] A.E. Nel, L. Mädler, D. Velegol, T. Xia, E.M.V. Hoek, P. Somasundaran, F. Klaessig, V. Castranova, M. Thompson, Understanding biophysicochemical interactions at the nano-bio interface, Nature materials 8 (2009) 543–557.

[15] N. Hoshyar, S. Gray, H. Han, G. Bao, The effect of nanoparticle size on in vivo pharmacokinetics and cellular interaction, Nanomedicine (London, England) 11 (2016) 673–692.

[16] S. Maslanka Figueroa, D. Fleischmann, S. Beck, A. Goepferich, The Effect of Ligand Mobility on the Cellular Interaction of Multivalent Nanoparticles, Macromolecular bioscience (2020) e1900427.

[17] C.A. Hunter, H.L. Anderson, What is cooperativity?, Angewandte Chemie International Edition 48 (2009) 7488–7499.

[18] D. Bucher, F. Frey, K.A. Sochacki, S. Kummer, J.-P. Bergeest, W.J. Godinez, H.-G. Kräusslich, K. Rohr, J.W. Taraska, U.S. Schwarz, S. Boulant, Clathrin-adaptor ratio and membrane tension regulate the flat-to-curved transition of the clathrin coat during endocytosis, Nature communications 9 (2018) 1109.

Chapter 5

Impact of Interferon-γ on the Target Cell Tropism of Nanoparticles

Published in Journal of Controlled Release

2023, **362**, 325-341

This chapter was published as: O. Zimmer, M. Walter, M. Remmert, O. Maier, R. Witzgall A. Goepferich, Impact of Interferon-γ on theTarget Cell Tropism of Nanoparticles. *Journal of Controlled Release* 362, 325–341 (2023).

Abstract

Interferon-γ (IFN-γ) is well known to reduce the infectivity of viral pathogens by altering their tissue tropism. This effect is induced by upregulation of cholesterol 25-hydroxylase (CH25H). Given the similarity of viral pathogens and ligand-functionalized nanoparticles in the underlying strategy of receptor-mediated cell recognition, it appears conceivable that IFN-γ exceeds similar effects on nanoparticles. Concretely, IFN-γ-induced activation of CH25H could decrease nanoparticle avidity for target cells via depletion of clathrin-coated pits. We hypothesized that this effect would cause deterioration of target-cell specific accumulation of nanoparticles. To prove our hypothesis, we investigated the cell tropism of angiotensin II functionalized nanoparticles ($NP_{Lys\text{-}Ang\ II}$) in a co-culture system of angiotensin II subtype 1 receptor (AT_1R) positive rat mesangial target cells (rMCs) and AT_1R-negative HeLa off-target cells. In the presence of IFN-γ we observed an up to 5-fold loss of target cell preference for $NP_{Lys\text{-}Ang\ II}$. Thus, our *in vitro* results suggest a strong influence of IFN-γ on nanoparticle distribution, which is relevant in the context of nanotherapeutic approaches to cancer treatment, as IFN-γ is strongly expressed in tumors. For the target cell tropism of viruses, our results provide a conclusive hypothesis for the underlying mechanism behind non-directed viral distribution in the presence of IFN-γ.

Graphical Abstract

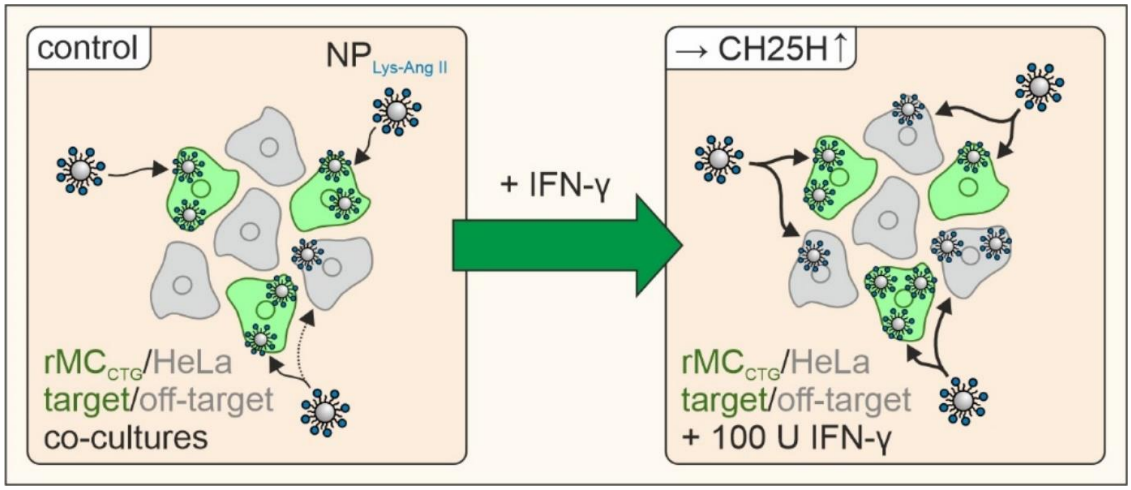

The graphical abstract illustrates that Interferon-γ (IFN-γ) was found to hinder target cell specific nanoparticle accumulation via upregulation of cholesterol 25-hydroxylase (CH25H). Interferon-γ was thus identified as a biologically relevant factor potentially affecting nanoparticle biodistribution by altering membrane morphology.

Introduction

Ligand-functionalized nanoparticles and viral pathogens show similarities in cell recognition. They share the strategy of using ligand-receptor interactions to identify target cells. In fact, many research groups successfully implemented virus-mimetic designs to achieve target-cell or tissue-specific nanoparticle accumulation [1–3]. This raises the question whether factors that influence distribution of viral pathogens may also be of relevance for the bio-distribution of nanoparticles. For instance, the cytokine interferon-γ (IFN-γ) is an essential component of the organism's immunological line of defense and has long been known to reduce *in vitro* infectivity [4]. It does so, by altering the tissue tropism of viral pathogens *in vivo* [5–11]. In the case of viral infections this reduces the avidity of viral particles for target cells and consequently their chances for replication. To the best of our knowledge, it has not been investigated whether IFN-γ affects the target cell avidity of nanoparticles to date. Investigating this issue is important because reduced target cell avidity could have relevant influences on *in vivo* particle biodistribution. Therefore, it was our goal to scrutinize if IFN-γ could have an impact on ligand-functionalized nanoparticle distribution as well.

Regarding the effects of IFN-γ on viral pathogens, upregulation of cholesterol 25-hydroxylase (CH25H) has been described as a key player for changing viral target cell tropism [12]. For the elucidation of the underlying mechanism, the focus has been almost exclusively on the impact of the oxidation product 25-hydroxycholesterol (25-HC) on cell physiology. Broad antiviral activity has been described for 25-HC *in vitro* and *in vivo* [13]. However, the threat that cholesterol extraction reduces endocytosis via clathrin-coated pits (CCPs) [14] has been ignored. In fact with our previous work [15], we have shown that the basic concept of nanoparticle-membrane interactions being mediated by local membrane curvature [16–20] is expandable to the case of ligand functionalized nanoparticles. The presence of CCPs, which excellently match nanoparticles in curvature and size [21–23], turns out to be essential for binding to their receptor-positive target cells. CCP depletion as a result of lowering the cholesterol content of cell membranes reduced nanoparticle avidity (K_D) by a factor of 50 [15]. A cholesterol lowering effect of CH25H and its metabolite 25-HC has been extensively described in literature demonstrating increased degradation [24,25] and excretion [26,27] as well as decreased synthesis [28,29] and uptake [30,31] of cholesterol. Therefore, we hypothesized that the presence of IFN-γ could have a significant effect on the target cell

specific nanoparticle accumulation in target/off-target cell co-cultures (Fig. 1). With this, we could shed a first light on the relevance of IFN-γ regarding nanoparticle biodistribution *in vivo*.

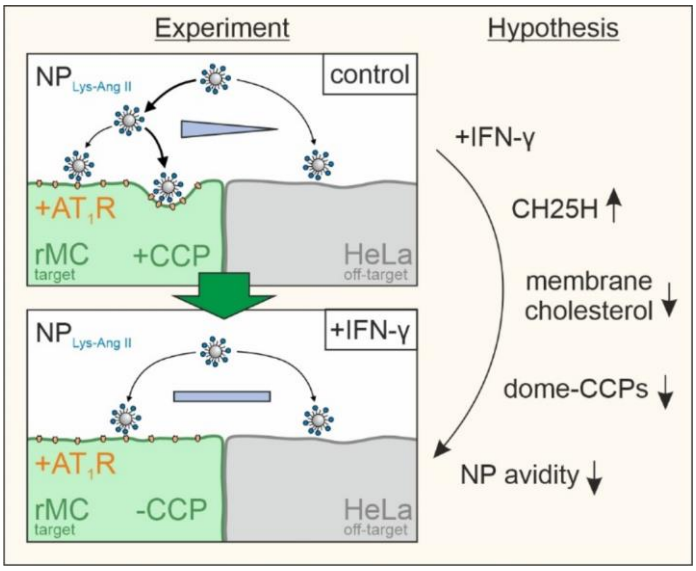

Figure 1: Hypothesis on IFN-γ induced impairment of target-cell specific nanoparticle accumulation. The aim of our experimental work was to investigate the influence of the cytokine IFN-γ on the biodistribution of a ligand-functionalized nanoparticle in a simple model system namely an rMC/HeLa (target/off-target) cell co-culture. Our hypothesis is that IFN-γ treatment lowers membrane cholesterol levels via inducing the expression of CH25H, thereby inhibiting the formation of CCPs. Based on our previous work on the role of CCPs in the binding of multivalent nanoparticles, in this case a reduction of the particles' avidity for its target cell would be expected. As a consequence of the lowered avidity, a reduction in target cell-directed accumulation of the particles can be expected (blue bars indicate particle binding preference). Abbreviations: $NP_{Lys\text{-}Ang\ II}$ – lysin-angiotensin II functionalized nanoparticle, AT_1R – angiotensin II receptor subtype 1, rMC – rat mesangial cell, (dome)-CCP – (dome-shaped) clathrin-coated pit, IFN-γ – interferon-γ, CH25H – cholesterol 25-hydroxylase.

To test our hypothesis, we used polymer-based nanoparticles functionalized with lysin-N-modified angiotensin II ($NP_{Lys\text{-}Ang\ II}$). This modification enabled angiotensin II subtype 1 receptor (AT_1R) mediated target cell recognition [32]. To investigate possible effects of IFN-γ on target/off-target cell co-cultures, we used AT_1R positive rat mesangial cells (rMCs) as target cells and AT_1R negative HeLa cells as off-target cells. We employed this experimental setup to follow the impact of IFN-γ on particle performance parameters

like preferential uptake of $NP_{Lys\text{-}Ang\ II}$ by rMC cells. Additionally, we investigated the ability of $NP_{Lys\text{-}Ang\ II}$ to accumulate in rMCs while increasing the spatial distance between target cells. We used flow-cytometry based analysis, to differentiate nanoparticle uptake by target- and off-target cells. Choi *et al.* and Kirpotin *et al.* had shown that ligand-functionalized nanoparticles have beneficial effects on target cell accumulation mainly on the tissue level, rather than affecting whole-body biodistribution [33,34]. Therefore, we considered the cell co-culture experiment setup as a suitable *in vitro* model for mimicking the *in vivo* situation. Also, since Singh *et al.* and Ouyang *et al.* previously observed dose dependent effects on nanoparticle biodistribution [35,36], we investigated the influence of IFN-γ on $NP_{Lys\text{-}Ang\ II}$ distribution in co-cultures as a function of molar particle concentration.

Overall our investigations are intended to enhance the limited understanding on the fate of ligand-functionalized nanoparticles in biological systems which has so far been a major hurdle in clinical development [37]. This dilemma becomes obvious when considering that none of the many promising candidates tested [38] has achieved approval for clinical use yet [39,40]. Therefore, our findings may also be of importance to application-oriented scientists aiming to optimize the biodistribution of nanoparticle-based therapeutics. Possible effects of IFN-γ could prove to be highly relevant considering targeted tumor therapy. Tissue concentrations of IFN-γ were found to be increased up to 10-fold in tumors [41–43] compared to healthy tissue. Therefore, *in vitro* observations regarding effects of IFN-γ on nanoparticle distribution might be highly relevant for nanoparticle based tumor therapies large proportions of which are targeted cancer therapy [44,45]. Efficient delivery in this context remains a largely unmet need to date [46].

Results

Particle development and Cell Co-Culture Model

The aim of our study was to investigate effects of IFN-γ on the distribution of ligand functionalized nanoparticles between target and off-target cells. For this purpose, we employed $NP_{Lys\text{-}Ang\ II}$ as a ligand functionalized model particle as the first building block of our experimental setup. The particles were characterized for size, size distribution, and particle concentration via nanoparticle tracking analysis (NTA). Results confirmed that particle size (d_{NP}) was in good correspondence with CCP morphology [21,47] (around 90 nm) and a narrow size distribution (PDI consistently ≤ 0.2, Eq. 1) for $NP_{Lys\text{-}Ang\ II}$ (Fig. 2A, SI Fig. 1A to D). We furthermore used NTA to confirm colloidal stability and absence of aggregation over the time of investigation. These properties can be considered as confirmed for our model particle, as no changes were observed for size or PDI over time (Fig. 2B, SI Fig. 1E to H). As further method for characterization of our nanoparticles, we employed transmission electron microscopy (TEM) (Fig. 2C).
As a second tool for our investigations, we required a target/off-target cell co-culture system. Since the chosen model particle carried angiotensin II as its targeting ligand, we decided to establish a co-culture of AT_1R-positive rat mesangial cells (rMC) and AT_1R-negative HeLa cells. This model was also chosen to draw on previous findings on the influence of established CCP inhibitors on particle-cell interactions for the interpretation of the results found here.

Finally, we attached a red-fluorescent label to our model particles and loaded rMC target cells with a green-fluorescent dye. Thus, using flow cytometric analysis, we were able to divide the obtained data sets into four sub-sets. These were: (1) HeLa cells that had not taken up particles ($HeLa^{-NP}$), (2) HeLa cells that had taken up particles ($HeLa^{+NP}$), (3) rMCs that had not taken up particles (rMC^{-NP}), and (4) rMCs that had taken up particles (rMC^{+NP}). Within these sub-sets, the number of events contained (N) and the particle fluorescence intensity (I_{NP}) were measured. This simple system was used to assess the distribution of particles between the two cell types and as a surrogate for nanoparticle biodistribution on the tissue level.

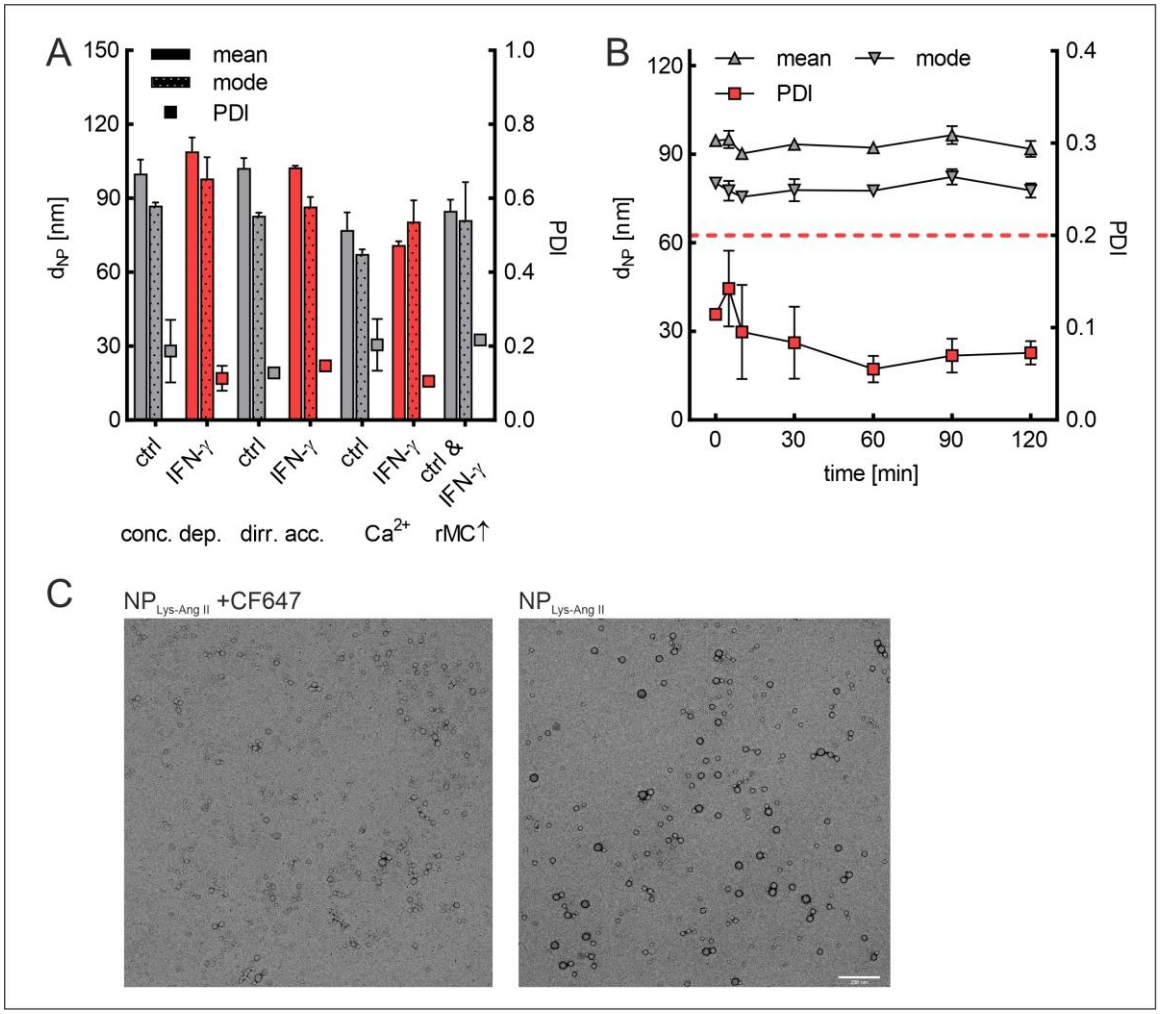

Figure 2: Size and polydispersity data for $NP_{Lys\text{-}Ang\ II}$ derived from nanoparticle tracking analysis. TEM images of the investigated particle species. (A) Mean and mode of hydrodynamic diameter (d_{NP}) and polydispersity indices (PDI) of prepared particle lots for experiments investigating concentration dependency (conc. dep.) of preferential uptake and targeting efficiency and directed accumulation (dir. acc.) in presence or absence of IFN-γ (IFN-γ /ctrl). Also, particle lots used for Ca^{2+} mobilization assay (Ca^{2+}) and investigation of particle distribution in rMC/HeLa co-cultures with increasing target cell proportion (rMC↑) were characterized for size and PDI. (B) Stability of $NP_{Lys\text{-}Ang\ II}$ in rMC/HeLa cell co-cultures was tested over the intended time of incubation to be applied in nanoparticle uptake experiments. Statistical significance of d_{NP} or PDI deviations from baseline (t = 0 min) was tested via one-way ANOVA with subsequent Dunnett's multiple comparison test (F_{mean} (DFn = 6, DFd = 12) = 2.63, P = .07; F_{mode} (DFn = 6, DFd = 12) = 1.85, P = .17; F_{PDI} (DFn = 6, DFd = 12) = 2.26, P = .11; error bars indicate SD). (C) Representative TEM images of uranyl acetate negative stained $NP_{Lys\text{-}Ang\ II}$ CF647 (left) and $NP_{Lys\text{-}Ang\ II}$ (right) samples (both 20,000- fold magnification, white bar indicates 250 nm).

Effect of IFN-γ on Particle Preferential Uptake and Targeting Efficiency

Our first aim was to investigate whether an IFN-γ-induced upregulation of CH25H [12] leads to a reduction of target cell-specific accumulation of ligand-functionalized nanoparticles. This effect could be expected as CH25H induces a decrease in membrane cholesterol content [48] which diminishes membrane fluidity [49,50] and the density of clathrin-coated pits [51,52] which are both beneficial for an endocytic cell uptake. To be able to correlate IFN-γ effects on nanoparticle distribution in cell co-culture with upregulation of CH25H, it was necessary to examine first the effect of IFN-γ on the target cell population. We quantified CH25H in untreated and IFN-γ pre-treated rMCs using a sandwich-ELISA. The same experiment was conducted on HeLa cells to serve as off-target population in order to investigate whether IFN-γ induced effects occurred equally in both cell lines or specifically in the target or off-target population. The measurements showed a significant increase of CH25H levels in IFN-γ treated rMCs. After 24 h in presence of 100 U/mL IFN-γ, CH25H levels increased by 55% (CH25H [ng/mL] in 90% confluent T75 flask, ctrl: 1.49±0.07 ng/mL, IFN-γ: 2.24±0.59 ng/mL, mean±SD). Meanwhile, no significant effect of IFN-γ on HeLa cells was detected (Fig. 3A and B). We also conducted $NP_{Lys\text{-}Ang\ II}$ cell binding studies on rMCs using a Ca^{2+} mobilization assay. Herein, we provide experimental data on the effect of IFN-γ on CCPs by comparing the measured shift in log EC_{50} value with the shift found for established CCP inhibitors in previous work [15]. Binding was investigated in presence and absence of 100 U/mL IFN-γ (24 h incubation ahead of measurement) (Fig. 3C) and a log EC_{50} shift of 1.3 log-steps was observed (Fig. 3D) which is in good alignment with established CCP inhibitors (e.g., methyl-β-cyclodextrin: 1.7 log-steps). The concentration of 100 U/mL IFN-γ in our experiments was chosen based on previous work on the influence of IFN-γ on the infectivity of viral pathogens [4,8,53] and on the progression of cancer [54], in which concentrations of this magnitude were used.

To investigate the impact of the observed CH25H upregulation on the cell co-culture distribution of our $NP_{Lys\text{-}Ang\ II}$ model particle, we performed particle uptake experiments on rMC_{CTG}/HeLa cell co-cultures pretreated with the same IFN-γ concentration. Our aim was to follow two distinct phenomena: (1) preferential uptake and (2) targeting efficiency. For this purpose, we defined two quantitative performance parameters derivable from flow cytometry data (methods Eqs. 4 and 5, SI text).

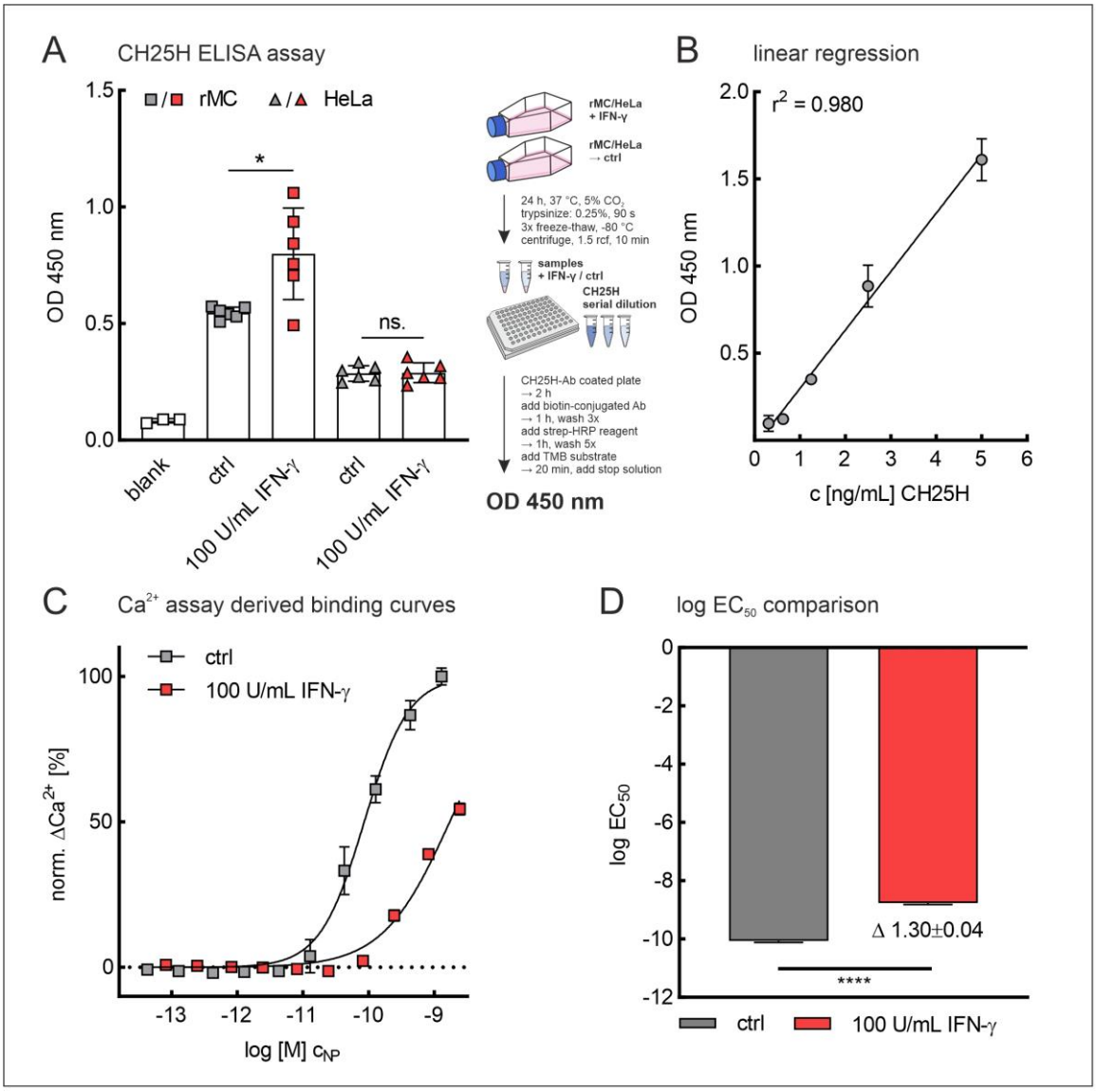

Figure 3: IFN-γ induces increase of CH25H levels in rMCs and decrease in $NP_{Lys\text{-}Ang\ II}$ binding ability. (A) Quantification of CH25H in rMCs and HeLa cells upon 100 U/mL IFN-γ treatment for 24 h using ELISA. Statistical significance of CH25H level changes were tested using Welch t-test (two-tailed, rMC: P = .025, t = 3.13, d_f = 5.16; HeLa: P = .918, t = 0.106, d_f = 9.47). (B) Linear regression obtained measuring CH25H standard serial dilution (5, 2.5, 1.25, 0.63, and 0.31 ng/mL). (C) Binding curves for $NP_{Lys\text{-}Ang\ II}$ obtained from Ca^{2+} mobilization assay performed on untreated rMCs (ctrl) and on rMCs pretreated with 100 U/mL IFN-γ for 24 h (100 U/mL IFN-γ). (D) Comparison of the calculated log EC_{50} values. Here, Δ indicates the number of log-steps (mean ± standard error of mean) by which log EC_{50} increased upon IFN-γ treatment. Statistical significance was tested using unpaired t-test (two-tailed, P < .0001, t = 35.4, d_f = 4; all error bars indicate SD).

During the acquisition of these performance parameters, first interesting observations regarding the concentration dependency of preferential uptake and targeting efficiency were made in control experiments. These experiments were conducted using rMC_{CTG}/HeLa co-cultures that were not treated with IFN-γ ahead of $NP_{Lys\text{-}Ang\ II}$ incubation. Preferential uptake was calculated as the ratio of particle number taken up by rMCs to particle number taken up by HeLa cells (Eq. 4). This ratio plotted against the logarithm of the molar particle concentration showed a broad maximum in the high picomolar to low nanomolar range (0.3 to 1 nM). At higher as well as at lower concentrations, the preferential uptake decreased (Fig. 4A). Targeting efficiency was calculated as the ratio of rMCs (target) to HeLa (off-target) cells which had taken up particles. By plotting the calculated targeting efficiency against the logarithm of the molar particle concentration, we found that at higher concentrations equal proportions of the target and off-target cell populations take up particles. At these concentrations, we obtain a target efficiency of about 1, which means that no targeting is detectable. Only at very low concentrations (10 pM), almost no off-target cells take up particles anymore, while still a significant fraction of target cells takes up particles. Consequently, we yield a targeting efficiency > 1. If we plot the proportions of the recorded data sub-sets against log c_{NP} in a heat map, we can clearly see that a targeting efficiency is only detectable at very low concentrations and that this is almost completely reversed by IFN-γ (Fig. 5A).

Next, we compared results obtained in these control experiments with results from rMC_{CTG}/HeLa co-cultures treated with IFN-γ. Again, we analyzed the quantitative performance parameters introduced in Eq. 4 and 5 as a function of particle concentration. Multiple effects of IFN-γ on particle distribution were apparent. Firstly, flow cytometry data sets obtained from rMC_{CTG}/HeLa incubated with 3 nM $NP_{Lys\text{-}Ang\ II}$ revealed a decrease of preferential uptake (Fig. 4B and C). While rMCs show a 3-fold higher particle uptake in untreated cell co-cultures, it is only 2-fold higher after IFN-γ treatment. This loss was mainly due to higher particle uptake by off-target HeLa cells, whereas uptake by rMCs remained almost unchanged.

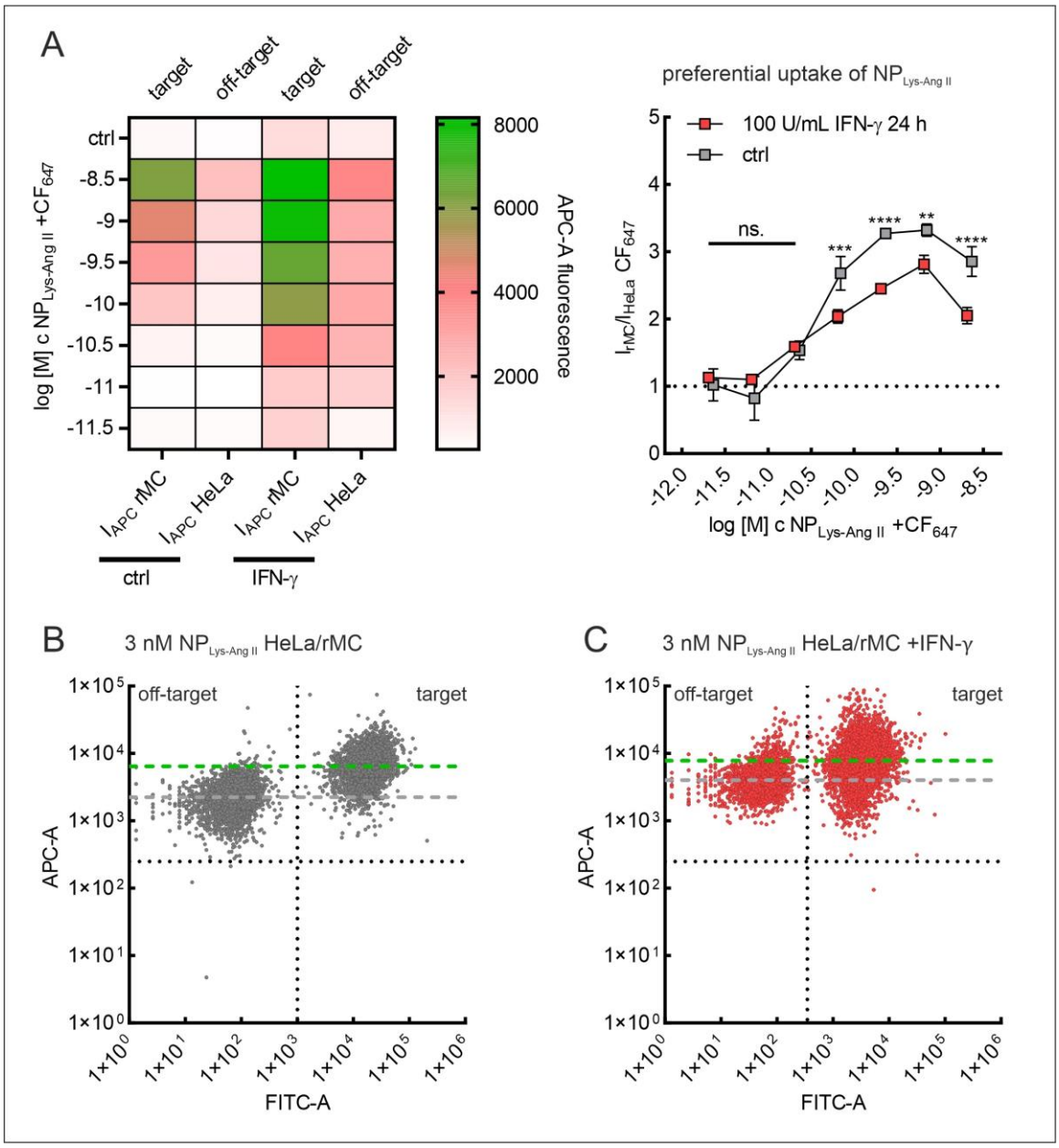

Figure 4. Flow-cytometry based assessment of IFN-γ treatment effect on preferential uptake of $NP_{Lys\text{-}Ang\ II}$. (A) Heatmap represents geometrical means of fluorescence intensity detected for each population in APC-channel. Plot of I_{rMC}/I_{HeLa} CF_{647} against logarithmic molar particle concentration indicates concentration dependency of $NP_{Lys\text{-}Ang\ II}$ preferential uptake into rMC target cells. Statistical significance of IFN-γ effect and concentration dependence were assessed using two-way ANOVA with subsequent Sidak's multiple comparisons test (ns. - not significant, ** P < .01, *** P < .001, **** P < .0001; $F_{IFN\text{-}\gamma}$ (DFn = 1, DFd = 26) = 37.1, P < .0001; F_{cNP} (DFn = 6, DFd = 26) = 139, P < .0001; error bars indicate SD). Representative FITC-A/APC-A dot plots of rMC_{CTG}/HeLa cell co-cultures incubated with 3 nM $NP_{Lys\text{-}Ang\ II}$ (2 h) untreated (B) or pre-treated with 100 U/mL IFN-γ for 24 h (C). Grey/green dashed line represents geometrical mean of HeLa/rMC_{CTG} population.

Secondly, flow cytometry data sets of rMC_{CTG}/HeLa cell co-cultures incubated with lower $NP_{Lys\text{-}Ang\ II}$ concentrations point in a similar direction for the effects of IFN-γ on targeting efficiency (Eq. 5). As for the case of preferential uptake described above, the sharp decrease in targeting efficiency is mainly due to a large increase in the proportion of HeLa cells that take up $NP_{Lys\text{-}Ang\ II}$ (ctrl: 4.7%, IFN-γ : 33%, 7-fold increase) (Fig. 5B and C).

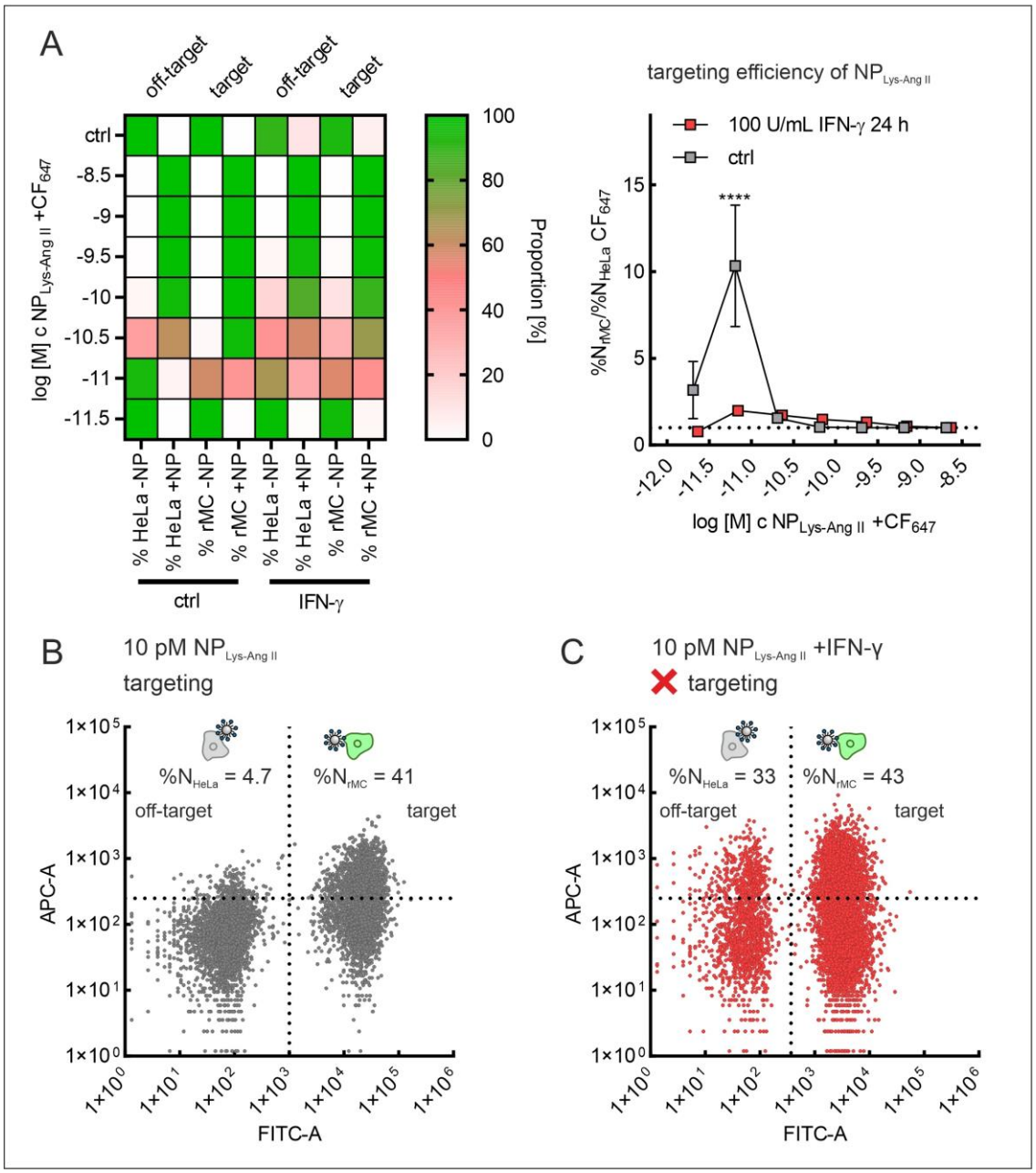

Figure 5. Flow-cytometry based assessment of IFN-γ treatment effect on targeting efficiency of $NP_{Lys\text{-}Ang\ II}$. (A) Heatmap represents the proportion of NP-negative or -positive events (-NP/+NP) events for target or off-target population (rMC/HeLa) in untreated or pre-treated cell co-cultures (ctrl/IFN-γ). Plot of $\%N_{rMC}/\%N_{HeLa}$ CF_{647} against logarithmic molar particle concentration. Statistical significance of IFN-γ effect and concentration dependence were assessed using two-way ANOVA with subsequent Sidak's multiple comparisons test (**** $P < .0001$; $F_{IFN\text{-}\gamma}$ (DFn = 1, DFd = 26) = 15.3, P = .0006; F_{cNP} (DFn = 6, DFd = 26) = 17.7, $P < .0001$; error bars indicate SD). Representative FITC-A/APC-A dot plots of rMC_{CTG}/HeLa cell co-cultures incubated with 10 pM $NP_{Lys\text{-}Ang\ II}$ (2 h) untreated (B) or pre-treated with 100 U/mL IFN-γ for 24 h (C). In addition, the graphs indicate the proportion of $NP_{Lys\text{-}Ang\ II}$-positive events for each population.

IFN-γ induced Loss of Particle Target Cell Tropism

To allow quantitative assessment of target cell tropism, we introduced a measure T for tropism ranging from -1 to 1 (T = -1 – absolute tropism in off-target cells; T = 0 – no tropism; T = 1 – absolute tropism towards target cells; see method section for equation and supplementary information for detailed derivation). We calculated T (Eq. 6) for our flow cytometry data sets and plotted it against molar particle concentration to find possible concentration dependencies of tropism. Indeed, like for targeting efficiency, the strongest tropism of $NP_{Lys\text{-}Ang\ II}$ was found in the low picomolar concentration range (30 pM; Fig. 6A). It was further observed that the data distributions broadened after treatment with IFN-γ, especially at lower particle concentrations (10-30 pM). To further investigate and to quantify this subjective impression, we plotted the particle fluorescence intensity ($I_{APC\text{-}A}$) data distributions for the rMC_{CTG} and HeLa populations from control experiments (no IFN-γ treatment) and IFN-γ treatment experiments in violin plots. These data distributions were analyzed for unimodality using the folding test for unimodality as introduced by Siffer *et al.* [55,56]. Determined folding statistics Φ ($I_{APC\text{-}A}$) were plotted against logarithmic particle concentration for rMC and HeLa populations (Fig. 6B). The calculated Φ ($I_{APC\text{-}A}$) statistics are given for each distribution (Fig. 6C).

As folding statistics Φ indicated multimodal data distribution for IFN-γ pre-treated rMC populations incubated with 30 or 10 pM of $NP_{Lys\text{-}Ang\ II}$, we decided to further investigate the nature of data distribution by calculating gap statistics [57]. While for rMC populations incubated with 30 pM $NP_{Lys\text{-}Ang\ II}$ all three replicates suggested the presence of two clusters (Fig. 7A), for 10 pM $NP_{Lys\text{-}Ang\ II}$ data two of three replicates suggested two clusters while for the third replicate one cluster was found (Fig. 7B). For rMC and HeLa populations from un-treated co-cultures as well as for HeLa populations pre-treated with IFN-γ a single cluster was found throughout (Fig. 7A and B, ctrl plots).

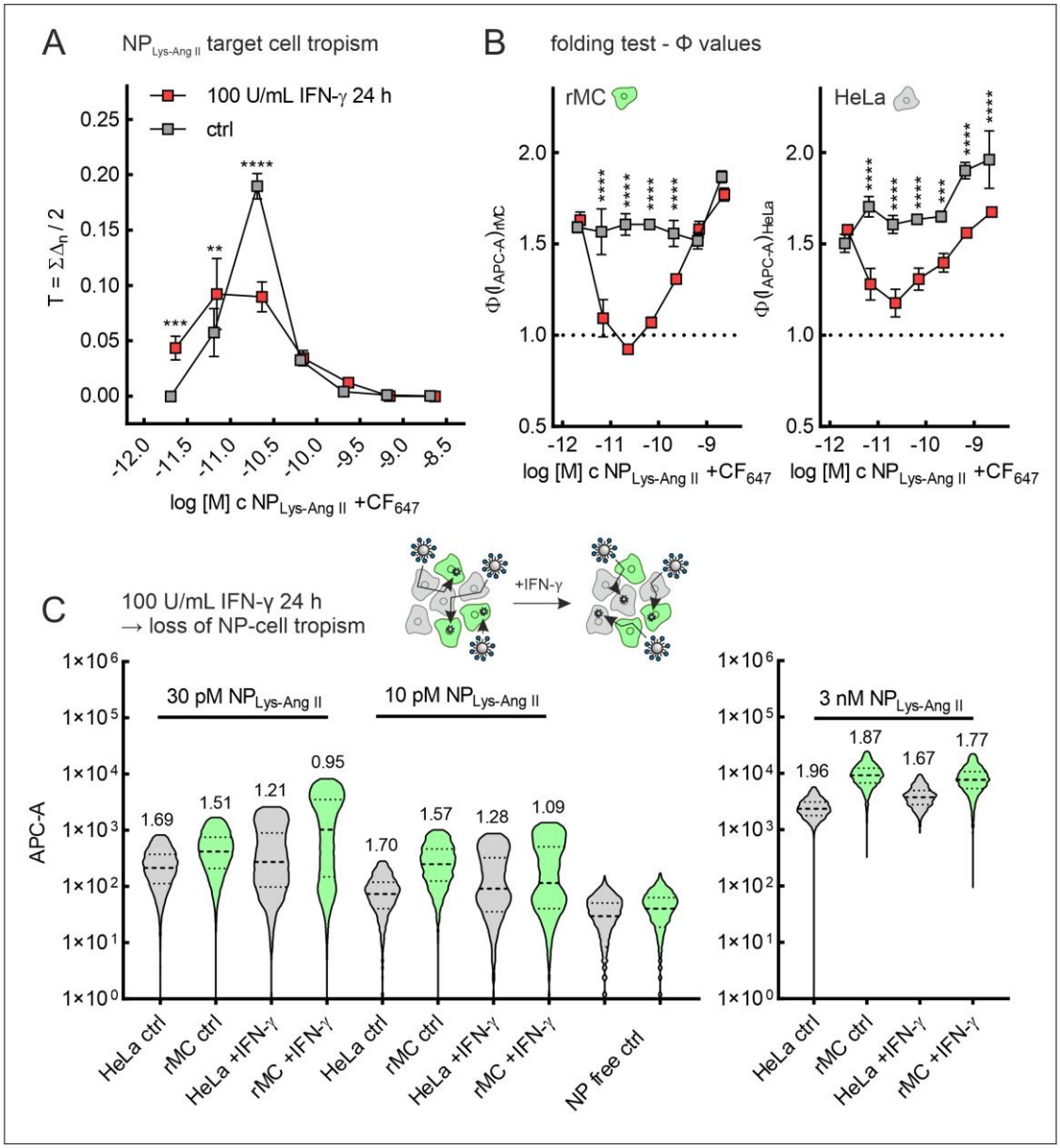

Figure 6. R-based folding test for investigation of multimodal distributions in flow-cytometry data. (A) Plot of target cell tropism T for $NP_{Lys\text{-}Ang\ II}$ on rMC_{CTG}/HeLa co-cultures untreated or pre-treated with 100 U/mL IFN-γ for 24 h against the logarithmic molar particle concentration (T = 1 - ideal-tropism, T = 0 - random distribution, and T = -1 - reverse tropism). Statistical significance of differences in T were tested via two-way ANOVA with subsequent Sidak's multiple comparison test (** P < .01, *** P < .001, **** P < .0001; $F_{IFN\text{-}\gamma}$ (DFn = 6, DFd = 28) = 0.627, P = .627; F_{cNP} (DFn = 6, DFd = 28) = 109, P < .0001; error bars indicate SD). (B) Plot of folding statistics $\Phi(I_{APC\text{-}A})$ for the rMC (left) and HeLa (right) populations of rMC_{CTG}/HeLa cell co-cultures untreated or pre-treated with 100 U/mL IFN-γ for 24 h against the logarithmic molar particle concentration. Statistical significance of differences in $\Phi(I_{APC\text{-}A})$ were tested via two-way ANOVA with subsequent Sidak's multiple comparison test (*** P < .001, **** P < .0001; rMC population: $F_{IFN\text{-}\gamma}$ (DFn = 1, DFd = 28) = 243, P < .0001; F_{cNP} (DFn = 6, DFd = 28) = 68.5, P < .0001; HeLa population: $F_{IFN\text{-}\gamma}$ (DFn = 1, DFd = 28) = 208, P < .0001; F_{cNP} (DFn = 6, DFd = 28) = 33.7, P < .0001; error bars indicate SD). (C) Violin plots of rMC and HeLa

populations at lower pM (left graph) and lower nM (right graph) particle concentrations. Figures above the plots indicate the respective value of $\Phi(I_{APC\text{-}A})$ for the distribution shown.

In order to extract information on the particle distribution in the confirmed sub-populations contained in the overall data, it was necessary to apply a method that allowed data-based sub-population assignment of individual events. For this, we employed an expectation maximization-based clustering algorithm optimized for use with large datasets [58]. This analysis was performed with the data sets of IFN-γ pre-treated rMCs incubated with 30 pM $NP_{Lys\text{-}Ang\ II}$ (Fig. 7C). Due to the inconclusive results of gap statistics calculations, the data of IFN-γ pre-treated rMCs incubated with 10 pM $NP_{Lys\text{-}Ang\ II}$ were also included (Fig. 7D).

Expectation maximization-based clustering calculated posterior probabilities (pp) for each event in flow cytometry data sets, allowing us to assign them to one of two sub-populations corresponding to lower or higher nanoparticle uptake (low $NP_{Lys\text{-}Ang\ II}$ uptake: $pp < 0.5$; high $NP_{Lys\text{-}Ang\ II}$ uptake: $pp > 0.5$). We plotted the rMC_{CTG} populations found after incubation with 10 or 30 pM $NP_{Lys\text{-}Ang\ II}$ in untreated rMC_{CTG}/HeLa cell co-cultures and compared them against the respective two sub-populations identified in cell co-cultures pre-treated with IFN-γ.

This comparison revealed an interesting nature of IFN-γ effect on the model particles distribution in cell co-culture. We examined the mean particle fluorescence intensities ($I_{APC\text{-}A}$) of the single population (control experiment, i.e., no IFN-γ treatment) or sub-populations (IFN-γ treatment) as a measure for mean particle quantity per cell. For co-cultures incubated with 30 pM $NP_{Lys\text{-}Ang\ II}$, comparison of the mean $I_{APC\text{-}A}$ values of un-treated populations and IFN-γ pre-treated sub-populations obtained from triplicate samples shows that the rMC population is divided into two sub-population. One of which shows a significantly decreased particle uptake and a second one that, in contrast, shows a significantly higher uptake. Mean particle uptake by HeLa cells was also slightly increased, with a marked broadening of the distribution (Fig. 7E). In co-cultures incubated with 10 pM $NP_{Lys\text{-}Ang\ II}$, two of the three replicates also showed a deviation into

two rMC sub-populations upon treatment with IFN-γ. In the third replicate, mean I_{APC-A} of the rMC population was slightly increased with a marked broadening of the distribution (Fig. 7F).

IFN-γ Inhibits Directed Particle Accumulation in Target-Cells

In addition to the parameters investigated so far, we also intended to study the directed accumulation of nanoparticles in co-culture. Directed accumulation in this context means a spatially directed transport of the particles towards target cells. The experiments described so far were carried out using rMC_{CTG}/HeLa cell co-cultures composed of approximately equal target and off-target cell proportions. Nanoparticles are therefore expected to encounter target and off-target cells with equal probability. *In vivo*, however, the particles encounter a large number of off-target cells before they even reach their target cell. To mimic this situation more closely, we prepared a series of rMC_{CTG}/HeLa cell co-cultures with decreasing target cell density. Assuming homogeneous distribution of the target cells in co-culture, this leads to an increasing distance between target cells. We measured particle distribution in this series of co-cultures using flow cytometry and investigated effects of IFN-γ.

We first defined quantitative performance parameters describing accumulation. Target cell accumulation was calculated as the ratio of the proportion of rMCs that had taken up particles to the proportion of rMCs that did not take up particles (Eq. 9). Off-target cell accumulation was calculated equivalently, considering the HeLa cell population (Eq. 10). Analysis of flow cytometry data sets obtained from rMC_{CTG}/HeLa cell co-culture uptake experiments showed that after 2 h of incubation with 10 pM $NP_{Lys\text{-}Ang\ II}$, IFN-γ pre-treatment led to a lower proportion of rMCs taking up particles compared to control experiments (considering data sub-sets: N rMC^{NP+} ↓; Fig. 8A, B, and C). Following Eq. 9, this is equivalent to a lower target cell accumulation. The strongest effect was observed at a rMC_{CTG}/HeLa (N/N) ratio of ≈1/3, where IFN-γ treatment induced an 18-fold increase of N rMC^{NP-} (ctrl: 2.8%, IFN-γ: 51.1%). The corresponding effect was significantly smaller for HeLa cells (NP- ctrl: 45.6%, IFN-γ: 79.0%, 1.7-fold increase). In general, IFN-γ treatment had significantly smaller effects on particle accumulation in HeLa cells over the entire range of target/off-target cell ratios covered, whereas

accumulation in rMCs was negatively affected throughout. A heatmap of the proportions acquired for all data sub-sets in flow cytometry clearly illustrates that while particle accumulation was barely affected in the HeLa population (Fig. 8D, left four columns: ctrl vs IFN-γ), the same parameter was massively decreased in the rMC population (Fig. 8D, right four columns: ctrl vs IFN-γ).

Next, we plotted target- and off-target cell accumulation (Eqs. 9 and 10) calculated from flow cytometry data against log N_{HeLa}/N_{rMC} (Fig. 8E). As a measure for directed accumulation we determined the slope target cell accumulation over log N_{HeLa}/N_{rMC}. We deemed this parameter suitable as in the presence of directed particle accumulation, it is to be expected that with decreasing target cell density in co-culture, accumulation of the particles will increase. This can be assumed because the number of particles available per target cell increases. Our analysis revealed that directed accumulation only takes place towards rMC target cells (dir. acc.: rMC ctrl = 14.4 (3.40-25.4); HeLa ctrl = 0.669 (0.292-1.05), mean (CI 95%), P = .026). IFN-γ treatment significantly inhibits this directed accumulation (dir. acc.: rMC IFN-γ = 0.902 (0.184-1.62), mean (CI 95%), P (rMC ctrl) = .029). In fact, directed accumulation appears to be completely inhibited as the value determined for the rMC population after IFN-γ treatment does not significantly differ from the HeLa control value (P > .99). Effect of IFN-γ treatment on directed accumulation in the HeLa population was also not significant (dir. acc.: HeLa IFN-γ = 0.390 (0.160-0.620), mean (CI 95%), P (HeLa ctrl) > .99) (Fig. 8F).

The data also showed that for our model particle $NP_{Lys\text{-}Ang\ II}$ strong directed accumulation towards rMCs only occurs up to an rMC_{CTG}/HeLa ratio of 1/3 (N/N). At lower rMC_{CTG}/HeLa ratios target cell accumulation decreases significantly.

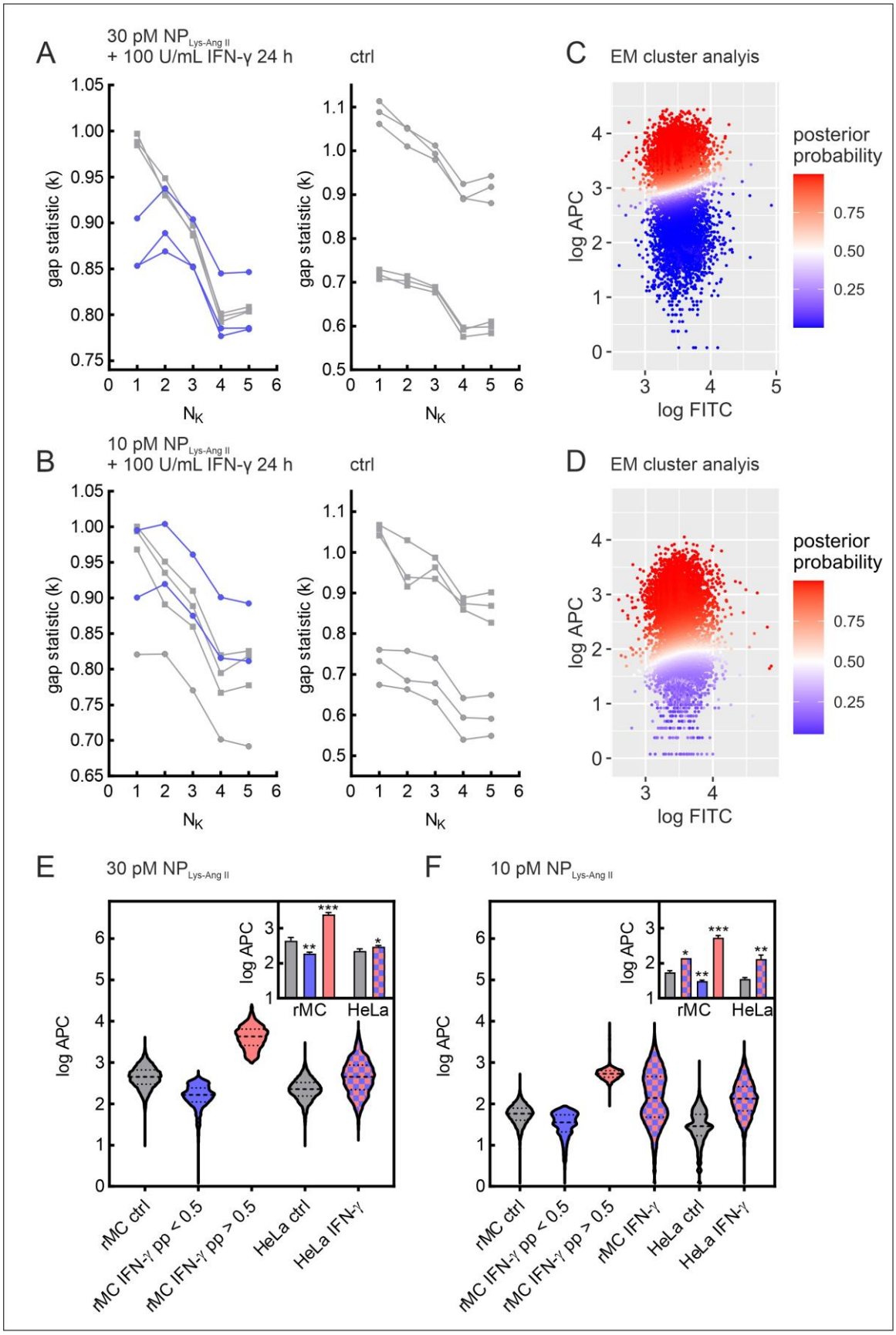
A
30 pM NP Lys-Ang II
+ 100 U/mL IFN-γ 24 h
ctrl
gap statistic (k)
N_K
B
10 pM NP Lys-Ang II
+ 100 U/mL IFN-γ 24 h
ctrl
C
EM cluster analyis
log APC
log FITC
posterior probability
0.75
0.50
0.25
D
E
30 pM NP Lys-Ang II
rMC
HeLa
rMC ctrl
rMC IFN-γ pp < 0.5
rMC IFN-γ pp > 0.5
HeLa ctrl
HeLa IFN-γ
F
10 pM NP Lys-Ang II
rMC IFN-γ

Figure 7. Determination of cluster number k and EM-cluster analysis. (A, B) Gap statistics (k) calculated for data distributions derived from IFN-γ pre-treated cell co-cultures showing low $\Phi(I_{APC\text{-}A})$ values (≤ 1) with the corresponding controls. Here, k was individually calculated for HeLa (squares) and rMC_{CTG} (circles) populations, incubated with 30 pM (A) or 10 pM (B) of $NP_{Lys\text{-}Ang\ II}$. Blue symbols indicate an optimum number of clusters (N_K) of 2. Grey symbols indicate an optimum of $N_K = 1$. (C, D) Plot of posterior probabilities (pp) calculated for each event using expectation maximization-based clustering algorithm introduced by Sharma *et al.*. Representative plots for IFN-γ pre-treated rMC_{CTG}/HeLa cell co-cultures incubated with 30 pM (C) or 10 pM (D) $NP_{Lys\text{-}Ang\ II}$. (E, F) Violin plots of data derived from untreated (grey) rMC_{CTG}/HeLa cell co-cultures, high-NP (red, pp > 0.5) or low-NP (blue, pp < 0.5) sub-populations of IFN-γ pre-treated rMCs, and IFN-γ pre-treated HeLa populations as well as IFN-γ pre-treated rMC population for which N_K was found to be 1 (blue-red checkered). Bar charts indicate mean $I_{APC\text{-}A}$ obtained from triplicates (for rMC IFN-γ, N = 1; rMC IFN-γ pp < 0.5 and pp > 0.5, each N = 2). Statistical significance of IFN- treatment on particle distribution was tested using Holm-Sidak method (α = .05, * P < .05, ** P < .01, *** P < .001; error bars indicate SD).

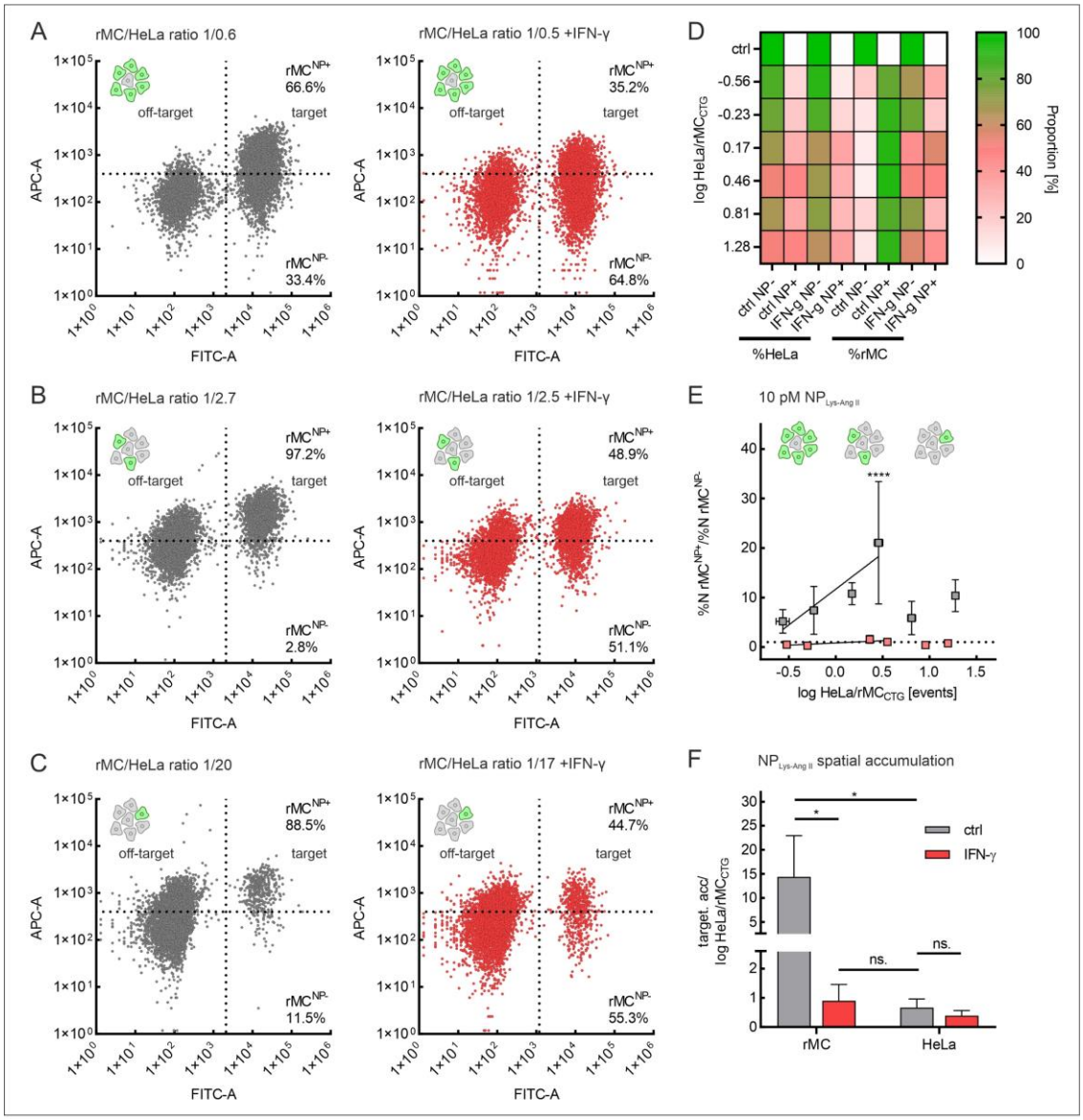

Figure 8. Effect of IFN-γ on directed accumulation of $NP_{Lys\text{-}Ang\ II}$. Representative FITC-A/APC-A dot plots derived from ≈2/1 (A), ≈1/3 (B), and ≈1/20 (C) (N_{rMC}/N_{HeLa}) rMC_{CTG}/HeLa cell co-cultures, untreated (grey symbols) or pre-treated with IFN-γ (red symbols). Figures in the graph indicate the proportion of rMC population in the top right (NP^+) or in the lower right (NP^-) quadrant. (D) Heatmap visualizing all %N $HeLa^{NP+/NP-}$ and %N $rMC^{NP+/NP-}$ values obtained from flow cytometry experiments. (E) Plot of NP^+/NP^- rMC events against logarithmic HeLa/rMC_{CTG} event ratio. Lines were derived from linear regression. P-values describing the significance of the slope deviating from zero are additionally given. The significance of the accumulation of $NP_{Lys\text{-}Ang\ II}$ in cell co-cultures with lower rMC content compared with the 2:1 cell co-culture was tested via two-way ANOVA with subsequent Sidak's multiple comparisons test (**** $P < .0001$; $F_{IFN\text{-}\gamma}$ (DFn = 1, DFd = 24) = 45.2, $P < .0001$; $F_{HeLa/rMC}$ (DFn = 5, DFd = 24) = 3.23, $P = .023$; error bars indicate SD). (F) Derived values for target/off-target directed accumulation (Eqs. 11 and 12) in untreated or IFN-γ pre-treated rMC_{CTG}/HeLa cell co-cultures. Statistical significance of IFN-γ induced effect on directed accumulation was tested via two-way ANOVA with subsequent Sidak's multiple comparisons test (ns. not significant, * $P < .05$;

$F_{IFN-\gamma}$ (DFn = 1, DFd = 8) = 7.74, P = .024; $F_{HeLa/rMC}$ (DFn = 1, DFd = 8) = 8.27, P = .021; error bars indicate SD).

In analogy to these studies, we performed another experiment in which we investigated the distribution of $NP_{Lys\text{-}Ang\ II}$ in rMC_{CTG}/HeLa co-cultures with increasing rMC content. With this model, we aim to provide a surrogate for the in-tumor situation. Here, the particle would not encounter many off-target cells and only few target cells as during its delivery, but on the contrary would be surrounded by a preponderance of target cells. However, in these studies we found no significant effect of IFN-γ on the distribution of $NP_{Lys\text{-}Ang\ II}$ (Fig. 9 A and B). The ratio of uptake in rMCs and HeLa cells remained constant in the presence and absence of IFN-γ over the range of rMC/HeLa ratios studied (Fig. 9D).

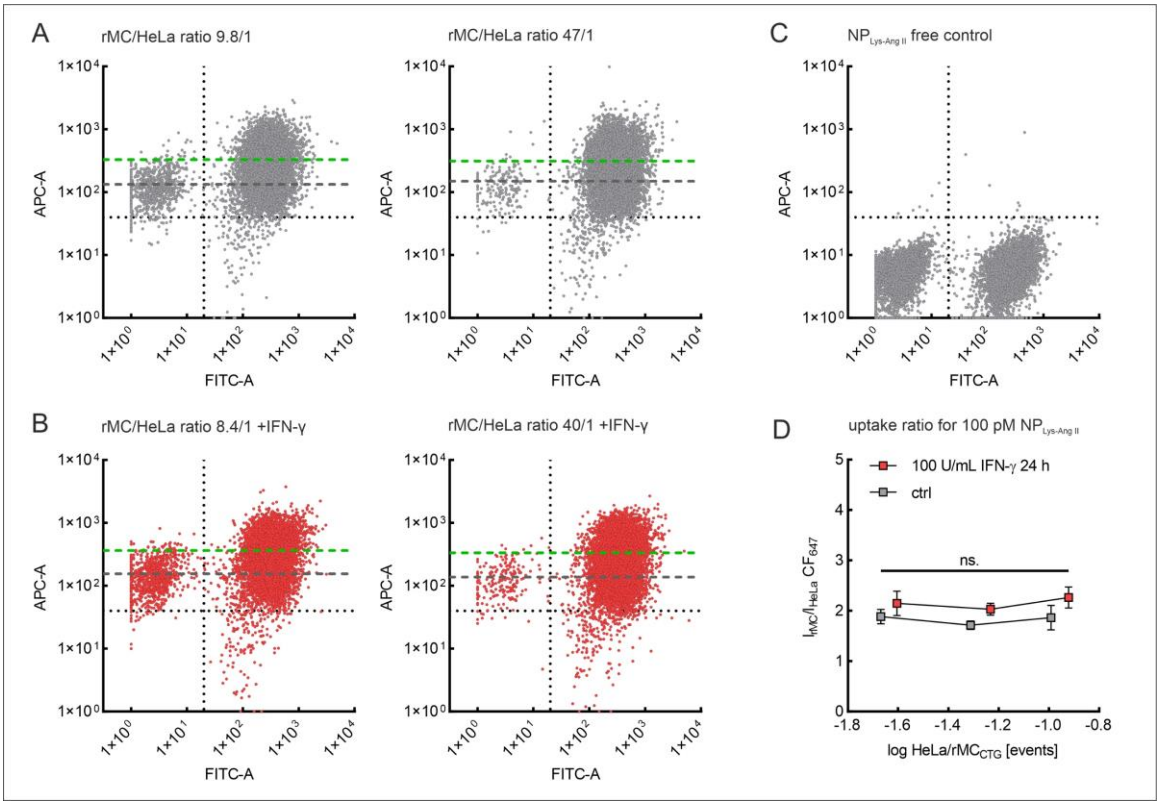

Figure 9. Effect of IFN-γ in rMC/HeLa co-cultures with increasing proportion of target cells. (A) Representative FITC-A/APC-A dot plots derived from ≈10/1 (A), and ≈50/1 (B) (N_{rMC}/N_{HeLa}) rMC_{CTG}/HeLa cell co-cultures, untreated (grey symbols) or pre-treated with IFN-γ (red symbols). (C) $NP_{Lys\text{-}Ang\ II}$-free ≈1/1 (N_{rMC}/N_{HeLa}) rMC_{CTG}/HeLa cell co-culture was used to set NP+/NP- threshold. (D) Plot of I_{rMC}/I_{HeLa} CF647 against the log HeLa/rMC_{CTG} ratio shows that as the proportion of target cells increases, IFN-g has no significant effect on particle distribution. Statistical significance of IFN-γ induced effect was tested via two-way ANOVA with subsequent Sidak's multiple comparisons test (ns. - not significant; $F_{interaction}$ (DFn = 3, DFd = 16) = 1.17, P = .353; error bars indicate SD).

Discussion

In our target/off-target cell co-culture model, treatment with IFN-γ significantly upregulated CH25H in rMCs (Fig. 3A), a factor known to exhibit broad antiviral activity. [59]. Our studies examined the impact of IFN-γ on a model nanoparticle's distribution in cell co-culture. Indeed, IFN-γ treatment affected all particle performance parameters investigated. Interestingly, these effects were consistently not exclusively due to an altered behavior of rMC target cells regarding $NP_{Lys\text{-}Ang\ II}$ interaction, but rather to overall changes in particle distribution between the target- and the off-target population. Another finding of our work is that the investigated performance parameters strongly depend on the particle concentration. We consider this observation to be highly relevant, as it could have implications for the practical application of targeted nanoparticles. This is that the dosage of nanoparticles could be a critical parameter for successful targeting and that it is apparently possible to overload cells with particles, thus counteracting the goals pursued by targeting.

Regarding the hypothesized effect of IFN-γ on CCP morphology, reduction in the binding ability of nanoparticles after treatment of rMCs with IFN-γ was demonstrated in the Ca^{2+} binding assay (Fig. 3C). The change in the binding properties of $NP_{Lys\text{-}Ang\ II}$ is in good agreement with the changes found with established CCP inhibitors. This similarity suggests a concordant mechanistic cause, and therefore the binding studies provide indirect evidence for depletion of CCPs by IFN-γ.

A closer look at the individual experimental observations allows us to propose an underlying mechanism behind these changes. This mechanism is consistent with our investigations on the role of clathrin-coated pits considering the avidity of ligand-functionalized particles for their target cells. When we investigated the nature of the effect of IFN-γ on the preferential nanoparticle uptake in rMCs it could not be explained merely by a reduced rate of endocytosis in rMCs. One would have expected a significantly reduced particle uptake in IFN-γ pre-treated rMCs in this case. In contrast, a slight increase in particle fluorescence intensity was observed in the rMC population, while a marked increase in particle uptake was found for HeLa cells. (Fig. 4A to C). Considering the massive reduction in nanoparticle avidity in the absence of CCPs that we described previously [15], this observation can be explained by a reduced adhesion of $NP_{Lys\text{-}Ang\ II}$ to target cells. This reduced adhesion consequently makes more particles

available for nonspecific uptake by HeLa cells. This is in line with observations for viruses. A reduced attachment in the presence of IFN-γ has been explicitly described for the influenza A virus, for example [60]. In view of the results of the CH25H ELISA, the work of Anderson et al. must be referred to in this context. Here it was observed that sterols lower the energetic barrier to be overcome during endocytosis [61]. Since IFN-γ showed no effect on the CH25H level of HeLa cells, no reduction of membrane cholesterol content is to be expected. Thus, endocytosis in HeLa cells can proceed unimpeded, whereas it is inhibited in rMCs, making more particles available for uptake into HeLa cells.

The maximum targeting efficiency of $NP_{Lys\text{-}Ang\ II}$ was found at low picomolar particle concentrations (10 to 30 pM). A closer examination of the effect of IFN-γ on particle targeting efficiency, similarly, suggests an underlying mechanism based on lowered adhesion of $NP_{Lys\text{-}Ang\ II}$ on target cells. Namely, in the presence of IFN-γ, there is a massive increase in the off-target cell population that had taken up particles. Also, the data distribution acquired for the target cell population showed a notable broadening. From this, it can be concluded that a greater number of particles were unbound in the presence of IFN-γ and that nonspecific uptake by HeLa cells increased at the expense of rMC uptake (Fig. 5A and B).

This conclusion is further supported by the results of expectation maximization-based cluster analysis of data obtained after incubation of rMC/HeLa cell co-cultures at low picomolar particle concentrations. Here, it was observed that in addition to an rMC sub-population that showed increased uptake of $NP_{Lys\text{-}Ang\ II}$, there was a further one that had taken up a significantly lower particle amount of compared to control experiments. At the same time, uptake by HeLa cells increased significantly (Fig. 7E and F). In conjunction with the exact nature of IFN-γ effects discussed above, this suggests that accumulation in HeLa cells increased at the expense of particle accumulation in rMCs. In conclusion $NP_{Lys\text{-}Ang\ II}$ lost their orientation towards rMCs mediated by high-avidity ligand-receptor interactions occurring in presence of CCPs due to IFN-γ treatment. The high variability of the IFN-γ effect with respect to CH25H elevation may also contribute to the phenomenon of splitting of the rMC population. While the CH25H level was almost doubled in some cases, hardly any change was observed in other measurements (Fig. 3A). In summary, IFN-γ reduces the rMC tropism for our model particle.

Our investigations of $NP_{Lys\text{-}Ang\ II}$ distribution using series of target/off-target cell co-cultures containing decreasing amounts of target cells revealed the method as suitable to investigate directed nanoparticle transport. While the parameters defined in Eq. 9 and 10 give us a numerical value allowing comparison of directed accumulation between distinct populations, plots of target accumulation (Eq. 9) against log HeLa/rMC_{CTG} (N/N) allows to estimate particle performance regarding directed accumulation (Fig. 8D and E). As with increasing proportions of off-target cells the mean distance between target cells increases (assuming uniform distribution of rMCs), the number of unspecific interactions of $NP_{Lys\text{-}Ang\ II}$ with HeLa cells is expected to increase as well. The strong decrease of target cell accumulation observed at log HeLa/rMC_{CTG} (N/N) ratios > 0.5 is most likely due to unspecific uptake by HeLa cells occurring by chance after a number of nanoparticle off-target cell interactions [62] (Fig. 10). The method found complete inhibition of target cell directed accumulation of $NP_{Lys\text{-}Ang\ II}$ in cell co-cultures pre-treated with IFN-γ.

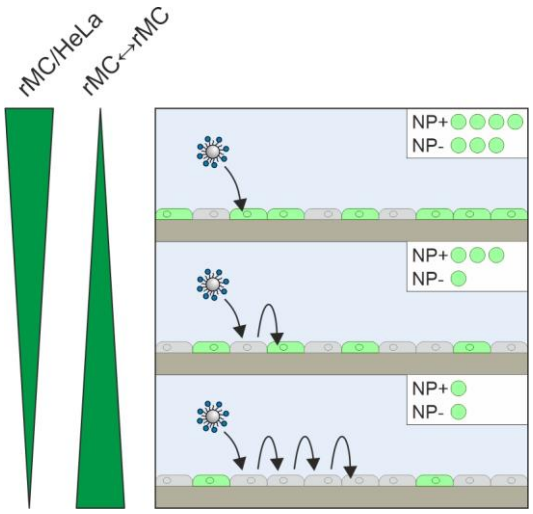

Figure 10. Directed accumulation of $NP_{Lys\text{-}Ang\ II}$ in rMCs. Scheme illustrating the expected effect of decreasing proportions of rMCs (green) in rMC_{CTG}/HeLa cell co-cultures resulting in an increased rMC-to-rMC distance and a maximum in target cell accumulation due to limited diffusion distance of $NP_{Lys\text{-}Ang\ II}$ before unspecific uptake takes place by chance.

Because no comparable effects were observed in co-cultures with increasing proportions of target cells (Fig. 9), we conclude that effects of IFN-γ might occur primarily with respect to the delivery of particles to their target compartments, during which the particles encounter many off-target cells. Effects on distribution within target compartments (e.g., tumors), where particles are almost exclusively surrounded by target cells, seem less likely based on our results.

In summary, our findings reveal a previously unknown factor influencing nanoparticle distribution to cells. Transferring the effects observed in our cell co-culture model to use cases of nanotherapeutic systems, such as targeted tumor therapy, allows the assumption that IFN-γ could counteract beneficial effects of particle ligand functionalization regarding target cell specific accumulation. This could lead to a lack of therapeutic efficacy or even to harmful side effects due to accumulation in off-target cells. Thus, the effects of IFN-γ could be a factor in the failure of targeted nanotherapeutics in clinical trials. From a recent review [63] and related literature [64–66], it appears that indeed the most common causes for failure of targeted nanoparticles are insufficient therapeutic efficacy or unacceptable side effects. Moreover, our results suggest that, in addition to the previously discussed role of reduced binding and entry of viral particles due to CH25H-induced reduction of membrane cholesterol levels and molecular effects of 25-hydroxycholesterol [13,59,67–69], altered tissue distribution of viruses may be an additional cause of the antiviral effects of IFN-γ. Further, regarding our approach of a knowledge transfer from the field of virology, this work opens a wide field for future research. Many other factors influencing viral pathogen tropism are known. One of which being other cytokines like type I (IFN-α/β) [6] and type III interferons (IFN-λ) [70–72] or TNF [73–75]. However, there are other factors as well. For example, Shaw *et al.* recently hypothesized a temperature dependence of viral tropism [76]. These are all factors whose influence on nanoparticle biodistribution have hardly been studied to date.

Finally, we like to point out and discus limitations inherent of the present work. So far, we used the rMC/HeLa co-culture as a surrogate target/off-target cell model to investigate distribution of targeted nanoparticles. This model was chosen to allow linkage of previous studies on the effect of established CCP inhibitors on particle-cell interactions and the observations made here regarding the effect of IFN-γ on particle distribution. However, to confirm the transferability of the presented results to particle

distribution in tumors, further investigations on cancer cell lines are required. Regarding the observed splitting of the rMC population with respect to particle uptake, we can provide two approaches for the underlying mechanism with the reduced avidity of particles and the variable effect of IFN-γ on CH25H level in rMCs, but we cannot determine it with absolute certainty. Moreover, to confirm the proposed mechanistic background of the observed phenomena, it is necessary to demonstrate the effect of IFN-γ on CCP morphology using direct measurement methods (e.g., electron microscopy).

Conclusion

The present work demonstrates that IFN-γ-induced upregulation of CH25H in rMCs almost completely abolishes target cell tropism of our model nanoparticles in target/off-target cell co-cultures. We found rMC oriented preferential uptake, targeting efficiency, and directed accumulation significantly reduced upon IFN-γ treatment. In summary, $NP_{Lys\text{-}Ang\ II}$ lost their tropism to rMCs in IFN-γ pre-treated co-cultures.

We, thus, identified a factor of *in vitro* nanoparticle distribution in cell co-culture that had not previously been described in the literature and that could only be identified as potentially relevant via the strategy of knowledge transfer from the field of virology.
We hope that our work can stimulate further research to investigate the significance of the effects found here *in-vivo*. In addition, it is our opinion that the approach of knowledge transfer from virology offers further opportunities to gain a better understanding of nanoparticle bio-distribution.

Materials and Methods

Materials

The polymers COOH-PEG_{5k}-PLA_{10k}, Lys-Ang II-PEG_{5k}-PLA_{10k}, and CF647-PLGA were synthesized using lysine-N-modified angiotensin II (Lys-Ang II, sequence: NH_2-KDRVYIHPF-COOH) synthesized to order (GenScript, Netherlands), carboxy-PEG_{5k} (JenKem Technology, United States), 3,6-Dimethyl-1,4-dioxane-2,5-dione, 1,8-Diazabicyclo[5.4.0]undec-7-ene (DBU, 1 M in THF), N,N-Diisopropylethylamine (DIPEA), 2-(1H-Benzotriazole-1-yl)-1,1,3,3-tetramethyluronium hexafluorophosphate (HBTU), N-(3-Dimethylaminopropyl)-N′-ethylcarbodiimide hydrochloride (EDC), N-Hydroxysuccinimide (NHS), Resomer® RG 502 H, acid-terminated, M_w 7,000-17,000 (COOH-PLGA), CF™ 647 amine, (all Sigma Aldrich, United States), and Spectrum™ Spectra/Por™ 1 RC dialysis membrane 6-8 kDa (RC membrane, Fisher Scientific Germany). For nanoparticle preparation we further used Resomer® RG 502, ester-terminated, M_w 7,000-17,000 (ester-terminated PLGA; Sigma Aldrich, United States). Nanoparticles were up-concentrated using Microsep™ Advance 30k centrifugal devices (Pall, United States). For Ca^{2+} mobilization assay we used Fura 2-AM, Leibovitz L-15 medium (Leibovitz; both Thermo Fisher Scientific, United States), probenecid, and Pluroninc® F-127 (both Sigma Aldrich, United States). The used cell-staining reagents were CellTracker™ Green (CTG) and CellTracker™ Deep Red (CTDR) (both Invitrogen™, Thermo Fisher Scientific, United States). Cell culture materials used were RPMI-1640 medium (+ L-glutamine, - sodium bicarbonate, powder), Dulbecco′s Modified Eagle′s Medium (DMEM +Pyr, + L-glutamine, + sodium pyruvate, - sodium carbonate), Hydrocortisone (HC) (all Sigma Aldrich, United States), Insulin-Transferrin-Selenium 100x (ITS, Gibco™, Thermo Fisher Scientific, United States), fetal bovine serum (FBS, P201004, PAN-Biotech, Germany). Used interferon-γ (IFN-γ, target species: rat, Miltenyi Biotec, Germany) and CH25H ELISA kit (Abbexa, United Kingdom) were purchased. MilliQ H_2O was taken from a Milli-Q® EQ 7000 device. TEM images were recorded on 3.05 mm Cu-TEM grids (400 mesh, Plano, Germany).

Polymer Synthesis and Nanoparticle Preparation

COOH-PEG5k-PLA10k Synthesis

COOH-PEG_{5k}-PLA_{10k} synthesis was previously published (9,10). Briefly, carboxy-PEG_{5k} was dried under vacuum at 45 °C for 12 h. 3,6-Dimethyl-1,4-dioxane-2,5-dione was recrystallized from boiling ethyl acetate (oil bath 90 °C, reflux). Supernatant ethyl acetate was decanted, and product was dried overnight under vacuum. 800 mg dried carboxy-PEG_{5k} were dissolved in dichloromethane (approximately 15 mL/g) under nitrogen atmosphere. 1600 mg 3,6-Dimethyl-1,4-dioxane-2,5-dione and 553 µL DBU 1M in THF were added. Reaction was stirred precisely for 1 h and quenched by adding 337.7 mg benzoic acid in dichloromethane. Reaction was precipitated in ice cold diethyl ether under vigorous stirring. Product was re-precipitated in ACN and dried under vacuum at 45 °C for 24 h.

Lys-Ang II-PEG_{5k}-PLA_{10k} Synthesis

To conjugate Lys-Ang II to the COOH-PEG_{5k}-PLA_{10k}, 200 mg of COOH-PEG_{5k}-PLA_{10k}, 66 mg EDC, and 40 mg NHS were dissolved in 1 mL *N,N*-Dimethylformamide (DMF). Reaction was stirred at 500 rpm for 3 h at room temperature. 2-mercaptoethanol was added to quench the reaction. 19.6 mg of Lys-Ang II peptide was dissolved in 500 µL DMF. Before adding the peptide solution, 23 µL of DIPEA were added to the polymer solution. The reaction was stirred at 500 rpm for an additional 48 h at room temperature. The mixture was diluted in 15 mL of milliQ H_2O to yield a DMF content below 10% (v:v). This solution was dialyzed against milliQ H_2O for 24 h using a 6-8 kDa RC membrane. Medium was replaced after 30, 60 min, 2, 4, 6, and 12 h. Finally, the solution was frozen at -80°C and lyophilized for four days (0.005 mbar, -20°C).

CF647-PLGA Synthesis

To link a cyanine-based fluorescent dye (CF647) to our nanoparticle core, 1 mg CF™ 647 amine, 123.8 mg COOH-PLGA, and 7.8 mg HBTU were dissolved in DMF. Next, 7.2 µL of DIPEA were added and the reaction was incubated for 12 h protected from light. Reaction was precipitated in ice cold diethyl ether and centrifuged at 3.0 rcf for 10 min. Diethyl ether was decanted and the product was dried for 12 h under nitrogen flow. The precipitate was taken up in 5 mL DMF, transferred to tared glass vials, and again dried for 12 h under nitrogen flow. CF647-PLGA was stored under argon atmosphere.

$NP_{Lys\text{-}Ang\ II}$ Preparation

We designed a fluorescently labeled nanoparticle ($NP_{Lys\text{-}Ang\ II}$ +CF647) to allow for measurement of *in vitro* biodistrubtion in rMC/HeLa cell co-culture assays via flow cytometry. $NP_{Lys\text{-}Ang\ II}$ was prepared by hand-mixing employing solvent evaporation technique. Stock solutions of 40 mg/mL Lys-Ang II-PEG_{5k}-PLA_{10k}, COOH-PEG_{5k}-PLA_{10k}, and CF647-PLGA in ACN were prepared. 39 µL Lys-Ang II-PEG_{5k}-PLA_{10k}, 138 µL COOH-PEG_{5k}-PLA_{10k}, and 75 µL CF647-PLGA (for $NP_{Lys\text{-}Ang\ II}$ CF647) or ester-terminated PLGA (for $NP_{Lys\text{-}Ang\ II}$) stock solutions were mixed with 748 µL ACN. This solution was added dropwise to 10 mL PBS stirring at 750 rpm. The reaction was stirred for 3 h protected from light. Particles were up-concentrated using 30 k microsep™ centrifugal device (40 min, 1.5 rcf).

Nanoparticle Tracking Analysis

Nanoparticle Characterization

Nanoparticle tracking analysis (NTA) was used to characterize $NP_{Lys\text{-}Ang\ II}$ hydrodynamic diameter d_{NP} and polydispersity index (PDI) as measure for size distribution. Preparation via hand-mixing employing solvent evaporation technique reproducibly yielded nanoparticles with d_{NP} around 100 nm and PDI consistently at or below 0.2 indicating monodisperse size distribution (Fig. 2A, Supp. Fig. 1A to D, supplementary movies).

All NTA measurements were done on a NanoSight NS300 device (Malvern Panalytical, United Kingdom). Samples for NTA measurements were drawn from the preparation after solvent evaporation was completed and ahead of up-concentration. 1 µL was taken from the reaction and diluted to 1 mL using PBS. These dilutions were manually injected into the measurement chamber using a 1 mL syringe. For each sample particle tracks were recorded for 60 s with advancing the sample after each measurement (N = 3). After each sample the measurement chamber was thoroughly rinsed using at least 5 mL of PBS.

Polydispersity Index (PDI) was calculated based on NTA data using the following equation, accounting for error propagation

$$PDI = \left(\frac{\sigma_d}{d_{NP}}\right)^2 \quad (1)$$

where d_{NP} is the mean nanoparticle diameter and σ_d is the according standard deviation.

Nanoparticle Stability Test

Stability of $NP_{Lys\text{-}Ang\ II}$ over the intended incubation was assessed in 1/1 rMC_{CTG}/HeLa cell co-cultures using NTA measurements. Over 2 h no significant change in hydrodynamic diameter or PDI was observed indicating absence of $NP_{Lys\text{-}Ang\ II}$ degradation or formation of aggregates (Fig. 2B, Supp. Fig. 1E and F, supplementary movie).

For stability testing of $NP_{Lys\text{-}Ang}$, 1/1 (N_{rMC}/N_{HeLa}) rMC/HeLa cell co-cultures were prepared on a 24-well-plate as described in detail below. Three replicate cell co-cultures were investigated per time point. To each cell co-culture 500 µL of a 1 nM $NP_{Lys\text{-}Ang\ II}$ dispersion were added. After 5, 10, 30, 60, 90, and 120 min 1 µL samples were taken and diluted to 1 mL using PBS. These samples were forwarded to NTA measurements conducted as described above. As measures of stability, we determined PDI (Eq. 1) as well as span and Pearson's mode skewness [77,78] (PMS) according to the following formulas (Eq. 2 and 3).

$$span = \frac{d_{90} - d_{10}}{d_{50}} \quad (2)$$

$$PMS = \frac{d_{NP}^{mean} - d_{NP}^{mode}}{SD} \quad (3)$$

Here, d_{10}, d_{50}, and d_{90} are the respective percentile values of the size distribution. PMS was calculated from the particles mean d_{NP}^{mean} and modal d_{NP}^{mode} diameter, and the standard deviation SD.

Transmission Electron Microscopy

For imaging of $NP_{Lys\text{-}Ang\ II}$ and $NP_{Lys\text{-}Ang\ II}$ CF647, particle lots were prepared as described above. Particles were then applied to a 9 nm carbon film floated onto a 3.05 mm Cu-TEM grid (400 mesh) for 1 min incubation (ambient conditions) and washed with bi-distilled H_2O. This cycle was repeated once after which the particles were negative stained by application of uranyl acetate (1 min, ambient conditions). The prepared grids were stored on tissue paper for drying prior to analysis.

Images were acquired at 20,000-fold magnification on a JEM2100F instrument (JEOL, Freising, Germany) using the SerialEM software.

ELISA-based CH25H Quantification

A commercial sandwich-ELISA kit was employed to quantify CH25H in rMCs and HeLa cells. For this, cells were grown to 90% confluency in T75 culture flasks (rMCs: RPMI-1640, 100 µM HC, 10% FBS, +ITS; HeLa: DMEM +Pyr, + L-glutamine, + sodium pyruvate, - sodium carbonate, 10% FBS). Medium was discarded and cells were washed once with PBS. For the IFN-γ treatment experiments, an identically composed RPMI-1640 or DMEM medium was added that additionally contained 100 U/mL IFN-γ. As control experiments, rMCs or HeLa cells in the same passage were treated identically, omitting the IFN-γ supplementation of the medium. Both, treatment and control experiments were incubated for 24 h (37 °C, 5% CO_2).

After IFN-γ incubation cells were detached using trypsin (0.25%, +EDTA, rMCs: 90 s, HeLa: 120 s, 37 °C, 5% CO_2), washed three times with ice cold PBS and centrifuged (0.2 rcf, 5 min). obtained pellets were resuspended in 1 ml PBS and lysed via three freeze-thaw cycles (-80 °C). The lysate was then centrifuged (1.5 rcf, 4 °C, 10 min) and 100 µL samples (N = 6) were drawn from the supernatant for quantification via sandwich-ELISA.

Sandwich-ELISA was performed, and reagents were prepared according to the manufacturer's instructions. Briefly, samples (ctrl and IFN-γ treatment, each N = 6), zero controls (sample dilution buffer, 100 µL, N = 3), and CH25H standard serial dilutions (each concentration, 100 µL, N = 3) were incubated on antibody-precoated 96-well-plate

for 2 h. Liquid was discarded, 100 µL of biotin-conjugated reagent A were added per well and incubated for 1 h. Wells were washed three times, 90 µL HRP-conjugated reagent B were added, and incubated for 1 h. Wells were washed five times, 50 µL TMB substrate were added and incubated for 20 min (All incubations carried out at 37 °C, 5% CO_2). Reaction was quenched by adding 50 µL stop solution. Optical density (OD) at 450 nm was measured on a FLUOstar Omega device (BMG Labtech, Germany).

Cell Culture

Cell co-culture Preparation

For cell co-culture experiments rat mesangial cells (rMCs) were stained with CTDR or CTG. Staining solutions were prepared by solving 15 µg CTDR in 20 µL DMSO or 50 µg CTG in 11 µL DMSO. CTDR stock was diluted to 1 mL and CTG stock was diluted to 11 mL using serum free RPMI 1640 medium (100 µM Hydrocortisone, +ITS). Initial optimization of cell co-culture preparation was done using CTDR and CTG to determine most suitable cell dye. For staining rMCs from one confluent T75 flask were washed using 10 mL PBS, detached using 5 mL of 0.25% Trypsin (90 s, 37°C and 5% CO_2) and centrifuged (200 rcf, 5 min). Obtained cell pellet was resuspended in CTDR or CTG staining solution and incubated on lab shaker (45 min, 37°C and 5% CO_2, 50 rpm). After staining rMCs were washed once using 5 mL PBS ($rMC_{CTDR/CTG}$).

HeLa cells were grown in DMEM +Pyr and harvested as described for rMCs via washing, trypsinization (2 min, 37°C and 5% CO_2), and centrifugation. For cell co-culture preparation $rMCs_{CTDR/CTG}$ and HeLa cells were resuspended in RPMI 1640 (10% FBS, 100 µM Hydrocortisone, +ITS). Cell concentration was adjusted using Neubauer-improved counting chamber (Paul Marienfeld, Germany) to seed a total of 60,000 cells per well into a 24 well-plate to obtain $rMC_{CTDR/CTG}$/HeLa ratios of approximately 1/1, 1/2, 1/5, 1/10, 1/20, and 1/50 (experiment Fig. 8) or 10/1, 20/1, and 50/1 (experiment Fig. 9). Cell co-cultures were incubated for 24 h (37°C and 5% CO_2) before proceeding with analysis or further experiments.

During establishment of rMC/HeLa cell co-culture preparation, two cell dyes were tested to be used to distinguish rMC and HeLa events in flow cytometry data sets. Using CTDR

to stain rMCs turned out to result in significant spillover of events between HeLa and rMC population in APC-A/FSC-A dot plots. FITC-A/FSC-A dot plots obtained from rMC/HeLa cell co-cultures after CTG staining of rMCs showed significantly less spillover (Supp. Fig. 2A and B). Furthermore, with increasing proportion of CTDR stained rMCs in cell co-culture we observed a right-shift of unstained HeLa population in the APC-A channel. This was observed to a much lesser extent for CTG (Supp. Fig. 2E and F). Taken together, these preliminary experiments led us to consider rMC_{CTG}/HeLa cocultures as more suitable. Hence, a far-red fluorescent dye was chosen for $NP_{Lys\text{-}Ang\ II}$ labeling. For this, we attached a CF647-tag to our core polymer PLGA.

In a further preliminary test, we checked whether it is possible to obtain rMC_{CTG}/HeLa cell co-cultures of a controlled predictable composition by seeding rMCs and HeLa cells onto a 24-well plate in different ratios. This is a necessary condition for our experiments on directed accumulation of $NP_{Lys\text{-}Ang\ II}$. We plotted logarithmic HeLa/rMC_{CTG} ratios seeded against logarithmic ratios observed in flow cytometry to assess correlation. While measured HeLa/rMC_{CTG} ratios were found to lay slightly beneath expected ratios throughout indicating a higher growth rate of rMCs, linearity of the measured ratios was still given, and a broad range of ratios was possible to cover (Supp. Fig. 2C and D).

Ca^{2+} Mobilization Assay

For nanoparticle binding studies, $NP_{Lys\text{-}Ang\ II}$ was prepared as described above, replacing CF647-PLGA with ester-terminated PLGA. One confluent T75 flask of rMCs was washed once using 10 mL PBS and harvested using 5 mL of 0.25% Trypsin (90 s, 37°C and 5% CO_2). A rMC cell pellet was obtained by centrifugation (200 rcf, 5 min). This cell pellet was resuspended in 6 mL of 8.3 µM Fura 2-AM loading buffer (2.5 mM probenecid, 0.03% (m:v) Pluronic® F-127 in Leibovitz). The cell suspension was transferred to a small culture dish and placed on a lab shaker (1 h, RT, 50 rpm, protected from light). Thereafter, the cell suspension was diluted with 6 mL washing buffer (2.5 mM probenecid in Leibovitz) and centrifuged (200 rcf, 5 min). The supernatant was discarded, and the obtained pellet was resuspended in 5 mL of washing buffer. Cell number was determined using Neubauer-improved counting chamber and adjusted to 1 Mio. cells/mL.

Logarithmic serial dilutions of $NP_{Lys\text{-}Ang\ II}$ were prepared. A triplicate of each concentration was pipetted into a white flat-bottom 96 well-plate (10 µL per well). Fluorescence intensity read-out was performed on a FLUOstar Omega plate-reader (BMG Labtech,

Germany). To each well 90 µL of Fura 2-AM loaded rMCs were added using the plate-readers pump system set to 100 µL/s. Each well was alternately excited at λ 340 nm and λ 380 nm while emission was measured at λ 510 nm for 30 s per well to obtain the λ 340 nm/380 nm fluorescence signal ratio (R). The ratiometric assay was calibrated using 1% Triton® X-100 (in 0.5 M NaOH) to measure maximal signal ratio (R_{max}) and 1% Triton® X-100 supplemented with 45 mM EGTA (in 0.5 M NaOH) to measure minimum signal ratio (R_{min}). Intracellular Ca^{2+} mobilization was calculated using the Grynkiewicz-equation [79].

Flow-Cytometry

Cell cell co-cultures were prepared for flow cytometry analysis by discarding RPMI 1640 (10% FBS, 100 µM Hydrocortisone, +ITS) and washing each well using 500 µL PBS. Subsequently, 200 µL of 0.25% Trypsin were added to each well and the plate was incubated for 2 min (37°C and 5% CO_2). After cells were detached 500 µL of cold RPMI 1640 (10% FBS, 100 µM Hydrocortisone, +ITS) were added to quench trypsinization. Cell co-cultures were centrifuged (200 rcf, 5 min, 4°C), supernatant was discarded, and the pellets were washed again using 500 µL PBS. For flow cytometry measurements, obtained pellets were resuspended in 300 µL PBS and kept on ice until measurement.

Data Analysis

Nanoparticle Performance Parameters

To draw quantitative conclusions about the effect of IFN-γ on $NP_{Lys\text{-}Ang\ II}$ distribution, it was necessary to define performance parameters in a form of numerical values. Preferential uptake was characterized using the ratio of the geometrical means of $NP_{Lys\text{-}Ang\ II}$ +CF647 fluorescent intensity $I_{APC\text{-}A}$ of NP-positive (NP+) rMC_{CTG} and HeLa events.

$$pref.uptake = \frac{I_{APC-A}\, rMC^{NP+}}{I_{APC-A}\, HeLa^{NP+}} \qquad (4)$$

Targeting efficiency was defined as the ratio of the NP+ proportions (%N) of rMC_{CTG} and HeLa populations.

$$target.eff. = \frac{\%N\ rMC^{NP+}}{\%N\ HeLa^{NP+}} \quad (5)$$

We additionally introduce a quantitative measure for nanoparticle cell tropism T describing overall distribution of the particle

$$T = \frac{\sum \Delta_n}{2} \quad (6)$$

where $\sum \Delta_n$ is the sum of the normalized differences Δ_n^{rMC} and Δ_n^{HeLa} calculated as follows.

$$\Delta_n^{rMC} = \frac{N\ rMC^{NP+} - N\ rMC^{NP-}}{N\ rMC} \quad (7)$$

and

$$\Delta_n^{HeLa} = \frac{N\ HeLa^{NP-} - N\ HeLa^{NP+}}{N\ HeLa} \quad (8)$$

Here, N rMC/HeLa^{NP+} is the number of $NP_{Lys\text{-}Ang\ II}$ positive rMC/HeLa events and N rMC/HeLa^{NP-} is the number of $NP_{Lys\text{-}Ang\ II}$ negative rMC/HeLa events. Refer to supplementary information for a detailed derivation of the parameter T.

To characterize the target cell specific accumulation of $NP_{Lys\text{-}Ang\ II}$, we formed a ratio of NP+ and NP- proportion of rMC_{CTG} populations. For off-target accumulation, the equivalent ratio was formed for the HeLa populations.

$$target.acc. = \frac{\%N\ rMC^{NP+}}{\%N\ rMC^{NP-}} \quad (9)$$

$$off-target.acc. = \frac{\%N\ HeLa^{NP+}}{\%N\ HeLa^{NP-}} \quad (10)$$

To furthermore quantify the directed accumulation of $NP_{Lys\text{-}Ang\ II}$ in rMCs based on flow cytometry data, we introduced the following expression defining directed accumulation

as an increase of target cell specific accumulation (Eq. 9) with increasing distance between target cells. As a measure for rMC-rMC distance we used the logarithmic HeLa/rMC$_{CTG}$ (N/N) event ratio. Directed accumulation in HeLa cells can be expressed as the equivalent ratio employing off-target accumulation (Eq. 10).

$$dir.acc._{rMC} = \frac{target.\ acc.}{\log N_{HeLa}/N_{rMC}} \quad (11)$$

$$dir.acc._{HeLa} = \frac{off-target.\ acc.}{\log N_{HeLa}/N_{rMC}} \quad (12)$$

Statistical Analysis

Data obtained in the Ca^{2+} mobilization assay was fitted using the following dose-response model.

$$Y = 100/\left(1 + 10^{(logEC_{50}-X)\cdot n}\right) \quad (13)$$

Here, Y is the normalized Ca^{2+} response measured in rMCs, X is the logarithmic molar particle concentration, and n is the Hill slope factor. This fitting and all statistical analyses were done using GraphPad Prism (v8.3.0, GraphPad Software, San Diego, USA).

Flow Cytometry

Raw data obtained from flow cytometry experiments conducted on BD FACSCanto™ II (Becton, Dickinson and Company, United States) was analyzed using Flowing Software (v2.5.1, Cell Imaging and Cytometry Core, Turku Bioscience Centre, Turku, Finland, with the support of Biocenter Finland).

Folding Test for Unimodality

The folding test for unimodality as introduced by Siffer *et al.* [56] was conducted in RStudio (v4.2.1) using the 'Rfolding' package [55] (code provided in SI).

Expectation-Maximization Cluster Analysis

Cluster analysis of flow cytometry data was done in RStudio (v4.2.1) using the 'DCEM' package [80] (code provided in SI) using an algorithm published by Sharma *et al*. [58].

References

[1] S. Maslanka Figueroa, A. Veser, K. Abstiens, D. Fleischmann, S. Beck, A. Goepferich, Influenza A virus mimetic nanoparticles trigger selective cell uptake, Proceedings of the National Academy of Sciences 116 (2019) 9831–9836.

[2] D. Fleischmann, S. Maslanka Figueroa, S. Beck, K. Abstiens, R. Witzgall, F. Schweda, P. Tauber, A. Goepferich, Adenovirus-Mimetic Nanoparticles: Sequential Ligand-Receptor Interplay as a Universal Tool for Enhanced In Vitro/In Vivo Cell Identification, ACS applied materials & interfaces 12 (2020) 34689–34702.

[3] Z. Karjoo, H.O. McCarthy, P. Patel, F.S. Nouri, A. Hatefi, Systematic engineering of uniform, highly efficient, targeted and shielded viral-mimetic nanoparticles, Small (Weinheim an der Bergstrasse, Germany) 9 (2013) 2774–2783.

[4] H. Sentsui, D. Wu, K. Murakami, T. Kondo, T. Matsumura, Antiviral effect of recombinant equine interferon-gamma on several equine viruses, Veterinary immunology and immunopathology 135 (2010) 93–99.

[5] G.K. Binder, D.E. Griffin, Interferon-gamma-mediated site-specific clearance of alphavirus from CNS neurons, Science (New York, N.Y.) 293 (2001) 303–306.

[6] G. McFadden, M.R. Mohamed, M.M. Rahman, E. Bartee, Cytokine determinants of viral tropism, Nature reviews. Immunology 9 (2009) 645–655.

[7] T.M. Kündig, H. Hengartner, R.M. Zinkernagel, T cell-dependent IFN-gamma exerts an antiviral effect in the central nervous system but not in peripheral solid organs, Journal of immunology (Baltimore, Md. 1950) 150 (1993) 2316–2321.

[8] M. Trilling, V.T.K. Le, A. Zimmermann, H. Ludwig, K. Pfeffer, G. Sutter, G.L. Smith, H. Hengel, Gamma interferon-induced interferon regulatory factor 1-dependent antiviral response inhibits vaccinia virus replication in mouse but not human fibroblasts, Journal of Virology 83 (2009) 3684–3695.

[9] R. Burdeinick-Kerr, D. Govindarajan, D.E. Griffin, Noncytolytic clearance of sindbis virus infection from neurons by gamma interferon is dependent on Jak/STAT signaling, Journal of Virology 83 (2009) 3429–3435.

[10] B. Parra, D.R. Hinton, N.W. Marten, C.C. Bergmann, M.T. Lin, C.S. Yang, S.A. Stohlman, IFN-gamma is required for viral clearance from central nervous system oligodendroglia, Journal of immunology (Baltimore, Md. 1950) 162 (1999) 1641–1647.

[11] A. Steed, T. Buch, A. Waisman, H.W. Virgin, Gamma interferon blocks gammaherpesvirus reactivation from latency in a cell type-specific manner, Journal of Virology 81 (2007) 6134–6140.

[12] M. Blanc, W.Y. Hsieh, K.A. Robertson, K.A. Kropp, T. Forster, G. Shui, P. Lacaze, S. Watterson, S.J. Griffiths, N.J. Spann, A. Meljon, S. Talbot, K. Krishnan, D.F. Covey, M.R. Wenk, M. Craigon, Z. Ruzsics, J. Haas, A. Angulo, W.J. Griffiths, C.K. Glass, Y. Wang, P. Ghazal, The transcription factor STAT-1 couples macrophage synthesis of 25-hydroxycholesterol to the interferon antiviral response, Immunity 38 (2013) 106–118.

[13] S.-Y. Liu, R. Aliyari, K. Chikere, G. Li, M.D. Marsden, J.K. Smith, O. Pernet, H. Guo, R. Nusbaum, J.A. Zack, A.N. Freiberg, L. Su, B. Lee, G. Cheng, Interferon-inducible cholesterol-25-hydroxylase broadly inhibits viral entry by production of 25-hydroxycholesterol, Immunity 38 (2013) 92–105.

[14] A. Subtil, I. Gaidarov, K. Kobylarz, M.A. Lampson, J.H. Keen, T.E. McGraw, Acute cholesterol depletion inhibits clathrin-coated pit budding, PNAS 96 (1999) 6775–6780.

[15] O. Zimmer, A.M. Goepferich, How Clathrin-Coated Pits Control Nanoparticle Avidity for Cells, Nanoscale Horiz. (2023).

[16] J. Agudo-Canalejo, R. Lipowsky, Adhesive Nanoparticles as Local Probes of Membrane Curvature, Nano letters 15 (2015) 7168–7173.

[17] J. Agudo-Canalejo, R. Lipowsky, Uniform and Janus-like nanoparticles in contact with vesicles: energy landscapes and curvature-induced forces, Soft matter 13 (2017) 2155–2173.

[18] Q. Yu, S. Othman, S. Dasgupta, T. Auth, G. Gompper, Nanoparticle wrapping at small non-spherical vesicles: curvatures at play, Nanoscale 10 (2018) 6445–6458.

[19] M Deserno, T Bickel, Wrapping of a spherical colloid by a fluid membrane, Europhysics Letters (EPL) 62 (2003) 767–774.

[20] A.H. Bahrami, R. Lipowsky, T.R. Weikl, The role of membrane curvature for the wrapping of nanoparticles, Soft matter 12 (2016) 581–587.

[21] V. Ramanan, N.J. Agrawal, J. Liu, S. Engles, R. Toy, R. Radhakrishnan, Systems biology and physical biology of clathrin-mediated endocytosis, Integrative biology quantitative biosciences from nano to macro 3 (2011) 803–815.

[22] J. Heuser, Three-dimensional visualization of coated vesicle formation in fibroblasts, The Journal of cell biology 84 (1980) 560–583.

[23] S.E. Miller, S. Mathiasen, N.A. Bright, F. Pierre, B.T. Kelly, N. Kladt, A. Schauss, C.J. Merrifield, D. Stamou, S. Höning, D.J. Owen, CALM regulates clathrin-coated vesicle size and maturation by directly sensing and driving membrane curvature, Developmental cell 33 (2015) 163–175.

[24] N. Sever, T. Yang, M.S. Brown, J.L. Goldstein, R.A. DeBose-Boyd, Accelerated degradation of HMG CoA reductase mediated by binding of insig-1 to its sterol-sensing domain, Molecular cell 11 (2003) 25–33.

[25] B.-L. Song, R.A. DeBose-Boyd, Ubiquitination of 3-hydroxy-3-methylglutaryl-CoA reductase in permeabilized cells mediated by cytosolic E1 and a putative membrane-bound ubiquitin ligase, Journal of Biological Chemistry 279 (2004) 28798–28806.

[26] J.G. Cyster, E.V. Dang, A. Reboldi, T. Yi, 25-Hydroxycholesterols in innate and adaptive immunity, Nature reviews. Immunology 14 (2014) 731–743.

[27] J. Luo, H. Yang, B.-L. Song, Mechanisms and regulation of cholesterol homeostasis, Nature reviews. Molecular cell biology 21 (2020) 225–245.

[28] M.S. Brown, J.L. Goldstein, Cholesterol feedback: from Schoenheimer's bottle to Scap's MELADL, Journal of Lipid Research 50 Suppl (2009) S15-27.

[29] A. Radhakrishnan, Y. Ikeda, H.J. Kwon, M.S. Brown, J.L. Goldstein, Sterol-regulated transport of SREBPs from endoplasmic reticulum to Golgi: oxysterols block transport by binding to Insig, Proceedings of the National Academy of Sciences of the United States of America 104 (2007) 6511–6518.

[30] A. Baldán, D.D. Bojanic, P.A. Edwards, The ABCs of sterol transport, Journal of Lipid Research 50 Suppl (2009) S80-5.

[31] N. Zelcer, C. Hong, R. Boyadjian, P. Tontonoz, LXR regulates cholesterol uptake through Idol-dependent ubiquitination of the LDL receptor, Science (New York, N.Y.) 325 (2009) 100–104.

[32] R. Hennig, K. Pollinger, J. Tessmar, A. Goepferich, Multivalent targeting of AT1 receptors with angiotensin II-functionalized nanoparticles, Journal of drug targeting 23 (2015) 681–689.

[33] C.H.J. Choi, C.A. Alabi, P. Webster, M.E. Davis, Mechanism of active targeting in solid tumors with transferrin-containing gold nanoparticles, Proceedings of the National Academy of Sciences of the United States of America 107 (2010) 1235–1240.

[34] D.B. Kirpotin, D.C. Drummond, Y. Shao, M.R. Shalaby, K. Hong, U.B. Nielsen, J.D. Marks, C.C. Benz, J.W. Park, Antibody targeting of long-circulating lipidic

nanoparticles does not increase tumor localization but does increase internalization in animal models, Cancer research 66 (2006) 6732–6740.

[35] R. Singh, M. Norret, M.J. House, Y. Galabura, M. Bradshaw, D. Ho, R.C. Woodward, T.G. St Pierre, I. Luzinov, N.M. Smith, L.Y. Lim, K.S. Iyer, Dose-Dependent Therapeutic Distinction between Active and Passive Targeting Revealed Using Transferrin-Coated PGMA Nanoparticles, Small (Weinheim an der Bergstrasse, Germany) 12 (2016) 351–359.

[36] B. Ouyang, W. Poon, Y.-N. Zhang, Z.P. Lin, B.R. Kingston, A.J. Tavares, Y. Zhang, J. Chen, M.S. Valic, A.M. Syed, P. MacMillan, J. Couture-Senécal, G. Zheng, W.C.W. Chan, The dose threshold for nanoparticle tumour delivery, Nature materials 19 (2020) 1362–1371.

[37] S. Hua, M.B.C. de Matos, J.M. Metselaar, G. Storm, Current Trends and Challenges in the Clinical Translation of Nanoparticulate Nanomedicines: Pathways for Translational Development and Commercialization, Frontiers in pharmacology 9 (2018) 790.

[38] R. Luxenhofer, M. Barz, M. Schillmeier, Quo vadis nanomedicine?, Nanomedicine (London, England) 9 (2014) 2083–2086.

[39] A.C. Anselmo, S. Mitragotri, Nanoparticles in the clinic, Bioengineering & translational medicine 1 (2016) 10–29.

[40] A.C. Anselmo, S. Mitragotri, Nanoparticles in the clinic: An update, Bioengineering & translational medicine 4 (2019) e10143.

[41] D. Jorgovanovic, M. Song, L. Wang, Y. Zhang, Roles of IFN-γ in tumor progression and regression: a review, Biomarker research 8 (2020) 49.

[42] A. Del Giúdice, L. Pagura, M.C. Capitani, L.E. Mainetti, O.G. Scharovsky, R.J. Di Masso, M.J. Rico, V.R. Rozados, Nonclassical roles for IFN-γ and IL-10 in a murine model of immunoedition, Future science OA 6 (2020) FSO589.

[43] A.M. Gocher, C.J. Workman, D.A.A. Vignali, Interferon-γ: teammate or opponent in the tumour microenvironment?, Nature reviews. Immunology 22 (2022) 158–172.

[44] J.M. Sasso, B.J.B. Ambrose, R. Tenchov, R.S. Datta, M.T. Basel, R.K. DeLong, Q.A. Zhou, The Progress and Promise of RNA Medicine—An Arsenal of Targeted Treatments, Journal of medicinal chemistry 65 (2022) 6975–7015.

[45] N. Dhiman, R. Awasthi, B. Sharma, H. Kharkwal, G.T. Kulkarni, Lipid Nanoparticles as Carriers for Bioactive Delivery, Frontiers in chemistry 9 (2021) 580118.

[46] Q. Dai, S. Wilhelm, D. Ding, A.M. Syed, S. Sindhwani, Y. Zhang, Y.Y. Chen, P. MacMillan, W.C.W. Chan, Quantifying the Ligand-Coated Nanoparticle Delivery to Cancer Cells in Solid Tumors, ACS nano 12 (2018) 8423–8435.

[47] T. Furuchi, K. Aikawa, H. Arai, K. Inoue, Bafilomycin A1, a specific inhibitor of vacuolar-type H(+)-ATPase, blocks lysosomal cholesterol trafficking in macrophages, Journal of Biological Chemistry 268 (1993) 27345–27348.

[48] M. Blanc, W.Y. Hsieh, K.A. Robertson, S. Watterson, G. Shui, P. Lacaze, M. Khondoker, P. Dickinson, G. Sing, S. Rodríguez-Martín, P. Phelan, T. Forster, B. Strobl, M. Müller, R. Riemersma, T. Osborne, M.R. Wenk, A. Angulo, P. Ghazal, Host defense against viral infection involves interferon mediated down-regulation of sterol biosynthesis, PLoS biology 9 (2011) e1000598.

[49] F.J. Byfield, H. Aranda-Espinoza, V.G. Romanenko, G.H. Rothblat, I. Levitan, Cholesterol depletion increases membrane stiffness of aortic endothelial cells, Biophysical journal 87 (2004) 3336–3343.

[50] A. Biswas, P. Kashyap, S. Datta, T. Sengupta, B. Sinha, Cholesterol Depletion by MβCD Enhances Cell Membrane Tension and Its Variations-Reducing Integrity, Biophysical journal 116 (2019) 1456–1468.

[51] S.K. Rodal, G. Skretting, O. Garred, F. Vilhardt, B. van Deurs, K. Sandvig, Extraction of cholesterol with methyl-beta-cyclodextrin perturbs formation of clathrin-coated endocytic vesicles, Mol. Biol. Cell. 10 (1999) 961–974.

[52] D. Bucher, F. Frey, K.A. Sochacki, S. Kummer, J.-P. Bergeest, W.J. Godinez, H.-G. Kräusslich, K. Rohr, J.W. Taraska, U.S. Schwarz, S. Boulant, Clathrin-adaptor ratio and membrane tension regulate the flat-to-curved transition of the clathrin coat during endocytosis, Nature communications 9 (2018) 1109.

[53] R.M. Presti, D.L. Popkin, M. Connick, S. Paetzold, H.W. Virgin, Novel cell type-specific antiviral mechanism of interferon gamma action in macrophages, The Journal of experimental medicine 193 (2001) 483–496.

[54] S. Tong, M.A. Cinelli, N.S. El-Sayed, H. Huang, A. Patel, R.B. Silverman, S. Yang, Inhibition of interferon-gamma-stimulated melanoma progression by targeting neuronal nitric oxide synthase (nNOS), Scientific reports 12 (2022) 1701.

[55] A. Siffer, Rfolding: The Folding Test of Unimodality. R package version 1.0, 2018.

[56] A. Siffer, P.-A. Fouque, A. Termier, C. Largouët, Are your data gathered?, in: Y. Guo, F. Farooq (Eds.), Proceedings of the 24th ACM SIGKDD International

Conference on Knowledge Discovery & Data Mining, ACM, New York, NY, USA, 2018, pp. 2210–2218.

[57] R. Tibshirani, G. Walther, T. Hastie, Estimating the number of clusters in a data set via the gap statistic, Journal of the Royal Statistical Society: Series B (Statistical Methodology) 63 (2001) 411–423.

[58] P. Sharma, H. Kurban, M. Dalkilic, DCEM: An R package for clustering big data via data-centric modification of Expectation Maximization, SoftwareX 17 (2022) 100944.

[59] J. Zhao, J. Chen, M. Li, M. Chen, C. Sun, Multifaceted Functions of CH25H and 25HC to Modulate the Lipid Metabolism, Immune Responses, and Broadly Antiviral Activities, Viruses 12 (2020).

[60] C.H.-Y. Fong, L. Lu, L.-L. Chen, M.-L. Yeung, A.J. Zhang, H. Zhao, K.-Y. Yuen, K.K.-W. To, Interferon-gamma inhibits influenza A virus cellular attachment by reducing sialic acid cluster size, iScience 25 (2022) 104037.

[61] R.H. Anderson, K.A. Sochacki, H. Vuppula, B.L. Scott, E.M. Bailey, M.M. Schultz, J.G. Kerkvliet, J.W. Taraska, A.D. Hoppe, K.R. Francis, Sterols lower energetic barriers of membrane bending and fission necessary for efficient clathrin-mediated endocytosis, Cell reports 38 (2022) 110371.

[62] X. Huang, X. Teng, D. Chen, F. Tang, J. He, The effect of the shape of mesoporous silica nanoparticles on cellular uptake and cell function, Biomaterials 31 (2010) 438–448.

[63] H. He, L. Liu, E.E. Morin, M. Liu, A. Schwendeman, Survey of Clinical Translation of Cancer Nanomedicines-Lessons Learned from Successes and Failures, Accounts of chemical research 52 (2019) 2445–2461.

[64] K. Miller, J. Cortes, S.A. Hurvitz, I.E. Krop, D. Tripathy, S. Verma, K. Riahi, J.G. Reynolds, T.J. Wickham, I. Molnar, D.A. Yardley, HERMIONE: a randomized Phase 2 trial of MM-302 plus trastuzumab versus chemotherapy of physician's choice plus trastuzumab in patients with previously treated, anthracycline-naïve, HER2-positive, locally advanced/metastatic breast cancer, BMC cancer 16 (2016) 352.

[65] J.M. Broderick, MM-302 Falls Short in Phase II HER2+ Breast Cancer Trial, 2016, https://www.onclive.com/view/mm302-falls-short-in-phase-ii-her2-breast-cancer-trial, accessed 31 January 2023.

[66] Merrimack Discontinues Development of MM-310, 2019, https://investors.merrimack.com/news-releases/news-release-details/merrimack-discontinues-development-mm-310, accessed 31 January 2023.

[67] Y. Liu, Z. Wei, Y. Zhang, X. Ma, Y. Chen, M. Yu, C. Ma, X. Li, Y. Cao, J. Liu, J. Han, X. Yang, Y. Duan, Activation of liver X receptor plays a central role in antiviral actions of 25-hydroxycholesterol, Journal of Lipid Research 59 (2018) 2287–2296.

[68] Y. Yuan, Z. Wang, B. Tian, M. Zhou, Z.F. Fu, L. Zhao, Cholesterol 25-hydroxylase suppresses rabies virus infection by inhibiting viral entry, Archives of virology 164 (2019) 2963–2974.

[69] P. Shrivastava-Ranjan, É. Bergeron, A.K. Chakrabarti, C.G. Albariño, M. Flint, S.T. Nichol, C.F. Spiropoulou, 25-Hydroxycholesterol Inhibition of Lassa Virus Infection through Aberrant GP1 Glycosylation, mBio 7 (2016).

[70] J. Wang, R. Oberley-Deegan, S. Wang, M. Nikrad, C.J. Funk, K.L. Hartshorn, R.J. Mason, Differentiated human alveolar type II cells secrete antiviral IL-29 (IFN-lambda 1) in response to influenza A infection, Journal of immunology (Baltimore, Md. 1950) 182 (2009) 1296–1304.

[71] N.W. Bartlett, K. Buttigieg, S.V. Kotenko, G.L. Smith, Murine interferon lambdas (type III interferons) exhibit potent antiviral activity in vivo in a poxvirus infection model, The Journal of general virology 86 (2005) 1589–1596.

[72] M. Mordstein, G. Kochs, L. Dumoutier, J.-C. Renauld, S.R. Paludan, K. Klucher, P. Staeheli, Interferon-lambda contributes to innate immunity of mice against influenza A virus but not against hepatotropic viruses, PLoS pathogens 4 (2008) e1000151.

[73] J.M. Bergelson, J.A. Cunningham, G. Droguett, E.A. Kurt-Jones, A. Krithivas, J.S. Hong, M.S. Horwitz, R.L. Crowell, R.W. Finberg, Isolation of a common receptor for Coxsackie B viruses and adenoviruses 2 and 5, Science (New York, N.Y.) 275 (1997) 1320–1323.

[74] T. Vincent, R.F. Pettersson, R.G. Crystal, P.L. Leopold, Cytokine-mediated downregulation of coxsackievirus-adenovirus receptor in endothelial cells, Journal of Virology 78 (2004) 8047–8058.

[75] R.T. Bailer, B. Lee, L.J. Montaner, IL-13 and TNF-α inhibit dual-tropic HIV-1 in primary macrophages by reduction of surface expression of CD4, chemokine receptors CCR5, CXCR4 and post-entry viral gene expression, Eur. J. Immunol. 30 (2000) 1340–1349.

[76] P.D. Shaw Stewart, J.L. Bach, Temperature dependent viral tropism: understanding viral seasonality and pathogenicity as applied to the avoidance and treatment of endemic viral respiratory illnesses, Reviews in medical virology 32 (2022) e2241.

[77] B.C. Arnold, R.A. Groeneveld, Measuring Skewness with Respect to the Mode, The American Statistician 49 (1995) 34–38.

[78] K. Pearson, X. Contributions to the mathematical theory of evolution.—II. Skew variation in homogeneous material, Phil. Trans. R. Soc. Lond. A 186 (1895) 343–414.

[79] G. Grynkiewicz, M. Poenie, R.Y. Tsien, A new generation of Ca2+ indicators with greatly improved fluorescence properties, Journal of Biological Chemistry 260 (1985) 3440–3450.

[80] P. Sharma, H. Kurban, M. Dalkilic, DCEM: Clustering Big Data using Expectation Maximization Star (EM*) Algorithm. R package version 2.0.5, 2022.

Chapter 6 – Supplementary Information

Impact of Interferon-γ on the Target Cell Tropism of Nanoparticles

Content:

Supplementary Figures

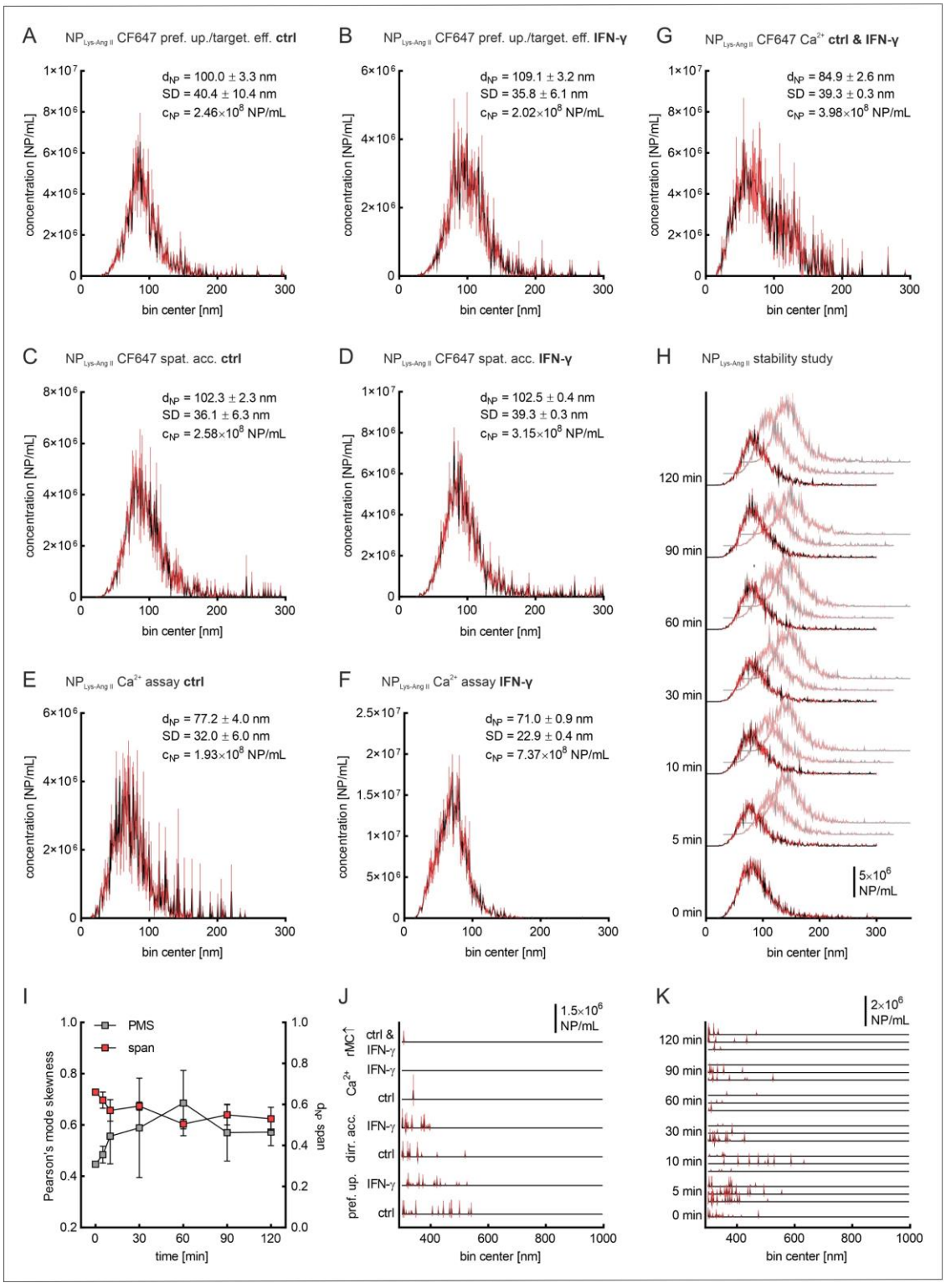

Supplementary Figure 1: Raw data derived from NTA-based characterization of $NP_{Lys\text{-}Ang\ II}$ and stability study. (A, B) Size distribution data of $NP_{Lys\text{-}Ang\ II}$ lots used for assessment of preferential uptake and targeting efficiency in untreated (A) and IFN-γ pre-treated (B) rMC_{CTG}/HeLa co-cultures. Equivalent data of $NP_{Lys\text{-}Ang\ II}$ lots used in experiments investigating spatial accumulation (C, D), in Ca2+ mobilization assay (E, F), and in investigation of $NP_{Lys\text{-}Ang\ II}$ distribution in rMC/HeLa co-cultures with increasing rMC proportion (G). Plots for untreated (C and E) and IFN-γ pre-treated (D and F) rMC_{CTG}/HeLa co-cultures are shown. For all lots mean d_{NP}, corresponding standard deviation SD, and sample particle concentration c_{NP} are given. Since samples for NTA measurements were drawn immediately after completion of preparation, the molar concentration of particles c_{NP}^{mol} in the up-concentrated sample was calculated using the following formula: $c_{NP}^{mol}[mol \times L^{-1}] = \frac{c_{NP}\, V_{in}}{N_A\, V_{yield}} 1 \times 10^6$, where V_{in} is the volume added to 30 k microsep™ centrifugal device, V_{yield} is the volume yield obtained after up-concentration, N_A is the Avogadro's constant, and 1×10^6 is a correction factor accounting for sample dilution ahead of NTA measurement and transformation of c_{NP} [NP/mL] to c_{NP}^{mol}. (H) Size distribution data obtained from $NP_{Lys\text{-}Ang\ II}$ stability study on rMC/HeLa co-cultures. Data for t = 0 min was acquired by measuring the sample immediately after preparation. For all other time points (5, 10, 30, 60, 90, and 120 min) 1 mL of 3 nM $NP_{Lys\text{-}Ang\ II}$ were incubated on rMC/HeLa cell co-culture (three replicates per time point) and 1 µL samples were drawn and diluted to 1 mL PBS for NTA measurements. (I) Calculated values for span and pearson's mode skewness (PMS) over time of stability study. (G, H) 300 to 1000 nm range of NTA data obtained from all nanoparticle lots used in experiments (G) and over the time of stability study (red bars indicate standard error of mean).

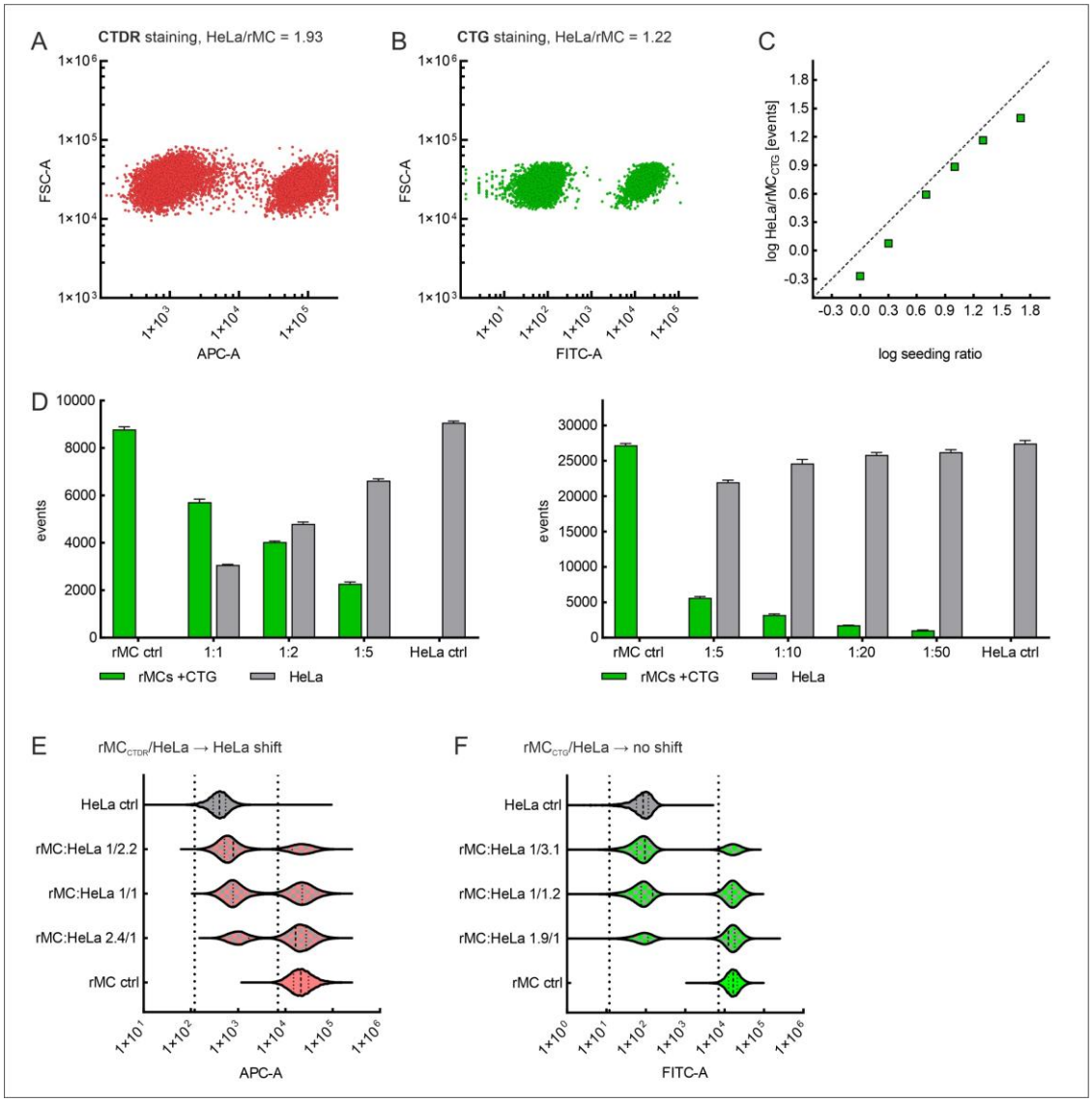

Supplementary Figure 2: Preparation and optimization of rMC/HeLa co-cultures. Representative APC-A/FSC-A (A) and FITC-A/FSC-A (B) dot plots obtained from rMC_{CTDR}/HeLa or rMC_{CTG}/HeLa co-cultures respectively. Large number of spillover events is visible between HeLa and rMC sub-population in rMC_{CTDR}/HeLa co-cultures. (C) Plot of logarithmic HeLa/rMC_{CTG} ratio calculated from flow cytometry data against the logarithmic seeding ratios. Dashed line represents the ideal correlation, where the seeded ratio corresponds exactly to the calculated ratio. (D) Event counts used to calculate log HeLa/rMC_{CTG} derived from preliminary rMC_{CTG}/HeLa co-cultures experiments. Low (left) and high (right) HeLa/rMC_{CTG} ratios were investigated separately. For low ratios approximately 9,000 events were recorded, while around 27,000 events were measured for high ratios (error bars indicate SD). (E, F) Violin plots of rMC_{CTDR}/HeLa (E) and rMC_{CTG}/HeLa (F) co-cultures with increasing proportions of rMCs. Both data sets are accompanied HeLa and $rMC_{CTDR/CTG}$ control samples obtained from pure HeLa or rMC cultures. HeLa populations in rMC_{CTDR}/HeLa co-cultures show a clear right-shift in APC-A channel with increasing rMC proportion. No comparable shift is seen in rMC_{CTG}/HeLa co-cultures.

Supplementary Text

Introduction of Flow Cytometry Data Sub-Sets

To evaluate particle performance, we defined performance parameters based on the introduced flow cytometry data sub-sets: (1) $HeLa^{NP-}$, (2) $HeLa^{NP+}$, (3) rMC^{NP-}, and (4) rMC^{NP+} (scheme 1).

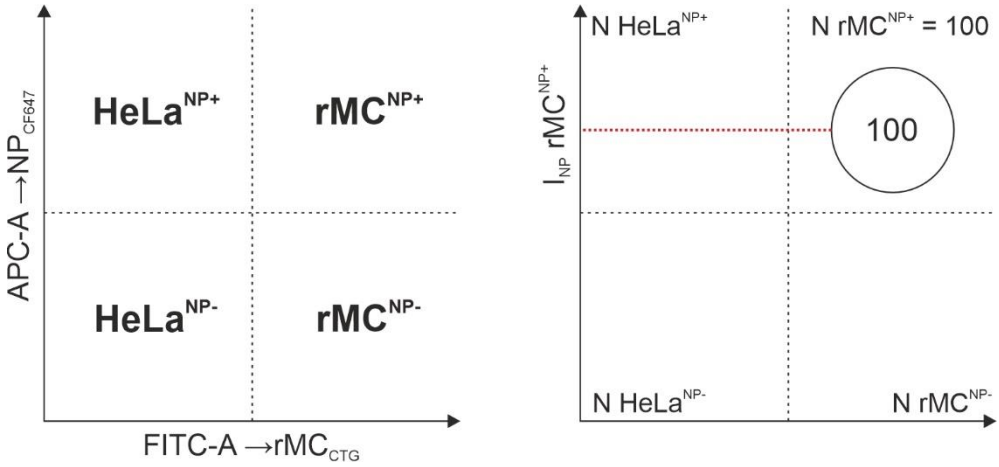

Scheme 1: The left scheme illustrates how staining of rMCs and CF64-labeling of PLGA core-polymer used for nanoparticle preparation enables derivation of the introduced four data sub-sets (black dashed lines). The right scheme illustrates the derivable sub-set parameters event number (N rMC^{NP+}) and particle fluorescence intensity (red dashed line, I_{NP} rMC^{NP+}) used to define performance parameters.

One goal of using ligand-functionalized nanoparticles is to achieve preferential uptake by target cells. This means an uptake of a greater number of particles into target cells compared to off-target cells:

$$I_{NP}\, rMC^{NP+} > I_{NP}\, HeLa^{NP+}$$

Secondly, ligand functionalized nanoparticles are employed to achieve a targeting effect. This refers to an accumulation of the nanoparticle in target cells while it ideally remains completely absent in off-target cells [1]:

$$N\,rMC^{NP+} > N\,HeLa^{NP+}$$

For derivation of particle performance parameters based on these considerations the reader is referred to the method section of the main text.

Derivation of Measure for Tropism

To derive a meaningful quantitative measure for tropism T, we consider a case of 'ideal tropism' where all cells of the target population show particle uptake while no cell of the off-target population does so. We will next consider a case of completely random distribution between the sub-populations. Finally, we will consider a hypothetical case 'reverse tropism' represented by full tropism to the off-target population. The following scheme illustrates flow cytometry data sets that correspond to these cases.

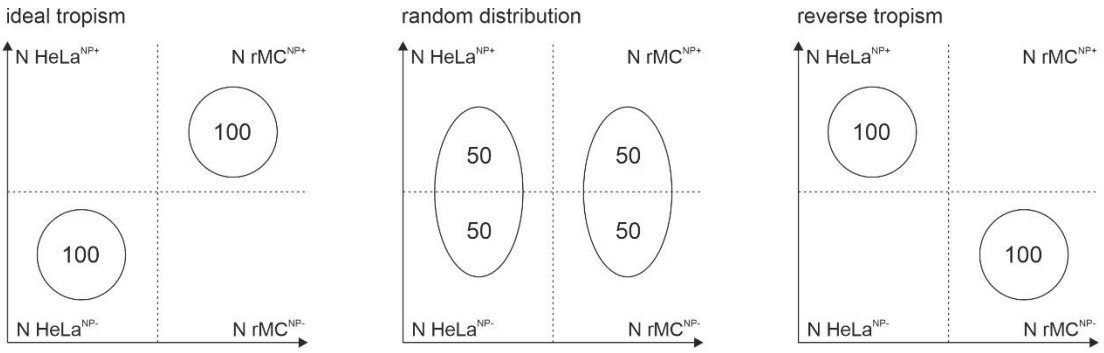

Scheme 2: Representation of ideal tropism, random distribution, and reverse tropism. Y-axis represents particle uptake and X-axis represents marker used to distinguish target and off-target population. Vertical dashed line indicates the limit X-value distinguishing the two populations (HeLa and rMC) while horizontal dashed line shows Y-threshold above which an event is to be considered particle positive (NP+). Numbers indicate fictional event counts in the respective sub-population. These explanations apply also to the following schemes, unless otherwise stated.

Considering the cases introduced above (scheme 2) it appears suitable to define a quantitative parameter for tropism T as follows starting by calculating the differences between particle positive N rMC/HeLa^{NP+} and negative N rMC/HeLa^{NP-} cells for the rMC and HeLa population.

$$\Delta^{rMC} = N\ rMC^{NP+} - N\ rMC^{NP-} \quad (1)$$

$$\Delta^{HeLa} = N\ HeLa^{NP-} - N\ HeLa^{NP+} \quad (2)$$

Next, we determine the sum $\sum \Delta$ of the two differences Δ^{rMC} and Δ^{HeLa} found.

$$\sum \Delta\ =\ \Delta^{rMC} + \Delta^{HeLa} \quad (3)$$

Which we finally normalize to half of the total event count.

$$T = \frac{\sum \Delta}{N} \quad (4)$$

Here N is the total number of events in the investigated flow cytometry data set. The parameter T as defined above (Eq. 4) yields T = 1 for ideal-tropism, T = 0 for random distribution, and T = -1 for reverse tropism.

To prove the general suitability of our parameter for tropism T, in a next step we will consider a series of cases of partial or non-ideal tropism, where 1. only a portion of target cells shows particle uptake while the off-target population shows no uptake (off-target ideal cases), 2. all target cells show particle uptake but also a portion of off-target cells shows particle uptake (target ideal cases), and 3. where both a portion of target and off-target cells show particle uptake (mixed cases).

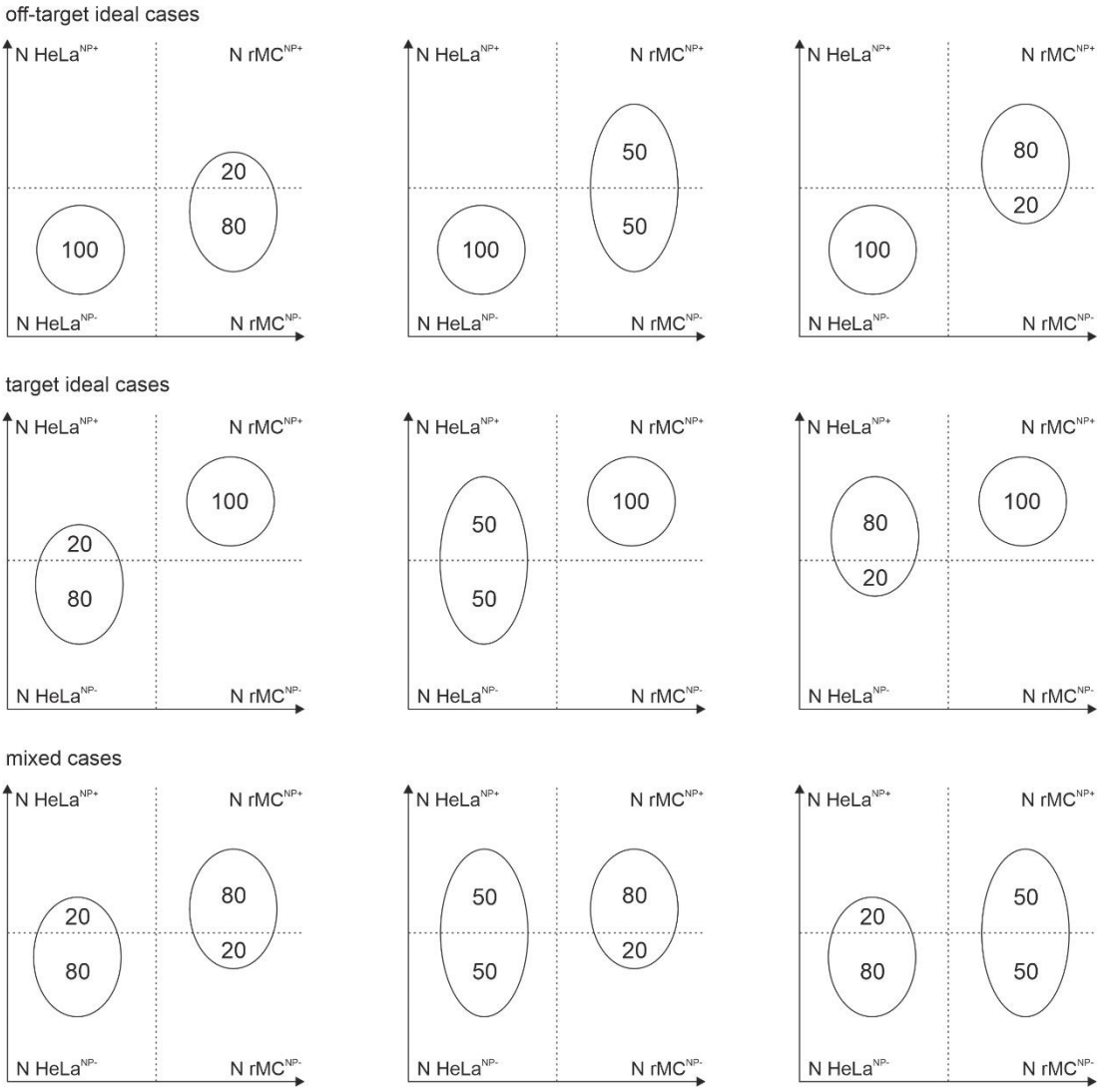

Scheme 3: Also refer to description for scheme 2. Representation of off-target ideal cases (top row), target ideal cases (middle row), and mixed cases (bottom row).

The definition of T introduced in Eq. 4 yields following values for the considered cases (scheme 3, from l. to r.): T = 0.2, 0.5 and 0.8 for off-target ideal cases, T = 0.8, 0.5 and 0.2 for target ideal cases, and T = 0.6, 0.3 and 0.3 for mixed cases.

As it is rarely the case to have the same number of events per sub-population in a flow cytometry data set, we next want to consider the case of varying event numbers for our parameter for tropism T (scheme 4). It would improve the general applicability of our approach if the parameter was to be able to account for such variations.

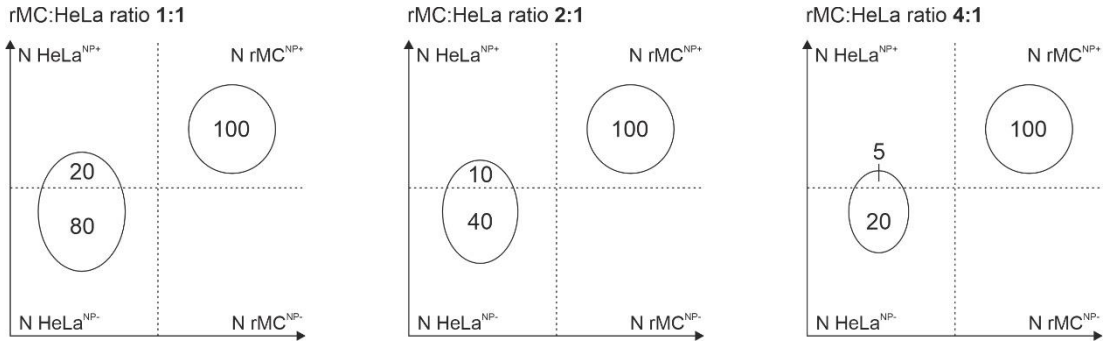

Scheme 4: Also refer to description for scheme 2. Representation of data set with constant relative distribution of the particle (Y-axis) but decreasing ratio of off-target to target events.

Consideration of these cases shows that the definition of the parameter T in its present form yields different values when the number of events of the sub-populations varies, despite identical relative distributions of the particles. We find $T_{1:1} = 0.8$, $T_{2:1} = 0.87$, and $T_{4:1} = 0.92$. This circumstance makes a reformulation of the definition necessary since a varying ratio of the rMC and HeLa sub-population would lead to an unjustified over- or underestimation of the tropism T for the examined particle.

This flaw can easily be fixed by normalizing the differences Δ^{rMC} and Δ^{HeLa} (Eqs. 1 and 2) for the number of events recorded for the respective sub-population N rMC or N HeLa.

$$\Delta_n^{rMC} = \frac{N\ rMC^{NP+} - N\ rMC^{NP-}}{N\ rMC} \qquad (5)$$

$$\Delta_n^{HeLa} = \frac{N\ HeLa^{NP-} - N\ HeLa^{NP+}}{N\ HeLa} \quad (6)$$

This yields the respective normalized differences Δ_n^{rMC} and Δ_n^{HeLa}. We again calculate the sum of these differences.

$$\sum \Delta_n = \Delta_n^{rMC} + \Delta_n^{HeLa} \quad (7)$$

By normalizing the difference of particle positive and negative events to the total number of events in the respective sub-population N rMC or N HeLa (Eqs. 5 and 6), we can set the number of events per sub-population to 1. Hence, we obtain a value of 2 for the overall total number of events N. Therefore, we yield the following expression for a measure of tropism accounting for possible variations in sub-population ratio.

$$T = \frac{\sum \Delta_n}{2} \quad (8)$$

Recalculating T for the third set of cases considered above using this adapted definition, we find a value of T = 0.8 independent of sub-population ratio.

Code for Cluster Analyses

Folding Test for Unimodality

Following code was employed for folding test for unimodality [2,3] using RStudio (R v4.2.1):

```
# Systematically named samples: IFN or ctrl states the experiment; rep_X (X = 1,2,3) states the replicate; sample_X (X = c for NP free ctrl; X = 1-7 for NP samples) states the sample. Required packages: "readxl", "tidyverse", "Rfolding".
# Flow cytometry data was exported from Flowing Software (v2.5.1 Turku Bioscience Centre) and inserted into Excel files.

# example code:
IFN_rep_1_sample_6 <- read_excel("IFN_rep_1_sample_6.xlsx",
                                 col_types = c("numeric", "numeric"))

r1_s6_rMC_pop_pre_F <- filter(IFN_rep_1_sample_6, FITC > 0)
r1_s6_rMC_pop_pre_A_F <- filter(r1_s6_rMC_pop_pre_F, APC > 0)
r1_s6_rMC_pop <- filter(r1_s6_rMC_pop_pre_A_F, FITC >= 370)
r1_s6_HeLa_pop_pre_F <- filter(IFN_rep_1_sample_6, FITC > 0)
r1_s6_HeLa_pop_pre_A_F <- filter(r1_s6_HeLa_pop_pre_F, APC > 0)
r1_s6_HeLa_pop <- filter(r1_s6_HeLa_pop_pre_A_F, FITC < 370)
log_r1_s6_rMC_pop <- log10(r1_s6_rMC_pop)
log_r1_s6_HeLa_pop <- log10(r1_s6_HeLa_pop)
APC_log_r1_s6_rMC_pop <- select(log_r1_s6_rMC_pop, APC)
APC_log_r1_s6_HeLa_pop <- select(log_r1_s6_HeLa_pop, APC)

folding.test(APC_log_r1_s6_rMC_pop)
folding.test(APC_log_r1_s6_HeLa_pop)
pivot.approx(APC_log_r1_s6_rMC_pop)
pivot.approx(APC_log_r1_s6_HeLa_pop)
```

Calculation of Gap Statistics

Following code was employed for determination of N_K via calculation of gap statistics using the packages cluster [4] and factoextra [5] in RStudio (R v4.2.1):

```
# Systematically named samples: X10_pM or X30_pM states NP concentration; rMC or HeLa states the cell population; IFN or ctrl states the experiment; 1, 2, or 3 states the replicate
# Flow cytometry data was exported from Flowing Software (v2.5.1 Turku Bioscience Centre) and inserted into Excel files.
# Required packages: "readxl", "ggplot2", "cluster", and "factoextra"

# example code:
 X10_pM_rMC_IFN_3 <- read_excel("10_pM_rMC_IFN_3.xlsx",
                                col_types = c("numeric", "numeric"))

X10_pM_rMC_IFN_3 <- na.omit(X10_pM_rMC_IFN_3)
X10_pM_rMC_IFN_3_scaled <- scale(X10_pM_rMC_IFN_3)
gap_stat_X10_pM_rMC_IFN_3 <- clusGap(X10_pM_rMC_IFN_3_scaled, kmeans, K.max = 5, nstart = 25, B = 500)

fviz_gap_stat(gap_stat_X10_pM_rMC_IFN_3)
gap_stat_X10_pM_rMC_IFN_3$Tab
```

EM-based Clustering Analysis

Following code was employed to conduct EM-based clustering analyses [6,7] using RStudio (R v4.2.1):

```
# Systematically named samples: X10_pM or X30_pM states NP concentration; rMC or HeLa states the cell population; IFN or ctrl states the experiment; 1, 2, or 3 states the replicate. Required packages: "readxl", "ggplot2", and "DCEM"
# Flow cytometry data was exported from Flowing Software (v2.5.1 Turku Bioscience Centre) and inserted into Excel files.

# example code:
X10_pM_rMC_IFN_2 <- read_excel("10_pM_rMC_IFN_2.xlsx",
                               col_types = c("numeric", "numeric"))
na_X10_pM_rMC_IFN_2 <- na.omit(X10_pM_rMC_IFN_2)
EM_X10_pM_rMC_IFN_2 <- dcem_star_train(na_X10_pM_rMC_IFN_2, seeding = 'improved')
```

```
EM_X10_pM_rMC_IFN_2$meu
EM_X10_pM_rMC_IFN_2$sigma
prob_X10_pM_rMC_IFN_2 <- EM_X10_pM_rMC_IFN_2$prob

write.csv(prob_X10_pM_rMC_IFN_2, file = "prob_X10_pM_rMC_IFN_2")
write.csv(na_X10_pM_rMC_IFN_2, file = "na_X10_pM_rMC_IFN_2")
```

Figure Preparation for EM-Clustering Results

The R package tidyverse [8] was used to visualize the results of the EM cluster analyses. Following code was employed for graphical representation of results obtained from EM-based clustering analyses using RStudio (R v4.2.1):

```
# Systematically named samples: X10_pM or X30_pM states NP concentration; rMC or HeLa states the cell population; IFN or ctrl states the experiment; 1, 2, or 3 states the replicate. Required packages: "readxl", and "ggplot2"
# Generated csv files "prob_X10_pM_rMC_IFN_2.csv" and "na_X10_pM_rMC_IFN_2" were imported into an Excel file named "prob_10_pM_rMC_IFN_2.xlsx"

# code example:
prob_10_pM_rMC_IFN_2 <- read_excel("prob_10_pM_rMC_IFN_2.xlsx",
                                   col_types = c("numeric", "numeric", "numeric",
                                                 "numeric"))

plot_prob_10_pM_rMC_IFN_2 <- ggplot(prob_10_pM_rMC_IFN_2,
aes(x=FITC,y=APC, color=prob)) +geom_point(size=0.2) +ylim(-0.1,4.7)
+scale_x_continuous(breaks = c(3,4,5))
plot_prob_10_pM_rMC_IFN_2 +scale_color_gradient2(midpoint = 0.5, low = "blue",
mid = "white", high = "red")+xlab("log FITC") +ylab("log APC")
+labs(color="posterior\nprobability") +theme(axis.text = element_text(size = 11))

ggsave(plot_prob_10_pM_rMC_IFN_2, device = "pdf", width = 71, height = 71, units = c("mm"), dpi = 1200)
```

References

[1] Q. Dai, S. Wilhelm, D. Ding, A.M. Syed, S. Sindhwani, Y. Zhang, Y.Y. Chen, P. MacMillan, W.C.W. Chan, Quantifying the Ligand-Coated Nanoparticle Delivery to Cancer Cells in Solid Tumors, ACS nano 12 (2018) 8423–8435.

[2] A. Siffer, Rfolding: The Folding Test of Unimodality. R package version 1.0, 2018.

[3] A. Siffer, P.-A. Fouque, A. Termier, C. Largouët, Are your data gathered?, in: Y. Guo, F. Farooq (Eds.), Proceedings of the 24th ACM SIGKDD International Conference on Knowledge Discovery & Data Mining, ACM, New York, NY, USA, 2018, pp. 2210–2218.

[4] M. Maechler, P. Rousseeuw, A. Struyf, M. Hubert, K. Hornik, cluster: Cluster Analysis Basics and Extensions. R package version 2.1.4, 2022.

[5] A. Kassambara, F. Mundt, factoextra: Extract and Visualize the Results of Multivariate Data Analyses. R Package Version 1.0.7, 2020.

[6] P. Sharma, H. Kurban, M. Dalkilic, DCEM: An R package for clustering big data via data-centric modification of Expectation Maximization, SoftwareX 17 (2022) 100944.

[7] P. Sharma, H. Kurban, M. Dalkilic, DCEM: Clustering Big Data using Expectation Maximization Star (EM*) Algorithm. R package version 2.0.5, 2022.

[8] H. Wickham, M. Averick, J. Bryan, W. Chang, L. McGowan, R. François, G. Grolemund, A. Hayes, L. Henry, J. Hester, M. Kuhn, T. Pedersen, E. Miller, S. Bache, K. Müller, J. Ooms, D. Robinson, D. Seidel, V. Spinu, K. Takahashi, D. Vaughan, C. Wilke, K. Woo, H. Yutani, Welcome to the Tidyverse, JOSS 4 (2019) 1686.

Chapter 7

Theoretical Model to Consolidate Findings on Particle Avidity and Biodistribution

Abstract

The previous chapters in brief summary showed that (A) the depletion of clathrin-coated pits (CCPs) via reduction of membrane cholesterol levels dramatically reduced nanoparticle avidity to cells, and that (B) treatment of target/off-target cell co-cultures with Interferon-γ - a factor proven to upregulate the cholesterol metabolizing enzyme CH25H and to affect nanoparticle binding to target cells to a degree comparable to established CCP formation inhibitors - resulted in a massive loss of nanoparticle target cell tropism. While these observations already imply that CCP impairment underlies the IFN-induced shift in particle distribution, in this chapter the connection between the findings obtained will be further explored. To investigate whether depletion of nano-scale high-avidity binding sites actually led to the observed micro-scale changes in particle distribution, differential equation system-based simulations were employed using the VCell software package. These simulations allowed to derive particle concentration gradients that occur between target and off-target cells. It was found that the absence of high-avidity binding sites (e.g., CCPs) on target cells strongly affects these concentration gradients. Particle flux towards target cells was slowed down or even inverted due to CCP binding site depletion.

Graphical Abstract

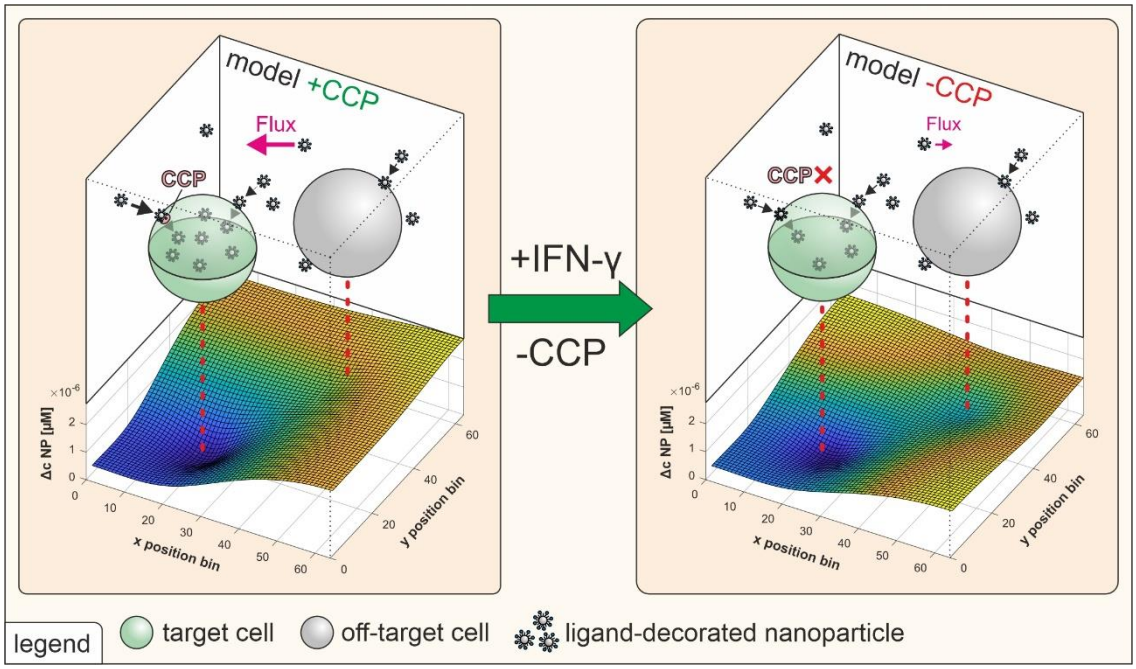

Computational investigations of nanoparticle distribution between target and off-target cells were conducted to consolidate the findings of the previous chapters. These studies suggest that the depletion of high-avidity binding sites on target cells induces significant reduction of target cell-directed nanoparticle flux in proximity to off-target cells.

Introduction

Findings from previously conducted experimental studies have led to two main conclusions. First, clathrin-coated pits (CCPs) represent hotspots for high-avidity interactions of ligand-functionalized nanoparticles with cell membranes [1]. Second, Interferon-γ (IFN-γ) almost completely suppresses ligand-induced target cell tropism of nanoparticles [2]. Its mode of action as well as first experimental investigations suggest CCP depletion to be causative for IFN-γ induced effects on nanoparticle distribution in cell co-culture. Thus, IFN-γ stimulates the expression of the cholesterol metabolizing enzyme cholesterol-25-hydroxlylase (CH25H) [3–5]. This has been shown to reduce cell membrane cholesterol levels [6–13], which in turn leads to CCP depletion [14,15]. Also, nanoparticle-cell binding studies conducted in presence of IFN-γ found a similar shift in binding parameters as it was observed for small molecules proven to inhibit the formation of CCPs [1,15–17]. Yet, as experimental data on the effect of IFN-γ on CCP structure is not available, this connection ultimately remains elusive to some extent. Here, we therefore intend to conduct further studies to address the question whether alteration of particle-membrane interaction avidity can result in a substantial change in distribution. The alternative hypothesis to this is that change in avidity only affects target cell membrane attachment but has no effect on particle distribution at a micrometer scale.

To address this research question and thereby potentially provide additional supportive evidence for the hypothesized connection of the previously conducted research outlined above, we turned to computational simulations. We decided to pursue this to gain experimentally inaccessible insight into the effect of high-avidity binding sites on particle transport at a micrometer-scale. Computational simulations, so far, have been employed to investigate nanoparticle behavior at whole-body level (i.e., continuum models, e.g., convection-diffusion-reaction kinetics, pharmacokinetic models), tissue level (i.e., hybrid models, e.g., continuum-hybrid models, tumor distribution models), and single-cell level (i.e., agent-based models, e.g., molecular dynamic models, nanoparticle-cell interactions) [18–20]. However, to the best of our knowledge, no computational study investigating the effect of varying particle attachment avidity on target/off-target particle distribution is available to date.

To estimate the performance of our model, we intend to compare the simulated distribution ratios against experimental data obtained in our studies on the effect of IFN-γ on particle distribution in target/off-target cell co-cultures.

Results

Set-up of Particle Distribution Simulations

To investigate particle distribution between a target cell and an off-target cell, we initially set up a model in form of a reaction scheme. This scheme defined all reactions to be considered in the simulations and the five compartments in which the reactions were to occur. In total, we defined three spatial compartments corresponding to (1) the extracellular space (EC), (2) the target cell compartment (target), and (3) the off-target cell compartment (off_target). Next to these, we defined two surface compartments corresponding to (1) the target cell membrane (m_target), and (2) the off-target cell membrane (m_off_target). This compartment model was applied to a geometrical model consisting of a 22 x 22 x 11 µm cube serving as the simulation space. This cube contained two spheres (d = 10 µm) which served as a target and off-target cell. Here, the sphere surface resembled the respective membrane and the enclosed volume the respective intracellular space. (Fig 1 A). All simulations were run for 120 min corresponding to the incubation time employed in experimental particle distribution studies.

As initial conditions for our simulations, we set a particle concentration in the extracellular compartment. This concentration was chosen to comply with the two highest concentrations investigated in experimental particle distribution studies and four higher concentrations that were not accessible to experimental investigation. As a second initial condition, we set a number of CCP binding sites on the target cell membrane corresponding to a coverage of 1% of the total membrane surface area.

Further parameter required to run simulations were initial density of high-avidity binding sites (i.e., CCPs) on target cells, rate of CCP internalization, and re-formation of CCPs on the target cell surface. The binding site density can be estimated based on the known

percentage of 1-2% of membrane surface internalized via clathrin-mediated endocytosis [21,22] and the mean lifetime of CCPs of about 30-60 s. I summary we yield a range of 0.5 to 2% of membrane surface covered by CCPs at the beginning of our simulation. Assuming a circular shape and a diameter of 100 nm for the CCPs, we yield an estimate of 1.27 CCPs per μm^2 (setting the membrane area covered by CCPs to 1%). The rate of CCP internalization was estimated as 0.05 s^{-1} based on transferrin internalization data published by Ehrlich et al. who found a time span of approximately 20-30 s [22]. For the derivation of a rate constant for occurrence of new CCPs we consulted data published by Boucrot et al. who observed formation of initial clathrin-structures to take about 3 s [23]. We divided the rate constant by the surface area available per CCPs to yield a coverage of 1%. This way, we yielded an estimate rate constant of 0.4 s^{-1} μm^{-2} for the formation of CCPs.

Outcome of Particle Distribution Simulations

In our simulations, we considered the particle association rate constants (K_f) relatively, setting the association rate constant of a particle binding to a flat receptor-carrying membrane (i.e., m_target; K_f^{target}) to 1. Since we had observed an approximate 50-fold loss of avidity after inhibition of CCPs in our experiments, we consequently set the association rate constant for binding to CCP entities (K_f^{CCP}) to 50. For initial preliminary simulations conducted for particle concentrations (NP_out) ranging from 1 nM to 1 µM (0.5 log-steps), we assumed the association rate constants to be equal for binding to target cell and non-target cell membranes ($K_f^{off\text{-}target} = K_f^{target} = 1$). These initial simulations found a sharp increase in target cell specificity in the low nanomolar range of particle concentration and were in acceptable alignment with our experimental distribution data. Furthermore, it was found that concentrations exceeding 3 nM fully inhibit target cell specificity in presence or absence of CCPs (Fig. 1B).

In a second set of simulations, we aimed to optimize our model to account for differences in particle attachment to receptor-carrying and receptor-free flat membranes. Regrettably, our investigations allow no conclusion regarding the rate of particle attachment to receptor-free membranes compared to receptor carrying ones (i.e., off-target and target cell membranes). We, therefore, decided to estimate the ratio of association constants K_f^{target} and $K_f^{off\text{-}target}$ as the value yielding the best fit with our experimental particle distribution data by running a series of simulations with varying

K_f^{target} / $K_f^{off\text{-}target}$ ratios. A ratio of 1:0.7 (K_f^{target} / $K_f^{off\text{-}target}$) was found to overlay best with the experimental data. (Fig. 1C).

Plots of particle uptake over time reveled, that changes in simulated distributions occurred due to decreased uptake in target cell and increased uptake in off-target cells. All together the findings in the conducted simulations led us to suspect the build-up of an extracellular particle concentration gradient. This, in turn, was hypothesized to trigger a target cell-directed particle flow. Caused by a flattening of the evolving particle concentration gradient occurring in the absence of CCPs (K_f^{CCP} ↓), alteration of this flux could be the mechanistic driving force underlying the experimentally observed change in particle distribution (Fig. 1D).

We, therefore, further analyzed extracellular particle concentration gradients obtained in the conducted simulations. First, one-dimensional concentration gradients recorded over simulation time were considered. It was found that in absence of high-avidity binding sites on target cells after 40 min a local minimum formed in proximity to the off-target cell (K_f^{target} / $K_f^{off\text{-}target}$ = 1/1) (Fig. 2A). Calculated particle flux was consequently significantly slowed down (K_f^{target} / $K_f^{off\text{-}target}$ = 1/0.7) or even reversed (K_f^{target} / $K_f^{off\text{-}target}$ = 1/1) (Fig. 2B). To gain a better understanding about the concentration gradient in our three-dimensional simulation, we plotted a two-dimensional concentration gradient on a xy-plane about 1 µm above the two cells. This gave us a first idea that absence of CCPs does not only affect particle transport close to the cells but altered the particle transport in the entire simulation space (Fig. 2C).

Calculation of Vector Fields describing Particle Concentration Gradients

However, to calculate the particle flux at any position in the simulation space, it was desirable to obtain an analytical function $f(x,y) = \Delta c$ describing the concentration gradient surface. This was achieved via polynomial fitting of surface cut-outs around points of interest. The following model equation was fitted to surface cut-outs of the extracellular particle concentration gradient derived from the conducted simulations:

$$\begin{aligned} f(x,y) = dc = {} & a_{00} + a_{10}x + a_{01}y + a_{20}x^2 + a_{11}xy + a_{02}y^2 + a_{30}x^3 + a_{21}x^2y + a_{12}xy^2 \\ & + a_{03}y^3 + a_{40}x^4 + a_{31}x^3y + a_{22}x^2y^2 + a_{13}xy^3 + a_{04}y^4 + a_{41}x^4y \\ & + a_{32}x^3y^2 + a_{23}x^2y^3 + a_{14}xy^4 + a_{05}y^5 \end{aligned} \quad (1)$$

Polynomial coefficients (Tab. 1) were obtained using the MATLAB curve fitting toolbox (MathWorks®, v.9.13). To determine the direction of diffusion for a particle resulting from the concentration gradient, we first determine the first order partial derivatives $f_x(x,y) = \partial f(x,y)/\partial x$ and $f_y(x,y) = \partial f(x,y)/\partial y$ of the polynomial function:

$$\begin{aligned} f_x(x,y) = \frac{\partial f(x,y)}{\partial x} & \\ = {} & a_{10} + 2a_{20}x + a_{11}y + 3a_{30}x^2 + 2a_{21}xy + a_{12}y^2 + 4a_{40}x^3 + 3a_{31}x^2y \\ & + 2a_{22}xy^2 + a_{13}y^3 + 4a_{41}x^3y + 3a_{32}x^2y^2 + 2a_{23}xy^3 + a_{14}y^4 \end{aligned} \quad (2)$$

$$\begin{aligned} f_y(x,y) = \frac{\partial f(x,y)}{\partial y} & \\ = {} & a_{01} + a_{11}x + 2a_{02}y + a_{21}x^2 + 2a_{12}xy + 3a_{03}y^2 + a_{31}x^3 + 2a_{22}x^2y \\ & + 3a_{13}xy^2 + 4a_{04}y^3 + a_{41}x^4 + 2a_{32}x^3y + 3a_{23}x^2y^2 + 4a_{14}xy^3 + 5a_{05}y^4 \end{aligned} \quad (3)$$

Based on the first order partial derivatives, we can now derive a gradient vector field describing particle diffusion:

$$\vec{\nabla} f(x,y) = \overrightarrow{dc} = \begin{pmatrix} \frac{\partial f(x,y)}{\partial x} \\ \frac{\partial f(x,y)}{\partial y} \end{pmatrix} \quad (4)$$

As the vector field resembles the steepest slope of concentration gradient at any given coordinate of the simulation, it can be understood as a roadmap for extracellular particles. Comparing the vector fields derived from simulations conducted in presence or absence of high-avidity binding sites on target cells, therefore, allows to us to estimate the effect of CCPs on nanoparticle transport on a micrometer-scale (Fig. 3).

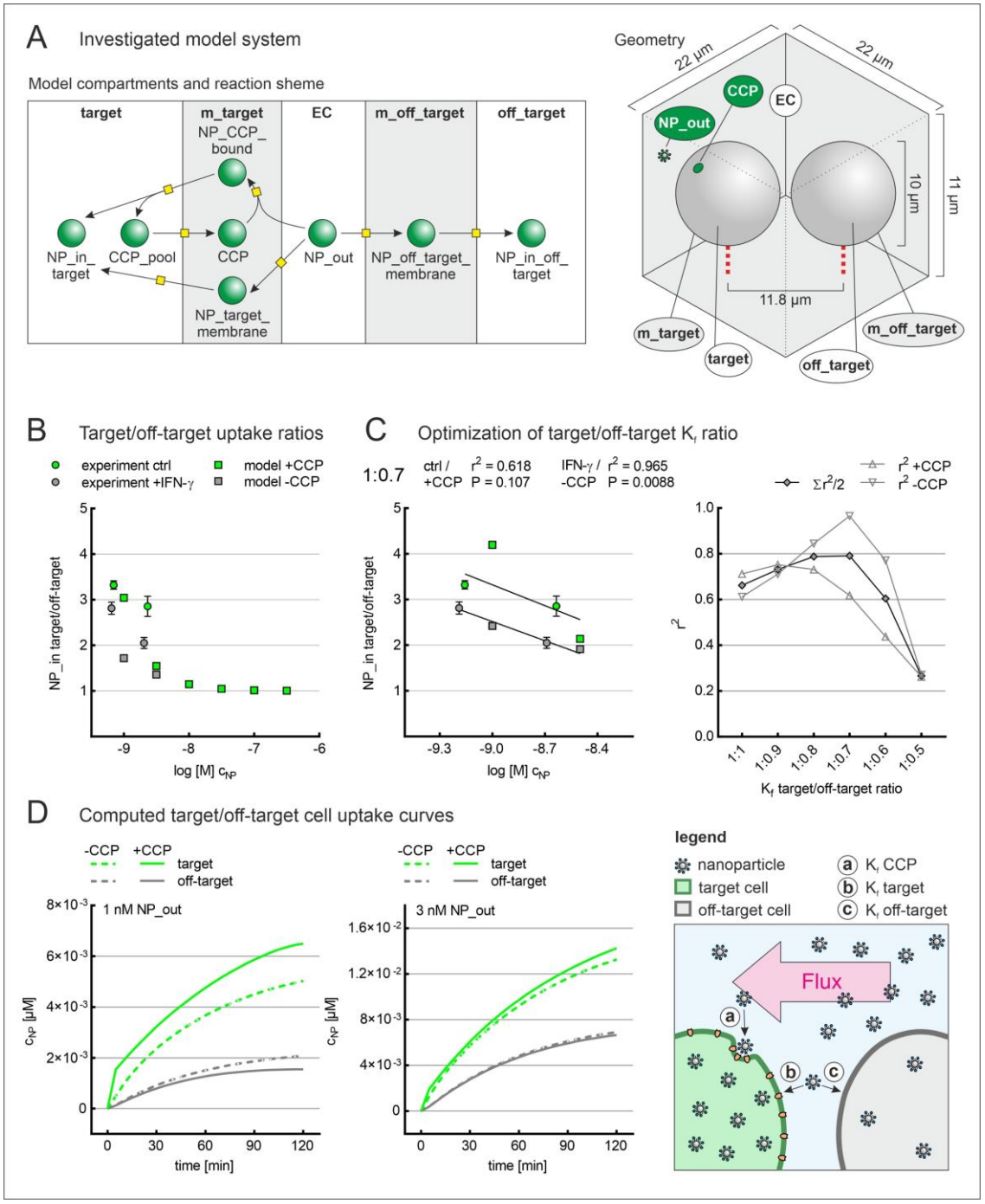

Figure 1: Simulations of target/off-target nanoparticle distribution in a two-cell model. (A) Illustration of the used compartment model containing the five spaces defined as well as all processes to be considered in the simulations is presented next to the accompanying geometrical model to which it was applied to investigate nanoparticle target/off-target distribution. (B) Results of initial preliminary simulations for a particle concentration range of 1 nM to 300 nM. Binding parameters were chosen to be K_f^{CCP} = 50, K_f^{target} = 1, and $K_f^{off\text{-}target}$ = 1. Results of the conducted simulations (cubes) were compared to data derived from experimental observations (circles). (C) To obtain a better estimation of the K_f^{target} / $K_f^{off\text{-}target}$ ratio, a set of simulations was conducted for the two experimentally investigated nanoparticle concentrations. This time, investigating a

series of decreasing values $K_f^{off\text{-}target}$ while K_f^{target} was kept constant. To identify the ratio in best alignment with experimental data, the correlation coefficient (r^2) was calculated for data simulated accounting for presence or absence of CCPs. To obtain a parameter describing the overall fit of the respective ratio, the mean r^2 was calculated (denoted as $\sum r^2/2$). Further simulations were conducted using the K_f^{target} / $K_f^{off\text{-}target}$ ratio for which the highest value $\sum r^2/2$ was determined. (D) Intracellular particle concentration for target and off-target cell over time in presence (solid lines) and absence (dashed lines) of CCPs. Data is presented for initial extracellular particle concentrations of 1 and 3 nM. The accompanying scheme illustrates the assumed underlying processes. As target cells appear to take up a greater number of particles more rapidly compared to off-target cells, it is conceivable that a particle concentration gradient will build up inducing a target cell oriented nanoparticle flux. Abbreviations: CCP - clathrin-coated pit, CCP_pool - hypothetical reservoir of clathrin pits from which new CCPs form on the membrane, EC - extracellular compartment, m_(off)_target - target (off-target) cell membrane, NP_CCP_bound - nanoparticle attached to CCP, NP_in_(off)_target - particle concentration in (off-) target cell, NP_(off)_target_membrane - particles attached to (off-) target membrane, NP_out - extracellular nanoparticle concentration, (off-) target - intracellular (off-) target compartment.

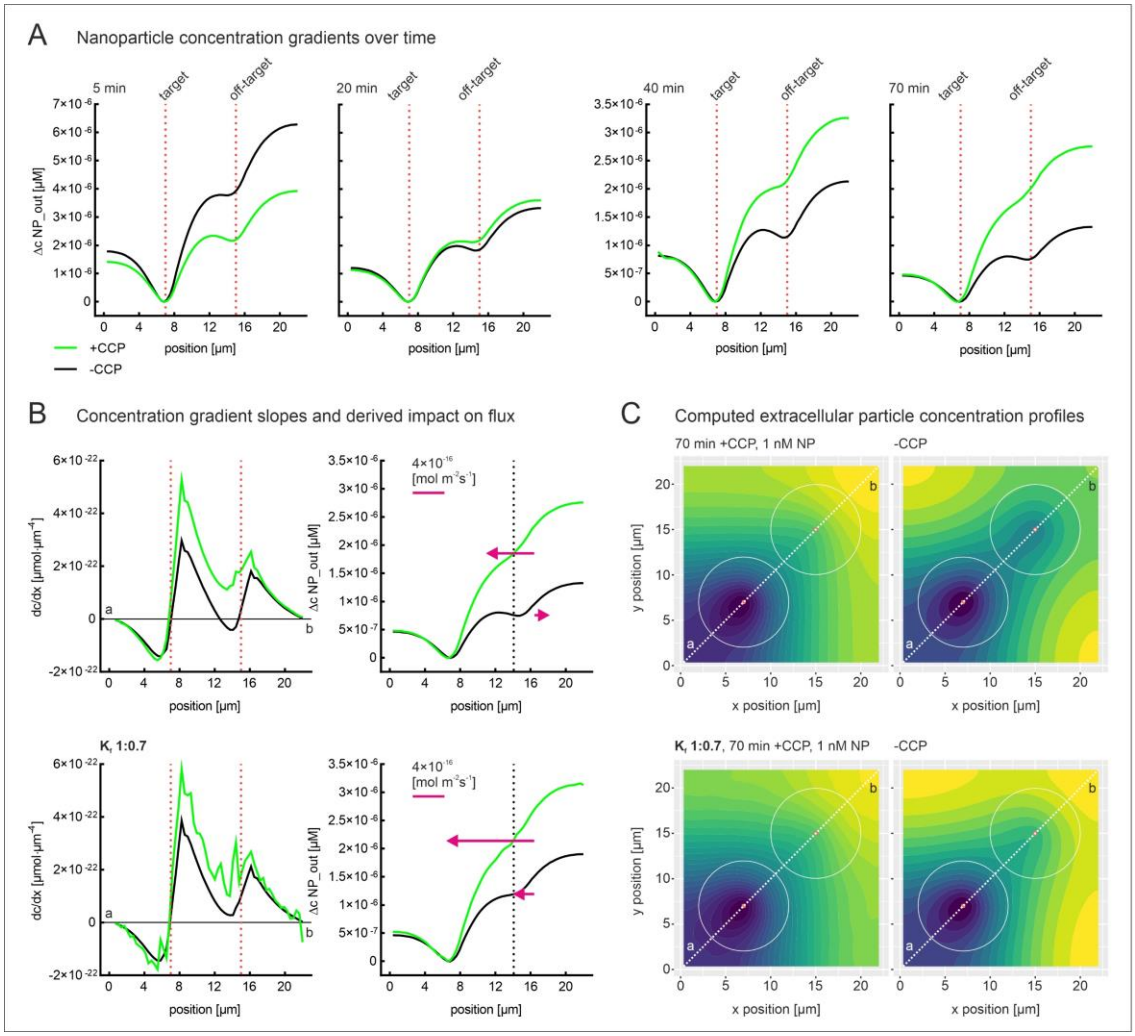

Figure 2: Extracellular particle concentration gradients and resulting particle flux. (A) The extracellular particle concentration gradient Δc was plotted against the coordinates of the diagonal running through both cell midpoints. The gradient is presented for simulation run in presence (green) or absence (black) of high-avidity binding sites. Plots illustrate gradients obtained at early timepoints (5 and 20 min) as well as mid- to late-stage (40 and 70 min) timepoints. (B) Based on the particle concentration gradient, the particle flux was calculated according to Fick's first law $J = -D(dc/dx)$. For this, the particles diffusion coefficient D was derived from nanoparticle tracking data, obtained from the particle lot also used for experimental target/off-target cell co-culture distribution studies. (C) The concentration gradients found in the xy-plane directly above the cells were plotted after 70 min simulation time. Data is presented for simulations ran in presence or absence of CCPs as well as applying a K_f^{target} / $K_f^{off\text{-}target}$ ratio of 1/1 or 1/0.7 respectively (white dashed circles indicate cell outlines). These graphs visualize that for a K_f^{target} / $K_f^{off\text{-}target}$ of 1 a diffusion barrier is established at this point in the simulation, while for a K_f^{target} / $K_f^{off\text{-}target}$ of 0.7 the slope of the concentration gradient is dramatically reduced.

Table 1: Parameters determined via polynomial fitting of simulation data. See equation 1 for the functional equation of the polynomial.

parameter	50, 1, 1	1, 1, 1	50, 1, 0.7	1, 1, 0.7
a_{00}	1.83E-05	6.13E-06	1.52E-05	1.13E-05
a_{10}	-5.64E-06	-2.22E-06	-5.78E-06	-3.64E-06
a_{01}	-4.44E-06	-1.15E-06	-3.35E-06	-2.55E-06
a_{20}	9.37E-07	5.19E-07	1.02E-06	6.86E-07
a_{11}	2.57E-07	-2.63E-07	2.00E-07	-3.73E-08
a_{02}	7.74E-07	3.49E-07	6.54E-07	5.24E-07
a_{30}	-5.29E-08	-2.97E-08	-5.86E-08	-3.88E-08
a_{21}	-6.74E-08	-2.52E-08	-7.35E-08	-4.26E-08
a_{12}	1.57E-08	5.21E-08	2.43E-08	3.59E-08
a_{03}	-7.01E-08	-4.17E-08	-6.43E-08	-5.31E-08
a_{40}	8.62E-10	4.00E-10	9.66E-10	5.84E-10
a_{31}	4.33E-09	2.27E-09	4.91E-09	3.09E-09
a_{22}	-4.24E-10	-1.27E-09	-6.16E-10	-8.83E-10
a_{13}	-3.06E-10	-2.08E-09	-5.45E-10	-1.31E-09
a_{04}	2.87E-09	2.01E-09	2.72E-09	2.34E-09
a_{41}	-5.15E-11	-1.35E-11	-6.03E-11	-2.88E-11
a_{32}	-6.75E-11	-5.32E-11	-7.53E-11	-5.86E-11
a_{23}	6.19E-11	7.44E-11	7.16E-11	6.80E-11
a_{14}	-1.82E-11	1.54E-11	-1.86E-11	1.32E-12
a_{05}	-4.25E-11	-3.34E-11	-4.07E-11	-3.68E-11

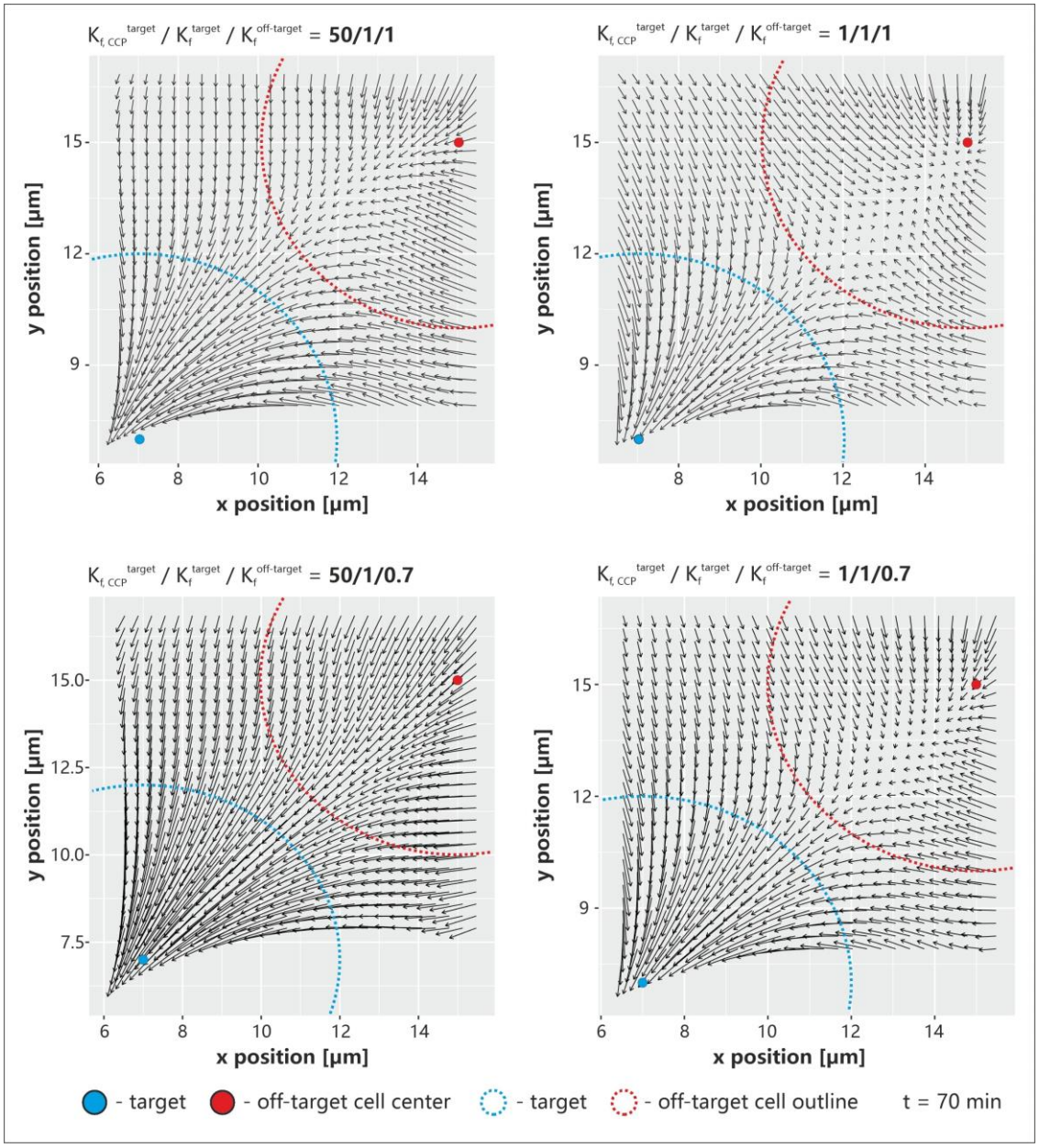

Figure 3: Plots of vector fields $\vec{\nabla} f(x,y) = \overrightarrow{dc}$ over simulation coordinates. Vector fields derived from polynomial fittings of extracellular particle concentration gradients derived from simulations. All four relevant settings regarding particle attachment reaction rates ($K_{f,CCP}^{target}$ / K_f^{target} / $K_f^{off\text{-}target}$) are illustrated. Data underlying the calculated vector fields was obtained from simulations with an initial extracellular particle concentration of 1 nM at the 70 min time-point. Starting points of the plotted vectors resemble the simulation coordinate in the extracellular particle concentration gradient. Vector direction and length are determined by the two principal gradients in x- and y-direction obtained by the partial first order derivatives $\partial f(x,y)/\partial x$ and $\partial f(x,y)/\partial y$ (i.e., arrow length corresponds to the steepness of the gradient slope). To facilitate orientation the cell positions are indicated (blue circles and dashed lines represent target cell center/outline; red circles and dashed lines represent off-target cell center/outline).

Discussion

In the presented computational investigations, we conducted simulations aiming to investigate the target/off-target distribution of nanoparticles. Our primary interest was the effect of varying particle attachment behavior on this distribution. The found target/off-target ratios were in excellent alignment with experimental distribution data. This observation supports the relevance of our model and indicates an acceptable accuracy of our parameterization. Also, depletion of high-avidity binding sites on target cells induced a decrease in nanoparticle target cell specificity. The magnitude of this shift was again comparable to experimental observations [2].

Despite this good agreement, it is necessary to point out simplifications and assumptions we made in setting up our model. Thus, we assumed all processes considered in the simulations to be first-order reactions. In this way, for example, the regulatory apparatus of CCP formation is disregarded. However, we consider this simplification permissible in this case since we were primarily interested in the presence or absence of CCPs in our simulations. Their exact molecular composition at each time point was less relevant for our purpose. Moreover, we considered the binding avidity relatively. Thus, we set the reaction constant for attachment of a particle to a flat target cell membrane equal to 1. We then accounted for binding to a CCP by increasing the reaction constant by the experimentally determined factor of 50. This factor corresponds to the decrease in avidity observed in binding studies after depleting CCPs on target cells. This simplification was necessary because, although we were able to determine values for avidity in our experimental binding studies, the determinant kinetic parameters k_{on} and k_{off} were inaccessible in the conducted functional assay [1].

Finally, we consider the results of our work in light of our initial hypothesis. Here, the derivation of vector fields $\vec{\nabla} f(x,y) = \overrightarrow{dc}$ from ploynomial fits of extracellular particle concentration gradients has provided insight. It was clearly shown that depletion of CCPs has massive influence on the behavior of extracellular particles. While in presence of CCPs a clear directional flow of particles towards the target cell is given, in absence of CCPs this flow is extremely slowed down or even reversed. This constitutes the formation of diffusion barriers. Consequently, since these diffusion barriers occur near off-target cells, it is likely that there will be a prolonged residence of particles in close

proximity to off-target cells. In this way, the computer-based studies presented here help to consolidate our experimental observations. They show that influencing binding sites on the nanometer scale can indeed have an impact on particle behavior on the micrometer scale relevant for particle distribution at a cellular level. Thus, they provide additional supportive evidence for our hypothesis that IFN-g leads to a loss of target cell specificity of nanoparticles through depletion of CCPs.

Conclusion

In a simple model system consisting of one target cell and one off-target cell, our simulations demonstrated that the absence of high-avidity binding sites on target cells (i.e., CCPs) results in a collapse of the extracellular particle concentration gradient driving target cell specific accumulation. The theoretical studies presented in this chapter thus consolidate the results of the experimental findings presented in the thesis, as they show that perturbing avidity-determining binding sites on target cells can indeed result in a massive change in target/off-target cell distribution of nanoparticles (e.g., upon IFN-γ exposure).

The particle ratios in target and off-target cell were in good correspondence to the distribution found in experiments. Therefore, these findings provide additional supportive evidence for our hypothesis that the observed effects of IFN-γ on particle distribution in cell co-culture occurred due to depletion of CCPs. This additional evidence is of great significance because there is no experimental evidence on the effect of IFN-γ on the morphology of CCPs available to date.

References

[1] O. Zimmer, A. Goepferich, How clathrin-coated pits control nanoparticle avidity for cells, Nanoscale horizons 8 (2023) 256–269.

[2] O. Zimmer, M. Walter, M. Remmert, O. Maier, R. Witzgall, A. Goepferich, Impact of interferon-γ on the target cell tropism of nanoparticles, Journal of controlled release official journal of the Controlled Release Society 362 (2023) 325–341.

[3] Q.D. Zhou, X. Chi, M.S. Lee, W.Y. Hsieh, J.J. Mkrtchyan, A.-C. Feng, C. He, A.G. York, V.L. Bui, E.B. Kronenberger, A. Ferrari, X. Xiao, A.E. Daly, E.J. Tarling, R. Damoiseaux, P.O. Scumpia, S.T. Smale, K.J. Williams, P. Tontonoz, S.J. Bensinger, Interferon-mediated reprogramming of membrane cholesterol to evade bacterial toxins, Nature immunology 21 (2020) 746–755.

[4] M. Blanc, W.Y. Hsieh, K.A. Robertson, K.A. Kropp, T. Forster, G. Shui, P. Lacaze, S. Watterson, S.J. Griffiths, N.J. Spann, A. Meljon, S. Talbot, K. Krishnan, D.F. Covey, M.R. Wenk, M. Craigon, Z. Ruzsics, J. Haas, A. Angulo, W.J. Griffiths, C.K. Glass, Y. Wang, P. Ghazal, The transcription factor STAT-1 couples macrophage synthesis of 25-hydroxycholesterol to the interferon antiviral response, Immunity 38 (2013) 106–118.

[5] S.-Y. Liu, R. Aliyari, K. Chikere, G. Li, M.D. Marsden, J.K. Smith, O. Pernet, H. Guo, R. Nusbaum, J.A. Zack, A.N. Freiberg, L. Su, B. Lee, G. Cheng, Interferon-inducible cholesterol-25-hydroxylase broadly inhibits viral entry by production of 25-hydroxycholesterol, Immunity 38 (2013) 92–105.

[6] A. Baldán, D.D. Bojanic, P.A. Edwards, The ABCs of sterol transport, Journal of Lipid Research 50 Suppl (2009) S80-5.

[7] N. Zelcer, C. Hong, R. Boyadjian, P. Tontonoz, LXR regulates cholesterol uptake through Idol-dependent ubiquitination of the LDL receptor, Science (New York, N.Y.) 325 (2009) 100–104.

[8] J.G. Cyster, E.V. Dang, A. Reboldi, T. Yi, 25-Hydroxycholesterols in innate and adaptive immunity, Nature reviews. Immunology 14 (2014) 731–743.

[9] J. Luo, H. Yang, B.-L. Song, Mechanisms and regulation of cholesterol homeostasis, Nature reviews. Molecular cell biology 21 (2020) 225–245.

[10] M.S. Brown, J.L. Goldstein, Cholesterol feedback: from Schoenheimer's bottle to Scap's MELADL, Journal of Lipid Research 50 Suppl (2009) S15-27.

[11] A. Radhakrishnan, Y. Ikeda, H.J. Kwon, M.S. Brown, J.L. Goldstein, Sterol-regulated transport of SREBPs from endoplasmic reticulum to Golgi: oxysterols

block transport by binding to Insig, Proceedings of the National Academy of Sciences of the United States of America 104 (2007) 6511–6518.

[12] N. Sever, T. Yang, M.S. Brown, J.L. Goldstein, R.A. DeBose-Boyd, Accelerated degradation of HMG CoA reductase mediated by binding of insig-1 to its sterol-sensing domain, Molecular cell 11 (2003) 25–33.

[13] B.-L. Song, R.A. DeBose-Boyd, Ubiquitination of 3-hydroxy-3-methylglutaryl-CoA reductase in permeabilized cells mediated by cytosolic E1 and a putative membrane-bound ubiquitin ligase, Journal of Biological Chemistry 279 (2004) 28798–28806.

[14] A. Subtil, I. Gaidarov, K. Kobylarz, M.A. Lampson, J.H. Keen, T.E. McGraw, Acute cholesterol depletion inhibits clathrin-coated pit budding, PNAS 96 (1999) 6775–6780.

[15] S.K. Rodal, G. Skretting, O. Garred, F. Vilhardt, B. van Deurs, K. Sandvig, Extraction of cholesterol with methyl-beta-cyclodextrin perturbs formation of clathrin-coated endocytic vesicles, Mol. Biol. Cell. 10 (1999) 961–974.

[16] P. Kozik, N.A. Hodson, D.A. Sahlender, N. Simecek, C. Soromani, J. Wu, L.M. Collinson, M.S. Robinson, A human genome-wide screen for regulators of clathrin-coated vesicle formation reveals an unexpected role for the V-ATPase, Nature cell biology 15 (2013) 50–60.

[17] T. Furuchi, K. Aikawa, H. Arai, K. Inoue, Bafilomycin A1, a specific inhibitor of vacuolar-type H(+)-ATPase, blocks lysosomal cholesterol trafficking in maceophages, J. Biol. Chem. 268 (1993) 27345–27348.

[18] P. Dogra, J.D. Butner, Y.-L. Chuang, S. Caserta, S. Goel, C.J. Brinker, V. Cristini, Z. Wang, Mathematical modeling in cancer nanomedicine: a review, Biomedical microdevices 21 (2019) 40.

[19] N. Sahai, M. Gogoi, N. Ahmad, Mathematical Modeling and Simulations for Developing Nanoparticle-Based Cancer Drug Delivery Systems: A Review, Curr Pathobiol Rep 9 (2021) 1–8.

[20] X. Zhang, G. Ma, W. Wei, Simulation of nanoparticles interacting with a cell membrane: probing the structural basis and potential biomedical application, NPG Asia Mater 13 (2021).

[21] S.H. Hansen, K. Sandvig, B. van Deurs, Internalization efficiency of the transferrin receptor, Experimental cell research 199 (1992) 19–28.

[22] M. Ehrlich, W. Boll, A. van Oijen, R. Hariharan, K. Chandran, M.L. Nibert, T. Kirchhausen, Endocytosis by random initiation and stabilization of clathrin-coated pits, Cell 118 (2004) 591–605.

[23] E. Boucrot, S. Saffarian, R. Massol, T. Kirchhausen, M. Ehrlich, Role of lipids and actin in the formation of clathrin-coated pits, Experimental cell research 312 (2006) 4036–4048.

Chapter 8

Summary & Conclusion

Summary

In the field of targeted nanomedicine, ligand-functionalization of nanoparticles is a widely applied approach aiming for tissue or even cell specific delivery of therapeutic payloads. The rationale behind this concept is a preferential accumulation of the ligand-decorated particle in the desired target compartment over off-target compartments occurring due to recognition of tissue or cell specific receptors. Therefore, this concept is expected to increase therapeutic efficacy and reduce side effects [1]. However, while a considerable number of systems designed based on this concept shows promising performance in *in-vitro* tests investigating target recognition and pharmacological efficacy, clinical translation remains a major challenge and most frequently an unmet goal [2–5]. It is particularly interesting to note that the most common reasons for failure in clinical development are (1) insufficient efficacy and (2) intolerable side effects [2,3]. Precisely the points that the concept of ligand-functionalized particles aims to tackle. Causes for these unsatisfactory observations can be found in the extensively studied *in-vivo* biodistribution of ligand-functionalized nanoparticles. Whole-body distribution studies confirm that particles, despite a receptor specific ligand decoration and confirmed strong binding to target cells, tend to accumulate in typical off-target organs (e.g., liver and spleen) [6,7]. Often only a small one digit percentage of the initial particle dose reaches the desired target compartment **(Chapter 1)**.

This discrepancy between theoretical concept and the actual observed *in-vivo* distribution of ligand-functionalized particles was the initial spark that inspired this work. It appeared to us that a piece of the puzzle was missing in our understanding of the interaction of nanoparticles with their target cells. We saw a need to broaden our view on this topic and thus decided to turn to a fundamental research approach to find missing aspects in the description of these interactions and to fill gaps in our knowledge. Our goal was to identify new causal factors for unsatisfactory distribution of ligand-functionalized nanoparticles.

The core of the concept of ligand-functionalized nanoparticles lies in the binding of the particles to their target cells via the formation of ligand-receptor interactions. Due to the multivalent nature of the particles, the particle binds much stronger than a single ligand. This phenomenon is described as the avidity effect. The equivalent binding property of a particle to the affinity of a single ligand is called avidity. The phenomenon of avidity

effect and avidity of particles have been previously studied in the literature [8–10]. However, in the vast majority of cases on artificial membranes or on cell membranes that had to be isolated for the study [11–13]. A drawback of these studies is that in the production of artificial membranes, morphological structures on the scale of nanometers that occur in natural membranes cannot be reproduced. These structures are also not preserved during the isolation of cell membranes. As for this reason, the influence of nanometer-sized morphological structures in the membrane is not known, our goal was to investigate this influence. Specifically, clathrin-coated pits (CCPs) were identified as structures that excellently match typical ligand-functionalized particles in terms of size and geometry. For this reason, it can be assumed that a significantly higher number of ligand-receptor binding can be formed when binding occurs in a CCP compared to a flat membrane section. We hypothesized that CCPs act as binding hotspots for nanoparticles and significantly determine avidity. This hypothesis was strengthened by preliminary theoretical work in the literature on the dependence of particle-membrane interactions on membrane curvature [14–16].

A model system was used to investigate the influence of CCPs on the binding of ligand-functionalized nanoparticles. This consisted of an angiotensin II functionalized particle whose binding to AT_1 receptor-bearing cells was measured. Inhibitors known from the literature that can freeze CCPs at different levels of maturation were used here. By comparing particle binding to inhibitor-pretreated and untreated cells, the influence of CCP geometry on particle binding was studied. Up to a 50-fold decrease in avidity was observed in the absence of dome-shaped CCPs, which have the best geometric match to the model particle. In addition to the experimental investigation, a theoretical model was developed. The objective of this model was to predict the change in particle avidity resulting from an induced absence of CCPs. Briefly, a ratio of the membrane area, matching the curvature of the particle, to that of the total particle surface area was formed. The particle valency was corrected for this ratio and the obtained effective ligand concentration was inserted into a classical binding model. This model allowed us to calculate particle avidity for any given degree of geometrical alignment with the membrane. Experimental data and the model-based predictions of avidity decrease derived from data on CCP geometry published in literature [17] showed excellent agreement **(Chapter 3, *SI Chapter 4*)**.

In the studies presented in the previous chapter, we considered the particle-membrane interaction isolated. However, we wondered what significance the gained knowledge might have for the overall process of particle distribution between target and non-target cells. Since we previously employed methods to achieve “artificial” downregulation of CCPs, we wondered what factors might naturally influence the formation of CCPs and thus affect the avidity of ligand-functionalized particles "in real life" (see Scheme below). In this context, we became aware of Interferon-γ (IFN-γ), which inhibits tropism of some viruses, i.e., prevents them from accumulating in their preferred tissues [18]. Given the similarity between viral pathogens and ligand-functionalized nanoparticles considering size and geometry as well as receptor-mediated target cell recognition, we hypothesized, for IFN-γ to have comparable effects on particle accumulation in desired target compartments. The fact that IFN-γ lowers cell membrane cholesterol levels via activation of CH25H [19], which is known to induce depletion of CCPs [20], strengthens our hypothesis. Also, IFN-γ is known to be present in significantly higher concentrations in tumor tissue compared to healthy tissue. Thus, negative effects of IFN-γ on target cell-specific accumulation of particles could be highly relevant to nanotherapeutic approaches for tumor treatment.

To investigate our hypothesis, we again employed a model system to study the distribution of particles between target and non-target cells. For this purpose, we used target/non-target cell co-cultures. To allow transfer of the findings from the experiments on the effect of CCPs on particle avidity to these studies, we performed the experiments with the same model particle. For the same reason, we used the identical AT_1 receptor-bearing cell line as before as target cells in the co-cultures. It was observed that IFN-γ strongly affected the distribution of the model particle and almost completely suppressed target cell-specific accumulation, especially at low particle concentrations. While in control experiments approximately 9 times more target cells had taken up particles compared to non-target cells, this ratio was almost balanced after IFN-γ treatment **(Chapter 5, *SI Chapter 6*)**. Transferred to the use case of a targeted nanoparticle-based therapy, this would be tantamount to a complete failure of the intended targeting concept.

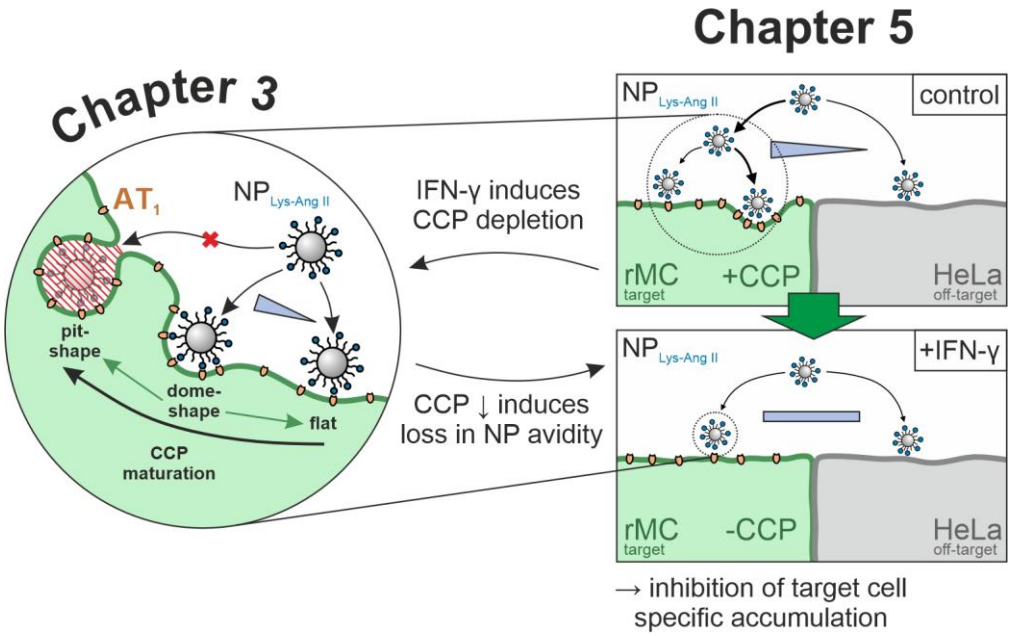

Scheme illustrating the interplay of the presented experimental chapters. Chapter 3 isolated considers the influence of CCP geometry on the binding avidity of the model particle $NP_{Lys\text{-}Ang\ II}$. It was found that the presence of dome-shaped CCPs strongly dictates avidity. Chapter 5 considers the distribution of the model particle between target and non-target cells and examines the influence of IFN-γ on this distribution. The known effects of IFN-γ on membrane cholesterol levels suggest that it will likely affect CCP geometry. In the context of the findings from Chapter 3, it can be concluded that the observed influence on target cell specific accumulation could be due to reduced avidity of the model particle for its target cells.

Finally, we employed computational simulations to consolidate the findings of our experimental studies. These simulations revealed the absence of high-avidity binding hotspots (i.e., CCPs) to significantly affect target-cell directed particle transport on a micrometer-scale. We observed the build-up of diffusional barriers inducing prolonged residence of particles in close proximity to off-target cells. Thus, the computer-based studies provide insights into the mechanistic connection of the experimental observations on the avidity of particles and their distribution in biological systems **(Chapter 7)**.

Conclusion

The work has identified a previously unknown factor dictating the interaction of ligand-functionalized nanoparticles with receptor carrying cells. It was shown that a geometric alignment of cell membrane and particle surface can shift the avidity by orders of magnitude. Furthermore, the cytokine Interferon-γ was identified as a factor influencing the biodistribution of nanoparticles, which possibly counteracts tissue specific deposition in tumor targeting. Computer-based studies, finally, provided evidence for the mechanistic relationship of the experimental observations. These studies suggest that the lack of a membrane-particle surface alignment may lead to the breakdown of target cell directed particle flow. Thus, prolonged retention of particles in proximity to nontarget cells is induced, increasing unintended particle exposition of these cells.

References

[1] M.J. Mitchell, M.M. Billingsley, R.M. Haley, M.E. Wechsler, N.A. Peppas, R. Langer, Engineering precision nanoparticles for drug delivery, Nature reviews. Drug discovery 20 (2021) 101–124.

[2] J. Chen, Z. Guo, H. Tian, X. Chen, Production and clinical development of nanoparticles for gene delivery, Molecular therapy. Methods & clinical development 3 (2016) 16023.

[3] A.C. Anselmo, S. Mitragotri, Nanoparticles in the clinic: An update, Bioengineering & translational medicine 4 (2019) e10143.

[4] W. Zhang, D.S. Kohane, Keeping Nanomedicine on Target, Nano letters 21 (2021) 3–5.

[5] S. Đorđević, M.M. Gonzalez, I. Conejos-Sánchez, B. Carreira, S. Pozzi, R.C. Acúrcio, R. Satchi-Fainaro, H.F. Florindo, M.J. Vicent, Current hurdles to the translation of nanomedicines from bench to the clinic, Drug delivery and translational research 12 (2022) 500–525.

[6] J.P.M. Almeida, A.L. Chen, A. Foster, R. Drezek, In vivo biodistribution of nanoparticles, Nanomedicine (London, England) 6 (2011) 815–835.

[7] H. Lee, B. Hoang, H. Fonge, R.M. Reilly, C. Allen, In vivo distribution of polymeric nanoparticles at the whole-body, tumor, and cellular levels, Pharmaceutical research 27 (2010) 2343–2355.

[8] M. Mammen, S.-K. Choi, G.M. Whitesides, Polyvalent Interactions in Biological Systems: Implications for Design and Use of Multivalent Ligands and Inhibitors, Angewandte Chemie International Edition 37 (1998) 2754–2794.

[9] A.J. Simnick, C.A. Valencia, R. Liu, A. Chilkoti, Morphing low-affinity ligands into high-avidity nanoparticles by thermally triggered self-assembly of a genetically encoded polymer, ACS nano 4 (2010) 2217–2227.

[10] J. Wang, J. Min, S.A. Eghtesadi, R.S. Kane, A. Chilkoti, Quantitative Study of the Interaction of Multivalent Ligand-Modified Nanoparticles with Breast Cancer Cells with Tunable Receptor Density, ACS nano 14 (2020) 372–383.

[11] H. Jung, A.D. Robison, P.S. Cremer, Multivalent ligand-receptor binding on supported lipid bilayers, Journal of structural biology 168 (2009) 90–94.

[12] S. Block, V.P. Zhdanov, F. Höök, Quantification of Multivalent Interactions by Tracking Single Biological Nanoparticle Mobility on a Lipid Membrane, Nano letters 16 (2016) 4382–4390.

[13] D. Di Iorio, M.L. Verheijden, E. van der Vries, P. Jonkheijm, J. Huskens, Weak Multivalent Binding of Influenza Hemagglutinin Nanoparticles at a Sialoglycan-Functionalized Supported Lipid Bilayer, ACS nano 13 (2019) 3413–3423.

[14] J. Agudo-Canalejo, R. Lipowsky, Adhesive Nanoparticles as Local Probes of Membrane Curvature, Nano letters 15 (2015) 7168–7173.

[15] M Deserno, T Bickel, Wrapping of a spherical colloid by a fluid membrane, Europhysics Letters (EPL) 62 (2003) 767–774.

[16] Q. Yu, S. Othman, S. Dasgupta, T. Auth, G. Gompper, Nanoparticle wrapping at small non-spherical vesicles: curvatures at play, Nanoscale 10 (2018) 6445–6458.

[17] N.J. Agrawal, J. Nukpezah, R. Radhakrishnan, Minimal mesoscale model for protein-mediated vesiculation in clathrin-dependent endocytosis, PLoS computational biology 6 (2010) e1000926.

[18] G. McFadden, M.R. Mohamed, M.M. Rahman, E. Bartee, Cytokine determinants of viral tropism, Nature reviews. Immunology 9 (2009) 645–655.

[19] J. Zhao, J. Chen, M. Li, M. Chen, C. Sun, Multifaceted Functions of CH25H and 25HC to Modulate the Lipid Metabolism, Immune Responses, and Broadly Antiviral Activities, Viruses 12 (2020).

[20] S.K. Rodal, G. Skretting, O. Garred, F. Vilhardt, B. van Deurs, K. Sandvig, Extraction of cholesterol with methyl-beta-cyclodextrin perturbs formation of clathrin-coated endocytic vesicles, Mol. Biol. Cell. 10 (1999) 961–974.

Appendix

Abbreviations

^{1}H-NMR Proton nuclear magnetic resonance

25-HC 25-Hydroxycholesterol

^{67}GA-DTPA Gallium-67 labeled diethylenetriaminepentaacetic acid

AFM Atomic force microscopy

APC Allophycocyanin

Apt Aptamer

AT_1R Angiotensin II subtype 1 receptor

AuNP Gold nanoparticles

Baf A1 Bafilomycin A1

BLI Biolayer interferometry

CCP Clathrin-coated pit

CH25H Cholesterol 25-hydroxylase

CI 95% 95% Confidence intervall

CT Computed tomography scan

CTDR Cell-tracker deep red

CTG Cell-tracker green

ctrl control

DAG Diacylglycerol

DLS Dynamic light scattering

DOTA 1,4,7,10-Tetraazacyclododecane-1,4,7,10-tetraacetic acid

Dyn Dynasore

EGFR Epidermal growth factor receptor

ELISA Enzyme-linked immunosorbent assay

EM-cluster analysis Expectation maximization cluster analysis

EpCAM Epithelial cell adhesion molecule

Eq. Equation

ER Endoplasmic reticulum

ErbB2 Human epidermal growth factor receptor 2

Exp3174 Losartan carboxylic acid

FITC Fluorescein

Fura-2 AM Fura-2 acetoxymethylester

GNPs Glucose-coated gold nanoparticles

HA Hyaluronic acid

HER2 Human epidermal growth factor receptor 2

HRP Horseradish peroxidase

ICAM-1 Intercellular adhesion molecule-1

ID Initial dose

IFN-α/β Interferon-α/β

IFN-γ Interferon-γ, Interferon-γ

IgG Immunoglobulin G

IP_3 Inositol trisphosphate

$\log EC_{50}$ Logarithmic half-maximum effect concentration

LPS Lipopolysaccharide

Lys-Ang II Lysin-angiotensin II

Mab Monoclonal antibody

MST Microscale thermophoresis

M-β-CD Methyl-β-cyclodextrin

NIR Near infrared

$NP_{Lys\text{-}Ang\ II}$ Lysin-angiotensin functionalized nanoparticle

O/W Oil-in-water

PAMAM Poly (amidoamine)

PCR Polymerase chain reaction

PDI Polydispersity index

PD-L1 Programmed cell death ligand-1

PECAM-1 Platelet-endothelial cell adhesion molecule-1

PEG Poly (ethylene glycol)

PEI Poly (ethyleneimine)

PET Positron emission tomography

PLA Poly (lactic acid)

PLGA Poly (D,L-lactide-co-glycolide)

PMS Pearson's mode skewness

PSMA Prostate-specific membrane antigen

PV1 Plasmalemmal vesicle associated protein-1

PVPh Poly (4-vinylphenol)

rMC Rat mesangial cell

RSS Residual sum of square

s.c. sub cutaneous

SD Standard deviation

sem Standard error of mean

SI Supllementary information

siRNA Small interfering ribonuclein acid

SLB Supported lipid bilayer

SPR Surface plasmon resonance

TEM Transmission electron microscopy

Tf Trasferrin

TfR Transferrin receptor

TNF Tumor necrosis factor

W/O Water-in-oil

Curriculum Vitae

Personal Information

Name:	Oliver Zimmer
Date of birth:	13th of September 1992
Place of birth:	Hamburg
Nationality:	German

Scientific education and work experience

11 / 2022 to date	**Research Assistant** Department of Pharmaceutical Technology, University of Regensburg
07 / 2018 – 11 / 2022	**PhD Candidate & Research Assistant** Department of Pharmaceutical Technology, University of Regensburg
07 / 2018 – 11 / 2022	**Structured doctorate program** Graduate School ChemPharm Faculty of Chemistry and Pharmacy, University of Regensburg
07 / 2018	**Licensure as Pharmacist**
11 / 2017 – 05 / 2018	**Practical Training** Apotheke zum Ritter St. Georg, Hamburg
05 / 2017 – 11 / 2017	**Practical Training** Allergopharma GmbH & Co. KG, Reinbek
10 / 2012 – 04 / 2017	**Pharmacy Studies** University of Hamburg
05 / 2016	**Research Internship** Institute of Pharmacy, AG Lemcke University of Hamburg

School education

05 / 2012	**Abitur / A levels**
08 / 2003 – 05 / 2012	**Grammar School** Stormarnschule, Ahrensburg

List of Publications

Peer-reviewed publications

1. J. Ousingsawat, R. Centeio, I. Cabrita, K. Talbi, O. Zimmer, M. Graf, A. Goepferich, R. Schreiber, K. Kunzelmann: Airway Delivery of Hydrogel-Encapsulated Niclosamide for the Treatment of Inflammatory Airway Disease. *International journal of molecular sciences* 23 (2022)
2. O. Zimmer, A. Goepferich: How clathrin-coated pits control nanoparticle avidity for cells. *Nanoscale horizons* 8, 256-269 (2023) **(Chapter 3)**
3. O. Zimmer, M. Walter, M. Remmert, O. Maier, R. Witzgall, A. Goepferich: Impact of Interferon-γ on the Target Cell Tropism of Nanoparticles. *Journal of Controlled Release* 362, 325-341 **(Chapter 5)**

Conference abstracts

1. O. Zimmer, A. Goepferich, The Effect of Clathrin Coated Pits on the the Binding of Ligand-Functionalized Nanoparticles to Cells. *CRS Virtual Annual Meeting*, Las Vegas, United States, 2020.
2. O. Zimmer, A. Goepferich, Impact of Pravastatin Induced Membrane Cholesterol Depletion on Nanoparticle Cell Binding. *13th World Meeting on Pharmaceutics, Biopharmaceutics, and Pharmaceutical Technology*, Rotterdam, Netherlands, 2022.

Acknowledgements

First and foremost, I would like to express my deepest gratitude to Professor Achim Göpferich. I thank him for the trust he placed in me and for the opportunity to be a part of his research group as well as for our many fruitful and exciting exchanges on our research. I am especially grateful for his motivating and friendly approach with which he guided and inspired me. I appreciate the liberty granted to me in the design of the research projects carried out.

I would also like to express my special thanks to Prof Miriam Breunig. In many inspiring conversations she supported me in my research projects. In this way, she has contributed significantly to the realization of this work, for which I am very grateful.

I would also like to thank all my dear current and former colleagues at the Department of Pharmaceutical Technology in Regensburg for their support, for the pleasant working atmosphere and for some unforgettable moments.

First of all, I would like to thank Dr Sara Maslanka Figueroa and Dr Sebastian Beck for providing me with advice and support from the beginning of my work and for always having an open ear for me. Without their helpfulness, kindness, and mentorship this work would not have been possible.

I thank Jonas Groner for being a superb lab-mate, and a good friend. I am grateful for many constructive discussions on research and many other topics.

I thank Dr Monika Stahl and Dr Tobias Sonntag for being great, supportive colleagues and friends. I appreciate your humorous nature and it was always a pleasure working with you.

I thank Dr Marilena Bohley for our continuing exciting collaboration and her support during my research projects. I am grateful for Dr Christian Ziegler and

Moritz Graf who made every walk to the cellar worthwhile and hope that we will continue our unfinished projects someday.

I would like to thank Dr Stefanie Thalhauser and Dr Raphael Mietzner for their friendly and supportive nature and their support during our time together.

I thank Heike Lehr and Dr Daniel Fleischmann for their support and for always having an open ear for me from the beginning of my work.

I thank Felix Bauman for his support in the conducted computer-based studies and for staying at my side even in darkest times.

I would like to thank Melanie Walter and Kathrin Schorr for many frank discussions about my research. I thank them for their friendship and for their active support of my research projects.

Furthermore, I thank Melanie Walter, Clara Barbey, Jonas Groner and Johannes Lang for our unforgettable time in Rotterdam. You proved to be great colleagues, good friends and even quite seaworthy.

I thank Marius Remmert for carrying on my projects and for his friendship which I highly value.

I thank Stefanie Klaus, Jan Birringer, Carsten Damm, Johannes Konrad, Stephan Melchner, and Andreas Schreiber for a great atmosphere during our lunch breaks and I promise to learn Schafkopf one day.

I am grateful to Eva Wrobel for her organizational support of my work. I thank Renate Liebel, Andrea Blaimer and Viktoria Messmann for their outstanding technical assistance.

I gratefully acknowledge the financial support by the German Research Foundation.

Finally, a very special thanks goes to my family and friends without whose unconditional love and support this work would not have come about.

Declaration in lieu of oath

I hereby declare that I have completed the dissertation presented without the impermissible help of third parties, without the use of resources other than those indicated, and that any data and concepts stemming directly or indirectly from other sources are indicated with citations to the literature.

No further persons were involved with the creation of the contents of the dissertation presented. In particular, I have not made use of the assistance of a doctoral consultant or other person in return for payment. No-one has received payment in kind either directly or indirectly for work which is associated with the content of the dissertation submitted.

The dissertation has not been submitted in the same or similar form to another examining authority, neither in Germany nor abroad.

Regensburg,

_____ (Oliver Zimmer)